TEXTILE EFFLUENT TREATMENT USING TAPERED INVERSE FLUIDIZED BED REACTOR - HYDRODYNAMIC AND RTD STUDIES, AN EXPERIMENTAL AND CFD APPROACH

Submitted in partial fulfillment of the requirements for the award of the degree of

DOCTOR OF PHILOSOPHY

In

CHEMICAL ENGINEERING

By

Mr. H.UPENDER
(Roll No. 701631)

Supervisor

Dr. ANAND KISHORE KOLA
Professor

DEPARTMENT OF CHEMICAL ENGINEERING
NATIONAL INSTITUTE OF TECHNOLOGY
WARANGAL-506 004, TELANGANA, INDIA

JULY 2021

Dedicated to my beloved Parents
And my brother

NATIONAL INSTITUTE OF TECHNOLOGY WARANGAL

CERTIFICATE

This is to certify that the thesis entitled "**Textile Effluent Treatment Using Tapered Inverse Fluidized Bed Reactor - Hydrodynamic and RTD studies, an Experimental and CFD Approach"** being submitted by **Mr. H.UPENDER** in partial fulfillment for the award of the degree of Doctor of Philosophy (Ph.D.) to the Department of Chemical Engineering, National Institute of Technology Warangal, India, is a record of the bonafide research work carried out by him under my supervision. The thesis has fulfilled the requirements according to the regulations of this Institute and in my opinion has reached the standards for submission. The results embodied in the thesis have not been submitted to any other University or Institute for the award of any degree or diploma.

Date:

Prof. Anand Kishore Kola Supervisor
Department of Chemical Engineering,
National Institute of Technology Warangal

DECLARATION

This is to certify that the work presented in the thesis entitled "**Textile Effluent Treatment Using Tapered Inverse Fluidized Bed Reactor - Hydrodynamic and RTD studies, an Experimental and CFD Approach**" is a bonafide work done by me under the supervision of **Prof. ANAND KISHORE KOLA** and was not submitted elsewhere for award of any degree.

I declare that this written submission represents my ideas in my own words and where other's ideas or words have not been included. I have adequately cited and referenced the original sources. I also declare that I have adhered to all principles of academic honesty and integrity and have not misrepresented or fabricated or falsified any idea/data/fact/source in my submission. I understand that any violation of the above will be a cause for disciplinary action by the institute and can also evoke penal action from the sources which have thus not been properly cited or from whom proper permission has not been taken when needed.

Mr. H.UPENDER

Roll No. 701631

ACKNOWLEDGEMENTS

I would like to express my sincere gratitude to my beloved Supervisor. **Prof. ANAND KISHORE KOLA** for his invaluable guidance and motivation throughout my Ph.D. I am highly indebted to him for his expertise while sharing his knowledge, understanding, encouragement and patience. I am immensely thankful to him for his valuable advice, correcting all my manuscripts, progress reports, Thesis reports with great concern and commitment and spending his precious time with good discussions regarding my research work. The discussions I had with Professor Kola have immensely helped me to come out with fruitful results when I had confusion and ambiguity. He was always there to support and encourage with his positive attitude. I would like to thank him the way he provided the flexibility choosing the research topic and continue it. My special thanks to Professor Kola for allowing me to attend conferences and workshops and even visits to the Research labs as part of my research work.

I would also like to thank the Head of the Department **Dr. S. Srinath** and former HODs **Prof. Shirish Hari Sonawane, Prof. A. Sarat Babu** & **Prof. Anand Kishore Kola** for their help and advice during the course of my Ph.D work.

I wholeheartedly thank **Prof. NV Ramana Rao,** Director, NIT Warangal for permitting me to utilize the facilities at NIT Warangal and allowing me to submit this research work in the form of thesis.

Heartfelt thanks to the members of my Doctorial Scrutiny Committee (DSC); **Prof. Y. Pydi Setty, Dr. S. Srinath**, **Dr. P. Sampath Kumar** and **Dr. R. Sathish Babu** for their suggestions in carrying out this research work. I am also thankful to their constant support and encouragement.

I would like to place on record my thanks to all the faculty and staff of Chemical Engineering Department, NIT Warangal for the knowledge they have imparted to me.

I would also like to thank my fellow research scholars Mr. D. Naresh Yadav, Mr. M. Sarath Kumar, Mr. D. Kishore and Mr. P. Narasimha. I am also thankful to Mr. P. Shiva Kumar and Mr. A. Amruth Raj, of CEP, NITW for their assistance.

Special thanks to my family. Words cannot express how grateful I am to my parents for all of the sacrifices that they have made for my growth. Your prayers for me were what I am today. I would like to thank my brother and my sister for the love they have shown on me.

Last but not the least; I want to express my deepest gratitude to God Almighty for giving me such a fulfilling life with the blessings of whom I believe nothing is impossible

(H.UPENDER)

Abstract

In the present research, determination of immersed heater to bed heat transfer coefficient, and related hydrodynamics were carried out at different bed angles (8^0 and 6.8^0) of tapered inversed fluidized bed reactor. Carboxyl methyl cellulose (CMC) was used to change the water viscosity by power law model. The hydrodynamics were compared at two different bed angles. Furthermore, minimum fluidization velocities were carried out for different apparent viscosities of the liquid and different bed angles and the results were compared with previous models. The heat transfer coefficient was found to be increasing with increased liquid velocity and bed Voidage respectively. It was also found that the bed Voidage was high for high diameter particles. A correlation was developed for bed expansion ratio and independent parameters using Response surface methodology (RSM) of design expert v.9. Tapered inverse fluidized bed hydrodynamics have been investigated both experimentally and numerically for the first time in literature. A numerical study has been conducted using computational fluid dynamics (CFD), ANSYS Fluent 17.2. Different low-density spherical polymer particles; low density polyethylene (LDPE), high density polyethylene (HDPE), and Polypropylene (PP) were used as solid media with the aid of water. Eight water velocities have been considered with three initial bed heights (0.04, 0.075, and 0.1m) of solid particles at two angles of tapered fluidized bed reactor (TIBR). The expanded bed height and bed void fraction have been determined. It was compared with different drag functions such as Gidaspow, Syamlal *O'Brien*, and Wen-Yu in CFD. The multiphase flow simulation of CFD was studied using Eulerian–Eulerian approach. The experimental outcomes were compared to the results of CFD simulations in 2 and 3 dimensions in Ansys Fluent 17.2. Both experimentally and numerically, the impacts of bed expansion ratio and bed pressure drop on bed performance were explored. The Gidaspow drag function was used for numerical investigations in CFD simulations and also to analyse the effect of elasticity of particle collision on the hydrodynamic characteristics of a TIBR patched with 900 kg/m^3 particles. The simulation is conducted using Eulerian multi fluid model, which is combined with the solid particle kinetic theory. The coefficients of exchange are determined by applying Gidaspow drag function. The numerical findings were confirmed with experimental data (bed height and Voidage) and demonstrated that the model is capable of predicting hydrodynamics of TIFBR. To determine the impact of elasticity of solids collision, various estimated values of restitution coefficient (RC) (0.85 to 1.0) were used in the numerical and their results were observed in detail. Simulations were done for two various solid-phase wall boundary (0.5&1.0) conditions.

Bubble development was not found for perfectly elastic collision. The evolution of the bubble started when the restitution coefficient was set below 1.0, and the space occupied by the bubbles in the bed grown with a decrease in the restitution coefficient. In the present work, computational investigation, residence time distribution (RTD) characteristics of liquid tracer in two phase tapered inverse fluidized bed with solid materials of three different densities (900, 930, and 970 kg/m^3) at two different bed angles (α) of 8º & 6.8º have also been studied. The results were obtained by carrying out experiments for Propionic acid as pulse tracer; water as fluid media and solid particles which have lower density than water as solid media. The mean residence time and dispersion coefficient have been investigated at different parameters such as superficial liquid velocity, particle size and particle density and bed angle experimentally. The tracer mass fractions were validated with CFD using commercial CFD software. The radial and tangential profiles of tracer in mass fraction were studied by varying fluid velocity, initial bed height and density of solids using CFD simulations. It was indicated that the liquid tracer mean residence time and axial dispersion coefficient depend effectively on particle density, bed angle, and superficial liquid velocity. Based on the experimental data, empirical correlation has been developed for mean residence time of tracer using RSM. The current work also aimed to analyze the removal of pollutants from textile effluent using raw wheat bran adsorbent prepared by coating low-density Polypropylene (PP) particles by batch experimental studies. The batch adsorption studies were performed for 36 hrs. The central composite design (CCD) technique was utilized to ascertain the impact of initial concentration, adsorbent dose, and pH on the removal of dye, COD, Turbidity and DO enhancement. The data obtained from experimental parameters were analyzed through the fitting of kinetic models like isothermal. The obtained coated raw wheat bran on PP was tested as an adsorbent. Prepared raw wheat bran was characterized by FTIR, SEM, and EDS. The obtained raw wheat bran has 58.53% carbon content. The prepared adsorbent was used to remove different pollutants from the prepared synthetic textile wastewater containing azo dye. Experiments have been conducted in batch adsorption processes with different variables such as initial dye pH, concentration, adsorbent dose and airflow timing on removal effectiveness of dye, COD, turbidity removal, and DO enhancement. Isotherm models such as Freundlich, Langmuir and Temkin were applied to batch experimental data for removal of azo dye, COD, Turbidity, and DO enhancement.

Table of Contents

LIST OF TABLES

LIST OF FIGURES

NOMENCLATURE

A	Across sectional area of the column (cm^2)
Ar	Archimedes number ($Ar=dp^3 g(\rho_l - \rho_s)\frac{1}{\mu_l^2}$)
D	column diameter (cm)
d_p	particle diameter
g	acceleration due to gravity
H	Tapered inverse fluidized bed height (cm)
H_0	Initial bed height (cm)
Δp	Pressure drop across the bed (gm/cm.sec2)
Re_t	Reynolds number at terminal velocity
Re_p	Particle Reynolds number
Re_{lmfo}	Reynolds number at minimum fluidization velocity (cm/sec)
U	Superficial liquid velocity (cm/sec)
U_{mf}	Minimum fluidization velocity (cm/sec)
a, b, c	are constants
HDPE	High-density polyethylene
LDPE	Low-density polyethylene
PP	Poly propylene
A	Surface area of the reactor (m^2)
C_p	Heat capacity of the liquid phase (J kg^{-1} K)
D_p	Particle diameter (m)
g	Gravitational acceleration (m s^{-2})
H	Bed height (m)
h	Heat transfer coefficient (w m^{-2} k)
k_L	Thermal conductivity of liquid phase
Q	Heat flow (J s^{-1})
ΔP	Pressure drop (kpa)
N_{Ga}	Galileo number
N_{Re}	Reynolds number

ΔV	Total bed volume (m^3)
V_0	Initial fixed volume (m^3)
$\dot{m}$	Mass flow rate of the liquid phase ($kg\ s^{-1}$)
q	Heat flow rate ($J\ s^{-1}$)
T	Temperature (C)
C	Outlet tracer concentration
c0	Initial concentration
M	Amount of tracer
V0	Initial Volumetric flow rate
Da	Experimental Axial Dispersion coefficient
Ul	Liquid Velocity
t	Time.
V_L	Volumetric Flow rate
(D/UL)	Vessel dispersion number
Di	Entrance Diameter of Tapered column
D2	Outer Diameter of tapered column
Dp	Size of the Particle
t_i	Outlet sample taking time
v1	Input sample volume
V2	Outlet sample volume
N1	Normality of input sample
N2	Normality of outlet sample
Ua	Auxiliary liquid velocity
Ar	Archimedes No.
D1	Top diameter of the tapered bed
D_p	Particle diameter
D_0	Bottom diameter of the tapered bed
H_s	Stagnant height of the particle bed
Greek letters	
Φ	Dimensionless radial coordinate σ^2 Variance
ρ_p	Density of fluidizing medium
θ	Apex Angle
ε	Voidage
ε_0	Fixed bed Voidage
t_m	Mean residence time
δ	Solids down flow film thickness
α	Tapered angle
ρ_s	Solid density
ϕ_s	Sphericity of solid particle

ρ_f	Fluid density
Greek symbols	
ε	Porosity of the bed
μ	Viscosity of liquid (gm/cm.sec)
ρ	density of liquid (gm/cm)
ρ	density of solids(gm/cm)
ε	Solid Voidage
α	Bed angle
ρ	Density (kg/m3)
μ	Apparent viscosity (kg m−1 s)
Subscripts s	
S	Solid phase
l	Liquid phase
h	Heater surface
o	Steady state
mf	Minimum fluidization velocity
Sq	Source term
τ q	q th phase stress-strain tensor, Pa
μq	Shear viscosity of the phase q, m s-1
λq	Bulk viscosity of phase q, m s-1
$F\ q$	External body force, N
$F\ lif\ ,$	Lift force, N
$F_{\ vm,}$	Virtual mass force, N
K_{pq}	Interphase momentum co-efficient, Kg s^{-1}
p_s	Solid pressure, Pa
K_{ls}	Fluid-solid exchange co-efficient, Kg s^{-1}
K_{pq}	Fluid-fluid exchange co-efficient, Kg s^{-1}
K_{ls}	Fluid-solid and solid-solid exchange coefficient, Kg s^{-1}
f	Drag function,
τ_p	Particulate relaxation time, s
Dp	Diameter of the bubbles of phase p, m
C	Drag co-efficient
Re	Reynolds number
μ_l	Viscosity of liquid phase, m s^{-1}
d_s	Diameter of the particles of phase s, m
$C_{f\ ,s}$	Coefficient of friction between the l^{th} and s^{th} solid Phase particles
d_l	Diameter of particle of solid l, m x
$g_{0,s}$	Radial distribution coefficient
e_{ls}	Co-efficient of restitution for particle collisions
$g_{0,s}$	Radial distribution function

Abbreviations	
SEM	Scanning electron microscope analysis
EDS	Energy dispersive X-ray spectroscopy
FTIR	Fourier transforms infrared spectroscopy
WB	Wheat bran

C_0	Initial metal concentration (mg/L)
C_t Ce	Dye concentration at equilibrium (mg/L) Equilibrium concentration in the liquid phase (kg/m^3)
R	Removal efficiency Removal
R_{Dye}	Efficiency of dye Removal efficiency
$R_{turbidity}$	Efficiency of Turbidity Removal efficiency
R_{Cod}	Efficiency of COD Removal efficiency
Vs	Volume of solution (L)
W	Weight of the adsorbent (g)
k_c	Rate coefficient ($m^3/kg.s$)
b_T	The gas constant (8.314 J/(mol.k))
k_2	The mean free energy (kJ/mol) Temkin constant (J/mol) Temkin constant related to the equilibrium binding energy (L/mg) The rate constant of pseudo first order adsorption The rate constant of pseudo second order adsorption (g/mg min)

CHAPTER - 1

INTRODUCTION

1.0 General

Inverse fluidization is a process, in which the thickness of solids is lower than that of liquid. The fluidization can be attained in the earthward direction by the downward flow of liquid. The fluidization can be operated in two ways, two phase system (liquid-solid) and three phase system (solid-liquid-gas).The hydrodynamic and Residence time distribution (RTD) studies can be carried out by experimental as well as computational fluid dynamic (CFD) simulations using solids of different density, weight and diameter and liquids of different viscosities in different angles of tapered beds. The wastewater treatment is also carried out using different adsorbents at different parameters in the tapered inverse fluidization.

1.1 Objectives of the Study

- To study the hydrodynamics of two phase tapered inverse fluidized bed with CFD simulations and experimental design module namely Response Surface methodology (RSM) for the bed expansion ratio of synthetic textile waste
- To study the Residence time distribution (RTD) at different angles of tapered inverse fluidized beds with CFD simulations and RSM for the tracer mean residence time of synthetic textile wastewater
- Wastewater treatment studies in tapered inverse fluidized bed by batch mode and experimental design module namely Response Surface methodology (RSM) for the removal of dye pollutants.

1.2 Organization of the Thesis

The thesis has been organized into five different chapters as follows.

Chapter 1 gives general introduction on hydrodynamics, RTD studies, and textile wastewater treatment by tapered inverse fluidization and its applications.

Chapter 2 presents the review of literature. The review of literatures pertains to hydrodynamics, RTD studies, and textile wastewater treatment.

Chapter 3 summarizes different methods; their importance and comparison of the existing methods with the proposed methods used in this work.

Chapter 4 explains the results and discussion on the works done in the thesis with detailed explanation.

Chapter 5 brings out conclusions of all case studies considered in the work and Recommendations for future work

1.3 Introduction to inverse fluidization

In recent times, commercial tasks for the treatment of wastewater and sewage output from many manufacturers such as distillation and wine industries utilize the inverse fluidization process because of its accessibility of operation. It is simple to handle, and is a low cost process. It is additionally has the advantages of low power intake and excessive effectiveness when contrasted with regular fluidization and other techniques. As a result of loads of special point of interest, for example, high reaching proficiency between various phases, mass-exchange rate, high heat, and low-pressure drop are advantageous schemes for persistent activity, 3-phase (gas-liquid- solid) fluidized beds was generally received as viable reactors and contractors in the areas of petrochemical, ecological, biochemical engineering and industries. In any case, in biomedical, food, and natural procedures, for example, solid materials those are, food particles, bio media and adsorbent or absorbent media were typically small, porous and less thick. Such sorts of adsorbent or permeable substrate material, whose thickness is lower than that of a steady fluid medium was sensibly fluidized by methods for the descending progression of a fluid medium. This prompts an increasingly mass exchange coefficient because of long residence time and high gas hold up.

Inverse fluidization might be practiced by a diminishing movement of predictable fluid phase counter to net lightness of lower thickness solid materials. Regardless of the way that different experimental works were completed on the distinctive physical properties and boundaries, the unpredictable hydrodynamics of inverse fluidization was not surely known taking into account the various advance affiliations prompting further bother. So, it is vital and essential to create a computational model for the two-phase inverse fluidization to be repeated

1.4 Introduction to tapered inverse fluidized bed

Inverse fluidization is the process in which, by interaction with a gas or solid, fine solids are converted into a liquid state. This technique has a variety of unusual features and fluidization engineering is concerned with making the most of this action and putting it to good use. The ease of fluidization of particles and the variety of operating conditions that support fluidization vary widely in gas-solid systems. Their ability to flow freely, agglomeration characteristics, static costs, vessel geometry, gas inlet configuration and other variables affect system fluidization features.

A conical fluidized bed could be very a good deal useful for the fluidization of a huge distribution of solids because the cross-sectional location increases along the bed height from the top to bottom of the bed, so the speed is exceedingly high at the bottom for the fluidizing medium, ensuring fluidization of the big solids and comparatively low at the top, stopping entrainment of the small particles. As the speed of the fluidizing medium at the lowest is reasonably excessive, this gives upward push to low particle awareness, for this reason resulting in low reaction time and decreased rate of heat release. Therefore the era of immoderate temperature area near the distributor can be prevented.

Because of the presence of velocity gradient of fuel through the height of tapered beds, there are a few favorable and special hydrodynamic qualities. The tapered bed has been extensively carried out in lots of manufacturing methods which consist of: Biological remedy of waste material, waste-water, Immobilized biofilm reaction, sulfide ores roasting, liquefaction and catalytic polymerization, coal gasification, sawdust and wood residue mixture fluidization contactor and compact powder fluidization.

The analysis of the hydrodynamic characteristics and RTD in tapered bed inverse fluidization studies focuses on the field of liquid-solid system. The hydrodynamic properties of tapered bed inverse fluidization, including liquid-solid structures, i.e. The fixed bed, in part of the fluidized bed and absolutely fluidized bed regimes had been defined by means of Kwauk as stated by with his principle of bubble less fluidization. Peng and Fan systematized the conditions for the progress with the flow system.

Whereas the solids weight on the top surface of the tapered bed is equivalent to or not exactly the drag force by means of liquid stream downwards, a totally fluidization takes place. The fluidization behavior for this flow is difficult to predict and is referred to as a partly fluidized bed system. These investigations are focused on idealized fluidization described by Kwauk, i.e.

As per the subsequent suspicions:

- Radial distribution of the fluid at any conical bed intersection is uniform;
- The fluid phase doesn't mix back;
- Ignoring the frictional force between the wall and the particles.

The fluidization characteristics of three flow regimes are investigated by means of a conical bed with two varies angles and a Geldart D powder, i.e. a fixed bed, a partly fluid bed and a fully fluidized bed. Its purpose is:

- Determine the hydrodynamic characteristics for liquid-solid conical inverse fluidized beds;
- Determine the RTD Studies for liquid-solid conical inverse fluidized beds;
- Determine the wastewater treatment by adsorbent studies in conical inverse fluidized bed.

1.5 Parameters influencing the performance of inverse fluidization

The quality of fluidization is affected by some of the variables such as:

Fluid inlet: Inlet flow rate of the fluid should be in that way that the fluid approaching the bed gets distributed uniformly.

Fluid flow rate: It has to be strong via to prevent the solids suspended however, this is not the case. Too high as it leads to channeling of fluid.

Bed height: Difficulty of fluidization increases with increase in bed height when the other variables are kept constant.

Particle size: Particles having wide range of sizes are used rather than the solids of uniform size to maintain fluidization.

Liquid and solid densities: To maintain smooth fluidization, the difference in relative densities of liquid and solid should be as less as possible.

Bed internals: Internals are provided in commercial fluidizers to perform the following functions:

- To stop bubble sizes from growing.
- To prevent the fluid and solids from moving laterally.
- To prevent slugging.
- To prevent fine-particle elutriation.

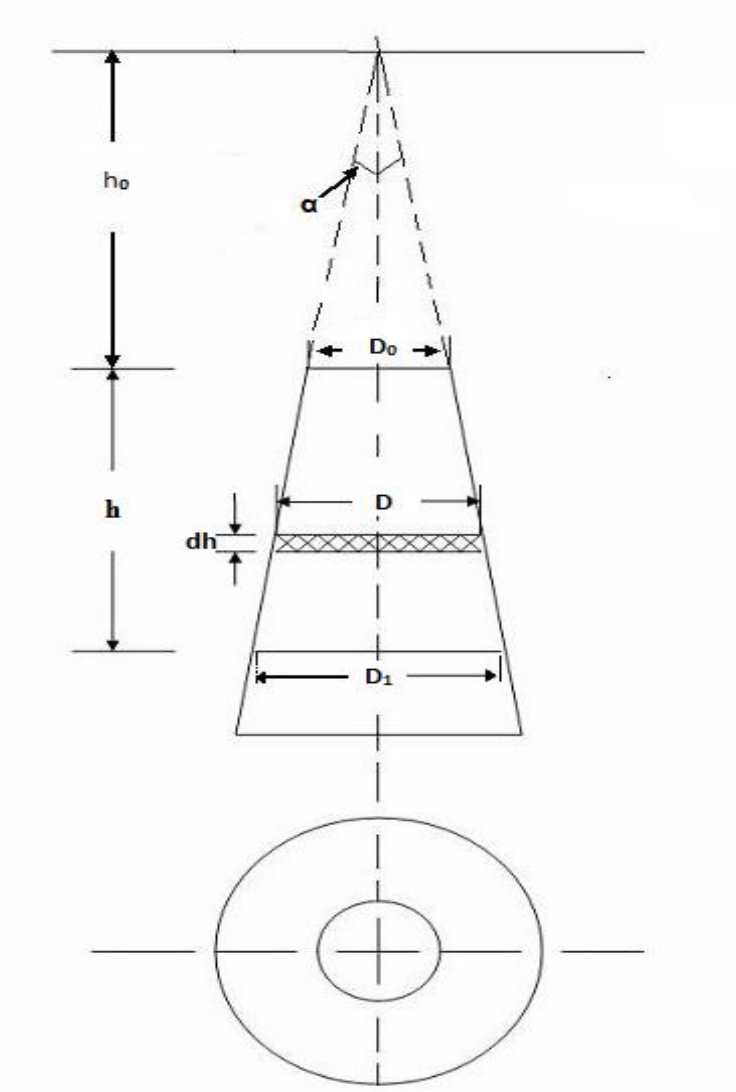

Fig-1.1 Structure of tapered inverse bed

1.6 The phenomenon of inverse fluidization

As fluid (liquid or solid) passes down via a bed of coarse solid particles, fluid at a low flow rate merely percolates between stationary particles via the void spaces. This is an adjustable bed. Particles shift apart in extended bed, and a few of them vibrate with flow rate increases. Further, the pressure drop in the bed increases at still higher velocities. The pressure drop through the bed at a particular velocity reaches a maximum value and a point is reached when the particles are just suspended in the liquid. At this particular point, the solid particles at the top of the bed start fluidizing and afterwards, the fluidization will extend from the top to the bottom of the bed and the pressure drop along the bed will decrease in a reasonable manner.

1.7 Background about the textile wastewater treatment

The textile industry is one of the most confounded ventures in the industry. Wastewater treatment is the most considerable serious issue looked by textile producers. An itemized investigation of the material cycles will uncover that there are many entangled cycles and synthetics utilized all through the creation. On account of assembling of woven polyester and cotton mixed texture, the material fundamental cycles start from fiber creation on account of manufactured fiber followed by turning to change over the fiber to yarns. Yarns are then reinforced with measuring synthetic substances like polyvinyl liquor, wax and starch so they can withstand energetic developments when the yarns are meshed into texture in rapid weaving looms. In the wake of weaving, weaved texture must be pretreated before they can be colored, printed and wrapped up. In the processes of pretreatment different synthetic concoctions being utilized. Texture is desized either with compound or oxidative synthetic substances and scoured utilizing sodium hydroxide and cleansers. Dying is done typically by utilizing hydrogen peroxide to eliminate the regular shade of the texture white. Texture is then mercerized utilizing high focus sodium hydroxide to balance out the texture. During coloring and printing, numerous sorts of colors are utilized for example scatter, responsive, tank and so forth along with coloring assistants and synthetics. Texture is at last completed to give the last touch and planned properties by utilizing gums, conditioners and other completing operators for example fluorocarbon, silicones and so forth. The mix of the cycles and items make the wastewater from textile industry contains various kinds of toxins. The coloring and completing activities are to such an extent that the dyestuffs, synthetic compounds, and material assistants utilized can differ from every day and once in a while even inside a few times each day (Lin and Chen, 1997). It contains different waste compound poisons, for example, measuring operators, wetting specialists, complexion operators, colors, shades, mellowing specialists, hardening operators, fluorocarbon, surfactants, oils, wax and numerous different added substances which are utilized all through the cycles. These toxins add to high suspended solids (SS), concoction oxygen request (COD), biochemical oxygen request (BOD), heat, shading, sharpness, basicity, and other dissolvable substances (Ahn et al., 1999). Value rivalry, requests in excellent items, new and creative items that are exceptionally sturdy put further strain on the business as they need to utilize more doses of synthetic substances and persistently vary to new synthetic substances to suit the market request. This will at long last outcome in the inconvenience in the wastewater that is being released. Hence there is a requirement for proceeds with study and examination on the wastewater treatment to discover new techniques for treatment so as to continue this industry.

Statistical optimization models were employed to optimize the adsorption of textile dye effluent onto Gracilaria edulis. Significant factors responsible for adsorption were determined using Plackett-Burman design (PBD) and were time, pH, and dye concentration. Box-Behnken (BB) design was used for further optimization(Venkataraghavan et al., 2020), The principal objective of this research was to demonstrate the sensitivity and selectivity of carbon paste electrode modified with Ocimum Sanctum leaf extract synthesized silver nanoparticles for simultaneous determination of Cd(II) and Pb(II) in discharged textile effluent(Amare et al., 2020), Wastewaters from the textile industry are hazardous effluents containing toxic complex components that without appropriate treatment severely impact the environment; causing harmful effects to the aquatic ecosystems, as well as to human health(Hynes et al., 2020),Chitosan is a pseudo-natural cationic polysaccharide in nature. Because of its wide range of physical and biochemical properties, chitosan and its hybrid materials are being used in various industrial sectors. The dyes and other industrial effluents extensively compromise the plant growth and affect the food chain, these substances may also induce toxicity, mutagenicity, and carcinogenicity (Qamar et al., 2020),The potential of using tea waste as a low-cost adsorbent for the removal of Eriochrome Black-T (EBT), an anionic dye from aqueous solution was studied. Batch sorption studies were conducted to study the effect of adsorbent dosage, initial dye concentration, pH and contact time(Bansal et al., 2020),

1.8 Problem Statement

The broad and critical literature review on the present research work excited to identify the following gaps.

- Most of the works carried out so far are based on conventional fluidization and few works are on inverse fluidization in cylindrical shape of fluidized beds only.
- Existing research works require more in-depth knowledge of the process.
- Existing works require more accuracy, power consumption and low cost for desired results.
- High rate of heat and mass transfer are more when the tapered inverse fluidization process is used compared to conventional fluidization.

Based on the above gaps identified from the literature, hydrodynamic studies, RTD studies and wastewater treatment are studied using a simple and new method namely tapered inverse fluidized with CFD simulations.

Textile cycles produce multi-part wastewater which can be hard to treat (O'Neill et al., 2000). This wastewater can cause 3 genuine ecological issues because of their high shading, a huge measure of suspended solids, and high concoction oxygen request (Kim et al., 2004). Standard release

cutoff points of material profluent are getting tougher lately making persistent issues for ventures to agree. The normal treatment of dyestuff containing wastewater involves natural oxidation, adsorption. Natural strategies are commonly modest and easy to utilized and are presently used to eliminate organics and shading from coloring and material wastewater. Anyway, this wastewater can't be promptly debased by regular organic cycles for example initiated slop measure in light of the fact that the structure of most business color mixes are commonly perplexing and numerous colors are non-biodegradable because of the concoction nature and sub-atomic size (Kim et al., 2004). At present, a few strategies have been created to treat material wastewater however they can't be utilized independently on the grounds that this wastewater has high saltiness, shading, and non-biodegradable organics. In coagulation measures, an enormous measure of ooze is made which may turn into a toxin itself and increment the treatment cost. Oxidation cycle, for example, ozonation viably decolorizes practically all colors aside from scattering colors yet doesn't eliminate COD adequately (Ahn et al., 1999). Electrochemical oxidation produces contaminations which expands the treatment cost (Kim et al., 2003). There is no single cycle equipped for satisfactory treatment primarily because of the mind-boggling nature of these effluents. The utilization of joined cycles has been recommended as of late to conquer the weakness of individual unit 4 cycles (Kim et al., 2003). The majority of the current cycles incorporate an underlying advance of enacted slop therapy to eliminate the natural issue followed by oxidation, UV radiation, film partition, or adsorption (Pereira et al., 2003). Adsorption is a powerful technique for bringing down the grouping of broke up colors in the emanating bringing about shading expulsion. Different methods for color expulsion, for example, substance oxidation, coagulation, and converse assimilation are commonly not possible because of monetary contemplations (Tsai et al., 2001).The adsorption cycle is one of the most effective techniques to eliminate colors from profluent. The cycle of adsorption has an edge over different strategies because of it slime free clean activity and complete expulsion of colors even from weaken arrangement (Malik, 2003). Actuated carbon is the most broadly utilized adsorbent on account of its all-inclusive surface region, microporous structure, high adsorption limit, and serious extent of reactivity. Be that as it may, financially accessible initiated carbons are pricey (Malik, 2003). There is a developing enthusiasm for utilizing ease monetarily accessible materials for the adsorption of shading. A wide assortment of ease materials, for example, rural side-effect (Kadirvelu et al., 2000), Indian rosewood sawdust (Garg et al., 2004), squander coir essence (Namasivayam et al., 2001), pine sawdust (Ozacar et al., 2005), banana substance (Namasivayam et al., 1998), rice husk (Low and Lee, 1997), orange strip (Namasivayam

et al., 1996), mechanical strong waste, for example, silica (Andrzejewska et al., 2007) and Fe(III)/Cr(III) hydroxide (Namasivayam et al., 5 2005) are utilized as ease options in contrast to initiated carbon. The contextual investigation is on wastewater from one of a material factory in Penang. The plant is fabricating polyester and cotton/cotton mix woven texture. The creation comprises of desizing, dyeing, scouring, coloring, and wrapping up. Polluted water from every one of these cycles are combined in a cushion tank.

1.9 Scope of present research

1. Hydrodynamic studies of materials of different density and liquid of viscosity in different angles of tapered inverse fluidized beds
2. CFD simulations and design expert software are also applied
3. RTD studies in different angles of tapered inverse fluidized bed and compared these results with CFD simulations as well as design expert software results
4. Synthesis of an effective adsorbent for elimination of unwanted pollutants from synthetic textile wastewater.
5. Optimization of process parameters for adsorption of pollutants and other impurities such as dye.
6. Study of batch adsorption for unwanted pollutants removal.
7. Modeling of batch adsorption operation for pollutants removal. Evaluation of removal efficiency of synthesized adsorbent in presence of other pollutants.

1.9.1 ADVANTAGES OF INVERSE FLUIDIZATION

One of the fundamental preferences of inverse fluidization is its high rate of mass exchange. As the fluid is acquainted with the current gas phase indicator, the drag power is applied to the gas bubbles. Along these lines, the mean residence time and the gas hold-up are much better than normal fluidization modes. Another big leeway is the low need for vitality due to the low fluid speeds that make this fluid bed more affordable. It is due to the fluidization is carried out along the weight bearing. The low speeds likewise use in limiting the strong whittling down and diminishing the disintegration of the vessel. As the bed grows downward, the solids that lie at the base may be extracted without much of a stretch. Taking into account these extraordinary favorable circumstances, opposite fluidized bed (IFB) is utilized to treat polluted water from local and cycle ventures [Calderon et al., 1998, Fan, 1989]. They have accurate control of the thickness of the biofilm. Bed expansion results as fluid and biogas streams provided by inverse methods [Garcia-Calderon et al., 1998].

1.9.2 APPLICATION OF INVERSE FLUIDIZATION

Considering the numerous main points of opposite fluidization, it is in these days being broadly utilized in petrochemical and natural industries. It is used for the treatment of wastewater from local and cycle industries [Rajasimman and Karthikeyan, 2006, Fan, 1989, Calderon et al., 1998]. In three phases of inverse fluidization, the thickness of the biofilm can be regulated at a thin range. As a result, organic robust wastewater treatment [Nikolov and Karamanev] may be used. It is also used as transport bioreactors. In addition, a couple of uses of anaerobic opposite fluid beds have been identified [Meraz et al, 1996, Spiess et al., 1991].

1.9.3 IMPORTANCE OF CFD FOR INVERSE FLUIDIZATION

Numerous trial simulations have been performed as recently as possible to understand the hydrodynamics of inverse fluidization. We may get data on the design of the stream in a fluidized bed in trial examines. In spite of the fact that these procedures have demonstrated to be vital, there are additional impediments and a full image of the stream field is frequently difficult to acquire. Computational Fluid Dynamics, normally denoted as CFD, is a strategy to display liquid stream utilizing a computer reproduction. Up to now, no big CFD analysis has been performed on inverse beds. Thus, it is needed to do a reproduction to comprehend the fluidization conduct all are with more accurately.

The overall bit of use of CFD is that it is a convincing, attentive, virtual displaying strategy with incredible representation abilities, and one can assess the presentation of a wide scope of framework designs on the PC without the time, cost, and disturbance needed to roll out genuine improvements on location. A portion of the numerous favorable circumstances that made CFD generally mainstream are the accompanying:

- Without altering and additionally introducing genuine frameworks, CFD can anticipate which configuration changes are generally pivotal to improve execution.
- Unmatched understanding into frameworks that might be hard to model or test through experimentation.
- CFD gives careful and point by point data about different boundaries. The advances in innovation require more extensive and additional intimation about the stream inside an involved zone, and CFD meets this objective superior to some other technique, (i.e., hypothetical or trial strategies).
- CFD costs considerably less than tests in light of the fact that physical alterations are redundant.

• The mathematical plans and techniques where upon CFD is depends are getting better and quickly,

So CFD outcomes are progressively fast. CFD is a reliable device for plan and investigation.

• CFD recreations can be carried out in a brief timeframe.

CHAPTER-2

LITERATURE REVIEW

2.1 Introduction

Fluidization is a mechanism by which is a solid particle bed rendered to act in a fluid fashion. It is possible to use the extraordinary actions shown by the fluidized solid to overcome the obstacles

it otherwise faced. Although fluidization happens from bottom to top in traditional fluidized beds, it happens in a downward motion in inverse fluidization. The inverse fluidization cycle comes into view when the device is concerned with particles of low density. The solid particles float over the fluidizing media; as a result, the traditional procedure is no longer viable.

With downward stream from the fluid against the force of net upward buoyancy on the solid particles, the 3-phase fluidized beds can be controlled. The gas flow is upward, compared to the liquid flow and bed expansion can be accompanied by the liquid phase (downward) and the gas bubbles (upward). These multistage systems are frequently used to refer to as turbulent inversion systems. The particles form a buoyant packed bed at low liquid or gas velocities, supported by the mesh at the top of the column. As the velocity of the liquid or gas increases, the bottom layer of the particles only fluidizes and the rest remain in compressed condition. As the velocity increases more, more and more particles are fluidized at the bottom of the packed bed, and the bed height increases. The whole bed is in fluidized condition at one particular speed. The velocity of this condition is called the "minimum velocity of fluidization." Although the whole bed is fluidized, the solids concentration does not constant along the bed axis. The solid holdup becomes constant entire bed, as the velocity continues to rise. From the available literature it is found that only minimal studies with respect to pressure drop and bed expansion studies are recorded in a reverse fluidized bed reactor.

Water is essential to practically all life forms on the planet, and it is thought that life began in water. Although water covers more than 70% of the earth's surface, the bulk of it is unfit for human consumption, and only a limited amount of drinkable water is available. The widespread use of chemicals for a variety of purposes in everyday life, along with increasing industrialization, resulted in inadvertent pollution of our environmental assets due to the discharge of a variety of organic and inorganic pollutants into the water system (Ramakrishna, 2013). Dye is a visible pollutant that is found in industrial wastewaters and is considered to be one of the most important pollutants from an aesthetic perspective.

Dyes are widely employed in the textile, paper, plastic, leather, cosmetics, and food sectors to colour their foodstuffs. They often have a synthetic origin and complex aromatic molecular structures, which make them more persistent and hard to decompose. The widespread usage of dyes frequently resulted in pollution issues in the form of colored effluent dumped into aquatic bodies (Aseel M. and Kadim Aljebori, 2010).

Today, more than 100,000 commercially accessible dyes exist, with over 7105 metric tonnes of dyestuff manufactured each year. Azo dyes are the most versatile of the chemical classes of dyes, accounting for more than half of yearly dye generation. Approximately 2% of dyes produced each year are released in wastewater from various manufacturing operations (Tan J. R., 2010).

Reactive azo dyes extensively utilized in textile dying process, they have good water solubility and easily hydrolyzed into insoluble forms. Textile dyes wastewater, in particular characterized by high level of chemical oxygen demand (COD), intense color, dissolved solids highly fluctuating pH (Meroufel & Zenasn, 2013). Among all this color is the first wastewater contaminant to be recognized, since a very small amount of dye concentration in water even (gas solubility (Adamu, 2008). Therefore, it is desirable to remove dyes from colored effluents for safe discharge in receiving water bodies to keep the environment sustainable.

To remove colors from textile wastewater, a variety of treatment methods have been used, including physical, chemical, and biological approaches. Among physicochemical methods mainly adsorption process is one of the most effective and economically feasible methods for dye removal from textile wastewater. A variety of natural adsorbents for dye removal have been reported in the literature (Beyene, 2014). Orange is a type of biological resource that is widely available in various places of the world. Cellulose, hemicelluloses, chlorophyll pigment, lignin, and other low molecular weight hydrocarbons make up the majority of orange peel. Orange peel has numerous functional groups such as carboxyl and hydroxyl groups, making it a viable adsorbent material for eliminating contaminants (Said & Mansour, 2012).

The present study was intended to performance of hydrodynamic, Residence time distribution (RTD) of tapered inverse fluidized bed and removal of direct red dye from aqueous solutions using wheat bran as a low cost bio adsorbent.

In batch adsorption approaches, the effect of working factors such as start pH, contact time, adsorbent dose, and initial dye concentration studies were explored, and the equilibrium effective conditions for these parameters were determined. The best suitable models for the dye adsorption process were provided after studying adsorption isotherms and kinetics (Tan J. R., 2010).

2.2 Hydrodynamic studies of inverse fluidized bed.

Many studies on bed dynamics for inverse fluidization have been published, including phase hold-ups, bed expansion, minimum fluidization velocity and bed pressure drop. In Table 2.1, some of the literature research is listed.

Table 2.1. Analysis of hydrodynamics on inverse fluidized bed

Investigator	Variables investigated
Fan et al. (1998)	Gas holdup and bed porosity
Briens et al. (1999)	The influence of inhibits on minimum fluidization velocity can be estimated based on their impact on gas holdup.
Han et al. (2002)	Surface hydrophilicity has an effect on critical fluidization velocity and phase hold up.
Bandaru et al. (2007)	Phase holdups, minimum liquid, pressure drop, and gas fluidization velocities
Hamdad et al. (2007)	Phase hold ups and gas velocity
Lee et al. (2007)	Liquid viscosity, liquid and gas velocities, and media particle kind
Myre et al. (2010)	Heat transfer coefficients and phase holdups and instantaneous.

Low-density solid particles have a wide range of applications in bioreactors for the treatment of aerobic waste water. Although there is a lot of work on moderate or low density solid particles, hydrodynamics studies of two-phase fluidized beds with low density particles are rare in the literature.

- Han et al. (2000) examined bed expansion in down comer. There are varies models for the association between superficial velocity and bed expansion of the liquid. The model suggested by Richardson and Zaki (1954) is used amongst all these correlations. It is known as the most minimal fluid superficial speed at which the down weight of the solid particles, the drag force because of the down progression of the fluid, just balances the upward buoyancy of the solid particles, for example the net upward force is equivalent to the net downward force. Pressure drops are seen to ascend as bed weight increments; however the minimum inverse fluidization velocity is practically steady and autonomous on the bed weight. Actually, there are two components affecting the minimum velocity of backwards fluidization, specifically the size and thickness of the particles.
- The minimum velocity of liquid fluidization refers to the velocity of the liquid at which the pressure gradient in the bed is minimal (Ibrahim et al., 1996) for all gas velocities.
- The minimum velocity of liquid fluidization is obtained at a constant gas velocity from a graph of pressure gradient vs. liquid velocity (Krishna et al., 2007).
- As the gas speed increases, as seen by a few different researchers, the fluid speed needed to keep up the bed under minimum fluidization conditions is diminished (Moletta and Buffiere, 1998; Lee et al., 2000; Ibrahim et al., 1996; Legile et al., 1992; Renganathan and Krishnaiah, 2004).

Despite the fact that a large series of experimental studies are aimed at quantifying flow pattern and identifying streams for output responses and physical characteristics, the detailed hydrodynamics of these reactors are still poorly understood due to complex particle-particle, liquid-particle, and particle-particle interactions are examples of phenomena (Jena, 2010) .Computational fluid dynamics (CFD) simulations provide extensive information on local pressure values, component of viscous, mean velocity, and turbulent kinetics energy, turbulent stresses, and turbulent energy dissipation rate, among other things. Such data can aid in the comprehension of transport phenomena in complex geometries such as fixed beds.

2.3. Liquid solid tapered fluidized bed

Based on statistical analysis, Ju-Sheng Huang [85] et al. investigated the hydrodynamic characteristics of anaerobic tapered bioreactors with taper angles of 5^0 and 2.5^0 and conventional fluidized beds. They found that, under the same operational conditions, tapered fluidized beds were superior to circulating fluidized beds. D.C. Sau [89] et al. found to correlate minimum and maximum fluidization velocity profile anywhere along axially for gas–solid tapered fluidized beds with various taper angles of usual and abnormal particles, verified by experiments, and especially in comparison to other designs like Peng & Fan[25] and Jing[78] et al. The [113, 114] equations that are correlated are listed below.

$$Fr = 0.2714(Ar)^{0.3197}(sin\alpha)^{0.6092}(\frac{\varepsilon_0}{\phi_s})^{-0.6108} \quad (2.1)$$

$$\Delta p_{max} = 7.457(\frac{D_1}{D_0})^{0.038}(\frac{d_p}{D_0})^{0.222}(\frac{H_s}{D_0})^{0.642}(\frac{\rho_s}{\rho_f})^{0.723} \quad (2.2)$$

Sun Liyan [91] et al. used the second-order moments approach to simulate gas and particles in a tapered bubbling fluidized bed and predicted particle frictional stresses as increasing with increasing taper angle, which they confirmed with practical predicted values. Yong Chen [93] and colleagues constructed a thermal gravimetric analyzer to describe particles in a tapering fluidization bed. Jing Shan [98] et al. investigated the hydrodynamic performance of small particle fluidization in three various angles of conical beds, comparing Geldart-A powder to Geldart-D powder, and concluded that the hypothesis of a homogenous distribution of gas velocity is not valid for a large bed cone angle. Chao Li [100] et al. used a 3D numerical model to investigate particle residence duration and flow characteristics in an opposing multi-burner gasified system. They used a discrete particle random trajectory model to describe the gas–solid two-phase flow. It has been used in 38 plants, and over 100 gasifies have been installed to transform coal or petcoke into liquid fuel.

J.G. Pieters et.al [108] created an Eulerian computational fluid dynamics (CFD) model for a gas–solid fluidized bed in a tapering reactor, estimated drag force, and explained momentum transfer between the gas and solid phases. They compared their results to other models and found that Gidaspow drag model had the best agreement. D.C. Sau [111] et al. calculated Reynolds number and Archimedes number correlations for the minimum fluidization velocity at 5000C in a tapering fluidized bed of 1mm diameter glass beads and compared them to data for sand particles in columnar beds available in the literature. Benjapon Chalermsinsuwan [115] et al. investigated the hydrodynamic and chemical reaction characteristics in the riser of a tapered circulating fluidized bed using CFD modelling, a two-dimensional transient Eulerian model, and a kinetic theory of granular flow. Hossein Askaripour and Asghar Molaei Dehkordi [116], studied impact of initial stable bed height on fractional conversion and bed pressure decrease were examined in tapered – in and tapered – out fluidized bed reactors. To model the behavior of tapered-in and tapered-out fluidized bed reactors, a typical 2D Two-Fluid Model (TFM) closed by the kinetic theory of granular flow (KTGF) was used in this research. The behavior of tapered-in and tapered-out fluidized bed reactors was simulated using a typical 2D Two-Fluid Model (TFM) closed by the kinetic theory of granular flow (KTGF).

The outputs of hydrodynamic simulations of bed pressure drop and bed expansion ratio were evaluated to experimental data available in the literature to confirm the CFD model predictions, and accurate result was found. The resulting simulation results clearly show that in a tapered-in reactor, there is an optimal static bed height at which the fractional conversion is maximized, whereas differences in static bed height in a tapered-out reactor have negligible effects on the fractional conversion. Furthermore, it was discovered that the gas phase's residence time, temperature, and turbulence intensity are three critical elements impacting fractional conversion in tapered fluidized bed reactors.

JSN Murthy [29] et al. studied the residence time distribution in a solid-liquid semi-fluidized bed of particles of diameters of 2.00 – 3.00 mm, 0.791 mm, 1.080 mm, and 1.524 mm, respectively. They discovered that the dispersed plug flow regime was the most acceptable flow phenomena and developed corrections for mean residence time and dispersion number for packed bed, fluidized bed, and semi fluidized bed based on dimensional analysis. The "tanks-in-series" model [11] was used to measure liquid flow residence time in a biofilm fibrous packing fixed bed reactor for waste water treatment in the presence of gas and

liquid with recycle superficial velocities up to 0.012 m/s, and liquid phase axial dispersion was found to be largely independent on recycle velocity. F. Berruti [49] et.al, RTDs for low density sand particles were tested in a fluidized bed reactor and were found to be extremely close to modelling results. Marianthi G. Ierapetritou et al., Marianthi G. Ierapetritou et al., Marianthi G. Ierapetritou et Residence Time Distribution (RTD) applications in various solid unit operations were reviewed. Sunun Limtrakul [60] et.al, applied Solids motion, time averaged velocity, and holdup profiles in liquid sold fluidized beds were studied using computer tomography of radioactive particle tracking systems and non-invasive gamma rays-based approaches. Anju Srivastava and Sankaran Sundaresan [63], studied Fluidization and fluidization of gas–solid (KL glass beads) in three different diameters of fluidized beds were investigated, and remarkable hysteresis was discovered. As a result, wall friction was also investigated in fluidization. T. Renganathan and K. Krishnaiah [65], Voidage, a property of a liquid–solid inverse fluidized bed, was investigated, and it was discovered that Voidage grows with Archimedes number and is independent of the initial static bed height. Shuyan Wang [74] et.al, performed computational fluid dynamic (CFD) models for particle flow behavior in a liquid-solid fluidized bed and found that solid concentrations were higher towards the walls and lower in the center. V. Idakiev and L. Morl [96], Studied

In a continuous two-stage fluidized bed apparatus and a continuous rectangular fluidized bed channel, the residence time of dispersed materials was investigated. Number of stages, weir height, number of weirs, air flow rate, and size of the under weir gap are all RTD effect parameters. The mean residence time decreases with increasing air flow, according to these characteristics. Prasad babu and Y. Pydi setty [97] constructed a model for residence time distribution curves in a fluidized bed that was contrasted to experimental findings on the same plot, with the divergence described by the root mean

square approach with time intervals, as shown in the formula follows.

$$\sigma = \left[\frac{1}{M}\sum_{K=1}^{M}\{(F_{K_{exp}}) - (F_{K_{model}})\}^2\right]^{1/2} \quad (2.3)$$

2.4 Residence time distribution studies (RTD)

A primary topic of research for any continuous process is the residence time distribution (RTD) of treated materials in the apparatus. As described in this work, a continuous tapered inverse fluidized bed is used. The material is frequently time-sensitive in these procedures, so a wide range of residence times should be avoided. As a result, a thorough understanding of the RTD of a liquid tracer in a tapered inverse fluidized bed provides a useful knowledge base for future research.

2.4.1 Fundamentals and theories for RTD study

In this section, several basic concepts and properties regarding RTD study are firstly illustrated.

2.4.2 Plug flow, mixed flow, and back-mixing flow:

According to Levenspiel (1999), the optimum granule flow pattern in a horizontal fluidized bed without any mixing effect (no overtaking or back-mixing) is plug flow, which indicates that each treated granule in the processing chamber should have the same residence time. In a mixed flow fluidized bed, Levenspiel (1999) presented another ideal flow pattern: the mixed flow (also known as ideal CSTR), which means that newly entered granules will instantly and thoroughly mix with the "old" granules.

However, in the real world, particle convection (forward directed) is disrupted by particle dispersion (forward and backward directed), preventing the ideal solid fluid flows from being obtained and resulting in a redistribution of residence time among the liquid.

2.4.3 RTD measurement methodology

The RTD is closely associated with the performance of the equipment for back-mixing flow of inverse fluidized bed because it may immediately reveal details about the degree of solids mixing, transportation, and segregation. As a result, the RTD of an inverse fluidized bed must be thoroughly researched, and appropriate tracing techniques can be used to measure the RTD using a tracer. Tracers are non-reactive materials with physical properties that are the same as or similar to those of the processed tracer. They're frequently employed in RTD studies.

Typically, when obtaining the RTD of a liquid tracer in an inverse fluidized bed, the tracer is introduced into the apparatus at the inlet after establishing a steady state of the liquid flow in the process chamber, and the tracer's concentration-time curve is monitored at the outlet at the same time. The pulse and stepwise input of a tracer (Levenspiel (2012)) are the two most frequent RTD measurement procedures. A small amount of tracer is used in the pulse test, as the name implies, and it has no effect on the ordinary liquid flow. The Cpulse and Cstep curves are the names given

to the observed RTD curves (concentration curves). After normalization, the corresponding curves are frequently translated into the E-curve and the F-curve for easier comprehension. Using the following equations, these normalized RTDs are related to one another and interconvertible:

$$F(t) = \int_0^t E(t)dt, \tag{2.4}$$

and

$$E(t) = \frac{dF(t)}{d(t)} \tag{2.5}$$

2.5 The mean and variance

The mean and variance2 are two of the most widely used properties for defining RTD curves, with the mean indicating the average duration particles stay in the fluidized bed and the variance indicating the curve's spread over time.

From a C_{pulse} curve, the following formulae can be used to compute the mean and variance.:

$$\tau = \frac{\int_0^\infty tC_{pulse}tdt}{\int_0^\infty C_{pulse}\, t\, dt}, \tag{2.6}$$

$$\sigma 2 = \frac{\int_0^\infty tC_{pulse}tdt}{\int_0^\infty C_{pulse}\, t\, dt} - \tau^2 \tag{2.7}$$

Therefore, the mean and variance of a Cpulse curve can be obtained as:

2.6 The dispersion coefficient

The particle dispersion coefficient, D, is a value that can describe the overall influence that the intensity of random particle motion has in relation to particle convection in a fluidized bed system. The dispersion of solids is more noticeable when the dispersion coefficient is high, resulting in a wider spread of the RTD curve.

The particle diffusion coefficient, also known as particle diffusivity, is a characteristic that quantifies particle movement at the micro scale. It sounds similar to the dispersion coefficient. When total particle flow rates are multiplied by the gradient of particle mass concentration, total particle flow rates are obtained. Taylor (1953), who determined the dispersion coefficient for a long cylindrical tube with laminar fluid flow, provided an early and demonstrative contrast between these two features. The diffusion coefficient of the molecules in the fluid is known in advance in Taylor's study. The dispersion coefficient is calculated by multiplying the dispersion coefficient by a factor resulting from the equipment geometry.

(Tube diameter) and flow field (laminar) to molecular diffusivity, and the results indicate that the dispersion coefficient might be significantly bigger than the diffusion coefficient. The particle diffusivity does not have to be equal to the dispersion coefficient in general.

2.7 Previous work on RTD studies: Mac Mullin et al. (1935) [33] appear to have been the first to propose to use the distribution of dwell time in the investigation of chemical reactor performance. It was an example of a succession of entirely mixed tanks that were all identical. Danckwerts (1952) [6] described how residence-time distribution functions can be formed and quantified for real systems under the premise that the flow across the system is continuous, although this notion was not applied until 1952. Danckwerts (1952) [6] illustrates the application of distribution functions by adding them into the computation of reactor and blender performances.

The following is a summary of a literature review of tracers used in various research in Table 2-2 and 2-3

Table 2.2 tracers used in different studies

Method of tracer detection	**Carrier fluid**	**Tracer**	**Instruments**	**Type of reactors**	**References**
Conductivity Salts	H_2O	$NaNO_3$	Thermal or electrical conductivity cells, recorder or potentiometer	Packed bed	[40]
				Fluidized bed	[40]
		NaC1 or KC1 or Cl- + NaCl or HC1	Thermal or electrical conductivity cells, recorder or potentiometer	tubes	[2]
				tanks	[35]
				packed bed	[40]
				fluidized bed	[40]

Table 2-3 Tracers used in a liquid-carrier system

Method of tracer detection	**Carrier fluid**	**Tracer**	**Instruments**	**Type of reactors**	Refer-ences
Conduc-tivity salts	Ethyl Acetate	NaCl	Thermal or electrical conductivity cells, recorder or potentiometer	tubes	**[40]**
	$Na_2S_2O_3$ + H_2O	KCl	Thermal or electrical conductivity cells, recorder or potentiometer	tanks	**[40]**
Color and light sensitive dyes	H2O + 40% of sugar solution	black dye	colorimeter	tubes	**[40]**
	H_2O	blue dye	photoelectric colorimeter	packed bed	**[40]**
		red dye	colorimeter	packed bed	**[40]**
		KMnO4	spectrophotometer	Tubes	**[40]**
		fluorescein	phototube mlliamper recorder	fluidized bed	**[40]**
Color and light	H_2O	Alizarin Saphirol	phototube	Packed bed	**[31]**
				fluidized	

sensitive dyes		SES		bed	**[31]**
		sulphate iodate, starch	spectrophotometer or photograph	tubes	**[40]**
Color and sensitive dyes	H_2O	light sensitive solution	colorimeter	tubes	**[40]**

2.8 Computational fluid dynamics (CFD):

CFD is an appropriate tool for predicting fluid dynamics in numerous modules, which allows for effective system design. It is a comprehensive method of analyzing not just heat and mass transportation operations, as well as fluid flow behavior. CFX , FLUENT, FLOW3D, PHONICS, and STAR-CD are some of the general-purpose CFD software in use. The majority among these software use the finite volume method to address fluid flow, heat transfer, and mass transfer issues. The fact that the FVM's approach fulfilled the conservation of mass, momentum, energy, and species is one of its most attractive properties. The solution domain is discretized into consecutive cells or control volumes in the FVM, with the parameters of interest at the centroid of the control volume, generating a grid. The differential form of the governing equations must then be integrated across each control volume. The change of the concerned parameters among cell centroids is then described using interpolation profiles.

For discretization of governing equations, numerous approaches can be utilized, including central averaging, upwind differencing, power law averaging, and quadratic upwind differencing. Discrete equations are the equations that result. The conservation principle for the parameter inside the control volume is expressed in this way by the discretized equation. These variables are used to create a set of algebraic equations that are solved at the same time using a particular technique.

2.9 Previous Works on Inverse Fluidized Bed Bioreactor:

Sok ol & korpal (2006) was investigated in the inverse liquid bed biofilm reactor (IFBBR) in which polypropylene particles with a density with 910 kg / m3 was fluidized by an upward co-

current stream of gas and liquid. Estimations of chemical oxygen demand (COD) versus residence time t are performed for different proportions of fixe bed volume to bioreactor volume (VB/VR) and air velocity u to determine the optimal working boundaries, for the reactor, that is, the estimations of (VB/VR), u and t for which the biggest decrease in COD happened. The loading of biomass in a bed depend upon the proportion (VB/VR) and an air speed u. In the way of culture developed after change in (VB/VR) at a set u, the consistent state mass of cells developed on the particles was accomplished after around 3 days of activity. With change in u at a set (VB/VR), the new consistent state biomass loading happened after development for around 2 days.

Sowmeyan and Swaminathan (2007) attempted to assess the feasibility of an opposite fluidized bed reactor for the anaerobic absorption of refinery effluent, with a transporter material that permits low vitality prerequisites for fluidization, and also provides a good surface for biomass connection and growth. Inverse fluidization carrier materials with a fixed gravity of a less than one are conducted in the bed.

Gomez et al (2006) immobilized soybean peroxide derivatives in a laboratory-scale fluidized bed reactor to determine their feasibility for use in the removal of phenol. The effect of the various operating factors on the mechanism is also studied in a reactor model based on experimental results, which predicts the behavior of the system in both steady and transient conditions. The model considers the fluidized bed reactor to be a plug flow reactor in series with an ideal mixer and follows a kinetic law based on the observed external mass transfer resistances in order to determine the process rate.

Benedict et al (2006) performed experiments using 6 mm diameter spherical low-density polyethylene (LDPE) and polypropylene (PP) particles with Carboxyl methyl cellulose (CMC) water and aqueous solutions. The minimum fluidization velocity, Umf, was found to have decreased with an increase in solid density and CMC concentration. A dimensionless correlation was suggested for the determination of bed height under fully fluidized conditions.

Vijaya Lakshmi et al. (2005) contemplated the hydrodynamic characteristics (bed extension and pressure drop) of low-thickness polyethylene (LDPE) and polypropylene (PP) (4, 6 and 8 mm) in a fluid-solid reverse fluidized bed reactor as a component of solid 8 breadth, fluid viscosity and thickness. The pressure drop bed expansion information is utilized to decide the minimum fluidization velocity in the solid width and abatement in solid thickness and was independent of initial bed height. Wlodzimierz Sokół et al.(2008) Examine the handling of wastewater biologically in the inverse fluid bed reactor (IFBR) in which 910 kg / m3 polypropylene (PP) solids have been liquidated by an upward flow of air. Finding of chemical oxygen demand (COD) versus residence time t was performed for different ratios of fixed bed volume to reactor volume (Vb / VR) and air velocity ug. The biggest COD expulsion was accomplished when the reactor

was worked at the proportion (Vb/VR)m = 0.55 and an air speed u_{gm} = 0.024 m/s. Under these conditions, the estimation of COD was essentially at consistent state for times more than 30 h. Subsequently, these estimations of (Vb/VR)m, u_{gm} and t can be accepted as the ideal working boundaries for a reactor when utilized in treatment of wastewater. R.W. Gaikwad (2012) endeavors the adsorption of lead particles on granular activated carbon (GAC) and evacuation of lead as heavy metal utilizing GAC concentrated in a backward fluidized bed. GAC is appropriate adsorbent especially to eliminate heavy metals from water.

A fluidized bed was more reasonable innovation for GAC, because of its specific favorable applications over packed bed. The only problem that exists in the fluidized bed is the low density (0.44 g / cm) of GAC, which makes it float on the fluid surface. A basic definition of an inverse fluid bed can be a better alternative. Experimental studies have been worked out in a reverse fluid bed. Result for GAC removal efficiency with change in change in solution pH, solution concentration change in change in residence time, GAC bed height was investigated. It has been found that the percent removal of lead increases with an increase in bed height and time as it decreases with an increase in the initial concentration of lead and the pH of the solution.

Abanti Sahoo and Tanmay Lima (2013) Analysis phenolic wastewater (steel effluent) was processed in an inverse fluid bed (IFB) bioreactor. Effects of the various operating conditions of the device (viz. residence time (t), settled bed to bioreactor volume ratio (Vb = Vr), static bed height, gas flow rate and water flow rate) on the removal of chemical oxygen demand (COD) were studied in order to determine the optimum parameters.

Ideal conditions relating to the biggest COD evacuation were acquired at Vb=Vr proportion of 0.55 and gas stream of 40 LPH with timeframe more than 62 h. COD expulsion was additionally estimated with the option of mineral salts in the wastewater. The outcomes accordingly acquired with and without the expansion of mineral salt to the wastewater were thought about. The impact of various sorts of salts on COD evacuation was likewise concentrated as for the biomass development. Transformations more prominent than 68% and 84% were accomplished with clump and nonstop mode activity individually, inferring that IFB bioreactor can be utilized effectively for the treatment of mechanical effluents.

Sowmeyan and G.Swaminathan (2007) the purpose of this work is to provide details regarding the physical qualities of transporter material (perlite), biomass development on the transporter material and the biogas creation in a backwards anaerobic fluidized bed reactor (IAFBR) for treating high quality organic wastewater. Prior to starting up the reactor, physical properties of the transporter material were resolved. One mm breadth perlite molecule is found to have a wet explicit thickness of 295 kg/m3 with explicit surface zone of 7.010 m^2/g. The biofilm fixation (as far as joined unpredictable solids (AVS)) connected to transporter material was discovered to be

0.66 g AVS/g solid. When the converse anaerobic fluidized bed system arrived at the consistent state, the natural load was expanded advance insightful by decreasing hydraulic rentation time (HRT) from 2 days to 0.16 day, while keeping up the steady feed of substance oxygen request (COD) feed.

A. Alvarado-Lassman et al. (2008) the goal of this work is two anaerobic inverse fluid bed reactors were used to analyses the removal of organic matter from the wastewater brewery, to add various OLR and to test two support materials. Hydrodynamic tests of chenging liquid flow and solid concentration have been established on the supports in order to find operating parameters. The batch colonization process was applied using 25 per cent of the active volume of the extended sphere and the crushed polyethylene as support materials. Subsequently, the reactors were run continuously with stepwise rises in the organic loading rate until limiting conditions were reached. For the aids tested, IFBR technology was ideal for the removal of organic matter present in wastewater breweries with COD removal efficiencies greater than 90 per cent. The reactor with crushed polyethylene support displayed excellent COD removal with OLR values of up to 10 g COD / L d, while the reactor with extended sphere support had excellent hydrodynamic and biologic actions operating with OLR values.

Ding Wang et al. (2010) the purpose of the work is various size ranges of surface-treated hydrophobic silica aerogels (Nanogels) are fluidized by the downstream flow of the oil-in - water emulsion in the inverse fluidization mode. The hydrodynamic properties of the Nanogel granules of various sizes are analyzed by calculating the pressure drop and the expansion of the bed as a function of the superficial water velocity. The thickness of the Nanogel granules is determined from the decrease in the plateau pressure after the bed is completely fluidized. The oil evacuation proficiency of a diluted (1000 ppm COD or lower), settled (utilizing the emulsifier Tween 80) oil-in-water emulsion and the limit of the Nanogel granules in the opposite fluidized bed are likewise considered. A model was created to determine the opposite fluidized bed experimental results dependent on equilibrium and kinetic batch estimations of the Nanogel granules and the settled oil-in-water emulsion. Denis Myre and Arturo Macchi (2010) in this research, surface-to-bed heat transfer experiments were done to gain insight into hydrodynamics and heat transfer in a three-phase inverse fluid bed. Tap water, polypropylene, air or 0.5wt per cent aqueous ethanol and were, liquid, gas and solid phases respectively. Particles loading ranged from 0 to 30 vols. Percent and surface gas and liquid velocity from 2 to 50 mm / s and from 0 to 21 mm / s respectively. Visual findings were correlated with calculated phase holdups and instantaneous coefficients of heat transfer. Larger gas velocities lead to a rise in the size of the bubble due to the transition to the coalesced bubble flow regime. The higher turbulence created by the larger bubbles increases the average coefficient of heat transfer.

On the other hand, adding ethanol decreases the coefficient of heat transfer. Solid concentrations up to 13 vol. Percent increase the average coefficient of heat transfer while higher solid concentrations tend to lower it. The distribution of the instantaneous heat transfer coefficient of peak height is broader at higher gas and liquid velocity, whereas the addition of a surfactant narrows it. Gas hold-ups and normal heat transfer coefficients are also compared to known correlations, which are then calibrated for better match.

Bimal Das. at al. (2010) Experiments have been performed to estimate the minimum inverse flow rate using single and binary systems of four varies polymeric solids and four different non-Newtonian liquids in two different columns. Empirical correlations have been developed to predict the minimum inverse fluidization velocity as a function of the system's physical and dynamic variables.

The statistical analysis of the correlation shows that the correlation coefficient is more than 0.99 of acceptable accuracy. Krishna S.V.S.R. Bandaru et al. (2007) to examine the hydrodynamics of 3-phase opposite fluidized bed is tentatively utilizing low thickness particles for various fluid and gas speeds. The hydrodynamic chearectersics examined incorporate pressure drop, minimum fluid and gas fluidization speeds and phase burglaries. The base fluid fluidization speed decided utilizing the bed pressure slope, diminishes with increment in gas speed. The axial profiles of phase holdup show that the fluid holdup increments along the bed tallness, while the particles holdup diminishes down the bed. Be that as it may, the gas holdup is practically uniform in the bed. L. Nikolov et al. (2014) investigation of reverse fluidization as a hydrodynamic method depends on the association between a down streaming liquid and a bed of solid particles with thickness lower than that of the liquid. The effective usage of this method in bioreactor designing requires information on the hydrodynamics of the backwards fluidized beds. The total pressure drop through the bed as a function of the liquid velocity is observed and discussed in this work. The extension of inverse fluidization by means of liquids of varying viscosities and solid particles with a broad range of diameters and densities is discussed in detail.

T.Renganathan and K. Krishnaiah (2004) The Liquid Phase Residence Time Distribution Studies are recorded for the first time in the literature in a 2-phase inverse fluidized bed. The device RTD, residence time, Peclet number and dispersion coefficient are calculated using the pulse tracer technique and deconvolution analysis tool. The coefficient of liquid phase axial dispersion increases with the rise in liquid velocity and the number of Archimedes and is independent of the static bed height. For the liquid phase axial dispersion coefficient in 2-phase IFB, an empiric association has been suggested.

T.Renganathan and K. Krishnaiah (2005) Concentrates on changes in void age, axial voidage profile and extension of bed are rendered by estimating the local voide fraction using large-scale particles in fluid-solid inverse fluid bed. The essence of fluidization is explained by shifts in local emptiness. The RMS voiding fluctuation depicts the most severe as for the usual bed void fraction and increases in the Archimedes number. The fluidization quality has been evaluated utilizing normal standardized RMS Voidage vacillation regarding Transition number. The axial void fraction is almost uniform in the bed, except for particles with a distribution of scale. Both literature and current experimental data on bed expansion are united in Richardson and Zaki equations using experimental terminal velocity.

A new connation is proposed for estimating the corrected experimental terminal velocity of the wall effect as a replacement for the traditional drag equation. Bed expansion data are also projected using the drift flow model. N.Ulaganathan and K.Krishnaih (1996) Experimental studies are conducted on the hydrodynamic behavior of a new method of liquid-solid fluidization, referred to as "inverse fluidization" in which low-density floating particles are fluidized with a downward flow of liquid. Experiments are carried out with low-density particles (< 534 kg / m3) which allow high throughput of liquids in the system. The experiments are done with low thickness particles (<534 kg/m3) which permit high fluid throughputs in the work. Three regimens, i.e. packed, semi-fluidized and fully fluidized, are encountered during operation. Empirical correlations are suggested to predict the pressure drop in each regime. The analytical technique is designed to model variation of the pressure drop at a fluid velocity.

2.9.1 Introduction about textile wastewater treatment

The treatment of textile effluents is of concern because of their harmful and cosmetic effects on the receiving water. Concerns regarding human and ecological health have prompted the government to set a hardly achievable discharge quality standard for textile effluent. Cleaner production techniques can help to reduce the strength and amount of wastewater but end pipe treatment is necessary to achieve the discharge standard set by the government. A variety of treatment technologies are available for the treatment of textile effluent but no single solution has been sufficient for the remediation of the broad range of textile waste. As the quality and composition of textile industry effluent varies with the type of fiber, the processes involved the way that processes are operated and the classification of textile industries will help understanding the variations. In this section the general' process flow in the textile industry is briefly described for better understanding of the sources of wastewater generated by that type of industries. Since the wet processing of fabric produces the most of the effluent it has been given due attention.

The materials used in the processing of textile determine the characteristics of the effluent and dictates the selection of treatment units. A brief description on the materials used is incorporated

in this chapter. Since in this thesis sequencing batch reactor (SBR) has been used, this process is stressed in this literature review. Again, as SBR is a modified version of activated sludge process, this process has also briefly described.

2.9.2 Textile Industries

The Textile industries comprise of an assorted, divided gathering of foundations that fabricate as well as procedure material related items (fiber, yarn, texture) for additional preparing into clothing, home outfitting, and modern items. Fibers are received and prepared by textile establishments; fibers are transformed into yarn, thread or webbing; yam is converted into fabrics or related products; and dye and finish those materials are manufactured at different stages. The textile industry involves the processing of yarn, cloth, and finished products in its broadest sense. The method of transforming raw fibers into finished apparel and no textile apparel products is complex; hence most textile mills are spent significant time in particular production (USEPA, 1997). Textile mills can be classified in several ways. One way is according to the formation process of fabrics that are finished by the industries. The significant techniques for fabrics make are weaving and sewing and the fabrics manufactured by those processes are called woven and knit fabric respectively. Another type of textile mill is stock and yarn dyeing and finishing. Textile industries can also be classified according to the fiber used to manufacture fabric. The fiber utilized in the textile industry might be extensively arranged into four gatherings: cotton, wool recovered, and synthetics (Rao, Datta 1987). Cotton and wool are natural fibers and regenerated and synthetics are manmade fibers. Regenerated fibers or cellulosic fibers for example rayon and acetate are made by using wood pulp to react to chemicals. Synthetic fibers are synthesized from organic materials, such as polyester and nylon (USEPA, 1997). 2.3 Process Flows in Textile Industries Raw materials and other inputs sllch as water and energy arc converted by the process into the finished product along with the waste. Any items that do not form part of the finished product can be regarded as waste. In general, textile mills include the production of yarn, fabric and finished products. The processes used in these mills can be grouped into four main stages:

1. Yarn formation

2. Fabric formation

3. Wet processing

4. Fabrication

Yarn formation

Yarn is formed from textile fibers by gathering and curving activities used to tie them together. Yarn can be produced from both natural and manmade fibers. The yarn production processes from these two types of fibers are almost similar. Production of yarn from fibers includes steps like, opening and cleaning, carding, combing, drawing, drafting, spinning. (USEPA, 1997). This yarn formation stage produces little or no wastewater.

Fabric formation

In this stage fabric is produced from yarn. Most fabrics are manufactured by two significant strategies: weaving and sewing. Weaving is done on looms. Weaving fabrics are created by interlacing one set of yarns with another set, crosswise oriented. The yarn is passed through a size solution before weaving operation is started which is called sizing / slashing. Starch is most commonly used for the purpose of sizing. Polyvinyl alcohol, the leading synthetic size, is also used for this purpose. Oils, waxes, and other additives are also used along with sizing agents to improve the yarn's softness and pliability. In the loom the steps include shedding, picking, battening, and taking up operations (US EPA, 1997). Knitted fabrics are made using hooked needles to interlock one or more yarn sets via a set of loops. Depending on the fabric's intent, the loops can be built either tightly or loosely. Methods for knitting are either warp or weft (USEPA, 1997). This fabric formation stage produces little or no wastewater except the sizing step. In this sizing step waste originate due to spills and the floor washings at the weekend.

Wet processing

In this stage the fabric is processed to make that suitable for manufacture apparel and other finished goods. For this purpose, the fabric is passed through several water intensive wet processing steps. Wet processing enhances the quality, appearance and serviceability of fabrics by turning undented and unfinished materials, known as gray or black products, into finished goods for customers. There are a number of steps used in wet processing, but most commonly used steps are singeing, Desizing, scouring, bleaching, mercerizing, dyeing, printing, heat set, mechanical finishing and chemical finishing. Few of the above mentioned steps can be skipped considering the type of fabric to be processed, type of dye used, and the extent of finishing required. The mostly used techniques in wet processing are briefly described in the following.

Singeing: This fabric preparation technique gives the fabric a smooth finish by removing the protruding fibers from yarn or fabrics. This is done on woven fabric.

Mercerizing: This phase is used to improve the capacity of cotton and cotton polyester fabric to colour, appearance and luster. During this method, the texture is gone through a cool 15-20%

caustic soda solution and afterward spread over a delicate edge where boiling water splashes eliminate a large portion of the acidic arrangement (Corbman, 1975). Multiple washings under tension following treatment remove the caustic. With a cold acid wash, remaining caustic can be neutralized, followed by few additional rinses to eliminate the acid. Mercerizing wastewater can contain significant amounts of high pH alkali, comprising around 20% of the product weight (USEPA, 1997).

Dyeing: This phase is used to add textiles intricacy and color, and to enhance the value of the product. To this end, a wide variety of colorings, methods and equipment are used. Most of the dyestuffs used in tinting are synthetic. Usually such dyes are extracted from intermediates based on coal tar and petroleum.

Printing: Fabric printing is done with pigment and color using different type of methods and machines. About 75 to 85 percent printing operations is done with pigments. Printings with pigments do not need any cleaning steps. So they produce a small amount of waste

2.9.3 Materials Used in the Process and Sources of Pollutants

A large variety of input materials is used in textile industries. A knowledge of the input materials will help to understand the nature of the effluent (e.g. whether biodegradable or not). The input materials which are used in textile dyeing and finishing may include: the fiber, water, cloth ego

wool or yarn polyester, cotton, and a certain amount of process chemicals. The process chemicals include:

• Acids, e.g. formic, acetic;

• Alkalis, e.g. sodium carbonate, potassium hydroxide, sodium hydroxide;

• Bleach, e.g. sodium chlorite, sodium hypochlorite, hydrogen peroxide;

• Dyes, e.g. pigment, vat, disperse, direct;

• Salts, e.g. sodium chloride;

• Size, e.g. PV A, starch;

• Stabilizers, e.g. organic stabilizers, sodium nitrate, sodium silicate;

• Surfactants;

• Auxiliary finishes, e.g. softeners (or handles modifiers), fire retardant.

The majority of wastewater of textile mill originates from wet processing operations. Wastewater types include water purification, process water, non-contact cooling water and storm water. Later two types of wastewater are sometimes not subjected to any treatment. Essential origin of biochemical oxygen demand (BOD) incorporate waste synthetic compounds or cluster dumps, starch estimating operators, sewing oils, and degradable surfactants. The volume of wastewater to be treated can be determined from the water use data of the textile mill. Depending on the various processes conducted at the industry, the equipment used and the prevailing water use management method, the amount of water used varies widely within the industry.

Given the broad variety of process steps involved, textile effluent typically contains a complex mixture of chemicals. The highest concentration of pollutants in textile effluent comes from the desizing step where the size chemicals used in the weaving processes are removed desizing processes. For wastewater, up to 50 per cent of the BOD load from wet production sometimes contributes (Snowden-Swan, 1995). Table 2.1 displays standard tons of BODs from process planning.

A significant portion of the industries wastewater originates from the dyeing operations. Wastewaters from these operations typically contain residual dye, by-products, and chemicals, auxiliary and cleaning solvents such as oxalic acid. Dyes in wastewater may bind to cloth fibers chemically. (ATMI, 1997).

Finishing methods typically contain wastewater that contains common and synthetic polymers and a variety of other possibly harmful ingredient (Snowden-Swan. 1995). Bleaching peroxide is not normally a significant concern, because water is the only bi-product of the peroxide reaction. Chemical storage, water quality, and high pH in the bleaching process are main contamination concerns.

2.9.4 Typical Textile Effluent Characteristics

The composition and quantity of wastewater from textile mills changed with the fiber type, the method contains and the manner in which the process is worked. Effluent efficiency is calculated with: Pre-processing amount of impurities in the raw fiber, the wash ranges configuration form, ex; batch or continuous, the kind of synthetic substances utilized and their concentration and the volume of water used and the rate of flow of the wash water.

Different variables influencing effluent attributes incorporate fashion necessities and evolving seasons, ie colors and shade (Environmental Technology Best Practice Programme, 1997).

The effluent characteristics of the same type of industries may vary because of the country the industry is situated in. This is because industries in developed countries like USA, UK, and Canada use more sophisticated equipment, more skilled labor than industries in third world countries. Monitoring of the effluent discharge quality is more regular and appropriate and the effluent discharge quality standard is also more stringent in the developed countries. This leads the industries in those countries to use less cost effective but more environmentally friendly dyes and chemicals and production processes.

Typical properties of the combined effluent from cotton production and synthetic blends can be described as follows:

Table 2.4: Typical properties of the combined effluent from cotton production and synthetic mixtures

Parameter	Woven fabric finishing	Knit fabric finishing	Stack and yarn dyeing and finishing
BOD(mg/l)	550-650	250-350	200-250
Suspended solids(mg/l)	185-300	300	50-75

COD(mg/l)	850-1200	850-1000	524-800
Sulfide	3	0.2	0-0.09
Color(ADMI units)	352	400	600
PH	7-11	6-9	7-12

Source: Environmental Technology Best Practice Programme, 1997.

Characteristics of typical effluent from textile mills using different types of fibers are summarized below:

Table 2.5: Characteristics of typical el'f1uent from textile mills using different types of fibers

Parameter	Cotton textile mill[a]	Woolen textile mill[b]	Synthetic textile mill[b]
BOD(mg/l)	760	900	50
Total solids(mg/l)	6170	3000	2500
Total suspended solids(mg/l)		100	
COD(mg/l)	1418		500
Total chromium(mg/l)	12.5	4	
Color		Brown	Grey-yellowish
PH	9.8-11.8	9-10.5	7.5
Total Alkalinity(mg/l)	17.35	600	Low

Ref[a]. (Kothandaraman, Aboo and Sastly, 1976) Ref[b]. (Rao and Datta 1987)

2.9.5 Treatment methods for removal of effluents

Discharge standard from textile mill effluent is getting stricter day by day due to the growing environmental awareness. Different treatment options have been developed to meet those strict discharge standards. Options for effluent treatment include: Biological/bio sorption techniques, Ultrafiltration, Ion exchange, Reverse osmosis, Adsorption, Coagulation/flocculation, Chemical oxidation, Photo catalytic oxidation and Electrolysis

It is very difficult to meet the discharge standard using only one of the above mentioned treatment techniques. In most cases it is required to combine two or more treatment techniques. Due to cost constraints and land requirement most often coagulation/flocculation and biological/biosorption techniques among the above mentioned techniques are used in Bangladesh. However coagulation flocculation process is the most popular because unlike biological treatment plants this type of treatment plant does not have to be operated 24 hours a day and 365 days a year.

Unit Processes of Effluent Treatment

Methods used for wastewater treatment are also called either unit operations or unit processes. Unit operations typically require the removal of pollutants by physical means, while unit processes include biological and/or chemical reactions. Wastewater typically contains several different types of contaminants.

It is practically impossible to remove all the contaminants of the wastewater by using a single unit process. A set of unit processes is chosen to reduce the contaminant level in the effluent down to an acceptable limit. Each unit process is used targeting to reduce or remove one or more but not all types of contaminants. The .most common unit processes used to treat the effluent from textile mills of Bangladesh are briefly described in the following sections

pH correction:

Many of the unit processes of wastewater treatment are critically dependent on the pH of the wastewater. So pH correction is very important. This is done with the help of acid or base.

Coagulation and flocculation:

Chemical coagulation is used aiming to remove suspended solids and turbidity of water and wastewater. Coagulation is a two-stage process involving particle destabilization followed by particle transport to facilitate collisions between the destabilized particles. Destabilization may be achieved by applying a suitable coagulant. With the correct mixing system, particle interaction is ensured. Promoting collisions between particles helps them to aggregate into larger particles. This aggregation is called the flocculation process by some authors. According to common engineering usage the term flocculation describes the particle transport step. While the term coagulation is used to describe the overall process of aggregation including both destabilization and transport (weber. 1972). In the field of water and waste water treatment coagulation is considered as a chemical destabilizing process by the addition of some reagent to the colloidal system which includes the aggregation of particles. Whilst flocculation implies the aggregation of particles under the influence of velocity gradients (Hossain. 1990).

Mechanisms of destabilization

The removal of colloidal and suspended particles by coagulation is dependent on the reduction of particle stability. Particle de stability can be achieved by four mechanisms:

(I) Double-layer compression.

(2) Adsorption and charge neutralization

(3) Enmeshment in a precipitate

(4) Adsorption and inter-particle bridging.

In practice, the colloidal destabilization is likely to be caused by more than one mechanism. The mechanisms of colloidal destabilization are briefly discussed in the following sections.

Double-layer compression:

The charged surface can impact ions that are present in the water or wastewater near the colloid. The first layer of cations attracted to the negatively charged surface is "bound" to the colloid, and will migrate with it, as a negatively charged colloid. Many ions in the vicinity of the colloid organize themselves with greater positive or counter-concentration, ions being near to the colloidal surface. 24 (Pcavy, from 1985). This arrangement generates a net charge at thc bound layer which is the highest and decreases exponentially from the colloid. The above mentioned two layers collectively known as defused layer contain a quantity of counter ions sufficient to valance the electrical charge on the particle. If an electrolyte is added to a colloid dispersion, the surface charge on the particles will remain unchanged if that charge originates from crystal imperfections (i.e., clay particles). However, the added electrolyte will increase the charge density in the diffuse layer and result in less volume of the diffuse layer being required to neutralize the surface charge. Thus, the diffuse layer is compressed toward the particle surface charge. The effect of this compression is to change the distribution of double-layer repulsion forces in the vicinity of the colloid and cause a reduction in surface potential with increasing electrolyte concentration, which allows the van dar Waals' attractive forces to be more dominant, thus enhancing particle aggregation.

Two interesting aspects of double-layer compression are (l) The amount of electrolyte needed to achieve double-layer compression coagulation is basically independent of the colloid concentration during dispersion; and (2) it is not possible to cause a charge reversal on a colloid by double-layer compression, regardless of how much electrolyte is added.

Adsorption and charge neutralization:

Many chemical compounds can be adsorbed by colloidal particles on the surface. If the adsorbed species carry an opposite charge to that of the colloids, such adsorption causes the colloidal particle to decrease its surface potential and result in destabilization. According to this mechanism the amount of coagulant required to coagulate colloids is linearly proportional to the surface area of colloids and at excess coagulant dose, restabilization can occur, leading to charge reversal.

Enmeshed in a precipitate:

When certain metallic salts are used as coagulants in water or wastewater rapid precipitation occurs in adequate quantities. Colloidal particles may serve as a condensation nucleus for these precipitates, or may become '25 \' enmeshed as precipitates settle. Coagulants those are AI (S04), FeCl, MgCO and Ca (OH) can induce coagulation by the formation of insoluble Al (OHh(s), Fe(OHh(s), Mg(OHh(s) and CaCOJ(s). Removal of colloidal particles in the mechanism is frequently referred to as sweep-floc coagulation. According to this mechanism, there is an inverse relationship exists between the optimum coagulant dosage and the concentration of colloid to be removed.

Adsorption and inter-particle bridging:

Ruehwein and Ward (1952) and LaMar and Healy (1963) have developed a chemical bridging theory that is consistent in explaining the observed behavior of polymeric compounds during coagulation process when added as coagulant. This theory proposed suggested that high molecular weight polyelectrolytes form interparticle bridges using segments of the molecule to attach themselves to each particle. Bridged particles become interlocked with other bridged particles during the flocculation process and three dimensional polymer particle complexes is formed having favorable settling characteristics. Attachment can result from columbic attraction if the polymer and particle are opposite loads or from the exchange of ions, hydrogen bonding or forces of Vander Waals if they are of similar charge (0' Melia 1972).

2.10 Adsorption

Adsorption is the method by which various molecules, atoms, and ions of a liquid or gas adhere to the surface. The adsorbent's surface is coated with a coating of adsorbate. This technique differs from absorption in that absorption occurs when the substrate, which is normally in the context of a fluid, percolates into the absorbent (Ramakrishna, 2013). As a result, absorption affects the entire substance, whereas adsorption only affects the surface. However, these phrases are combined into a single term termed "sorption," while "desorption" is the inverse of "sorption." In recent years, adsorption has shown to be a better and more efficient way of waste water treatment. It is the process of developing a solid or gaseous layer on a substrate. As a result of the adsorption process, the substance is separated from the fluid phase and accumulates on the solid phase substrate (Abbas F. S., 2013).

The majority of solid adsorbents used in large industrial applications have a complicated porous structure with pores of various sizes and shapes. In terms of adsorption science, total porosity is

usually split into three categories. Microspores are described as pores with a width of 50 nanometers or less, according to the International Union of Pure and Applied Chemistry (IUPAC) (Hasan, 2008).

The impact of porous structure on the adsorption of numerous pollutants in aqueous solution, on the other hand, is little understood. When it comes to physisorption on porous materials, it's widely known that the adsorption mechanism and method may alter greatly due to the porous structure. A powder can also be easily identified as a mass of little dry particles, but the correct definition is inevitably arbitrary. The word fine powder is also used loosely, however it is appropriate to use it to describe a material with particles smaller than roughly 1m. A fine powder's unit mass contains a large number of tiny particles and has a significant surface area (Serin & Selen, 2012)

A variety of additional parameters, such as the cost of processing materials, 14 wastewater selectivity, and material regeneration, all have a significant impact on the choice and feasibility of waste materials as adsorbents. When evaluating materials for use as adsorbents, cost is a major consideration. It is widely accepted that a material is low-cost if it requires little processing, is abundant in nature, or is a waste product or byproduct from another business (Eng-Cheong Khoo, 2011).

2.10.1. Adsorbent for dye removal

Although almost any solid surface has the ability to adsorb sorbate, the efficacy of these particles in the wastewater treatment process is determined by their degree of polarity, structure, specific area and porosity. The adsorbate could be an organic compound having unwanted characteristics like colour, odour, and so on. Activated carbon, organic polymers, and silica-based compounds are the three main forms of adsorbents (Muhi Mohammed, 2011).

A. Commercial activated carbons

Solid sorbent adsorption techniques are commonly employed to remove certain types of chemical contaminants from water, particularly those that are almost unaffected by standard biological wastewater treatment. However, among all of the adsorbent materials considered for the removal of contaminants from wastewater, activated carbon is the most preferred. Adsorption on commercial activated carbons, in particular, has proven to be a successful way for removing a wide range of colours from wastewaters, making it a viable option to more conventional treatment modalities. This is owing to their chemical nature, which can be easily adjusted by chemical treatment to boost their attributes, as well as their structural traits and porous texture, which provides them a vast surface area (Singh & M.K., 2000).

Activated carbon, on the other hand, has a number of drawbacks. It's quite pricey; the better the quality, the more expensive it is; it's also nonselective and useless against disperse and vat dyes. Saturated carbon regeneration is very costly and leads in a loss of adsorbent. In contrast, in recent years, the use of alternative low-cost materials with high adsorption ability to alleviate environmental problems has gotten a lot of attention (EngCheong Khoo, 2011).

B. Raw agricultural solid waste

As adsorbents, raw agricultural solid wastes and waste materials from the forest industry, such as sawdust and bark, were employed. Because of their physico-chemical properties and inexpensive cost, these materials are readily available in large quantities and may have promise as sorbents. Agricultural waste materials have little or no economic value and often pose a disposal problem, so utilization of the material is of great significance (Eng-Cheong Khoo, 2011).

Several agricultural waste materials are being investigated for their ability to remove various dyes from aqueous solutions under various load conditions. These contains mangrove bark (Tan J. R., 2010), wheat straw (Nader Yousefi A. F., 2011) and orange peel and rice husk (Y.C.Wong and K.N. Ranjini, 2014). Many researchers have been investigating the suitability of many of agricultural by products as bio-adsorbent to remove organic pollutants including different groups of synthetic dye which is the focus of this study that is to explore the feasibility of powdered orange peel (POP) as bio-adsorbent to remove azo dye (Reactive red DEXF) from aqueous solution.

C. Wheat bran as an adsorbent

Wheat bran (WB) is an agricultural by-product made from the shells of flour mill wheat seeds that can be used to remove heavy metals. It is cost-effective, biodegradable, and rich in nutrients like minerals, fatty acids, dietary fibers, and protein (Kaya et al., 2014). It has a surface area of 441 m2/g and a fixed carbon content of 31.78 percent, and it has diverse organic functional groups (Singh et al., 2009).

Wheat bran was also used as removal of dye from industrial wastewaters [21]. Surface and pH have the major role to remove the methyl blue on wheat bran [22]. Ammonium salts-based modified wheat brans are used to remove the anionic dyes [23].Different nonconventional adsorbents, including guar gum-based hydrogels, wheat bran, clay [24, 25, 26].

The key components of wheat bran contain hemicellulose (29.2%), cellulose (32.1%), extractives (22.3%), and lignin (16.4%). Wheat bran can be used to extract toxic materials as an effective adsorbent.

Due to various hydroxyl groups that exist in cellulose, hemicellulose, and lignin structures, wheat bran exhibits low adsorption efficiency for anionic dyes. Practical and efficient surface modification of wheat brains to increase their an-ionic dye adsorption ability. To achieve a positive adsorbent, Yue et al. added amine groups to the structure of wheat bran by chemical modification [17]. Magnetic graphene oxide and Fe_3O_4 nanoparticles were loaded on the surface of wheat bran [27]. Dehydrated wheat bran is also the most effective adsorbent for the removal of methylene blue [28]. Different diameters of wheat bran particles have much removal efficiency for the Astrazon yellow 7G [29]. The tartaric acid-washed wheat bran is used as the most effective adsorbent for the removal of chromium from an aqueous solution [30, 31].

2.10.2 Adsorption isotherm

Adsorption is usually depicted by isotherms, which are plots showing the amount of adsorbate on the adsorbent as a function of pressure (in the case of a gas) or concentration (in the case of a liquid) at a constant temperature. To allow comparison of diverse materials, the amount of adsorbate adsorbed is virtually continually standardized by the mass of the adsorbent. Equilibrium investigations on adsorption processes give information on the adsorbent's activity (Serin & Selen, 2012).

A concentration (loading) of adsorbate in the solid phase (qe mg/g) in dynamic equilibrium with a solute concentration in the liquid phase (Ce mg/L) characterizes the equilibrium state. A wide range values of qe versus Ce values may be obtained by varying the amount of adsorbent (m, g), the initial concentration of solute (Co, mg/L), and the volume of liquid (Asgher, 2011). Normally, one or more equilibrium isotherm models can be used to fit the association between these qe and Ce. Many models exist to characterize the equilibrium activity of pollutants in water adsorption (Nader Yousefi A. F., 2011).

1. Langmuir model

The Langmuir model Equation (1) was created to explain and quantify sorption on a collection of discrete localized adsorption sites, but it has since been applied to both physical and chemical adsorption. The following are the basic factors that underpin this model (langmuir, 1916).

• Each active site interacts with only one adsorbate molecule.

• The saturation coverage of adsorbate molecules equates to complete occupancy of well-defined localized locations.

• There is no interaction between nearby adsorbed molecules since the adsorption sites are all energetically equal (homogeneous). The Langmuir relationship between qe and Ce can be calculated using these assumptions:

$$\frac{1}{q_m} = \frac{1}{q_0} + \frac{1}{q_0 K_L}\frac{1}{c_e} \quad (2.8)$$

Where, q_m (mg g^{-1}) and k_L (L mg^{-1} Freundlich model) are the Langmuir constants related to the capacity of adsorbent and energy of adsorption respectively. This is the most commonly used adsorption isotherm, and it has shown high similarity with a wide range of experimental data (Abbas & Kadim, 2010).

2. Freundlich model

The Freundlich equation discusses the adsorption of solutes from a liquid to a solid surface using empirical data. The Freundlich model (Equation (2.9)) adsorption is defined in terms of the amount of adsorbate present. (Meena Soni and Ashok Sharma, 2012). Linearized form of the Freundlich equation is as follows:

$$\ln q_e = \ln K_f + \frac{1}{n}\ln C_e \quad (2.9)$$

Where, k_f and 1/n are Freundlich isotherm constants related to adsorption capacity and adsorption intensity respectively.

2.10.3 Adsorption kinetics

The investigation of adsorption kinetics explains the solvent uptake rate and obviously, this rate regulates the residence time of adsorbate uptake at the solid sample interface. The kinetics of the dye removal on adsorbent was studied utilizing pseudo-first-order and pseudo-second-order [44].

A. Pseudo-first order equation

The rate of adsorption is directly proportional to the number of vacant sites when considering reversible binding contaminants and adsorption on active sites present on the adsorbent surface. The equation of pseudo-first-order was expressed by Eqn. 2.91

$$\frac{dq}{dt} = k_1 (q_e - q_t) \quad (2.91)$$

Where q_t and q_e are the adsorption capacity at time t and equilibrium, respectively (mg/g). k_1 is the rate constant (min^{-1}). Integrating and implementing the above equation boundary conditions from t = 0 to t = t, and q_t = 0 to $q_t = q_t$, the integrated form of Eqn.2.92 becomes

$$\log (q_e - q_t) = \log (q_e) - \frac{k_1 t}{2.303} \quad (2.92)$$

Eqn. 2.92 is applies to the experimental results. The rate constant in this model was investigated by the slope of the graph of ln (Qe − Qt) over time (t).

B. Pseudo second order equation

In this model, it was considered that capability of adsorption of adsorbate on the adsorbent surface is affected by chemical forces, instead of physical attrition forces.

Non-linear form of the model is given as

$$\frac{dq}{dt} = k_2 (q_e - q_t)^2 \quad (2.93)$$

Upon integration with boundary conditions from $q_t = 0$ at $t = 0$, $q = q_t$ at $t = t$, the above equation **(**Eqn.2.93) Reduces to desired eqn (2.94)

$$\frac{t}{q_t} = \frac{1}{k_2 q_e^2} + \frac{t}{q_e} \quad (2.94)$$

Where q_t and q_e are the adsorption capacities time t, and at equilibrium respectively (mg/l). k_2 is the rate constant (g/mg.min).The rate constant can be investigated for different dye concentrations according to the graph of t/q_t versus t. The determined (R^2) were observed to be greater than 0.98, and the determined Qe varied from the experimental ones. Depending on the results of the pseudo-second-order kinetic model, Qe, cal had better coincidence with the experimental Qe, exp. This characterization shown in the pseudo-second-order model was a good model to illustrate the adsorption method of azo dye removal on wheat bran.

2.10.4 Optimization of operating parameters

There is a necessity of optimum parameters to make batch study effective for polluents removal.As the rate of adsorption depends on operating parameters such as initial concentration, temperature, adsorbent dose, pH, contact time and stirring speed (Sahu et al. 2009). Zulkali et al., 2006 has optimized a batch process for polluents removal for various parameters (initial concentration, temperature, adsorbent dose and pH) using central composite design in Response Surface Methodology by Design Expert Version 5.0.7 (Stat Ease, USA). The optimum conditions obtained were 50 mg/L initial concentration, 60^0C temperature, 0.2 g adsorbent dose and pH 5 for 98.11% lead removal.

Similarly Kataria & Garg 2018 has removed polluents using ZnO and optimized with central

composite design in response surface methodology, observed optimum conditions were 0.8 g/L adsorbent dose, 100 min contact time, 6 pH and 10 mg/L metal concentration. Supported on wood husk, optimum conditions such as pH of 3.72 and 5.48, initial chromium concentration 10 and 16.91 mg/L and adsorbent dose of 6.95 and 8.20 g/L were obtained by central composite design (Asri et al., 2018). However, Lung et al., 2018 has used Box-Behnen Design for optimization of batch process for polluents removal (cadmium, lead and arsenic) and 20 mg/L initial ion concentration, 5 g/L adsorbent dose and pH 5.5 was obtained as an optimum condition. Similarly Box-Behnen Design was used by Rahman & Nasir 2018 for optimization of batch process for cadmium removal using poly (o- phenylene diamine)/hydrous zirconium oxide composite and optimum conditions obtained were 50 mg/L initial metal concentration, 25 mg/mL adsorbent dose, pH 6 and contact time 45 min for 99.6% cadmium removal. Khobragade et al., 2016 has removed nickel, copper using surfactant modified alumina using a three-factor, three-level Box–Behnken experimental design. The optimum values found for nickel were pH 8.2 adsorbent dose 5 g/L and contact time 60 min for 93.83% removal and for copper the optimum values were pH 5.3 adsorbent dose 4 g/L and contact time 75 min for 97.23 % removal. For lead, copper and cadmium removal optimal conditions obtained were 25 mg/L initial metal concentration, pH 6 and 2 g/L of adsorbent dose using pseudomonas azo to form an bacterium and Box-Behnken design (Choińska-Pulit et al., 2018) for 63.32% copper, 78.23% lead, % 44.67% cadmium removal. For optimization, use of Box-Behnken design is useful over central composite design because it requires less number of experiments (Rakic et al., 2014).

2 .10.5 Design of experiments

In experimental optimization technique, it is difficult to understand the effect of interacting parameters on removal. Therefore nowadays various statistical methods have been adopted for optimization such as design of experiments, Mini tab.

Design of experiments is a statistical technique being used since 1990s. Experimental design includes experimental statistics and it can produce explicit results. Main effects and interaction effects can be calculated using design of experiments (Lee et al., 2006).

Cao et al, 2014 has used central composite design in design of experiments with four variables (temperature, pH, initial concentration and adsorbent dose) and 30 experiments for chromium removal using amine- functionalized MCM-41.

From ANOVA analysis, it was clear that the predicted results are close to the experimental results and optimum values obtained were temperature 40^0C, pH 3.5, initial metal concentration 10 mg/L and removal 98.70% and adsorbent dose 5 g/L. Similarly, Singh et al., 2010 has used Box–Behnken design in design of experiments with three levels, four variables (temperature, pH, initial conc. and adsorbent dose) and 29 experiments for lead, cadmium and copper removal using Trichoderma varied as an adsorbent and ANOVA ensures that model is significant because probability value is less than 0.05 and predicted and adjusted R-square value are in the range of 0.84-0.99.

Similarly, unwanted components were removed from wastewater using Box- Behnken design in design of experiments with three levels, four factor (temperature, pH, initial metal concentration and adsorbent dosage) and 29 experiments (Ahmadi et al., 2014) using magnetite nanoparticles.

CHAPTER - 3
MATERIALS AND METHODS

3.1 Introduction

This chapter explains materials and methods used for (i) Hydrodynamic studies, (ii) Residence time distribution (RTD), and (iii) Synthetic textile wastewater treatment in tapered inverse fluidized bed by adsorption in batch processes.

(i) Hydrodynamic studies

The bed heat transfer coefficient and related hydrodynamics were determined along with different angles (8^o and 6.8^o) of the tapered inversed fluidized bed. Carboxyl methylcellulose was used to change the water viscosity by using a power-law model. The hydrodynamics was compared for two different angles of beds. Furthermore, minimum fluidization velocities were carried out for different liquid apparent viscosities and different angles of beds and compared with previous models. The correlation was developed between the bed expansion ratio and independent parameters by response surface methodology in design expert software v.9. The CFD software was also used to find the hydrodynamic studies in 3D and 2D model.

(ii) Residence time distribution (RTD)

Residence Time Distribution (RTD) characteristics of liquid tracer in two phase tapered inverse fluidized bed with solid materials of three different densities (900-970 kg/m^3) at two different bed angles (α) of 6.85 &8^0.For the experiments Propionic acid used as pulse tracer, water is used as fluid media, and solid particles which have lower density than water were used as solid media. And also validated with the computational fluid dynamics (CFD) using a commercial CFD software. An empirical correlation has been developed for the mean residence time of tracer by the Response surface methodology (RSM) using Design expert software.

(iii) Synthetic textile wastewater treatment in tapered inverse fluidized bed.

Preparation of different adsorbent without modification for removal of COD, Turbidity, color of textile dye, and DO increment. This chapter also includes design of experiments (DOE). It is a method to determine the relationship between factors affecting a process and output of the process. The design and fabrication of experimental setup was also explained in this chapter. This experimental setup was fabricated at the Chemical Engineering Department, National institute of technology, Warangal. Various correlation and model parameters were also discussed.

Characterization techniques for adsorbent were also included. All the characterization was carried out in Centre for Automation and Instrumentation (CAI), National Institute of Technology NIT Warangal.

3.2 Materials and Chemicals used

HDPE (High density polyethylene), LDPE (Low density polyethylene), PP(Polypropylene), Beads, Propionic acid, Phenapthaline indicator, Water heater, Thermo couples, Potassium dichromate (K), Sodium hydroxide (NaOH), Ferrous ammonium sulphate (FAS), Sodium thiosulphate($Na_2S_2O_3$),Sulphuric acid(H_2SO_4), Calcium chloride($CaCl_2$), Manganous Sulphate($MnSo_4$), Phosphate Buffer Solution, Ethylene diamante traacetic acid (EDTA), ammonium buffer indicator, Erochrom black T, Carboxy Methyl Cellulose(CMC) (Merck, Germany) were purchased from local market. Wheat bran was collected from local bakery shop and flour mill at Warangal. Sodium hydroxide (NaOH) and Hydrochloric acid (HCl, Rankem) all are analytical reagent grade was purchased from local market.

High Density Polyethylene (HDPE):

High Density Polyethylene (HDPE) or High Density Polyethylene (PEHD) is petroleum based polyethylene thermoplastic. Known for its high strength to density ratio, HDPE is widely used in the manufacture of corrosion-resistant tubing, plastic bottles, plastic lumber and geo-membranes. HDPE is known for its high density ratio. The mass density of high density polyethylene will range from 0.93 g / cm^3 to 0.97 g / cm^3 and crystal density from 0.947 cg / cm^3. HDPE has little branching, which makes it tensile strength and stronger intermolecular forces. The variation in strength is greater than the difference in density, giving HDPE a higher basic strength. It is also stronger and more invisible and can withstand slightly higher temperatures (120 ° C/248 ° F for short periods, 110 ° C/230 ° F continuously). In comparison to polypropylene, high-density polyethylene cannot withstand standard autoclaving conditions. The lack of branching is assured by an acceptable choice of catalysts (e.g., Ziegler-Natta catalysts) and reaction conditions. The HDPE includes the chemical composition of hydrogen and carbon.

Low Density Polyethylene (LDPE):

Low-density polyethylene (LDPE) is a thermoplastic made of monomeric ethylene. It was the first grade of polyethylene developed by Imperial Chemical Industries (ICI) in 1933 using a high-

pressure process by free radical polymerization. Today, its manufacture employs the same process. Despite competition from more advanced polymers, LDPE is still an important grade of plastic.

LDPE is characterized by a density range of 0.91 0-0.940 g / cm^3 and a crystal density of 0.928 g / cm^3. It is not reactive at room temperatures, except for strong oxidizing agents, and certain solvents cause swelling. It can endure temperatures of 80 ° C continuously and 95 ° C for a limited period of time. Made in transparent or opaque variations, it is very flexible and tough yet brittle.

LDPE has more branching such that its intermolecular forces are weaker, its tensile strength is lower, and its resistance is higher. Also, because its molecules are less tightly packed and less crystalline due to the side branches, its density is lower. The LDPE includes the chemical elements of carbon and hydrogen.

Polypropylene (PP):

Polypropylene (PP), also known as polypropylene, is a thermoplastic based polymer used in a wide range of applications including stationery, packaging and labeling, plastic parts and reusable containers of various types, loudspeakers, laboratory equipment, polymer banknotes and automotive components. An addition polymer made of monomer propylene; it is rugged and unusually resistant to acids and bases, many chemical solvents.

Polypropylene is typically hard and flexible, particularly when copolymerized with ethylene. This allows polypropylene to be used as a plastic engineering material that competes with materials such as ABS. Polypropylene is relatively inexpensive and can be rendered translucent when uncolored, though not as easily transparent as polystyrene, acrylic or certain other plastics. It's always opaque or colored with pigments. Polypropylene has a high tolerance to tiredness.

Polypropylene bulk density is between 0.855-0.940 g / cm^3 and crystal density is 0.917 g / cm^3. The melting point of polypropylene occurs within a range, so the melting point is determined by finding the highest temperature of the differential calorimetric scan table. The optimal isotactic PP has a melting point of 171 ° C. Industrial isotactic PP has a melting point between 160 and 166 ° C.

There are three general forms of polypropylene: homopolymer, block copolymer and random copolymer. The co-monomer is widely used for ethylene. The addition of ethylene-propylene

rubber or EPDM to polypropylene homopolymer improves its low temperature impact power. Randomly polymerized ethylene monomer applied to polypropylene homo polymer reduces the crystallinity of the polymer and renders the polymer more transparent.

3.3 Tapered inverse fluidized bed column

3.3.1 Design of experimental setup and methods

The conical inverse fluidized bed (fig.3.1) was made of 0.22 m bottom diameter, 0.073 m top diameter and 0.59 m high acrylic material. The mesh is used at the top and bottom of the column as a distributor to avoid particle escape, and to display a uniform flow distribution. The flowrates are controlled using the ball valves. For hydrodynamic studies, the pressure tapings on the side of the column were mounted to measure the pressure drop at each flow rate. For heating purposes, a heater (25.4 mm o.d. × 1.5 m length) was vertically placed at the center in the fuidizedbed. The temperatures at the heater surface and the fuidizedbed proper were measured by the iron-constantan thermocouples (J type), which were mounted on the column at 20 cm height intervals. This heater was connected to a temperature controller that was used to control and maintain continuously the desired temperatures.

a) b)

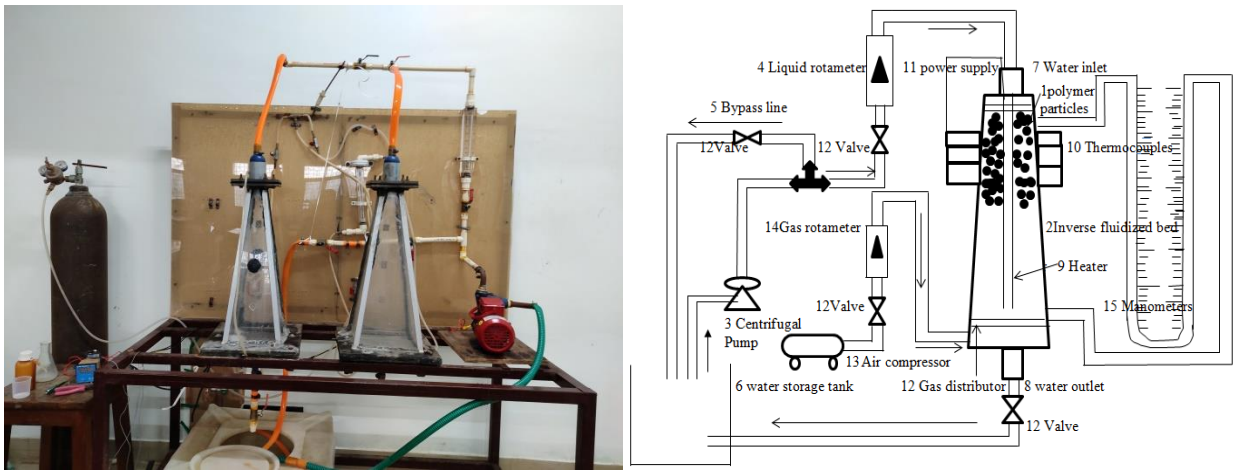

Fig. 3.1: Experimental setup (a) In laboratory, for continuous operation (b) Schematic diagram

A big change in the fluidizing bed took place for different fluid velocity. In that process, pressure drop was also calculated in the bed from one consistent was fluidizing state to another as a function of liquid velocity. When a new consistent state was reached, the temperatures were measured again. The equation below was used to calculate the heat transfer coefficient was

$$h = \frac{q}{A(T_h - T_m)} \tag{3.1}$$

q is the heat flux, acquired from DC electricity supply, and the temperature difference between the dipped in water heater and bed is determined with the aid of

$$T_h\text{-}T_m = \frac{\int_0^R U(r)[(T_h - T_.(r)]rdr}{\int_0^R U(r)rdr} \tag{3.2}$$

The velocity distribution in radial direction expression changed from suspect to uniform to that proposed for the fully advanced flow in inverse fluidized bed .The energy used to determine the heat flux was

$$q = \dot{m}C_{pl}(T_{mo} - T_{mi}) \tag{3.3}$$

Measurement of Heat transfer

The radial temperature profiles along in the bed was observed it was seen that the temperature at heater surface was much steeper than that of bed proper. Heat transfer coefficient was calculated in different angles of beds at different apparent viscosity of liquid flowrates using the above equation (1).

The nusslet number equation (4) was calculated in terms of bed Voidage equation (9) from Wen-Yu and heat transfer coefficient.

$$Nu = hd_p \frac{(1-\varepsilon_s)}{K_l \varepsilon_s} \tag{3.4}$$

Minimum fluidization studies

It is estimated from the correlation obtained from the experimental data relating to the minimum fluidization velocity, Archimedes number and density difference

Correlation

$$U_{mf} = a[Ar]^b [\frac{\rho_l - \rho_s)}{\rho_l}] \tag{3.5}$$

a=8.464*10^-3

b=0.459

c=0.301

10^4<Ar<8*10^4

Some of the models were used to estimate the minimum fluidization velocity and compared with experimental results

Khani et al.

$$Re_{mf} = 10.396(Ar)^{0.367}(\frac{d_p}{D_0})^{0.889}(\frac{\varepsilon_0}{\phi_s})^{-0.731}(cos\alpha)^{-10.437} \; for \; \alpha > 4.5 \tag{3.6}$$

Where Re_{mf} is the modified Reynolds number:

Ar is Archimedes number

α is the angle in the reactor

Biswal et al. $U_{mf} = \frac{-A1+SQRT(A1^2+4B1C1)}{2B1}$ (3.7)

Where $A_1 = COS(\frac{\alpha}{2})$ [3717tan$(\alpha)^{-0.47} \frac{\mu(1-\varepsilon_0)^2}{gd_p{}^2\varepsilon_0} \frac{r_0(r_1-r_0)}{r_1}$]

B1= 0.75 $COS(\frac{\alpha}{2})\frac{\rho_l(1-\varepsilon_0)}{gd_p{\varepsilon_0}^3}\frac{r_0({r_1}^3-{r_0}^3)}{3{r_1}^3}$, C1=$r_1(1-\varepsilon_0)(\rho_l-\rho_s)$

r_0, r_1=bottom and Top radius of the bed

ε_0=bed Voidage

d_p=Diameter of particles

ρ_l=liquid density

ρ_s =solid density

Modified Ergun eqn: $A\, u_{mf}$+B$\frac{r_0}{r_1} u_{mf}{}^2$.-(1-$\varepsilon^2{}_{mf}$)$(\rho_l - \rho_s)g\frac{r_0{}^2+r_0 r_1+r_1{}^2}{3r_0{}^2}$ (3.8)

$$Where\ A = 150\frac{(1-\varepsilon^2{}_{mf})}{\varepsilon_{mf}{}^3}\frac{\mu_l}{(\phi_s d_p)^2},\ \ B = 1.75(\frac{1-\varepsilon_{mf}}{\varepsilon_{mf}})\frac{\rho_l}{\phi_s d_p}$$

μ_l is the liquid viscosity

ϕ_s is the solids porosity

Measurement of Bed Voidage, Bed Volume and pressure drop:

To understand the characteristics of the in the inverse tapered fluidized bed, based on mathematical model bed expansion was determined and pressure drop was advanced based on the addition of bed characteristics in a sequence of individual bed volumes up the bed. It was considered that the bed Voidage in each bed increment could be determined by the correlation of Wen and Yu:

$$\varepsilon_s=[\frac{18\ N_{Re}+2.7N_{Re}{}^{1.687}}{N_{Ga}}]^{0.213} \quad (3.9)$$

$$\text{where}\ \ N_{Ga} = \frac{[d_p{}^8\rho_f(\rho_f-\rho_s)g]}{\mu^2}$$

The pressure drop over on each bed increment was determined by the force needed to support the bed in gravitational field:

$$\Delta p = (1-\varepsilon_s)\big(\rho_f - \rho_s\big)gh \quad (3.10)$$

The solid volume in the bed can be determined by a simple material balance around each increment.

$$\Delta V_s = (1-\varepsilon)Ah = (1-\varepsilon)\Delta V \quad (3.11)$$

:

The total bed volume is determined when a summation of the incremental solids equals the original solids volume with the bed at rest:

$$\sum(1-\varepsilon)\Delta V = (1-\varepsilon_0)V_0 \qquad (3.12)$$

Developing of Empirical model by using Response surface methodology (RSM):

Response surface method (RSM) used different statistical, graphical and mathematical techniques to broaden, enhance, or optimize procedures, it was also used for modeling and evaluation of problems if the response variables were encouraged through several unbiased variables.

Surface Response Methodology (RSM) data modeling, used an inbuilt utility of Design expert package (version 9) in the present work to derive the regression models in terms of different process parameters like Velocity of liquid, Temperature of liquid, Viscosity of liquid, density of solids and different angles of reactors. This model equation was used to get the influence of process parameters on bed expansion ratio through the reactor. The confidence level of data was kept at 0.95 for bed expansion ratio. The levels of all process variables were specified based on the current task's experiments, and the level values of the individual parameters used in the experiments are shown in Table 3.1.

Table 3.1: Symbols and levels of independent parameters were used in response surface methodology.

Symbol	Parameters	Units	No of Level	Levels							
				1	2	3	4	5	6	7	8
A	Temperature	^{O}C	4	33	45	63	80				
B	Apparent viscosity	Kg/m.s	3	0.00089	0.0014	0.0036					
C	Density of	Kg/m^3	3	930	945	970					
D	Bed angle	^{o}	2	6.8	7.85						
E	Velocity of liquid	m/sec	8	0.14	0.34	0.56	0.65	0.71	0.85	1.25	1.35

3.4 Computational fluid dynamics (CFD) design for hydrodynamic studies

There are 2-schemes for the study of multiphase flow simulation: the Eulerian-Lagrangian method and the Eulerian–Eulerian approach (TFM). In this section, the Eulerian-Eulerian approach was used and related governing, momentum, continuity equations, boundary, and preliminary conditions are described in addition to the simulation processes used inside the CFD modeling shown in table 3.2. The physical properties of solid materials are given in table 3.5.

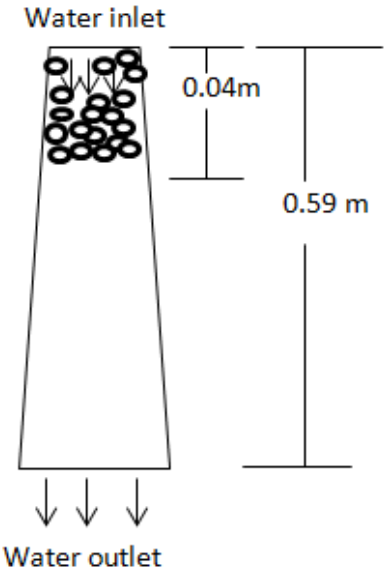

Fig 3.2 Schematic of geometry of the tapered inverse fluidized bed.

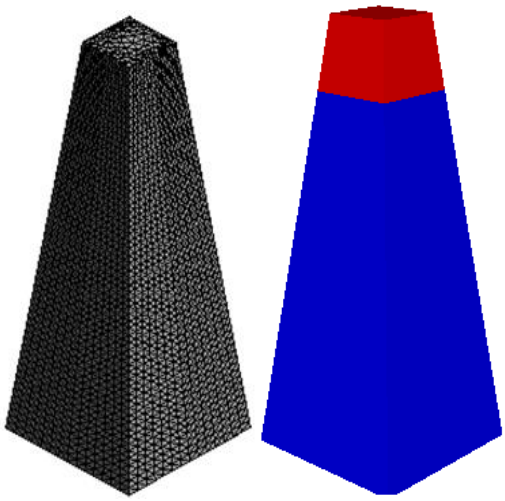

Fig 3.3 Schematic of mesh generated of tapered inverse fluidized Bed

Table 3.2 Model equations in Fluent 17.2 CFD code

$\partial/\partial t(\alpha_q \rho_q) + \nabla.(\alpha_q \rho_q$ Continuity equations

$\partial/\partial t(\alpha_l \rho_l \overrightarrow{v_l}) + \nabla.(\alpha_l \rho_l \overrightarrow{v_l}\overrightarrow{v_l}) = -\alpha_l \nabla p + \nabla.\overline{\overline{\tau_l}} + \alpha_l \rho_l g + K_{sl}(\overrightarrow{v_s} - \overrightarrow{v_l})$ Momentum equation

$\partial/\partial t(\alpha_S \rho_S \overrightarrow{v_S}) + \nabla.(\alpha_S \rho_S \overrightarrow{v_S}\overrightarrow{v_S}) = -\alpha_l \nabla p - \nabla.\overline{\overline{\tau_S}} + \alpha_S \rho_S g + K_{sl}(\overrightarrow{v_l} - \overrightarrow{v_s})$

$$\overline{\overline{\tau_l}} = \alpha_l \mu_l \left(\nabla \overrightarrow{v_l} + \nabla \overrightarrow{v_l}^T\right) - \frac{2\alpha_l \mu_l}{3}(\nabla.\overrightarrow{v_l})\overline{\overline{I}}$$

$K_{sl} = \frac{3}{4} C_D \alpha_s \alpha_l \rho_l \frac{|\overrightarrow{v_s} - \overrightarrow{v_l}|}{d_s} \alpha_l^{-2.65}$ Wen and Yu

$K_{sl} = \frac{3}{4} C_D \frac{\alpha_s \alpha_l \rho_l (\overrightarrow{v_s} - \overrightarrow{v_l})}{d_s} \alpha_l^{-2.65}$ For $\alpha_l > 0.8$ Gidaspow model

$K_{sl} = 150 \frac{\alpha_s (1-\alpha_l)\mu_l}{\alpha_l d^2{}_s} + 1.75 \alpha_s \rho_l \frac{(\overrightarrow{v_s} - \overrightarrow{v_l})}{d_s}$ For $\alpha_l \leq 0.8$

$C_D = \frac{24}{\varepsilon_l Re_s}[1 + 0.15(\alpha_l Re_s)^{0.687}]$ For $Re_s \leq 1000$

0.44 For $Re_s > 1000$

$$Re_s = \rho_l d_s \frac{|\overrightarrow{v_s} - \overrightarrow{v_l}|}{\mu_l}$$

Where Re is the Reynolds number and C_D is the drag coefficient

$K_{ls} = \frac{3 c_D}{4 u_{r,s}{}^2} \rho_l \frac{|\overrightarrow{v_s} - \overrightarrow{v_l}|}{d_s} \left(\frac{Re_s}{u_{r,s}}\right) \alpha_l \alpha_s$ Syamlal and o′Brien

Where $c_D = (0.63 + \frac{4.8}{\sqrt{\frac{Re_s}{u_{r,s}}}})^2$

$\mu_{S,kin} = \frac{\alpha_{sd_s \rho_s} \sqrt{\Theta_s \Pi}}{6(3+e_{ss})}[1 + \frac{2}{5}(1+e_{ss})(3e_{ss} - 1)\alpha_s g_{0,ss}]$ Syamlal et al.

$\mu_{s,fr} = \frac{\rho_s \sin\phi}{2\ sqrt(I_2 D)}$ Schaeffer et al.

$P^*{}_s = \alpha_s \rho_S \Theta_s + 2\rho_S g_{o,ss} \alpha_s{}^2 \Theta_s (1 + e_{ss})$ Solid pressure

$K_a = \frac{\Delta P_{tap}}{\Delta P_{con}}$,

$k_C = f(\alpha_{l,0}, \rho_s, d_s, \rho_l, \mu_l, v_{g,s})$,

$\lambda_s = \frac{4}{3} \alpha_s \rho_S d_s g_{o,ss}(1 + e_{ss})(\frac{\Theta_s}{\Pi})^{1/2}$ Bulk viscosity (Lun et al.)

$g_{o,ss} = [1 - (\frac{\alpha_s}{\alpha_{s,max}})^{\frac{1}{3}}]^{-1}$ Ding and Gidaspow

Table 3.3 Properties of liquid and solids used in CFD simulations

Properties	Value	Units
Liquid properties		
Viscosity	0.001	kg/m s
Density	998.25	kg/m3
Inlet liquid velocity	0-1.35	m/s
Solid properties		
Diameter	0.015, 0.02 and 0.03	m
Density	930,945 and 970	kg/m^3
Top diameter of beds	0.095 and 0.072	m
Bottom diameter of beds	0.25 and 0.22	m
Total height of the bed	0.59	m
Angle of beds	6.8 and 8	^{o}(angle)
Initial bed heights	0.04, 0.075 and 0.1	m

Table: 3.4 Boundary Conditions used in simulations.

Parameter	Value	Units
Particles density	970,940,930	Kg/m^3
Water density	990	Kg/m^3
Initial solid packing	0.6	-
Superficial liquid velocity	Eulerian–Eulerian, with kinetic theory.	-
Static bed height	No-slip condition for liquid and solid	-
Inlet boundary condition type	SIMPLE	-
Outlet boundary condition type	Second-order upwind	-
liquid–solid model	0.9	-
Wall boundary	0.9	-
Pressure–velocity coupling	0.01	s
Discretization scheme for convective	$10^{\wedge -3}$	-

Specularity coefficient	0.9	-
Coefficient of restitution	Eulerian–Eulerian, with kinetic theory.	-
Time step	No-slip condition for liquid and solid	-
Convergence criteria	SIMPLE	-
Maximum number of iterations	Second-order upwind	-

Table.3.5 Solids physical properties of solids that were used in experiments and CFD Simulations.

S.NO	Type of Material	Size(m)	Density(m)	Initial bed
1	High density	0.015	970	0.04,0.075,0.1
2	Poly propylene(PP)	0.025	930	0.04,0.075,0.1
	Low density	0.035	945	0.04,0.075,0.1

Voidage of solids in tapered bed is calculated by

$$\varepsilon = [\frac{18Re+2.7Re^{1.687}}{Ga}]^{0.213} \quad (3.13)$$

Where Ga is the Grashof no $Ga = \frac{{d_p}^8 \rho_{l(\rho_l-\rho_s)}}{{\mu_l}^2}$

3.4.1 Solution procedures

With the commercial CFD package FLUENT, the above equations have been solved and the bed hydrodynamics have been determined with the applications of initial and boundary conditions. The Setup is shown in figs 3.2, 3.3 with an inlet and outlet of the desired amount of solids are adapted on the top of the bed [22]. The properties of fluids and boundary conditions are shown in table 2&3 and the corresponding nomenclature shown in table 4.The phase-coupled SIMPLE algorithm, an extension of the multiphase flow SIMPLE algorithm (Patankar, 1980), was used for the coupling of pressure-velocity. A second-order implicit scheme was used for unstable formulation, and the QUICK algorithm was used to discrete convective terms. The simulations were carried out for a period of 30 s, whereas the interval between 5 and 30 s was used to obtain the time-averaged and the convergence criterion for the cumulative residual between values. To prevent instability, a small-time step of 1*10−4 s was used, and two iterations were set to 1*10−4 s. The simplified simulation algorithm flow sheet is indicated in fig 3.4.

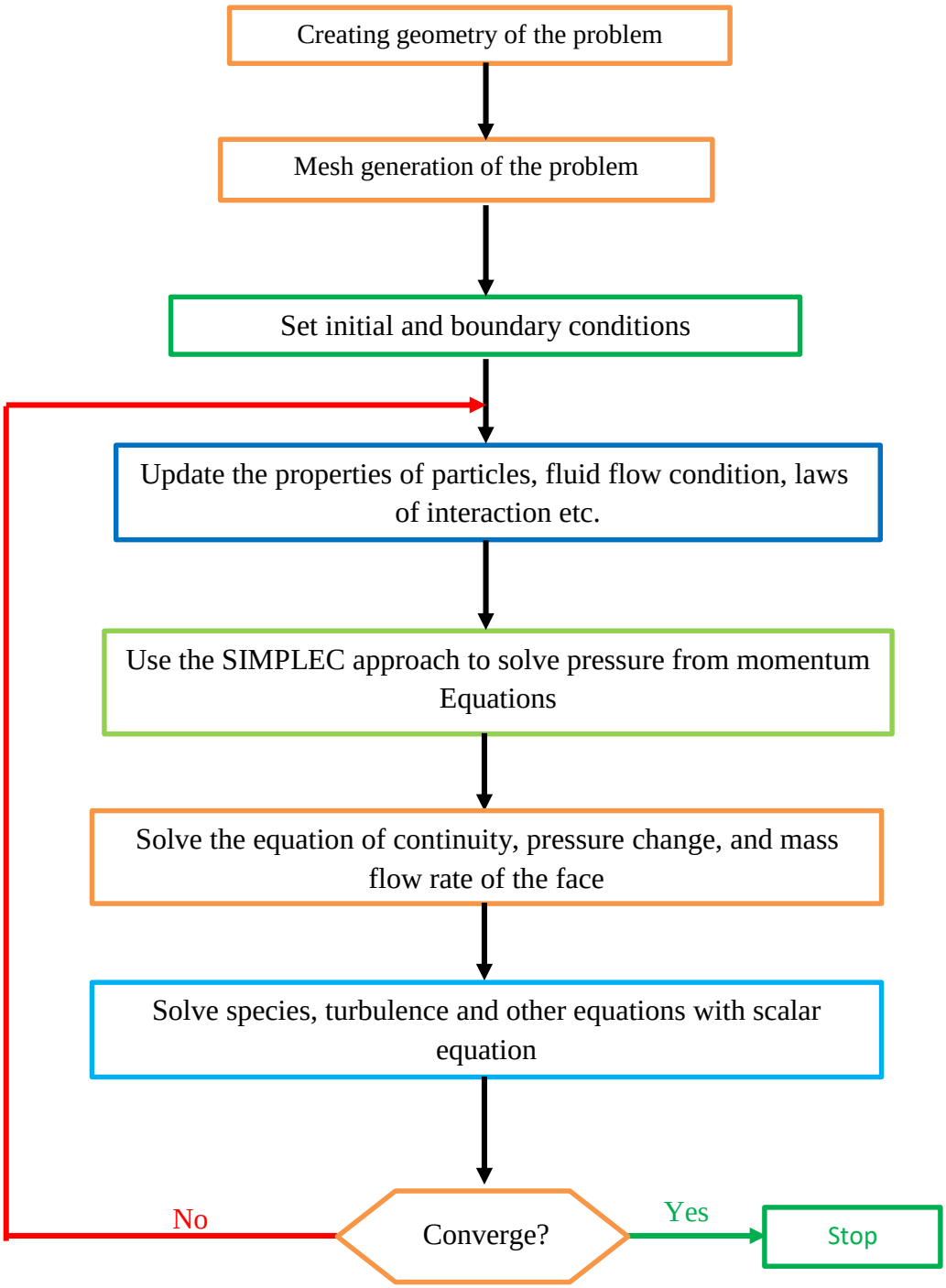

Fig 3.4 Simplified simulation procedural flow sheet.

3.4.2 RTD (residence time distribution) calculation

RTD can be determined by performing tracer or stimulus-reaction tests, in which a tracer is injected promptly (a pulse input) at the channel of a stream framework, and its focus, *C(t)*, is estimated at the exit as an element of time. RTD investigation is commonly relevant to a stream framework with a one-channel stream where a tracer was injected; however, this limitation can be removed in the numerical simulation and the test for one-inlet, one-outlet stream framework by presenting a transporter liquid (water) with a stream rate. This decreases dead volumes inside the system and adequately makes the stream framework a one-bay, one-outlet framework as required, with essentially no stream aggravation. The exit concentration of the tracer, and solution of a blender, was estimated utilizing 0.0005N NaOH; the experiment of the tracer RTD was studied at various angles of the tapered inverse fluidized bed. The bed was patched with solids up to some height from the top with water flowing continuously from the top. After stable fluidization was reached, the (5ml) propionic tracer was injected into the bed within a short period. At the same time, the outlet mixer of water and tracer were collected in separate vessels at every 2 min time intervals.

The below described equations [*Octave Levenspiel]* were used to find the liquid tracer desired values

The tracer concentration of the sample c (t) at any time t is:

$$C(t) = \frac{M_{tracer}}{M_{tot}} \quad (3.14)$$

$$E(t) = \frac{C}{\text{Area under the C Curve}} \quad (3.15)$$

$$\text{Mean residence time } (\bar{t}) = \frac{\sum c_i t_i}{\sum c_i} \quad (3.16)$$

$$\text{Varience}(\sigma^2) = \frac{\sum c_i {t_i}^2}{\sum c_i} - \bar{t}^2 \quad (3.17)$$

$$\sigma^2{}_\theta = \frac{\sigma 2}{\bar{t}\text{^}2} \quad (3.18)$$

Now for closed vessel the relation between the variance to$(\frac{D}{uL})$

$$\sigma^2{}_\theta = 2\frac{D}{uL} - 2\left(\frac{D}{uL}\right)^2\left(1 - e^{\frac{-uL}{D}}\right) \quad (3.19)$$

Where D is the dispersion coefficient (m^2/sec) of tracer

U is the velocity (m/s) of liquid

L is the length (m) of tapered inverse fluidized bed.

3.4.2.1 CFD Model for RTD Studies

In this study, RTD was analyzed by several numerical investigations with a full 3D Computational Fluid Dynamic model using FLUENT, while the used approach was based on (a) steady-state calculations of the flow velocity pattern and (b) transient calculations of RTD. The motion through the fluidic module of superimposed massless tracer particles was monitored using previously computed velocity fields. The pressure-based solver was utilized for the arrangement of the liquid stream and species transport, in which particular conditions were tackled in a successive way utilizing proper limit conditions and numerical calculations. The unfaltering state solution for the stream conditions was acquired by indicating as limit conditions: the mass stream rate at the inlet feeds, no-slip condition at the walls, and measure pressure of zero at the outlet of the arrangements. Utilizing the arrangement of enduring state liquid stream conditions, the tracer species condition was illuminated as a shaky reproduction, by determining zero diffusive transition as a limit condition at the walls and its solution was then utilized for RTD analysis. Species mass portions of one (for time t = 0 s at pulse inlet of tracer into water) were determined at the channel zone and kept up for resulting time steps. Utilizing the coordinated postprocessor, tracer focus information was obtained at the outlet from time-dependent nodal estimations of the mass fraction of the tracer. Here, the Eulerian-Eulerian was used to study the RTD of liquid tracer in a 3D tapered inverse fluidized bed and the kinetic theory of granular flow (KTGF) was used for the solid phases. Besides the liquid phase, the solid phase was also like infiltrating continua in the model. The liquid (water) and tracer were assumed as the primary phase, whereas the single or particles phases were assumed as the secondary phase.

In the KTGF model, the irregular movement of the particle was assumed analogous to the motion of molecule in the liquid, was used to close the overseeing conditions for each solid phase. The equation of mass and momentum for the liquid, for single or paired molecule phases in addition to

the solid phase, and fluctuating energy were summarized in Table 2 [22, 23]. It is known that the drag between liquid-solid phases was generally reliant on the stream behavior, therefore, an accurate definition of drag force is crucial for the correct simulation of tapered inverse fluidized bed RTD studies, which further influence the prediction of RTD.

In the present work, simulations were carried out to find the RTD (mass fraction and volumetric flow rate) behavior of liquid trace when the liquid tracer was injected for 30 s into the reactor. After reaching the steady-state condition, the simulation was run till the liquid tracer reached zero concentration for different velocity, bed heights and different densities of solid materials at different angles of the tapered inverse fluidized bed. The summary of simulation conditions is listed in Table 3.6. The mesh and 3D computational domain of the tapered inverse fluidization are shown in Figure 2a and 2b, respectively.

Table 3.6. Fluid Initial Conditions and Physical properties of solids which were used in experiments.

S.NO	**Type of Material**	**Size(m)**	**Density(m)**	**Weight(kgs)**	**Initial bed heights(m)**	**Velocity of liquid(m/sec)**
1	HDPE	0.02	970	0.05,0.08,0.1	0.03,0.04,0.053	0.133,0.214,0.303,0.341
2	PP	0.025	930	0.05,0.08,0.1	0.03,0.04,0.053	0.133,0.214,0.303,0.341
3	Beads	0.035	900	0.05,0.08,0.1	0.03,0.04,0.053	0.133,0.214,0.303,0.341

Table 3.7 Summary of boundary conditions used in CFD

Parameters	Numerical value	Units
Reactor size	0.59*0.25*0.09,0.59*0.22*0.75	M
Grid number	50*600	-
Convergence criteria	10^-3	S
Maximum iterations	20	S
Time step size	0.01	S
Discretization method	First order upwind scheme	-
Model precision	Double	-
Initial volume	0.6	-
e_{sw}	0.9	-
Operating pressure	1.013 × 105	Pa
Granular viscosity	Gidaspow (1994)	Pas
Granular bulk viscosity	Lun et al. (1984)	Pas
Solid pressure	Lun et al. (1984)	Pa
Radial distribution	Lun et al. (1984)	-
Drag model	Gidaspow	-
e_{ss}	0.9	-
Φ (specularity coefficient)	No slip condition	-
Velocity(liquid)	(0.133-0.341)	m/s
Particle diameter	(0.02-0.035)	M
Density of particle (ρ_s)	(0.9-0.970)	Kg/m^3
Density of water(ρ_l)	1000	Kg/m^3

3.4.3 Boundary conditions used in the simulations:

In this present work, simulations were done to find the RTD (mass fraction and volumetric flow rate) behavior of liquid trace when the liquid tracer was injected for 30 sec into the reactor. After reaching the steady state condition, the simulation was run till the liquid tracer reached zero concentration for different velocity, bed heights and different densities of solid materials at different angles of tapered inverse fluidized bed. The remaining boundary conditions which were used in simulations are shown in table 3.7, and the schematic mesh and Computational 3D domain with the boundary conditions of tapered inverse fluidized bed

3.5 A new empirical model

Response surface methodology (RSM) is a gathering of scientific and measurable methods for observational model building. Through a careful outline of trials, the goal is to streamline a response (yield variable) that is impacted by a few input factors. The analysis is a progression of tests, called runs, in which changes are made in the information factors to recognize the purposes

behind changes in the yield reaction. RSM was produced to demonstrate test reactions [35], and afterwards relocated into the display of numerical analyses. The difference is in the sort of error produced by the response. In the advancement of the models, all the levels of experimental parameters were kept independent in all the investigations. The levels of all process variables were specified based on the current task's experiments, and the level values of the individual parameters used in the experiments are shown in Table 3.8. Under various sets of investigating variables, the response of the mean residence of liquid tracer from the inverse tapered fluidized beds shows variation with different independent variables.

Moreover, the results obtained from the model equation show that the mass of solid was affected very less compared to particle density and velocity of the liquid, while the angle of tapered inverse fluidized bed impacted the mean residence time of the liquid tracer.

Table 3.8: Symbols and levels of independent variables were used in response surface methodology

Symbol	**Parameter**	**Unit**	**Level**	**Level**			
				1	2	3	4
A	Velocity	m/sec	4	0.133	0.214	0.303	0.341
B	Solid mass	kg	3	0.05	0.08	0.1	
C	Particle density	kg/m^3	3	900	930	970	
D	Reactor Angle	^{o} degree	2	6.8	8		

3.6 Adsorbent preparation

3.6.1 Wheat bran

Wheat bran was obtained at Warangal, India, from local flour mill. To avoid soluble impurities, the collected wheat bran was washed off with DI water (De-ionized water). The bran washed was dried for 1-2 h in the oven at 70^{o} C. Screening was done on the dried wheat bran. Upon screening for adsorbent preparation a fraction of 400 microns was obtained. Different grams of screened wheat bran fraction were taken in experiments for wastewater treatment .Adsorbent pellet preparation (Fig. 3.5(a)).

Fig. 3.5 Adsorbent prepared in the laboratory

3.6.2 Adsorbent coating on the low density solid particles

1) Weight the required amount of low density of Polypropylene (PP) solid particles and wheat bran on weighing balance.
2) Now, add the binder to the PP Particles.
3) Using a spatula/hand, coat the wheat bran on the PP particles properly and leave the adsorbent until it dries.

3.7 Characterization techniques for prepared adsorbents

Developed adsorbents were analyzed for their physical, chemical properties using different characterization techniques. The methodology for characterization and analysis are discussed as follows.

3.7.1 Scanning electron microscope (SEM) and Energy dispersive spectroscopy (EDS):

Scanning electron microscopy (SEM) images and Energy dispersive spectroscopy of prepared adsorbent was recorded by SEM-EDS system (Nova Nano 450) at NIT, Warangal (Fig. 3.6). Scanning electron microscope was used for adsorbent surface analysis and Energy dispersive spectroscopy (EDS) was used for surface elemental analysis of prepared adsorbent.

In scanning electron microscope a high energy electron beam is passed across the adsorbent surface. Usually, this sample is coated with gold or platinum to improve contrast and signal to noise ratio. As the beam passes through the adsorbent surface, interaction between electron beam and adsorbent surface takes place and it resulted in various electron signals. These electronic signals are collected, processed, and converted into pixels form, on a monitor. This forms an image of the adsorbent surface. Energy dispersive spectroscopy (EDS), is a technique for the elemental analysis.

3.7.1.1 Principle of SEM and EDS*:*

Accelerated electrons in SEM carry kinetic energy and this energy is released in the form of signal when interaction between electron and sample takes place during deceleration of electron inside the sample. These electrons have secondary electrons, backscattered electrons and diffracted backscattered electrons. Secondary and backscattered electrons are helpful in imaging samples, secondary electrons are important for showing morphology and topography on sample. Backscattered electrons are helpful in showing contrast in composition of sample. X-ray is generated when collisions of incident electrons with electrons in shells of atoms in the sample takes place. In SEM analysis generated X-rays do not lead to volume loss of sample thus same material can be analyzed repeatedly. In EDS analysis sample is bombarded with a beam of electrons and it emits X-ray spectrum for elemental analysis.

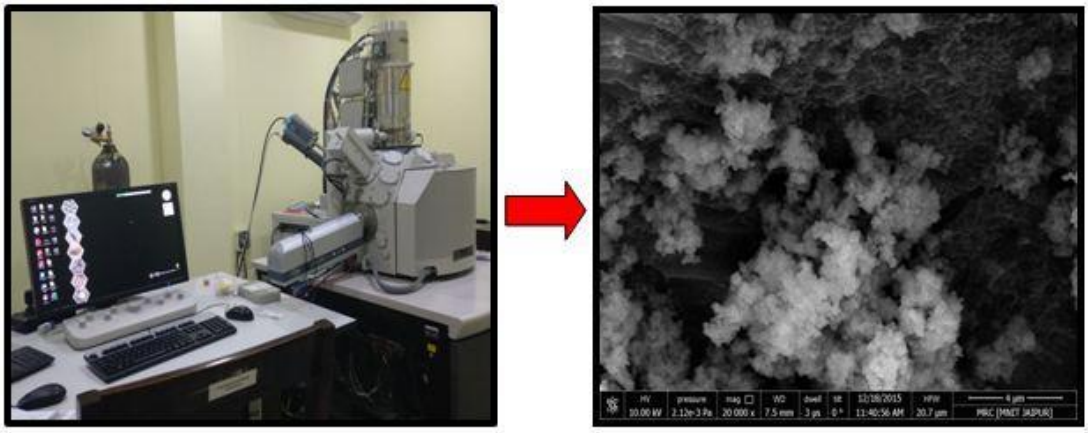

Fig. 3.6: NOVA NANSEM -450 for surface morphology analysis

3.7.2 Fourier Transform Infra-Red (FTIR) spectroscopy:

Fourier Transform Infra-Red (FTIR) spectrophotometer (Perkin Elmer, Model- FT-IR spectrum 2) was used for identification of functional groups present in prepared adsorbent at NIT, Warangal. Fourier Transform Infra-Red (FTIR) spectroscopy was recorded by FTIR spectroscope (PerkinElmer) as shown in Fig. 3.7. The technique of Fourier-transform infrared spectroscopy is used to obtain an infrared absorption spectrum or emission of a solid, liquid or gas. In FTIR, analysis, infrared radiation is passed through the adsorbent, a portion of radiation is absorbed by the adsorbent and other portion passes through the adsorbent (is transmitted). A spectrum is obtained on detector which represents molecular structure of the adsorbent.

3.7.2.1 Principle of FTIR

In FTIR technique, there is an interaction between infrared radiation and sample. FTIR gives information about vibration and rotation of chemical bonding and molecular structure. FTIR analysis is the fingerprint of sample with absorption peaks showing frequency of vibration between bonds of the atom. The size of FTIR peak shows the amount of material present. The infrared region is commonly divided into three smaller areas: near – Infrared region (400 - 10 cm), mid – Infrared region (4000 - 400 cm^{-1}), and far infrared region (14000 – 4000 cm^{-1-1}).

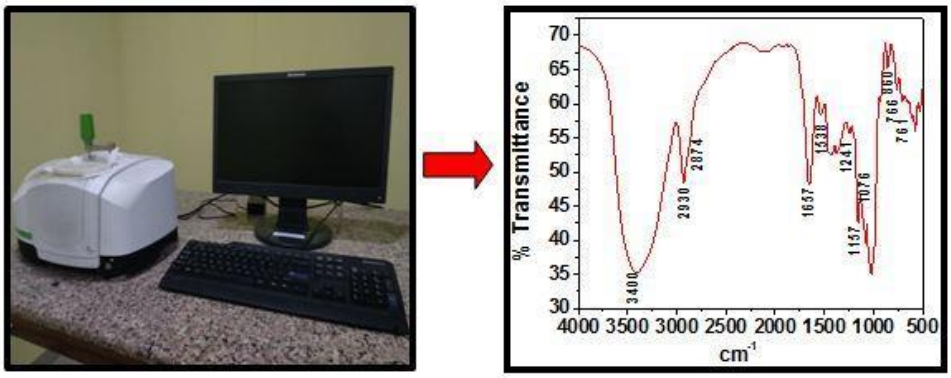

Fig. 3.7 Perkin Elmer, Model- FT-IR spectrum 2 for FTIR analysis

3.8 Preparation of stock solution

The stock solution containing 1000 mg / L of textile dye was prepared by dissolving 0.5 g of textile dye powder in 1000 mL of double distilled water. Spectrophotometer was used to measure absorbance.

3.8.1 Calculation of percent removal and adsorption capacity

The percent removal of concentration of dye was calculated using the following equation.

$$\%R = \frac{C_0 - C_t}{C_0} \times 100 \ldots\ldots \quad (3.20)$$

Where R is the colour removal efficiency, C is the dye Concentration in solution before reaching equilibrium (mg/L), and C0 is the dye concentration in solution after reaching equilibrium (mg/L). The amount of dye adsorbed on adsorbent at equilibrium is called adsorption capacity and calculated using following equation.

$$\%\ q_e = \frac{(C_0 - C_e)V}{W} \ldots\ldots \quad (3.21)$$

Where, qe, Co and Ce are the adsorption capacity (mg/g), initial and equilibrium dye concentration (mg/L), respectively, V is the volume of solution (L), and W is the weight of adsorbent (g).

3.9 Analysis of dye

3.9.1 Ultra visible spectrophotometer

Ultra-visible spectrophotometer (UV-1800 Shimadzu) was used for determining the dye intensity in samples at NIT, Warangal. In ultra-visible spectroscopy, a substance absorbs the light and it increases energy of atoms present inside of that substance. This light may be visible light or ultra-visible light. It produces a spectrum (Fig. 3.8).

3.9.1.1 Principle of ultra-visible spectrophotometer

Ultra-visible spectroscopy works on Beer-Lambert law. According to Beer Lambert‘s law, when a monochromatic light passes through a solution containing any absorbing material. There is decrement in the radiation intensity and this is proportional to the radiation and solution concentration. The formula for Beer Lambert‘s law can be written as follows,

Absorbance = log (intensity of incident light / intensity of light leaving from Cell) = molar absorptivity * solute molar concentration * length of light travel

Fig. 3.8 Laboratory Ultra visible spectrophotometer (UV-1800 Shimadzu)

3.10 Factors affecting adsorption of pollutants

There are many factors which affect heavy metal removal efficiency of adsorbents from wastewater. These factors are initial concentration, adsorbent dose, pH and air flow contact time (Sahu et al., 2009). To optimize these parameters, batch adsorption experiments were carried out using design expert software.

3.11 Design of experiments

Design of experiments was employed in our study to optimize design parameters and removal efficiency, and four parameters are used: initial concentration, pH, air flow timing, and adsorbent dose. 3-level, 4-factor central composite design (CCD) was used to determine effect of these parameters on removal percent of Dye, COD, and Turbidity and DO enhancement. The use of central composite design (CCD) has the advantage of allowing complex response functions to be determined using only a few combinations of variables (Muthukumar et. al., 2003).In our work, total 29 experiments were carried out for each pollutant in individual.

When a parameter's effect is positive, the reaction increases as the factor changes from low to high levels. If the consequences are unfavorable, the response to a high amount of the same component is reduced (Cojocaru & Zakrzewska-Trznadel 2007).

3.12 Batch fixed bed column

3.12.1 Design and fabrication of experimental setup

The conical inverse fluidized bed (fig.3.9) was made of 0.22 m bottom diameter, 0.073 m top diameter and 0.59 m high acrylic material. The mesh is used at the top and bottom of the column as a distributor to avoid particle escape, and to display a uniform flow distribution. The flowrates are controlled using the ball valves. For pressure studies, the pressure tapings on the side of the column were mounted to measure the pressure drop at each flow rate. The air compressor connected to the gas rotameter, these flowrates are controlled using the ball valves. The column was filled with the adsorbent pellets. The textile effluent solution was filled at the bottom of the glass column to increase the contact time of air through a gas rotameter up to desired flowrate. The effluent samples were collected at specified time interval until the outlet concentration reaches to 95% of the feed concentration. In this work, batch experiments the tests of samples were performed for each pollutant i.e. dye removal, COD and turbidity removal, DO enhancement.

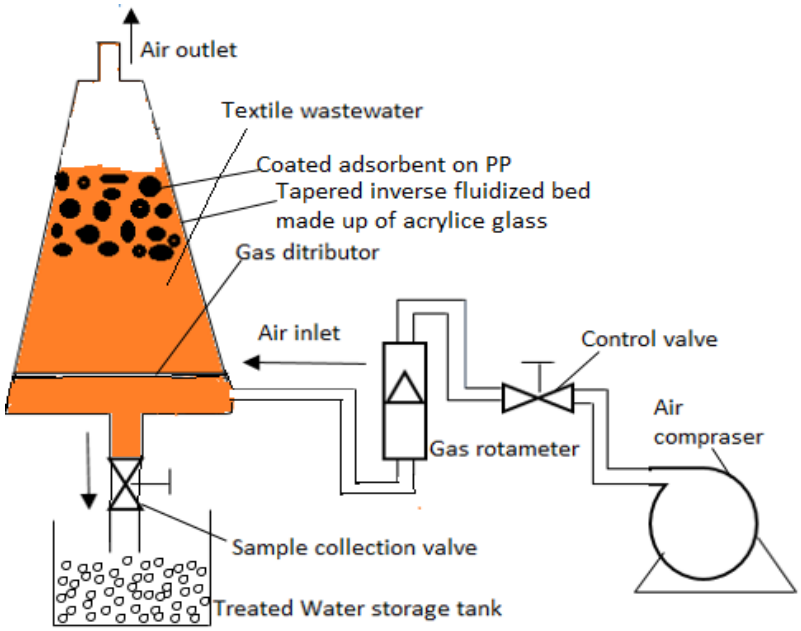

Figure.3.9 Shamanic diagram of experimental setup: for batch operation

3.13 Experimental Methodology for water treatment

In this section the overall experimental methodology has been explained. There have been little changes in different approaches of the research. Detail methodology for each approach has been explained in the treatment approach section of this study.

After Preparing synthetic textile waste and transporting into the laboratory the wastewater sample was analyzed to determine the untreated effluent characteristics. For this research work the samples were analyzed for seven parameters which were Dissolved oxygen (DO), Chemical Oxygen Demand (KMn04 value), Color, and Turbidity. The tests of those parameters were performed following standard methods (AWW A, 1998).

After determination of the untreated effluent characteristics the wastewater was subjected to adsorption processes. For proper mixing of the adsorbents the air was sending continuously. And collect the treated samples every 4 hrs.

The supernatant samples were then analyzed to determine color removal, DO enhancement, COD reduction and turbidity reduction.

3.13.1 Parameters Considered

The effluent discharge standards for textile industries set by DoE. It was observed that there exist some serious limitations in the effluent discharge standard set by Department of Environment (DoE). It is needed to find out the critical parameters through extensive research. Discharge standard of those critical parameters should also be determined. Setting up proper discharge standard will help the ETP designers/operators to evaluate and monitor their design /performance of the ETP.

The information of the critical parameters was not available. However, six parameters were considered for efficiency determination of ETPs based on following reasons.

Color removal: Dyes are synthetic organic aromatic compounds that are molecularly dispersed and bound to the substrates by intermolecular forces and have high application potential in the industrial sector as coloring material. The textile industry ranks first in the consumption of the dyes and effluents released from textile dyeing, which are intensely colored and pose serious problems to various segments of the environment. The persisting color, non-biodegradable, toxic and inhibitory nature of spent dyebaths has considerable deleterious effects on the water and soil environment. Presence of coloring matter in significant quantities in receiving water would not

only reduce light penetration and photosynthetic activity, but would also render their appearance unaesthetic (Karthikeyan 1988). Therefore, it becomes imperative that color be removed from dye effluents before disposal of the effluent

COD: Chemical oxygen demand is the measurement of organic content present in wastewater. The oxygen equivalent of the organic matter that can be oxidized is measured by using a strong chemical oxidizing agent in an acidic medium. The COD test result helps to determine the suitability of biological treatment of textile effluent. From BOD and COD values one can identify the amount of biodegradable and non-biodegradable organic matter present in wastewater and also determine the treatment options for the textile effluents.

Turbidity: There is no discharge standard for turbidity in the environmental conservation rules 1997. But as of color, turbidity is also important for the public perception of a factory. Therefore, the industries are more interested in removing turbidity than other environmentally hazardous parameters.

DO: Dissolved oxygen is the amount of oxygen found in a sample of an effluent or water waste at the time of collection (Gimba 2001). It determines the level of survival of aquatic organisms and therefore its determination in any effluent discharged into rivers is very important

Chapter-4

Results and discussion

This chapter presents the research work carried out on hydrodynamics, Residence time distribution (RTD) studies and textile effluent treatment studies in tapered inverse fluidized bed.

Different case studies have been considered for carrying out the tasks cited above and are illustrated with the proposed methods followed by detailed discussion. The case studies considered are hydrodynamic studies, Residence time distribution (RTD) and synthetic textile waste water treatment studies all the above cited processes using proposed methods have been presented here.

4.1. Hydrodynamics experimental results:

Experiments were conducted for low density polymer particles as reported in chapter-3 by changing the liquid velocity, the solid density, liquid viscosity, bed angle and the outcomes are visually depicted.

4.1.1. Bed expansion ratio:

Awareness of the height of the bed is important for the design of the device. For a fluid velocity greater than the minimum fluidization, the static solid bed is extended to and fro with solids. As the velocity profile reaches the minimum fluidization, the bed is steadily increased to higher heights. In the present analysis, the enlarged bed height was measured through visual observation. The bed expansion analysis carried out by changing liquid velocity (at constant liquid velocity), varies static bed heights and different liquid velocity (at constant liquid velocity) was presented in Figs. 4.1 to 4.5. Bed expansion is often reflected by the Voidage of the bed. Bed Voidage is the proportion of the extended bed that comprises liquid in the case of two-phase inverse fluidization. The graph 4.5 indicates an improvement in the bed expansion ratio with an improvement in the liquid velocity of the liquid. It is found that the bed expansion ratio is not a function of the initial static bed height, and thus, for a higher initial static bed height, the extended bed height is more a function of the specific value of the liquid velocity. Fig. 4.1 indicates the difference in the bed expansion ratio with the liquid velocity. The plot indicates a rise in the expansion ratio of the bed with a decrease in the liquid velocity, i.e. higher liquid velocity raised to a higher height in the bed. For the increase in the liquid velocities, the expansion ratio of the bed increases, but monotonically for varying slopes, the initial slope adjusts halfway and is again reached. At zero liquid velocity, there is no bed expansion, as the liquid is introduced into the bed, the bed expands, but not all the particles are in liquidation, few of the particles riveted by the liquid and, when the liquid velocity increases there, the bed expands, the rate of expansion decreases and increases again.

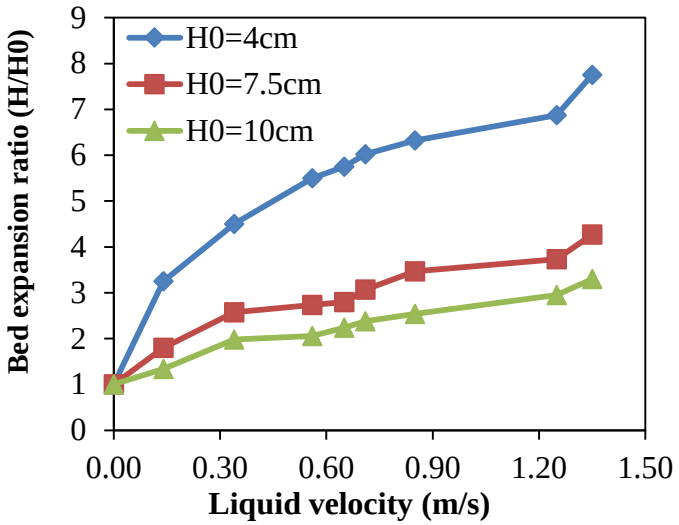

Fig. 4.1 Varation of bed expansion ratio with liquid velocity for 0.015m HDPE polymer particles and viscosity of liquid 0.014 kg/ms at different initial bed heights

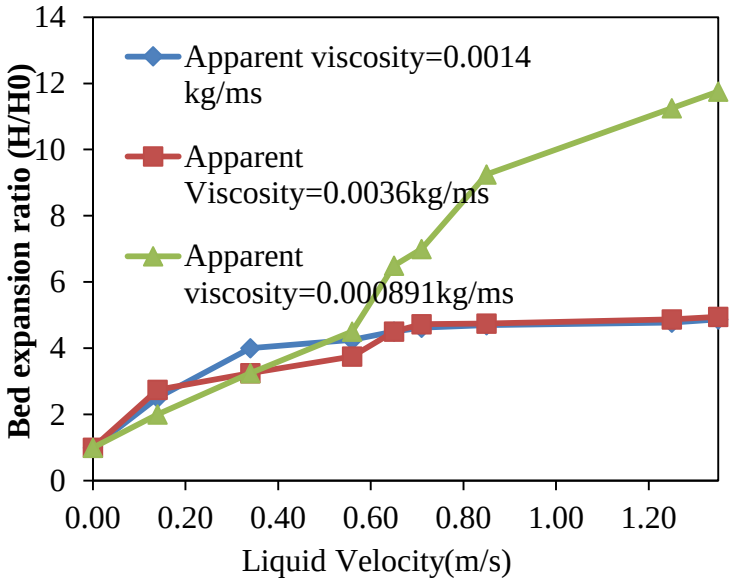

Fig. 4.2 Varation of bed expansion ratio with liquid velocity for 0.015m HDPE polymer particles and at room temparature of liquid and at different viscositys of liquid.

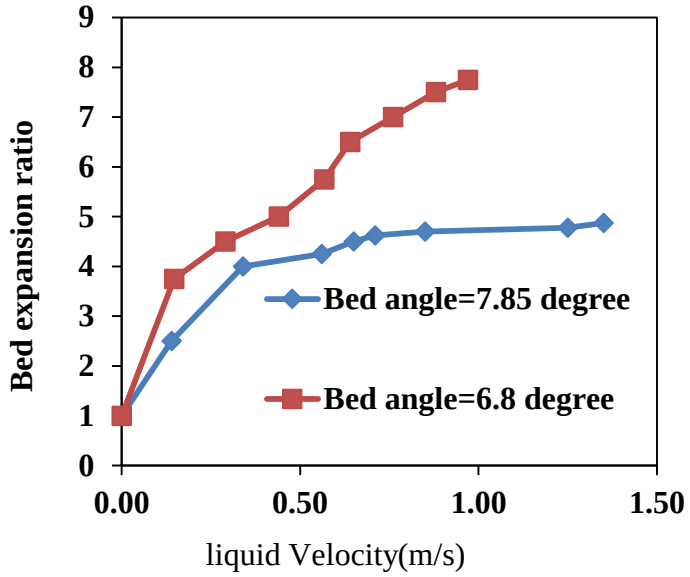

Fig.4.3 Varation of bed expansion ratio with liquid velocity for 0.015m HDPE polymer particles and at room temparature of liquid and at different bed angles.

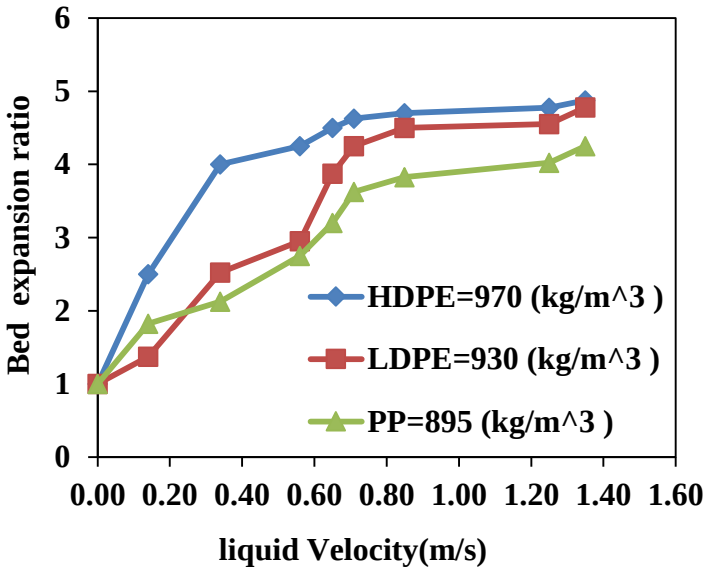

Fig. 4.4 Varation of bed expansion ratio with liquid velocity at room temparature of liquid and angle of bed is 6.85 at different density of polymer particles.

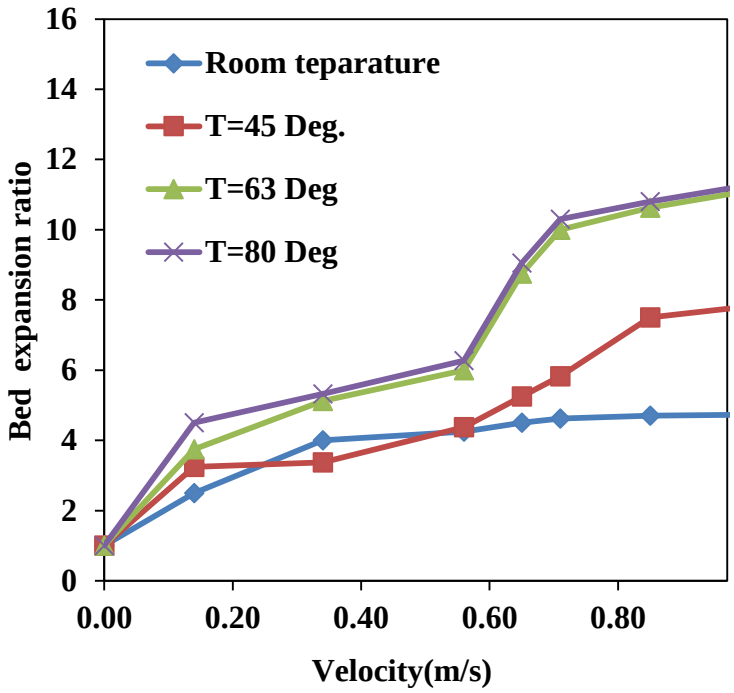

Fig.4.5 Varation of bed expansion ratio with liquid velocity for 0.015m HDPE polymer particles and viscosity of liquid 0.014 kg/ms at different temparatures.

4.1.2. Bed pressure drop and minimum fluidization velocity:

In the current investigation, the pressure drop in the fluidized bed was calculated utilizing manometers filled with carbon tetrachloride as a monomeric fluid connected to the pressure tap in the column experimental setup as stated in Chapter 3. All experiments were begun with the column fully filled with water and plastic beads up to the desired height with the initial manometer level set to zero. The liquid flow rate was steadily increased for the liquid-solid experiment. The liquid-solid experiment with various liquid flow rates has been performed in various ways: They were with a small flow of liquid near zero, the solids initial bed was kept constant and eventually raised to the desired flow rate, after which the flow rate of the liquid was increased and the readings taken, and the other holds the flow rate of the liquid constant at some value, which could be the minimum flow rate of the liquid or at some fraction or multiple, and the initial bed height, density of the solids, different diameter of solids and temarature, viscosity of liquid eventually varied. Figs 4.6 to 4.13 shows the effect of minimum fluidization velocity and pressure drop on different parameters such as initial bed height, liquid viscosity, particle diameter, particle density and bed angle. The effect of initial bed heights on minimum fluidization velocity for different apparent

viscosity of liquids is shown in Fig. 4.6. From the figure, it was observed that the minimum fluidization velocity was independent of the weight of materials, but it varied for different viscosities of the liquid. For the high viscous nature of liquids, the minimum fluidization velocity was very high, the reason being that the contact area of each particle with water was high in high viscosity of liquids so that it needed more velocity to lift the particles from the top of the bed downwards. From Fig.4.7, it is find that the minimum fluidization velocity is dependent of the viscosity of liquid, under it varied for different density of particles. It was high for the low density of particles and low for the high density of particles the reason was that low-density particles floated on the water, and it needed high velocity to lift the particles compared to particles of high density

It is estimated from the correlation obtained from the experimental data relating to the minimum fluidization velocity, Archimedes number and density difference correlation

$$U_{mf} = a[Ar]^b[\frac{\rho_l-\rho_s)}{\rho_l}] \quad (4.1)$$

a=8.464*10^-3

b=0.459

c=0.301

10^4<Ar<8*10^4

Some of the models were used to estimate the minimum fluidization velocity and compared with experimental results

Khani et al.

$$Re_{mf} = 10.396(Ar)^{0.367}(\frac{d_p}{D_0})^{0.889}(\frac{\varepsilon_0}{\phi_s})^{-0.731}(cos\alpha)^{-10.437}\ for\ \alpha > 4.5 \quad (4.2)$$

Where Re_{mf} is the modified Reynolds number:

Ar is Archimedes number

α is the angle in the reactor

Biswal et al. $$U_{mf} = \frac{-A1+SQRT(A1^2+4B1C1)}{2B1} \quad (4.3)$$

Where $$A_1 = COS(\frac{\alpha}{2})\,[3717\tan(\alpha)^{-0.47}\,\frac{\mu(1-\varepsilon_0)^2}{g{d_p}^2\varepsilon_0}\,\frac{r_0(r_1-r_0)}{r_1}]$$

$$B1= 0.75\,COS(\frac{\alpha}{2})\frac{\rho_l(1-\varepsilon_0)}{g{d_p}{\varepsilon_0}^3}\frac{r_0({r_1}^3-{r_0}^3)}{3{r_1}^3},\ C1=r_1(1-\varepsilon_0)\,(\rho_l-\rho_s)$$

r_0, r_1=bottom and Top radius of the bed

ε_0=bed Voidage

d_p=Diameter of particles

ρ_l=liquid density

ρ_s =solid density

Modified ergun Eqn: $$A\,u_{mf}+B\frac{r_0}{r_1}{u_{mf}}^2\text{-}(1\text{-}{\varepsilon^2}_{mf})(\rho_l-\rho_s)g\frac{{r_0}^2+r_0r_1+{r_1}^2}{3{r_0}^2} \quad (4.4)$$

$$Where\ A = 150\frac{(1-{\varepsilon^2}_{mf})}{{\varepsilon_{mf}}^3}\frac{\mu_l}{(\phi_s d_p)^2},\ \ B = 1.75(\frac{1-\varepsilon_{mf}}{\varepsilon_{mf}})\frac{\rho_l}{\phi_s d_p}$$

μ_l is the liquid viscosity

ϕ_s is the solids porosity

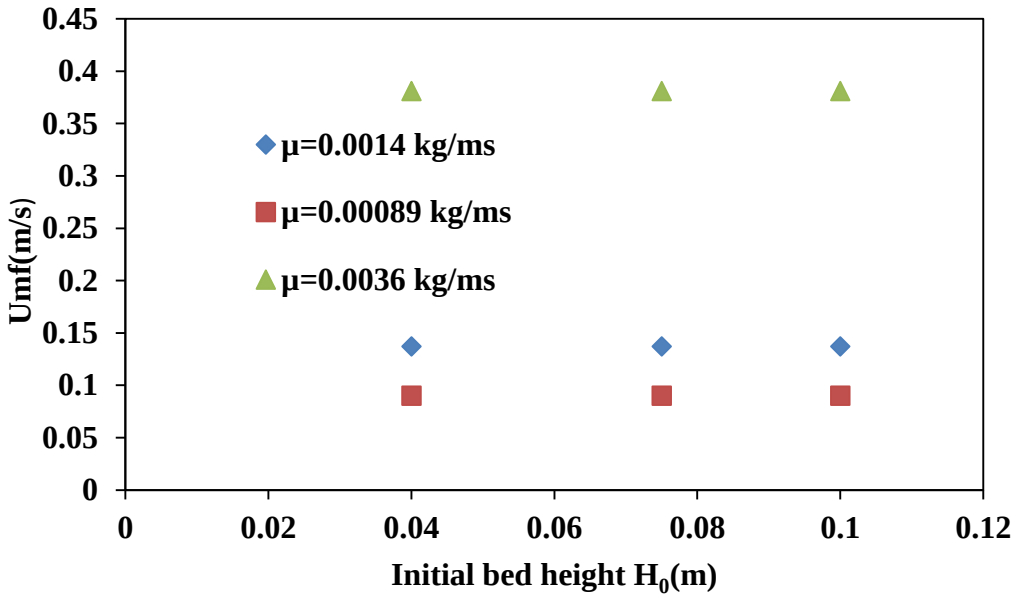

Fig.4.6 Varation of minimum fluidization velocity with initial bed heights for 0.015m HDPE polymer particles and viscosity of liquid 0.014 kg/ms under different viscosity of liquids.

Figure 4.8 shows the effects of solids on diameter on minimum fluidization velocity at different angles of beds. As expected, the Umf value attains the lowest value with an increase in the diameter of solids. The reason was that the solid holdup increases with a diameter, so it needs low Umf to move the particles from the top of the bed. Umf was also varied with different angles for fluidized beds for the large angle of beds; Umf was low when compared to the low angle of the fluidized bed. The reason is the increase in the cross-sectional area, so it needs immense velocity to lift the particles.

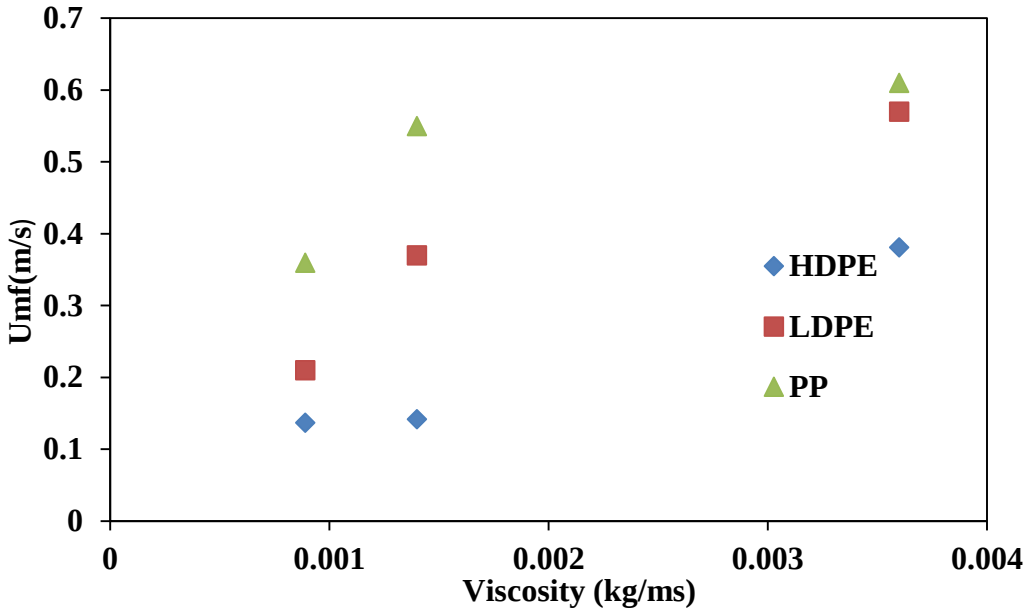

Fig.4.7 Varation of minimum fluidization velocity with viscosity of liquids for 0.015m HDPE polymer particles and viscosity of liquid 0.014 kg/ms under different density of solids.

The impact of the diameter of particles on minimum fluidization velocity for different models from the literature and experimental data is shown in Fig. 4.9. It was found that the minimum fluidization velocity was higher for low-density particles and low for high-density particles. The reason is that the phenomenon of the bouncy force was acting in the opposite direction to the gravitational force, i.e., in an upward direction. The graph for the abovementioned models shows different minimum fluidization velocities. This was because, in those different models, the bed was considered in some of the equations, and bed angle was considered in some of the equations.

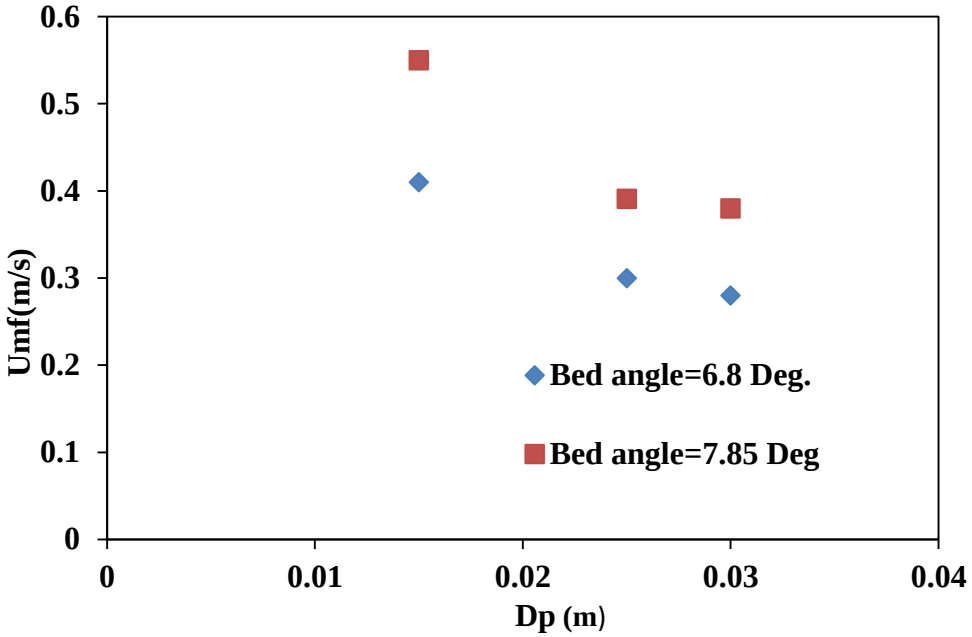

Fig.4.8 Varation of minimum fluidization velocity with different diameter of solids for 0.015m HDPE polymer particles and viscosity of liquid 0.014 kg/ms under different angle of beds.

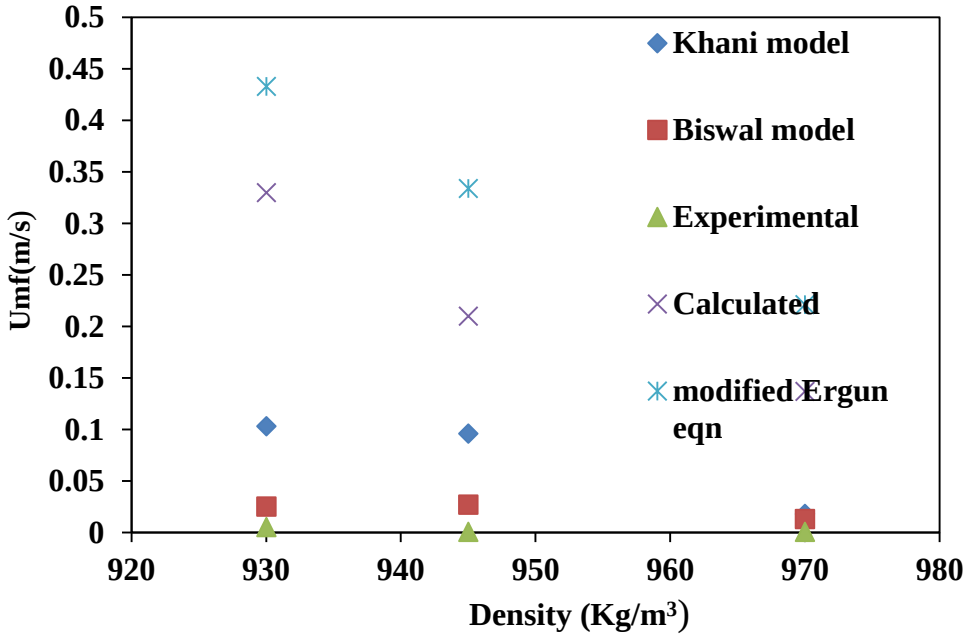

Fig.4.9 Varation of minimum fluidization velocity with different density of solids for 0.015m HDPE polymer particles and viscosity of liquid 0.014 kg/ms under different models.

From the Fig.4.10 the bed pressure drop with liquid velocity will increased up to minimum velocity is reached after that pressure drop was constant throughout the experiment. From fig 4.11 for low density of solid particles the pressure drop is high when compare to high density of solid particles because the buoyancy forces from the downward direction was easily over come in the high density of solids. From fig 4.12,4.13 these will shows that the pressure drop will also depends on the viscosity of liquid and bed angle.

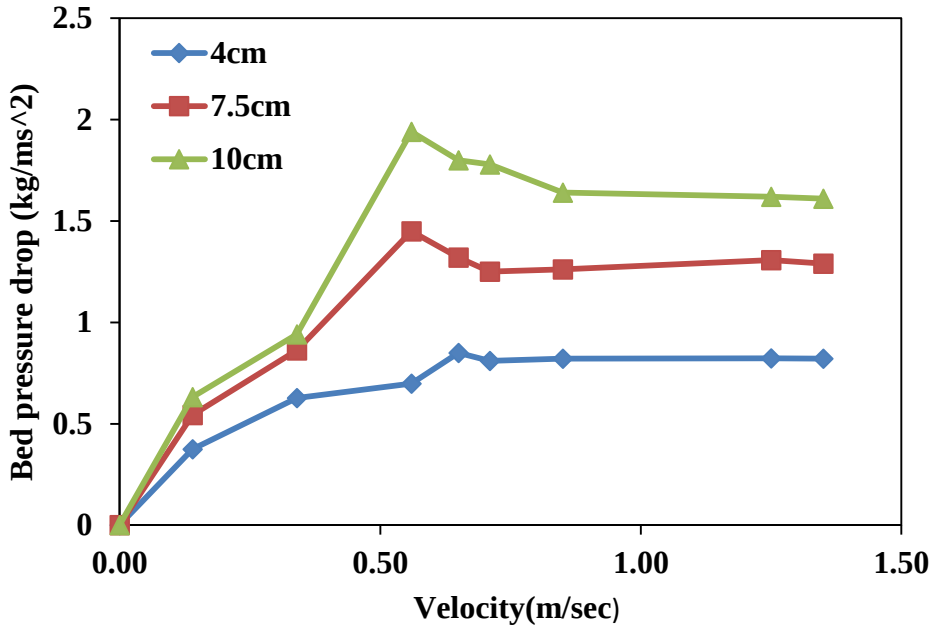

Fig.4.10 Varation of bed pressure drop with different velocity of liquid for 0.015m HDPE polymer particles and viscosity of liquid 0.014 kg/ms under different initial bed heights.

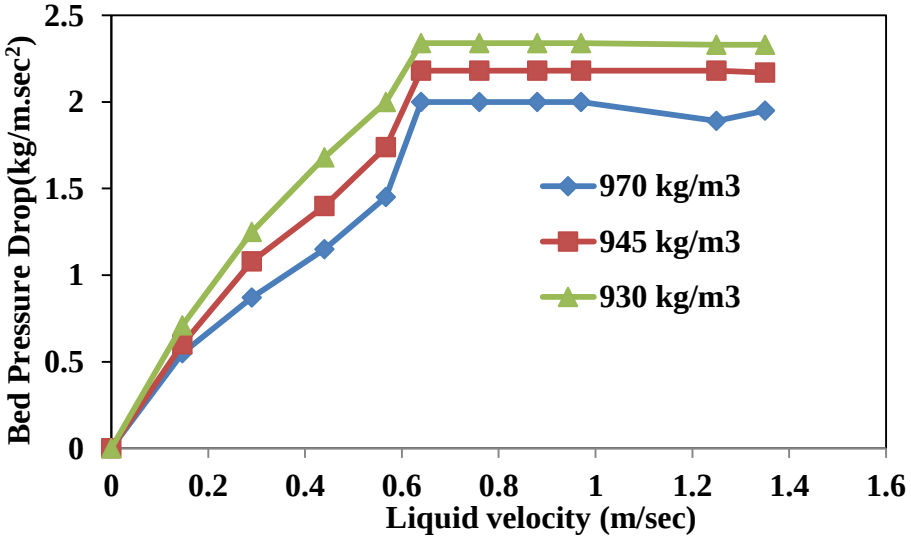

Fig.4.11 Varation of bed pressure drop with different velocity of liquid for 0.015m HDPE polymer particles and viscosity of liquid 0.014 kg/ms under different density of solids

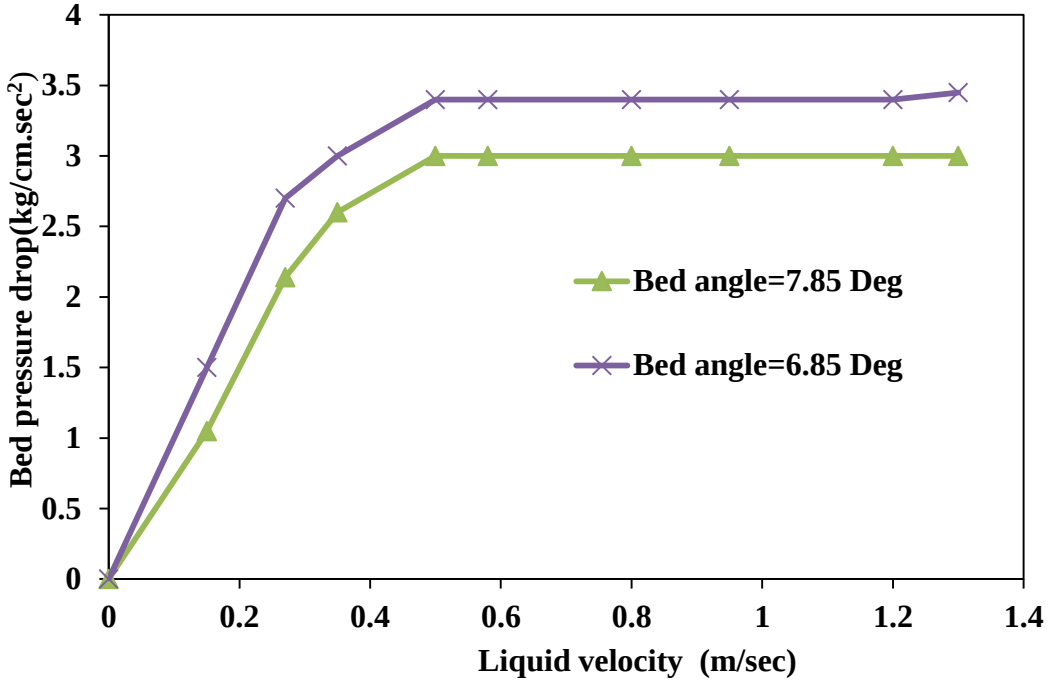

Fig.4.12 Varation of bed pressure drop with different velocity of liquid for 0.015m HDPE polymer particles and viscosity of liquid 0.014 kg/ms under different bed angles.

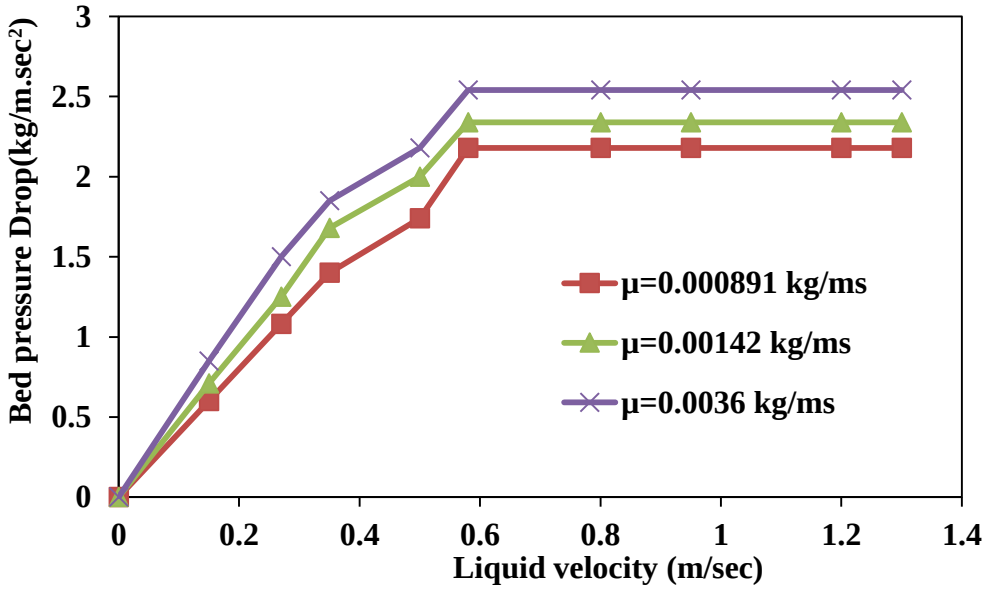

Fig.4.13 Varation of bed pressure drop with different velocity of liquid for 0.015m HDPE polymer particles and viscosity of liquid 0.014 kg/ms under different viscosity of liquid.

4.1.2.1 Heat Transfer in Two-Phase inverse Fluidized Beds:

The heat transfer coefficients in the two-phase (liquid-solid) inverse fluid beds were obtained without the injection of air into the beds. Effects of fluid velocity on the heat transfer coefficient in liquid-solid inverse fluid beds can be seen in Figure 6. Since the minimum fluidization velocity is 0.8 and 1.2 cm / s in the beds of HDPE, LDPE and PP particles, respectively (Figure 3), the U_L experiments were started at 0.14 m/s. In Figure 6, the heat transfer coefficient increases with increasing U_L; however, it decreases with a further rise in liquid velocity, with a maximum point in both HDPE, LDPEE and PP beds. This pattern of the heat transfer coefficient (h) is very close to that of traditional beds. The explanation why the h value exhibits the highest value with the U_L variance may be a shift in the solid holdup and solid flow behavior. In the lower U_L range, the particles cannot be sufficiently fluidized to produce adequate turbulence for heat transfer in the beds. Thus, the increase in U_L leads to an increase in turbulence in this U_L range which results in an increase in the coefficient of heat transfer. In the higher U_L range, however, the solid holdup decreases dramatically with an additional rise in U_L. Due to the presence of fluidized solid particles, this may minimize turbulence. As a result, the heat transfer coefficient continues to decrease with a further rise in U_L. It can also be noted in this figure that the coefficient of heat transfer in HDPE beds is higher than that of LDPE and PP particles. This means that particles with a relatively high density may be more efficient for heat transfer than those with a lower density Kang et al. pointed out that the fluidized solid particles can increase the heat transfer coefficient by reducing the thickness of the liquid thin film around the heater surface due to regular contact with the heater surface. This contacting would be more successful in the beds of particles with a relatively high density than those with a lower one, since the density of these particles is smaller than that of the continuous liquid phase in the inverse fluid beds. The liquid velocity at which the maximal value of the heat transfer coefficient is seen is lower in the beds of LDPE, PP particles than in the beds of HDPE. This can be attributed to the fact that the minimum fluidization velocity of the former is lower than that of the latter. The wettability effects of water may be equally weak and almost the same in both situations, since the contact angle of each particle with water is almost the same. It has been established that the wettability of the particles is closely related to the separation energy of the particles per unit area of the interface, which can be determined from the contact angle by Dupre's equation.

Experimental setup

Experiments were performed in two phase system in different angles of tapered inverse fluidized bed made up of an acrylic column 0.59 m in height, with 0.09m diameter at the top and bottom diameter of column is 0.25m. The experimental scheme is depicted in this diagram represented in fig 4.14.

For heating purpose, a heater (25.4 mm o.d. × 1.5 m length) was vertically placed at the center in the fluidized bed. The temperatures at the heater surface and the fluidized-bed proper were measured by the iron-constantan thermocouples (J type) which were mounted on the column at 20 cm height intervals. This heater was connected to a temperature controller that was used to control and maintain continuously the desired temperatures. A big change in the fluidizing bed took place for different fluid velocity. In that process, heat transfer coefficient was calculated in the bed from one consistent was fluidizing state to another as a function of liquid velocity. When a new consistent state was reached, the temperatures were measured again. The equation below was used to calculate the heat transfer coefficient was

$$\mathrm{h} = \frac{\mathbf{q}}{\mathrm{A}(\mathrm{T_h} - \mathrm{T_m})} \tag{4.5}$$

q is the heat flux, acquired from DC electricity supply, and the temperature difference between the dipped in water heater and bed is determined with the aid of

$$T_h\text{-}T_m = \frac{\int_0^R U(r)[(T_h - T(r)]rdr}{\int_0^R U(r)rdr} \tag{4.6}$$

The velocity distribution in radial direction expression changed from suspect to uniform to that proposed for the fully advanced flow in inverse fluidized bed .The energy used to determine the heat flux was

$$q = \dot{m}C_{pl}(T_{mo} - T_{mi}) \tag{4.7}$$

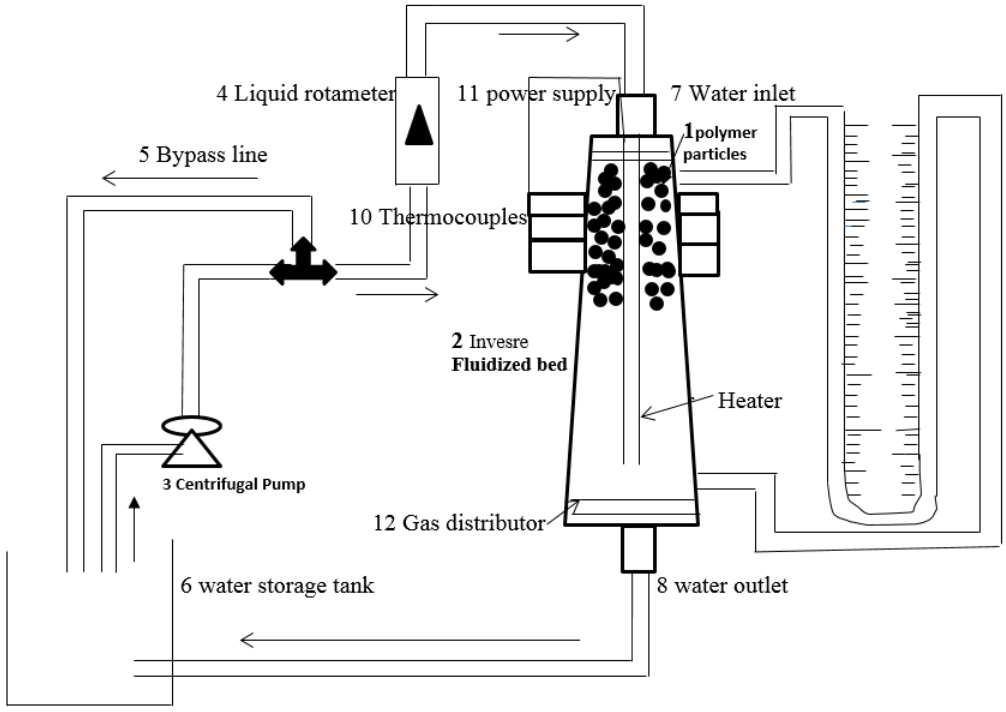

Fig 4.14: Schematic diagram of Tapered inverse fluidized bed

Table 4.1: Geometry of Acrylic tapered inverse fluidized beds.

Bed height(m)	**Top diameter(m)**	**Bottom diameter(m)**	**Tapered angle(α)^{o}**
0.59	0.09	0.25	8
0.59	0.075	0.22	6.8

Table 4.2: Fluid Initial Conditions and Physical properties of solids which were used in experiments

S.No.	Type of Material	Size (m)	Density (kg/m3)	Weight (kgs)	Initial bed heights(m)	Temperatures	Liquid viscosity(kg/m.s)
1	HDPE	0.015	970	0.08,0.159,0.206	0.04,0.075,0.1	45,63,80	0.000891,0.0014, 0.0036
2	PP	0.025	947	0.08,0.159,0.206	0.04,0.075,0.1	45,63,80	0.000891,0.0014,0.0036
3	LDPE	0.03	930	0.08,0.159,0.206	0.04,0.075,0.1	45,63,80	0.000891,0.0014,0.0036

4.1.2.2 Measurement of Heat transfer

The radial temperature profile along in the bed was observed it was seen that the temperature at heater surface was much steeper than that of bed proper. Heat transfer coefficient was calculated in different angles of beds at different apparent viscosity of liquid flowrates using the above equation (4.7).

The nusslet number equation (4.8) was calculated in terms of bed Voidage equation (9) from Wen-Yu and heat transfer coefficient.

$$Nu = hd_p \frac{(1-\varepsilon_s)}{K_l \varepsilon_s} \tag{4.8}$$

Effect of bed Voidage on heat transfer coefficient

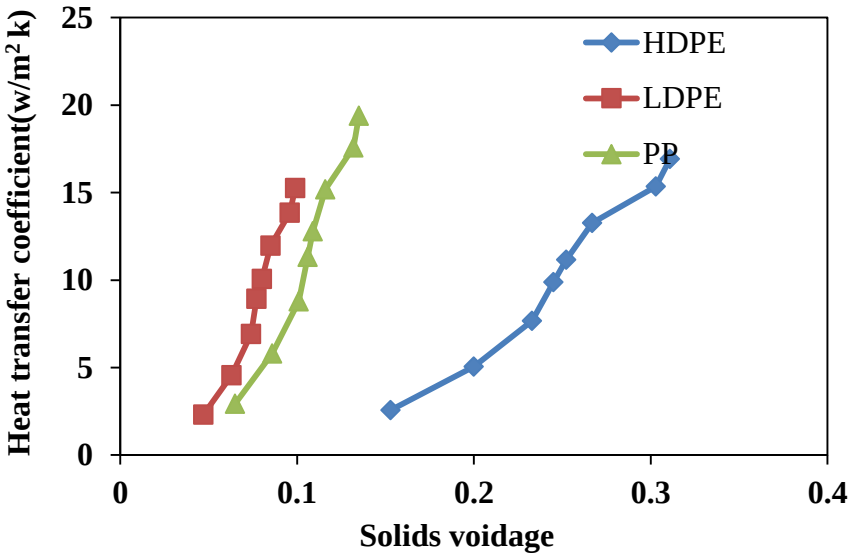

Fig 4.15 Effect of heat transfer coefficient with bed Voidage under different density of materials at H0=0.04m

From fig 4.15, it was observed that the particles hold up decreased with increasing bed Voidage, therefore, the heat transfer coefficient also exhibited maximum valve with increase in the bed Voidage and it varied with different density of materials.

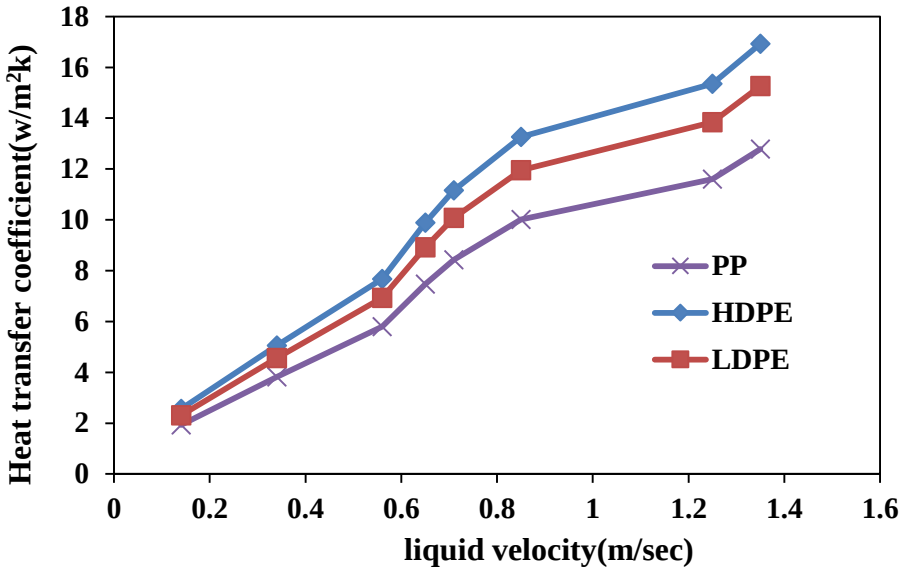

Fig 4.16 Effect of heat transfer coefficient with liquid velocity under different density of materials at H_0=0.04m

The heat transfer coefficient was affected by the liquid velocity as shown in fig.4.16. As anticipated, h valve increased by increasing the liquid velocity. The cause may be to the decrease of the particle hold up and the alteration of solids drift regime. In other attributed words, we can say that, the solid holdup decreases unusually with increasing liquid velocity in the higher range of liquid velocity. This results in inadequate contact among the fluidized solids and the heater surface; consequently, the liquid thin film across the heater surface cannot be eroded efficaciously. Consequently, h decreases with additional increase in liquid velocity. Further, the turbulence inside the bulk vicinity could be decreased by lowering solid holdup in the higher liquid velocity range.

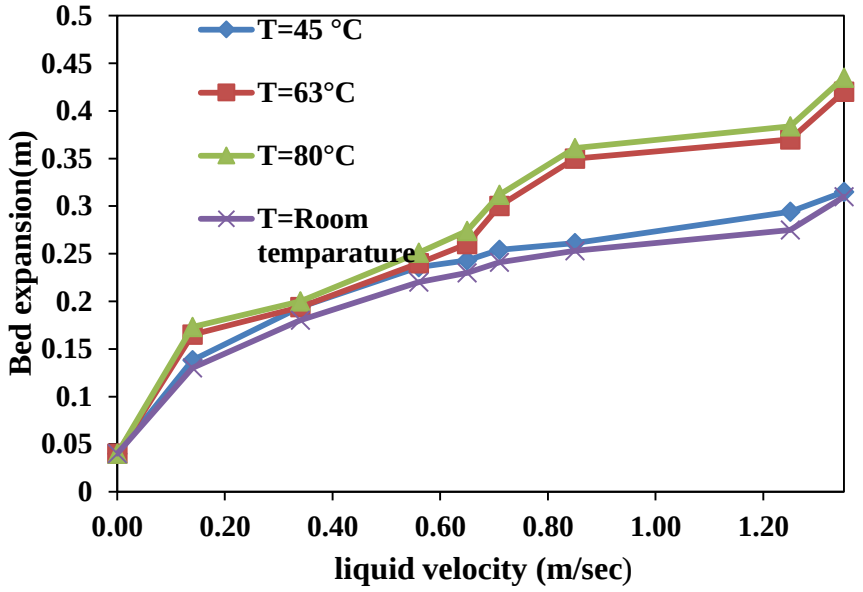

Fig 4.17 Effect of bed expansion with the liquid velocity at 0.014g/m s, H_0=0.04m HDPE under different temperatures of liquid

The effect of liquid velocity on bed expansion at different temperatures can be seen in fig 4.17. By increasing the temperature of the liquid, the bed expanded highly at high temperature. The cause may be defined through the decrease of the particle hold up and the transition of the solids drift regime, due to viscous nature of water at low temperature. In other words, the solid Voidage and flow regime increased at high temperature conditions.

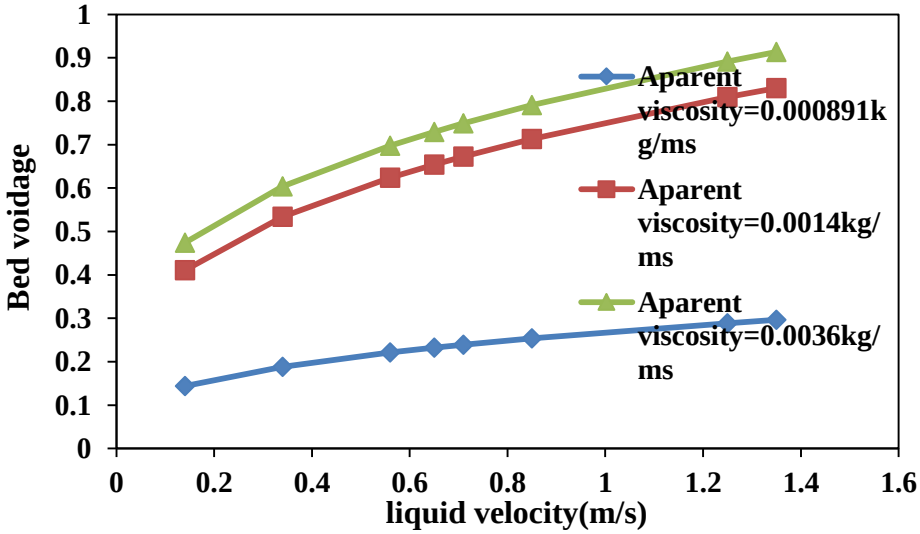

Fig 4.18 Effect of bed Voidage with liquid velocity under different viscosity of liquid

The bed Voidage was effected by increasing liquid velocity as sown in fig 4.18. By increasing the liquid velocity, the turbulence of the solids increased and Voidage increased, as in other words, at different apparent viscosity of inlet liquids, the Voidage decreased with increasing viscosity of liquids.

The effect of liquid velocity on bed expansion at an angle of 7.85 degree inverse fluidized bed at different densities of HDPE, LDPE and PP particles .Note in this fig that bed expansion of different particles increases with increasing liquid velocity in all the instances studied. In other words, the bed expansion was high for high density of particles compared to lower density of particles, the reason behind this is increased liquid velocity from the top of the bed and at the same time bouncy force phenomenon working in opposite direction to the bed expansion from the bed. There the particles should overcome this forces and expand downwards of the bed.

4.1.2.3 Measurement of Bed Voidage, Bed Volume:

To understand the characteristics of the in the inverse tapered fluidized bed, based on mathematical model bed expansion was determined and pressure drop was advanced based on the addition of bed characteristics in a sequence of individual bed volumes up the bed. It was considered that the bed Voidage in each bed increment could be determined by the correlation of Wen and Yu:

$$\varepsilon_s=\left[\frac{18\,N_{Re}+2.7{N_{Re}}^{1.687}}{N_{Ga}}\right]^{0.213} \tag{4.9}$$

$$\text{where}\quad N_{Ga}=\frac{[{d_p}^8\rho_f(\rho_f-\rho_s)g]}{\mu^2}$$

The pressure drop over on each bed increment was determined by the force needed to support the bed in gravitational field:

$$\Delta p=(1-\varepsilon_s)\left(\rho_f-\rho_s\right)gh \tag{4.10}$$

The solid volume in the bed can be determined by a simple material balance around each increment.

$$\Delta V_s=(1-\varepsilon)Ah=(1-\varepsilon)\Delta V \tag{4.11}$$

:

The total bed volume is determined when a summation of the incremental solids equals the original solids volume with the bed at rest:

$$\sum(1-\varepsilon)\Delta V = (1-\varepsilon_0)V_0 \qquad (4.12)$$

Effect of liquid apparent viscosity on bed Voidage

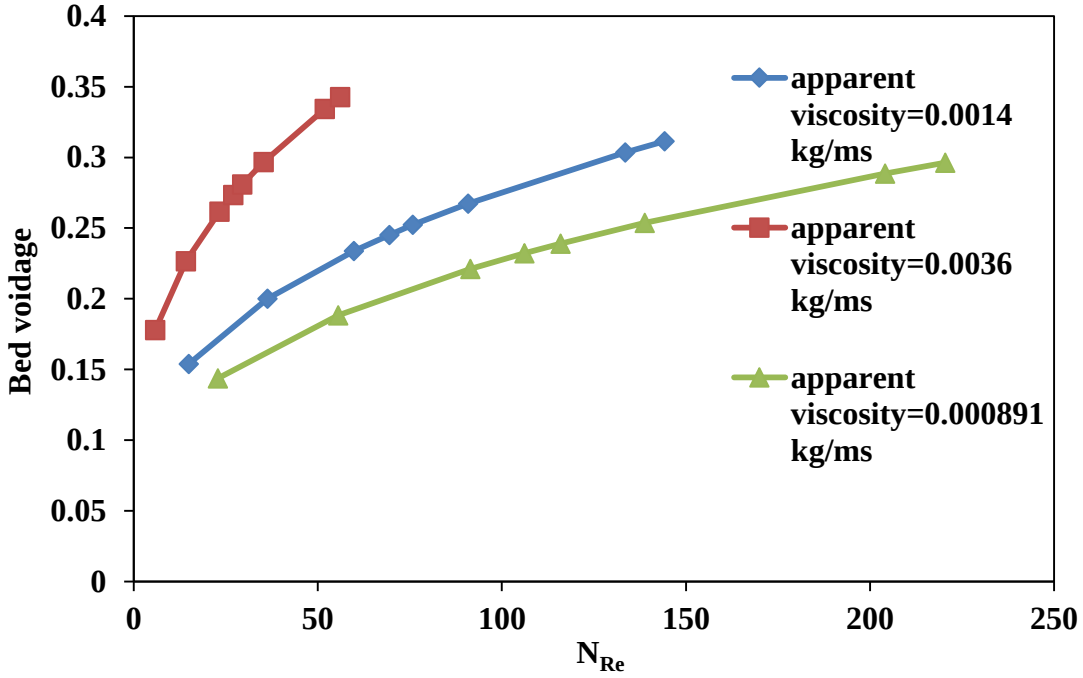

Fig 4.19 Comparison of bed Voidage profiles under different viscosity of liquids with Reynolds no (angle=6.8)

Effect of Reynolds number on bed Voidage is represented in fig 4.19.By increasing liquid velocity the Reynolds no also increased and the bed Voidage increased. The reason was that at increased velocities, the solids hold up increased. The bed Voidage was also dependent on the apparent viscosity of liquid by increasing the apparent viscosity of liquid bed Voidage was also increased due to Reynolds no which was inversely proportional to the Reynolds no.

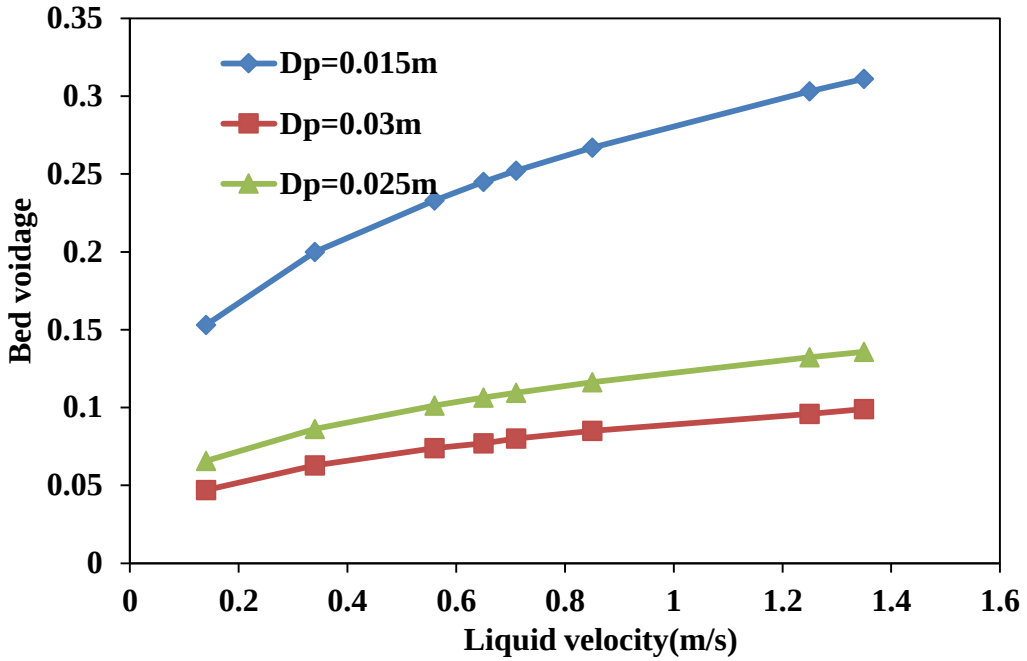

Fig 4.20 Comparison of bed Voidage profiles under different diameter of solids with velocity of liquids (angle=6.8)

Effect of particle diameter on the bed Voidage graphical representation is shown in fig 4.20.By increasing the liquid velocity, the bed Voidage increased with different diameters of solids. For large diameter of particles, the Voidage was low because of which a huge amount of buoyancy force was needed to lift the solids.

4.1.2.4 Effect of initial bed height on total bed volume

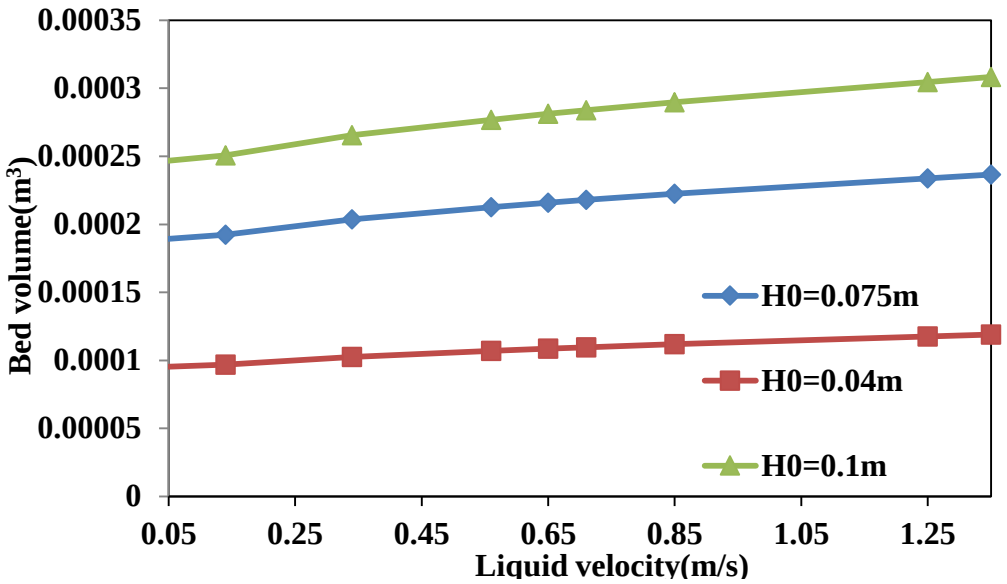

Fig 4.21 Comparison of bed volume profiles for different initial bed heights with velocity of liquid (angle 6.8)

The effect of initial bed height on the bed volume with liquid velocity is shown in fig 4.21. By increasing the liquid velocity, the bed volume increased and it was varied for different initial bed heights. The reason was the weight of solids bed area because of which increased from the top to bottom of reactor.

Developing of Empirical model by using Response surface methodology (RSM):

Response surface method (RSM) used different statistical, graphical and mathematical techniques to broaden, enhance, or optimize procedures; it was also used for modeling and evaluation of problems if the response variables were encouraged through several unbiased variables.

Surface Response Methodology (RSM) data modeling, used an inbuilt utility of Design expert package (version 9) in the present work to derive the regression models in terms of different process parameters like Velocity of liquid, Temperature of liquid, Viscosity of liquid, density of solids and Different angles of reactors. This model equation was used to get the influence of

process parameters on bed expansion ratio through the reactor. The confidence level of data was kept at 0.95 for bed expansion ratio.

Table 4.3: Symbols and levels of independent parameters were used in response surface methodology.

Symbol	Parameters	Units	No of Levels	Levels							
				1	2	3	4	5	6	7	8
A	Temperature	^{O}C	4	33	45	63	80				
B	Apparent viscosity	Kg/ms	3	0.00089	0.0014	0.0036					
C	Density of solids	Kg/m^3	3	930	945	970					
D	Bed angle	Degree	2	6.8	7.85						
E	Velocity of liquid	m/sec	8	0.14	0.34	0.56	0.65	0.71	0.85	1.25	1.35

Table 4.4 ANOVA Table for Response Surface for hydrodynamics studies

Source	**Sum of Squares**	**F Value**	**p-value Prob > F**
Model	4940.42	134.18	< 0.0001
A-Temperature	72.61	29.58	< 0.0001
B-apparent viscosity	364.24	148.39	< 0.0001
C-density	208.28	84.86	< 0.0001
D-bed angle	3.41	1.39	0.2393
E-velocity	3778.84	1539.53	< 0.0001
AB	24.62	10.03	0.0016
AC	18.86	7.68	0.0058
AD	21.42	8.73	0.0033
AE	31.73	12.93	0.0004
BC	51.61	21.03	< 0.0001
BD	30.91	12.59	0.0004
BE	12.44	5.07	0.0248
CD	9.06	3.69	0.0552
CE	18.36	7.48	0.0064
DE	3.95	1.61	0.2050

Linear regression (R^2) 0.90 R^2 adjusted 0.8832

Correlated Equation of mean residence time in Terms of Factors:

Bed expansion ratio (H/H_0) = 90.327-0.717*A +17575.5*B-0.0892*C-14.52*D-23.82*E-9.88*A*B+6.147*10^0.004-A*C*+0.02*A*D+0.033*A*E-15.47*B*C-376.37*B*D-322.91*B*E+0.014*C*D+0.027*C*E+0.04*D*E (4.13)

Equation (4.13) was developed in terms of independent parameters. The corresponding p and F values, the linear regression coefficient and the adjusted regression coefficients are represented in Table.4.4. It was observed from Tab. 4.4 that the values of the linear regression coefficient (R^2) and the adjusted (R^2) were almost same in magnitude. Furthermore, the value of Probability was found to be F, which signifies that the independent parameters were trustworthy. Moreover, the results from the model equation was that the bed angle effect very less while the velocity of liquid, apparent viscosity of liquid, Temperature of liquid and density of solids are affected bed expansion ratio. Figure 4.22 represents the response surface designed for the optimization of processes variables for the bed expansion ratio utilizing the system. The parameters were analyzed in terms of numerical coefficients. Moreover, the results obtained from the model equation showed that the mass of solid was less affected in comparison to particle density and velocity of the liquid, while the angle of tapered inverse fluidized bed impacted the bed expansion ratio. Figure 4.23 shows the residual error of the bed expansion ratio. It can be seen that residuals errors were within ±5%. On the other hand, the comparison between the experimental and predicted results in bed expansion ratio showed that there was approximately a 15 % difference, which indicated a reasonably good estimation of the bed expansion ratio.

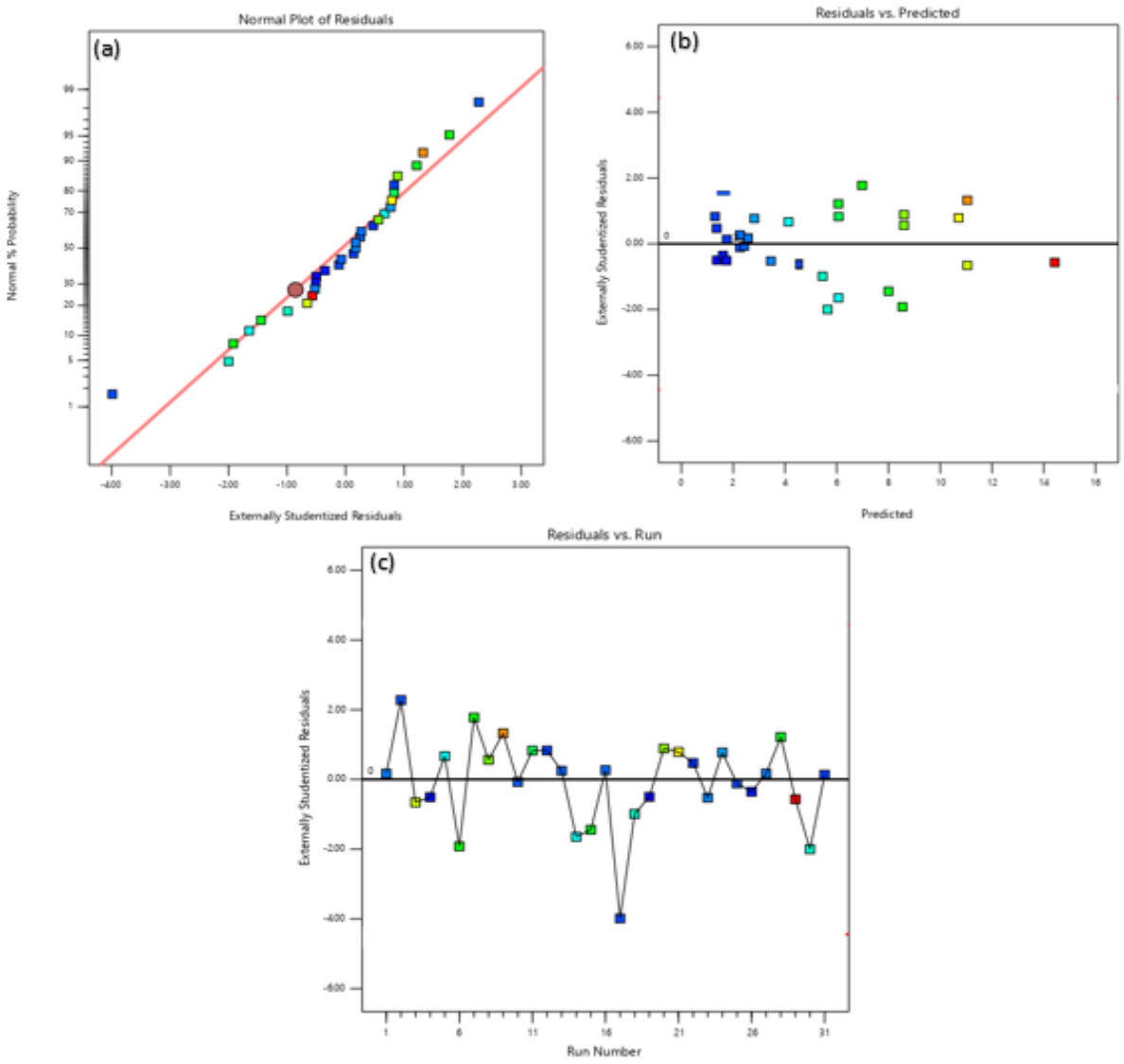

Figure 4.22. (a)#Normal plot of Residuals, (b) Residuals vs Predicted, (c) Residuals vs Run number for bed expansion ratio.

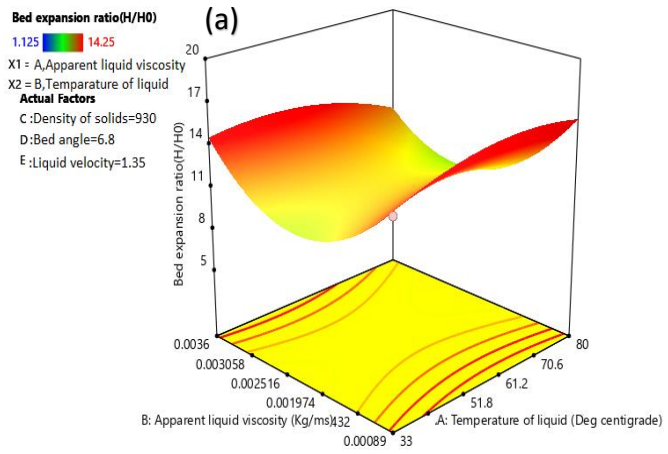
(a)
Bed expansion ratio(H/H0)
1.125
14.25
X1 = A,Apparent liquid viscosity
X2 = B,Temparature of liquid
Actual Factors
C :Density of solids=930
D :Bed angle=6.8
E :Liquid velocity=1.35
Bed expansion ratio(H/H0)
B: Apparent liquid viscosity (Kg/ms)
A: Temperature of liquid (Deg centigrade)

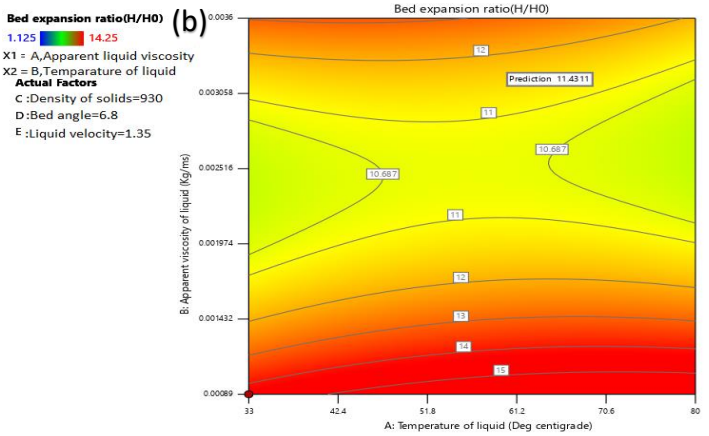
(b)
Bed expansion ratio(H/H0)
1.125
14.25
X1 = A,Apparent liquid viscosity
X2 = B,Temparature of liquid
Actual Factors
C :Density of solids=930
D :Bed angle=6.8
E :Liquid velocity=1.35
Prediction 11.4311
B: Apparent viscosity of liquid (Kg/ms)
A: Temperature of liquid (Deg centigrade)

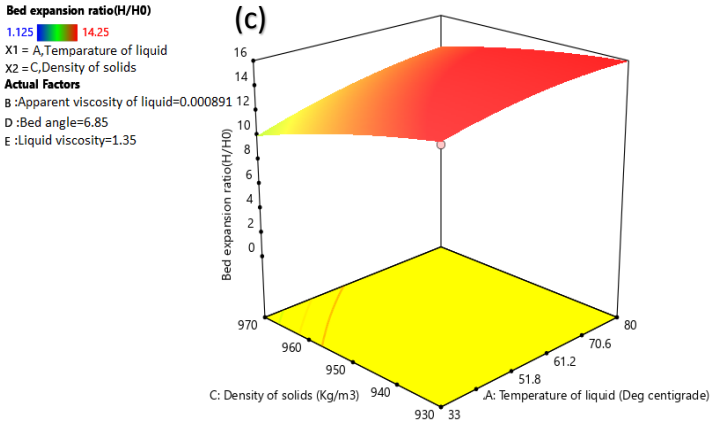
(c)
Bed expansion ratio(H/H0)
1.125
14.25
X1 = A,Temparature of liquid
X2 = C,Density of solids
Actual Factors
B :Apparent viscosity of liquid=0.000891
D :Bed angle=6.85
E :Liquid viscosity=1.35
Bed expansion ratio(H/H0)
C: Density of solids (Kg/m3)
A: Temperature of liquid (Deg centigrade)

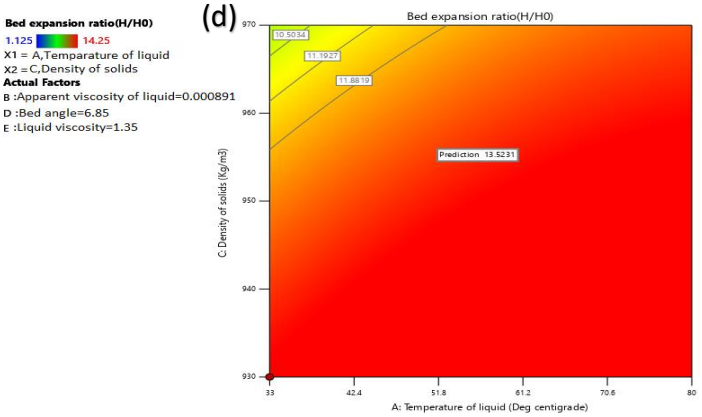
(d)
Bed expansion ratio(H/H0)
1.125
14.25
X1 = A,Temparature of liquid
X2 = C,Density of solids
Actual Factors
B :Apparent viscosity of liquid=0.000891
D :Bed angle=6.85
E :Liquid viscosity=1.35
Prediction 13.5231
C: Density of solids (Kg/m3)
A: Temperature of liquid (Deg centigrade)

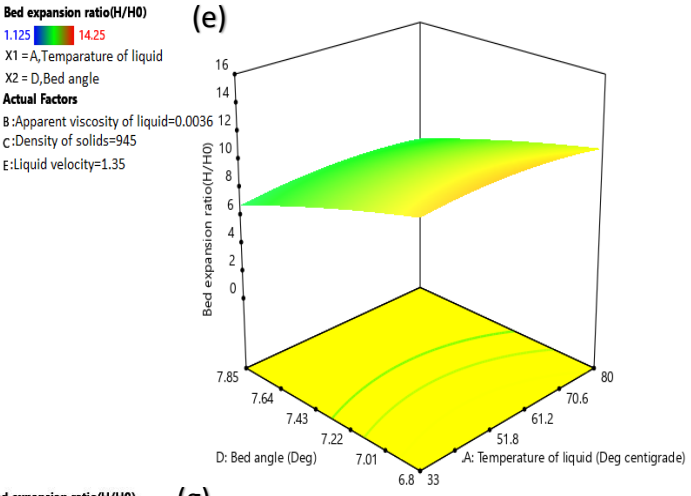
(e)
Bed expansion ratio(H/H0)
1.125
14.25
X1 = A,Temparature of liquid
X2 = D,Bed angle
Actual Factors
B :Apparent viscosity of liquid=0.0036
C :Density of solids=945
E :Liquid velocity=1.35
Bed expansion ratio(H/H0)
D: Bed angle (Deg)
A: Temperature of liquid (Deg centigrade)

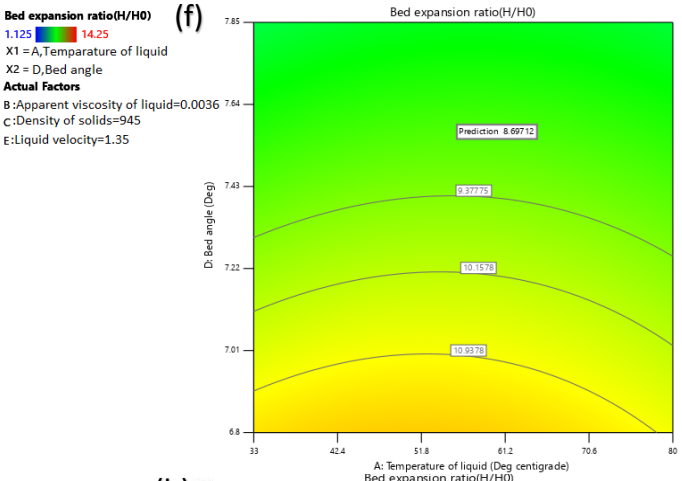
(f)
Bed expansion ratio(H/H0)
1.125
14.25
X1 = A,Temparature of liquid
X2 = D,Bed angle
Actual Factors
B :Apparent viscosity of liquid=0.0036
C :Density of solids=945
E :Liquid velocity=1.35
Prediction 8.69712
D: Bed angle (Deg)
A: Temperature of liquid (Deg centigrade)

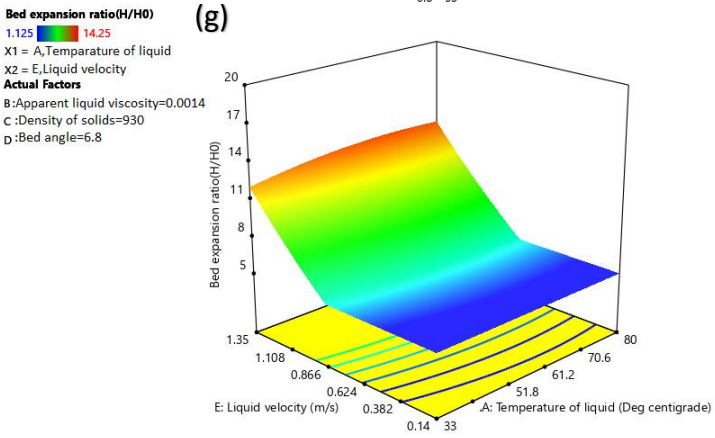
(g)
Bed expansion ratio(H/H0)
1.125
14.25
X1 = A,Temparature of liquid
X2 = E,Liquid velocity
Actual Factors
B :Apparent liquid viscosity=0.0014
C :Density of solids=930
D :Bed angle=6.8
Bed expansion ratio(H/H0)
E: Liquid velocity (m/s)
A: Temperature of liquid (Deg centigrade)

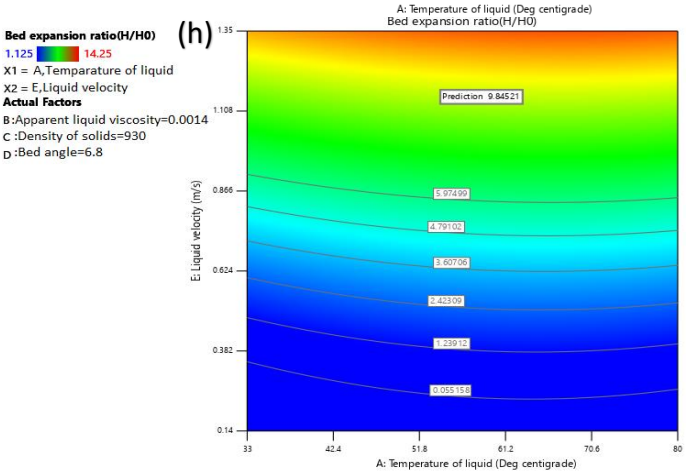
(h)
Bed expansion ratio(H/H0)
1.125
14.25
X1 = A,Temparature of liquid
X2 = E,Liquid velocity
Actual Factors
B :Apparent liquid viscosity=0.0014
C :Density of solids=930
D :Bed angle=6.8
Bed expansion ratio(H/H0)
Prediction 9.84521
E: Liquid velocity (m/s)
A: Temperature of liquid (Deg centigrade)

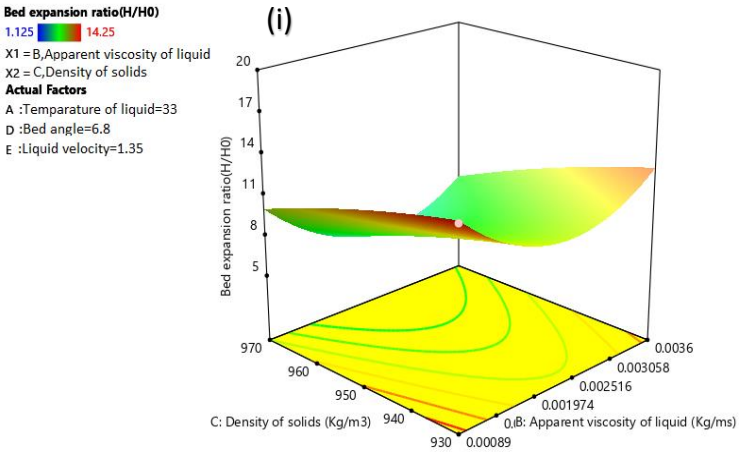
Bed expansion ratio(H/H0)
1.125
14.25
X1 = B,Apparent viscosity of liquid
X2 = C,Density of solids
Actual Factors
A :Temparature of liquid=33
D :Bed angle=6.8
E :Liquid velocity=1.35
(i)
Bed expansion ratio(H/H0)
C: Density of solids (Kg/m3)
B: Apparent viscosity of liquid (Kg/ms)

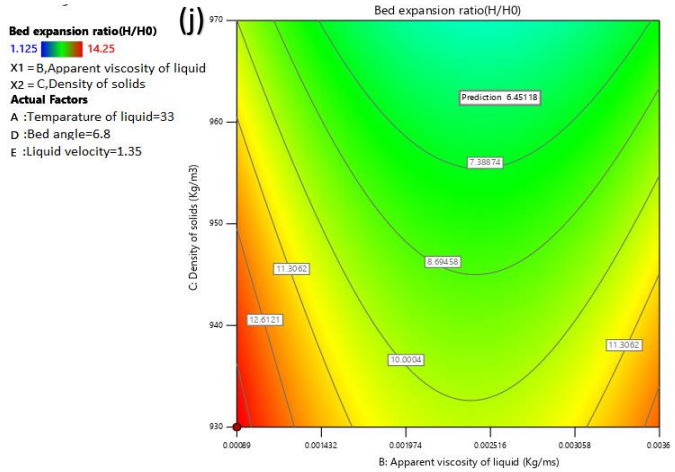
Bed expansion ratio(H/H0)
1.125
14.25
X1 = B,Apparent viscosity of liquid
X2 = C,Density of solids
Actual Factors
A :Temparature of liquid=33
D :Bed angle=6.8
E :Liquid velocity=1.35
(j)
Bed expansion ratio(H/H0)
Prediction 6.45118
C: Density of solids (Kg/m3)
B: Apparent viscosity of liquid (Kg/ms)

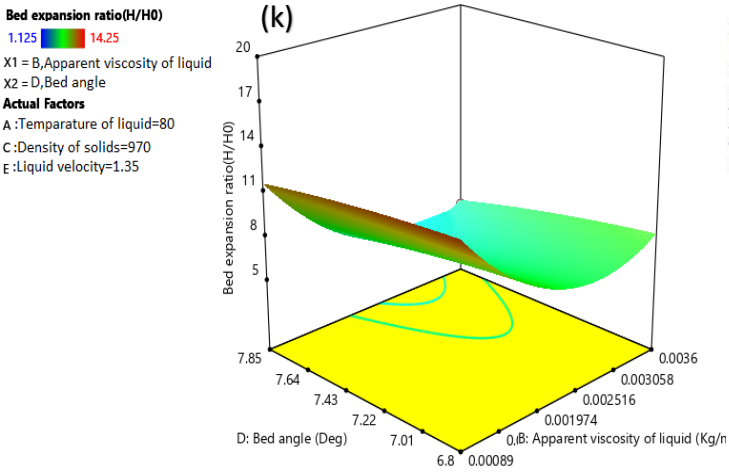
Bed expansion ratio(H/H0)
1.125
14.25
X1 = B,Apparent viscosity of liquid
X2 = D,Bed angle
Actual Factors
A :Temparature of liquid=80
C :Density of solids=970
E :Liquid velocity=1.35
(k)
Bed expansion ratio(H/H0)
D: Bed angle (Deg)
B: Apparent viscosity of liquid (Kg/n

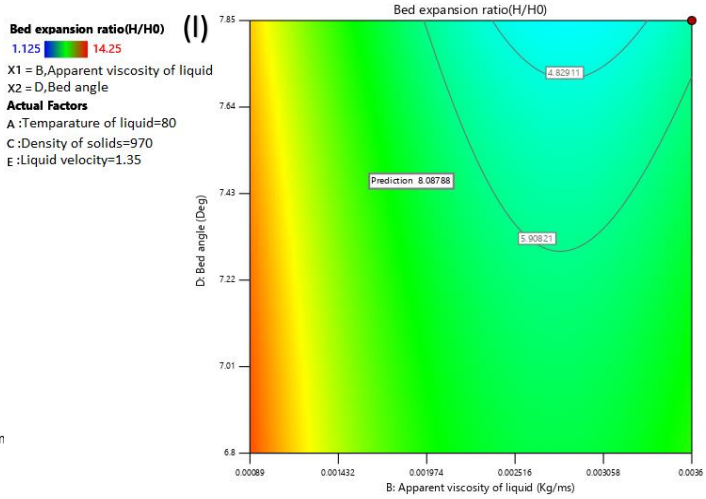
Bed expansion ratio(H/H0)
1.125
14.25
X1 = B,Apparent viscosity of liquid
X2 = D,Bed angle
Actual Factors
A :Temparature of liquid=80
C :Density of solids=970
E :Liquid velocity=1.35
(l)
Bed expansion ratio(H/H0)
Prediction 8.08788
D: Bed angle (Deg)
B: Apparent viscosity of liquid (Kg/ms)

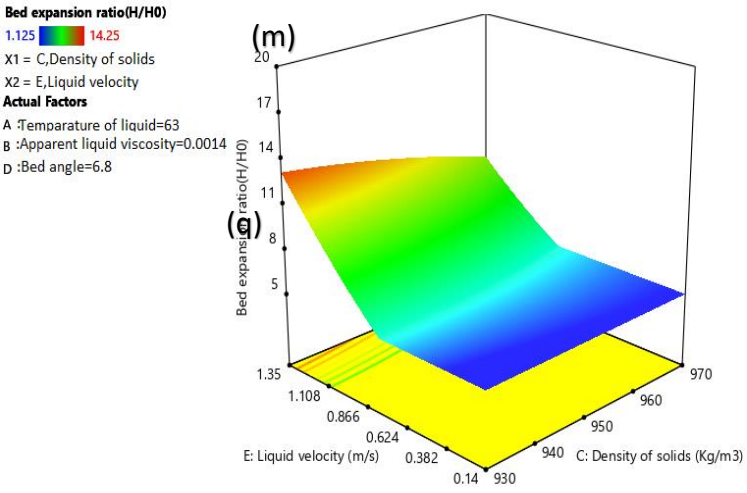
Bed expansion ratio(H/H0)
1.125
14.25
X1 = C,Density of solids
X2 = E,Liquid velocity
Actual Factors
A :Temparature of liquid=63
B :Apparent liquid viscosity=0.0014
D :Bed angle=6.8
(m)
(q)
E: Liquid velocity (m/s)
C: Density of solids (Kg/m3)

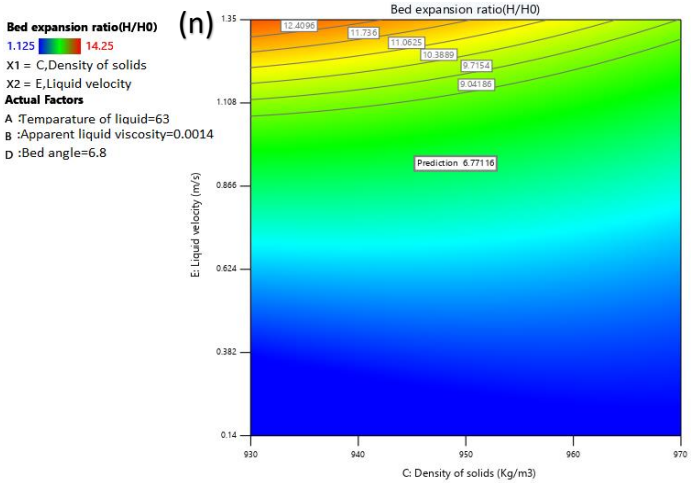
Bed expansion ratio(H/H0)
1.125
14.25
X1 = C,Density of solids
X2 = E,Liquid velocity
Actual Factors
A :Temparature of liquid=63
B :Apparent liquid viscosity=0.0014
D :Bed angle=6.8
(n)
Bed expansion ratio(H/H0)
Prediction 6.77116
E: Liquid velocity (m/s)
C: Density of solids (Kg/m3)

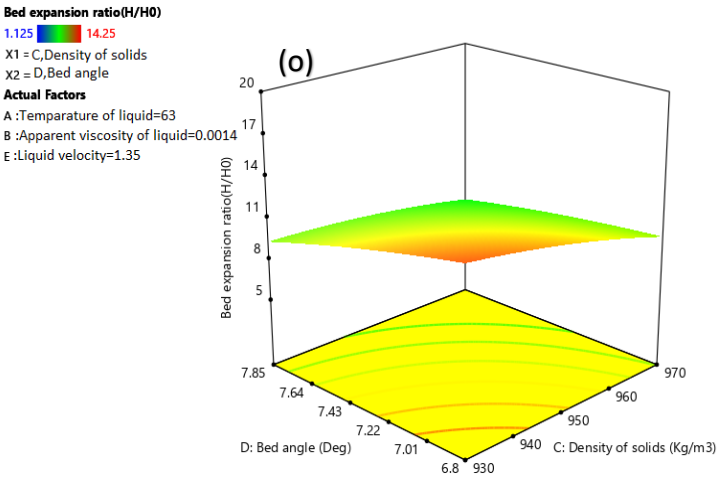
Bed expansion ratio(H/H0)
1.125
14.25
X1 = C,Density of solids
X2 = D,Bed angle
Actual Factors
A :Temparature of liquid=63
B :Apparent viscosity of liquid=0.0014
E :Liquid velocity=1.35
(o)
Bed expansion ratio(H/H0)
D: Bed angle (Deg)
C: Density of solids (Kg/m3)

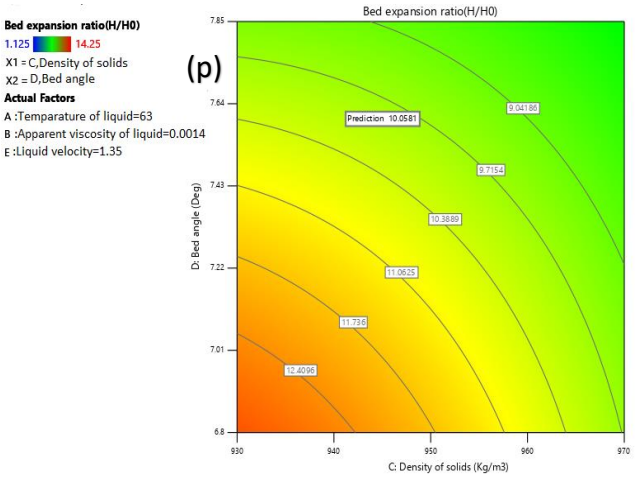
Bed expansion ratio(H/H0)
1.125
14.25
X1 = C,Density of solids
X2 = D,Bed angle
Actual Factors
A :Temparature of liquid=63
B :Apparent viscosity of liquid=0.0014
E :Liquid velocity=1.35
(p)
Bed expansion ratio(H/H0)
Prediction 10.0581
D: Bed angle (Deg)
C: Density of solids (Kg/m3)

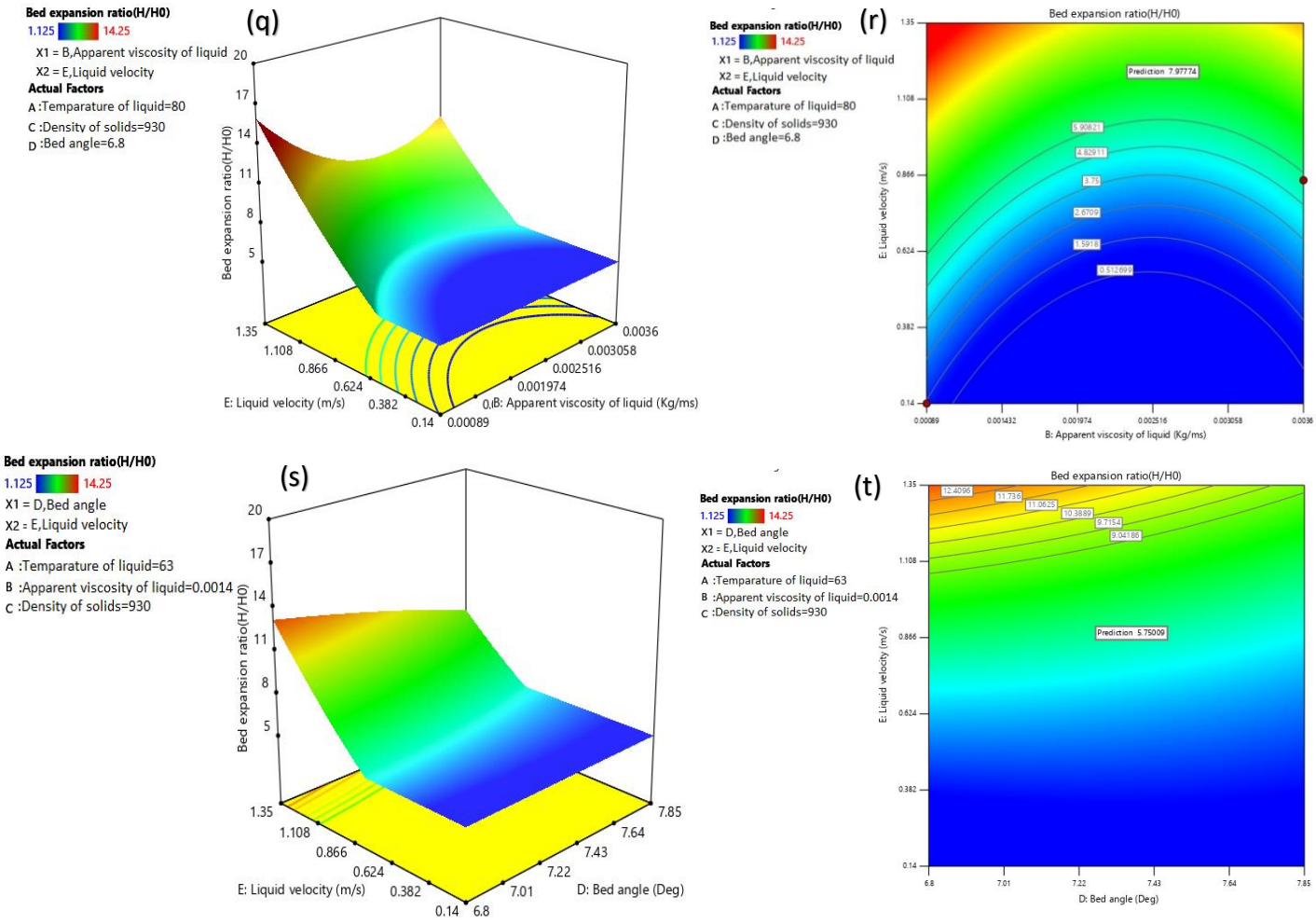

Figure 4.23. Response surface graphs indicating mutual interactions between the input parameters to effect on bed expansion ratio. (a) Apparent viscosity Vs Temperature of Liquid. (c) Density of solids Vs Temperature of Liquid. (e) Bed angle Vs Temperature of Liquid. (g) Liquid velocity Vs Temperature of Liquid. (i) Density of solids Vs Apparent viscosity of liquid. (k)Bed angle Vs Apparent viscosity of liquid. (m) Liquid velocity vs apparent viscosity of liquid. (o) Bed angle vs Density of solids. (q) Liquid velocity vs Density of solids. (s) Liquid velocity vs Bed angle. and 4.23 (b,d,f,h,j,L,n,p,r,t) are contour plots.

Optimization

Numerical analysis was used to attempt additional optimization. The best local maximum value is found is at temperature of liquid is 35.28 ^{0}C, apparent viscosity of liquid 0.0028 kg/ms, particle density 959.64 kg/m3, reactor angle 6.93 deg and liquid velocity is 1.1m/s. Bed expansion ratio obtained at these conditions is 5.55; the desirability for this is 1.00 (Fig. 4.24). Further, the mean residence time was verified with experimental results, which showed 5, ensuring that the results produced utilizing Optimal (custom) design. Thus it indicated that Optimal (custom) design is suitable for usage.

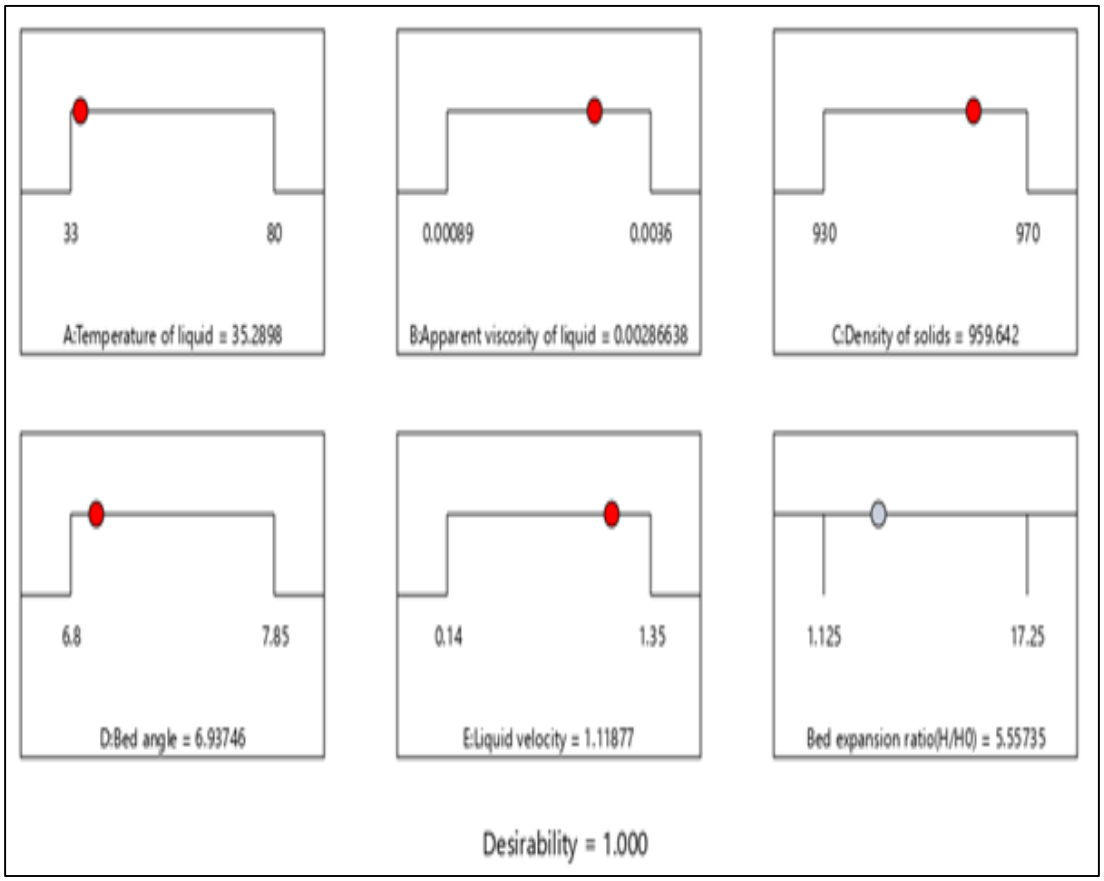

Fig. 4.24 Desirability ramp for numerical optimization obtained by software Design Expert®

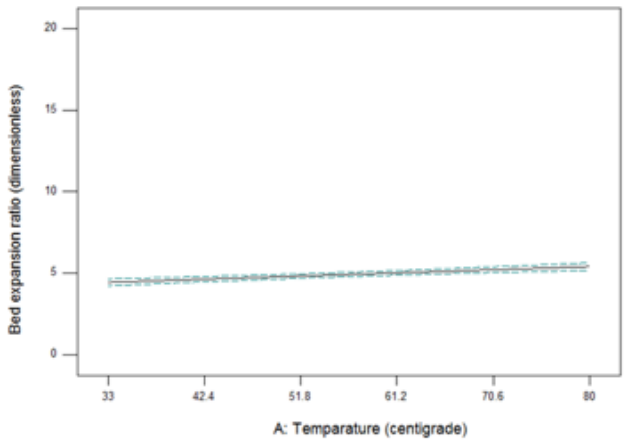

Fig 17.

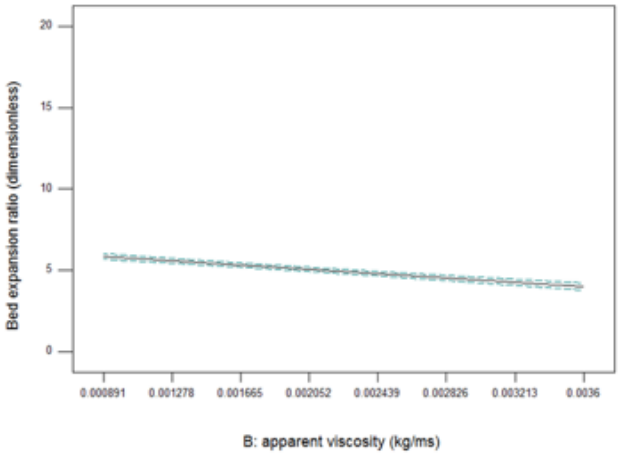

Fig 18.

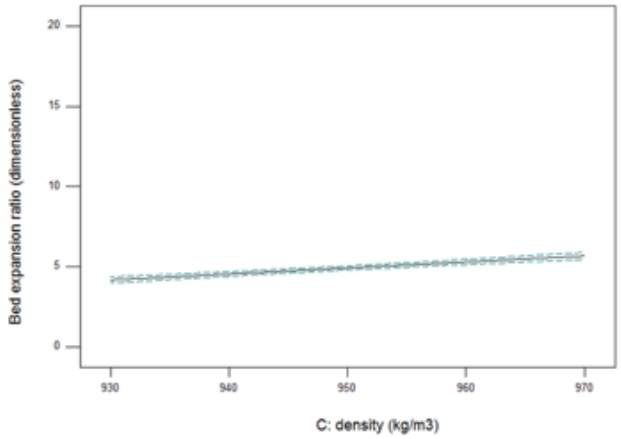

Fig 19.

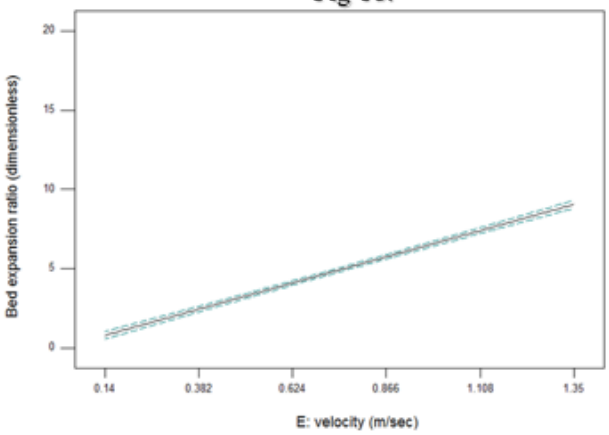

Fig 20.

Fig 4.25. 17, 18, 19 and 20 shows the effect of temarature, apparent liquid viscosity, solids density and liquid velocity on bed expansion ratio respectively.

From 4.25, Fig 17 it was observed that by increasing the temperature of the liquid, which was continuous the reactor bed expansion ratio also increased, the viscous nature of liquid decreased and the solid holdup was high

The effect of liquid apparent viscosity on bed expansion ratio was observed in fig 18.It was observed that the bed expansion ratio was decreased by increasing liquid apparent viscosity. The reason was that the solid holdup phenomenon was less for high viscous liquids.

The effect of solid density on bed expansion ratio is shown in fig 19. It was observed that the bed expansion ratio increased by increasing solid density. The reason was that the solid holdup

phenomenon was high for high density solids because it will easily overcome the bouncy force acting in upward direction.

The effect of liquid velocity on bed expansion ratio is shown in fig 20.It was observed that the bed expansion ratio for increased by increasing liquid velocity. The reason was that the solid holdup phenomenon was high for high velocity of liquids.

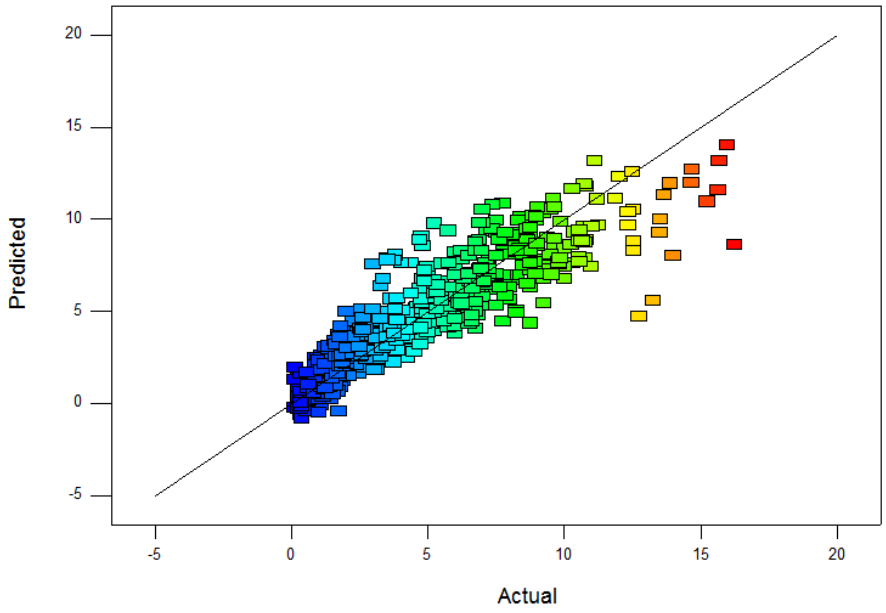

Fig 4.26 Comparison of actual and predicted bed expansion ratios by design expert software

From fig 4.26 it was observed that the experimental and predicted bed expansion ratio values were almost same

4.1.2 .5 Computational results:

Various numerical estimation are done by ANSYS FLUENT 17.0 and the outcomes are introduced graphically so as to show the impact of factors, for example, superficial liquid velocity on the hydrodynamic characteristics of the two-phase tapered inverse fluidized bed. As referenced, before two various geometric models are considered for simulation in the current work: 2D geometry, 3D geometry with orifice size distribution 0,001 m. This was done in order to compare the results of the simulation with the experimental results of the 2D and 3D models without distributors under similar conditions and to compare the results provided from the simulation of the 2D and 3D

models without the distributors due to the need for high computational power that is beyond the reach of the present work. A time phase size of 0.001s has been used for all simulations. The convergence requirements for all numerical simulations were focused on the monitoring of the residual mass flow and the value of 1.0 e-03 was set as the converging value. The residual plot of simulation development is observed in Fig. 4.27. The accompanying under unwinding factors has been utilized for various stream quantities: density = 1, pressure = 0.3, momentum = 0.2, body forces = 1, granular temperature = 0.2, volume fraction = 0.5, turbulent dissipation rate = 0.8, turbulent kinetic energy = 0.8 and turbulent viscosity =1. All the simulations was done still the system reach the quasi steady-state, the normal stream behaviors are time independent. This is done by checking the height of the extended bed and the phase volume fractions. Liquid and solid phase dynamics have been described in the form of contours, vectors and XY plots and are analyzed. Fig. 4.28 indicates the difference in the bed profile with the physical simulation time. The figure shows that the bed profile is almost the same after 25 seconds of simulation time. The simulation ends for 30 seconds and the average of the last 30 seconds is used in the study.

From figs. 4.29, 4.30 and 4.31 describes the comparison of 2D and 3D fluidized bed expansion, bed Voidage and pressure drop with distributor. Hydrodynamics of 2D and 3D tapered inverse fluidized bed with distributor found to be close to understanding. Hence, all ensuing work reproductions for the subsequent work for the 2D and 3D models of tapered inverse fluidized bed with the distributor have been done.

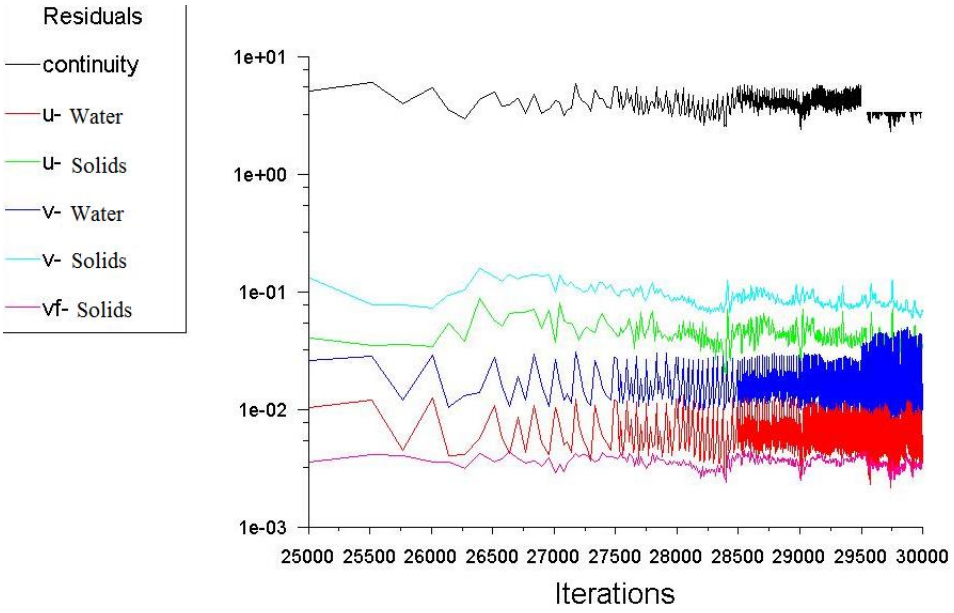

Fig. 4.27. Graph of residuals indicated the progress of simulation.

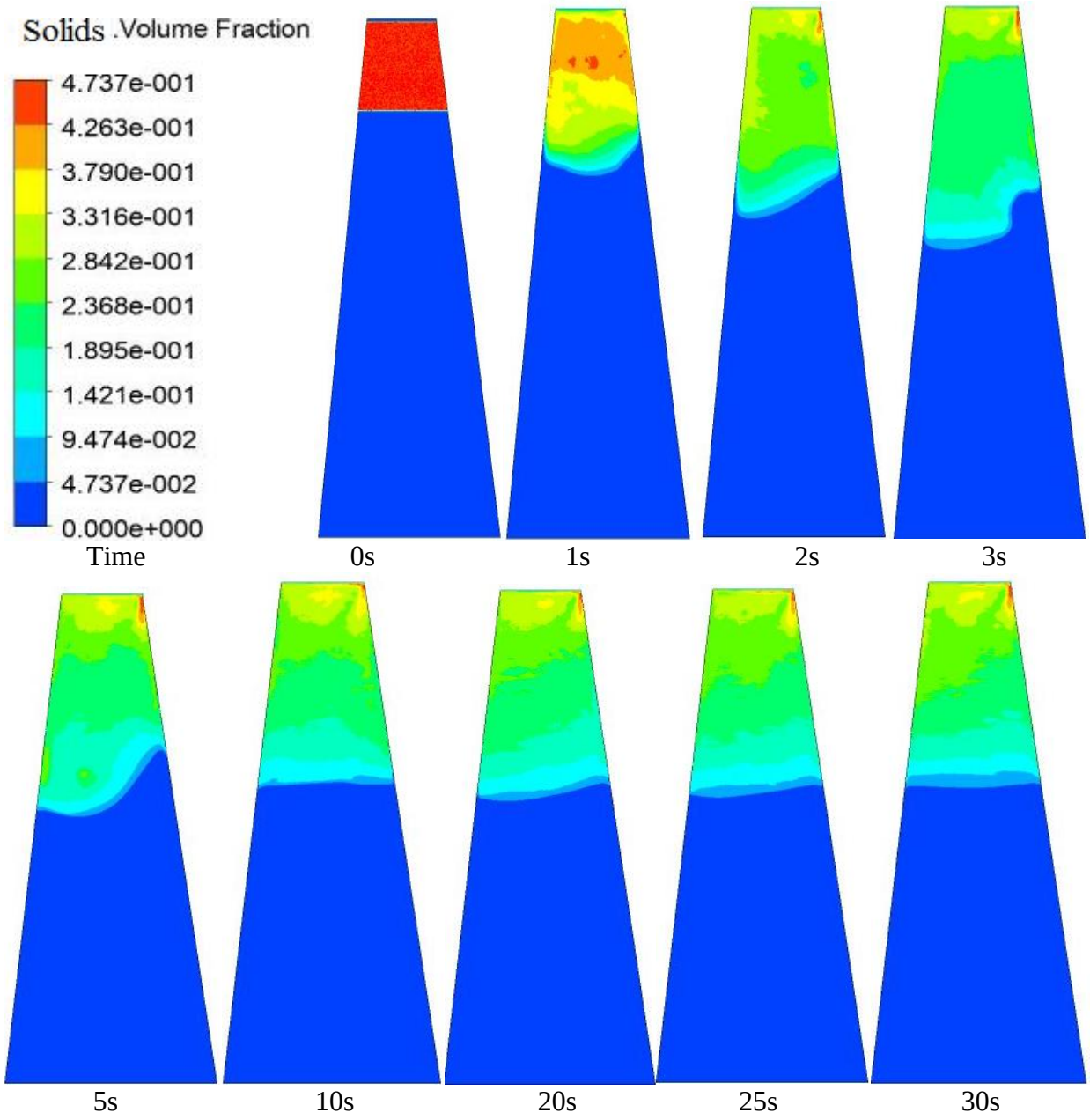

Fig. 4.28. Contour of volume fraction of HDPE solids of initial bed height of 0.1 m inside 2D fluidized bed at liquid velocity of 0.56 m/s of wen-yu model at different physical time of simulation.

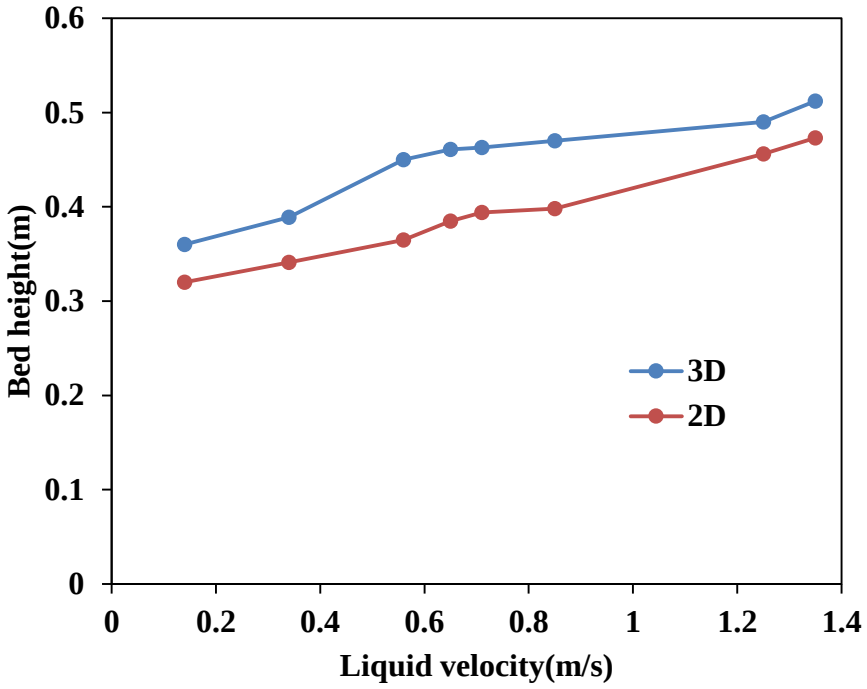

Fig. 4.29. Comparison of bed height of 2D and 3D fluidized bed.

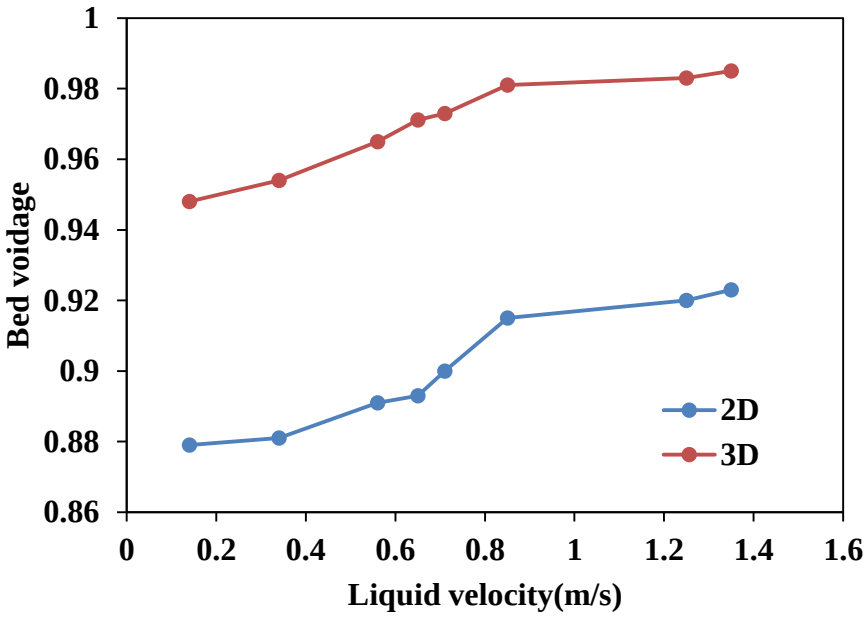

Fig. 4.30. Comparison of bed Voidage of 2D and 3D fluidized bed.

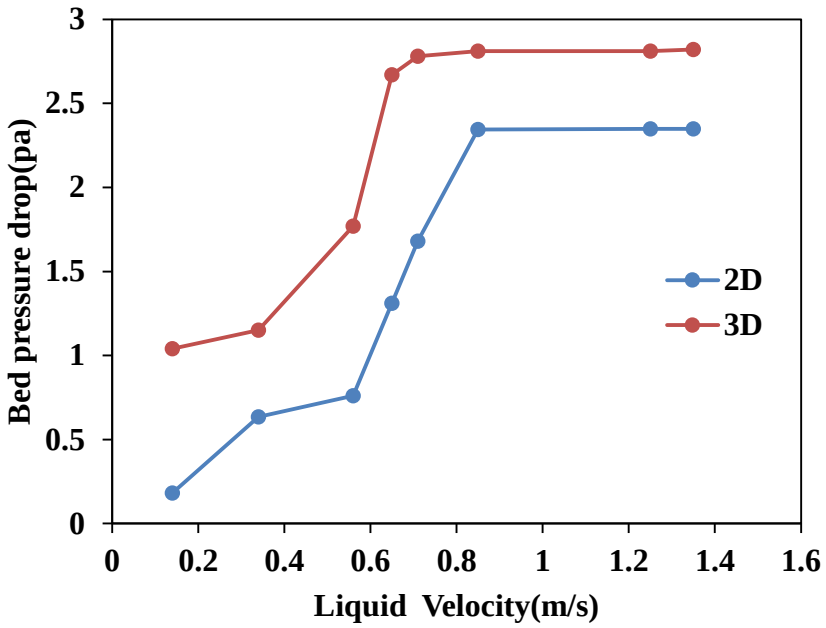

Fig. 4.31. Comparison of bed pressure drop of 2D and 3D fluidized bed.

4.1.2.6 Phase volume fractions

The volume fraction of solid and liquid in the bed is indicated by contours. After the quasi steady state is attained, Fig. 4.32 presence the contour of volume fraction of solid and liquid in the column provided at liquid velocity of 0.85 m/s and liquid viscosity of 0.000891 kg/ms for initial bed height 0.1 m LDPE diameter 0.015 m in 3D fluidized bed. Fig. 4.33 shows the contour of volume fraction of solid and liquid at liquid velocity 0.85 m/s and liquid viscosity 0.000891 kg/ms for initial bed height 0.1 m and LDPE diameter of 0.015 in 2D fluidized after steady state is obtained. From Figs. 4.32 and 4.33, when comparing the 2D fluidized bed model to the 3D fluidized bed model, it is found that the distribution of volume fraction of all phases inside the fluidized section is not uniform. Water is less in the fluidized part than the two-phase segment above it, according to the volume fraction of water contour.

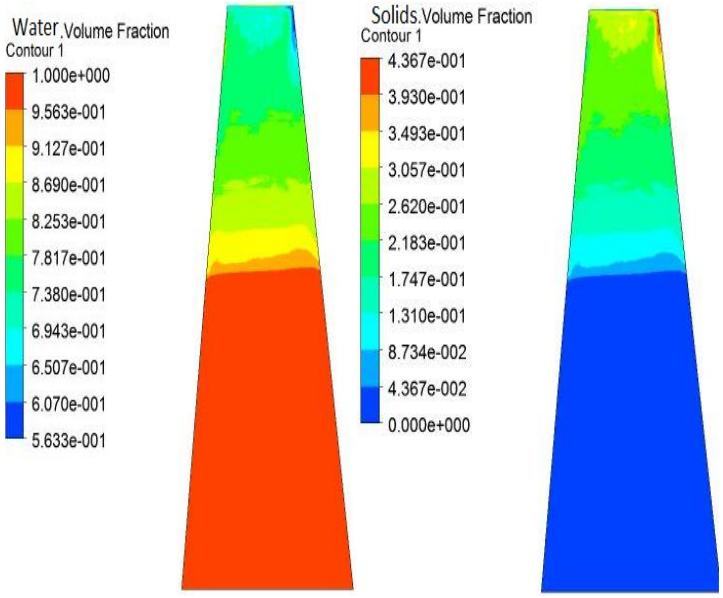

Fig. 4.32. Contour of volume fraction of Solid and liquid and at liquid velocity 0.85 m/s and 0.000891 of liquid viscosity at gidaspow model for initial bed height of 0.1 m in 3D inverse fluidized bed.

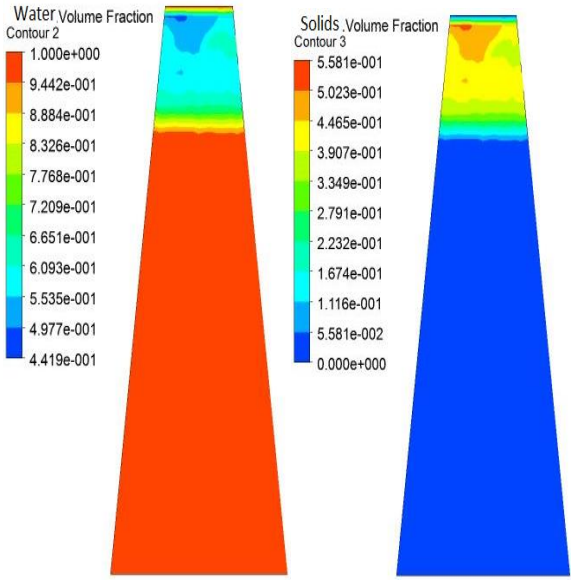

Fig. 4.33. Contour of volume fraction of Solid and liquid and at velocity 0.85m/s and 0.000891 of liquid Viscosity at gidaspow model for initial bed height of 0.1m in 2D inverse fluidized bed.

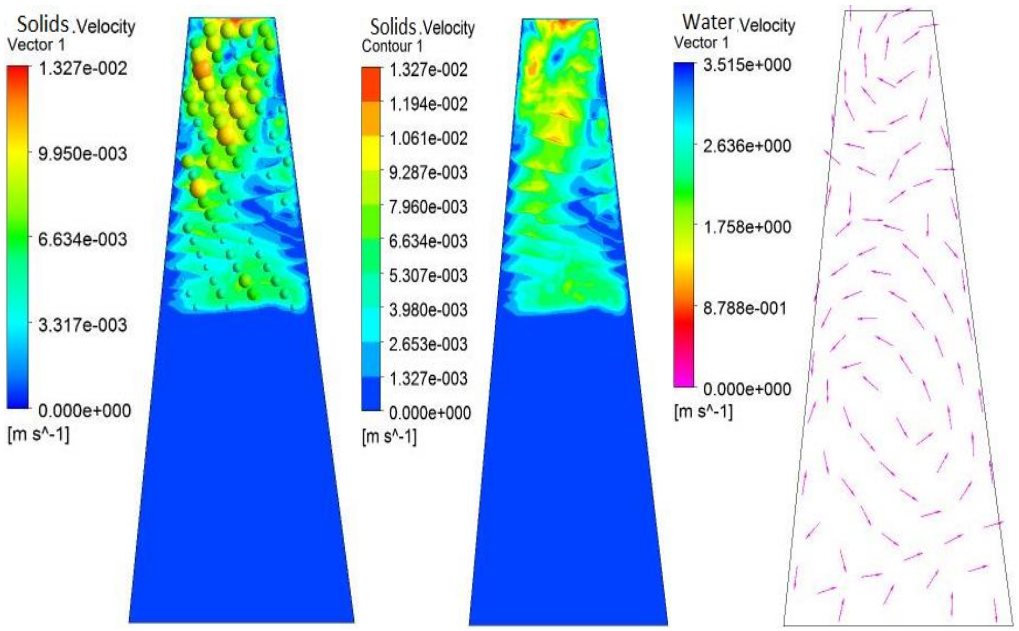

Fig. 4.34. Velocity vector and contour of solid and velocity vector of liquid inside the tapered inverse fluidized bed.

Fig. 4.34 indicated that the contour it is observed that the velocity vector of water is more in the fluidized section compared to that of solid-phase. Fig. 4.35 indicated the comparison of solids volume fraction, water volume fraction, and water velocity and solids velocity contour profiles for 3D tapered inverse fluidized. From the figure it is observed that volume fractions and velocity profiles varied in solids and liquid at the same conditions.

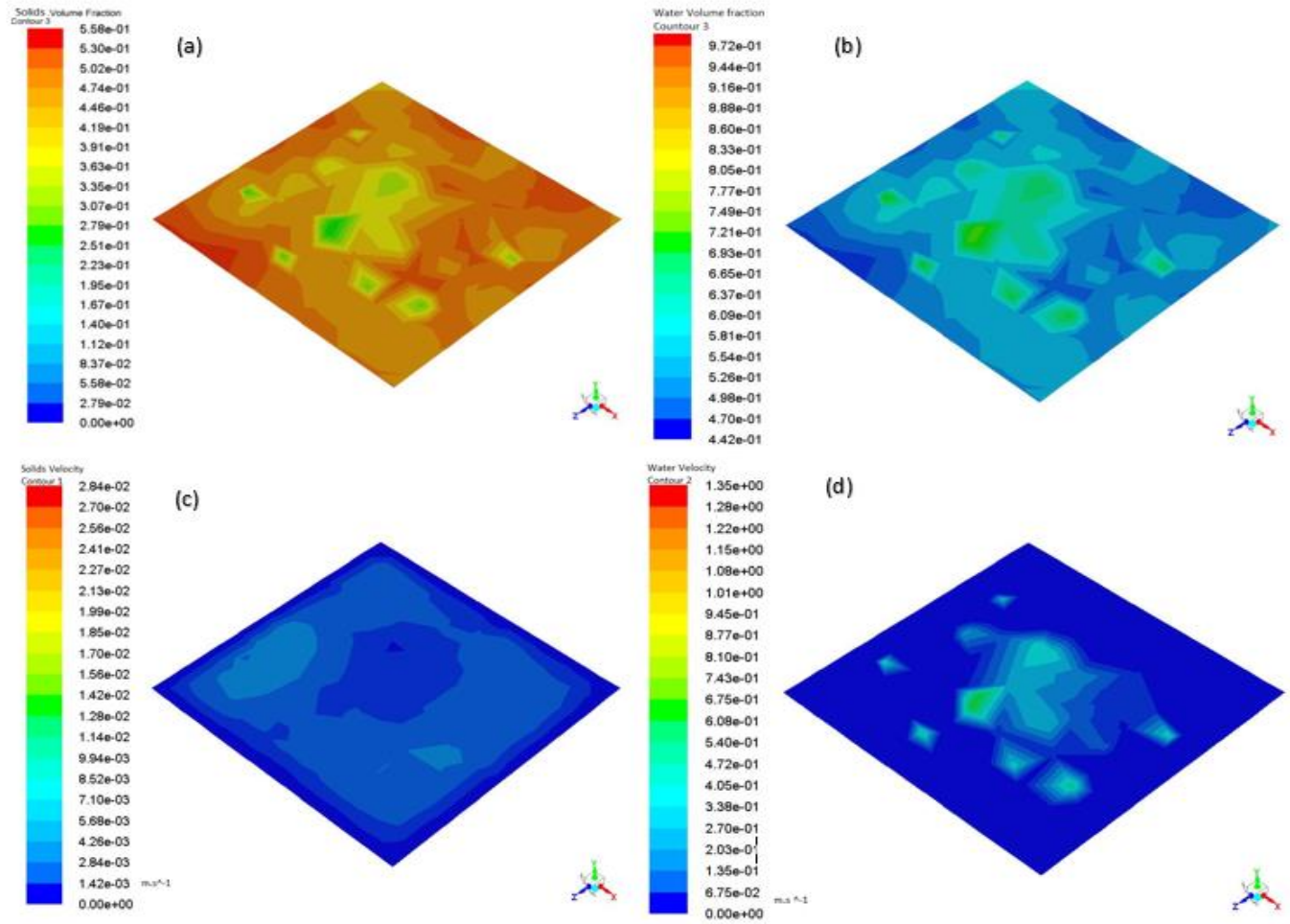

Fig. 4.35. (a) Solids volume fraction, (b) liquid volume fraction, (c) Solids velocity contour and (d) Liquid velocity contours at liquid velocity 0.56 m/s for static bed height of 0.1 m in 3D fluidized bed.

Fig. 4.36 indicated the comparisons for liquid axial velocity of 2D fluidized bed having distributor of pore size 2 mm at inlet liquid velocity 0.14 m/s and initial bed height 0.1 m. It is evident from the plot that the axial velocity in 0.0008 kg/ms viscosity of liquid is more in magnitude and fluctuating type as compared to that in the 0.00142 kg/ms and 0.0036 kg/ms viscosity of liquids. This is due to the presence of viscous nature between them. The water molecules are observed to be in to and fro motion in the plot, sometimes in the direction of solid and liquid flow and sometimes in the opposite direction of liquid and solid phase flow.

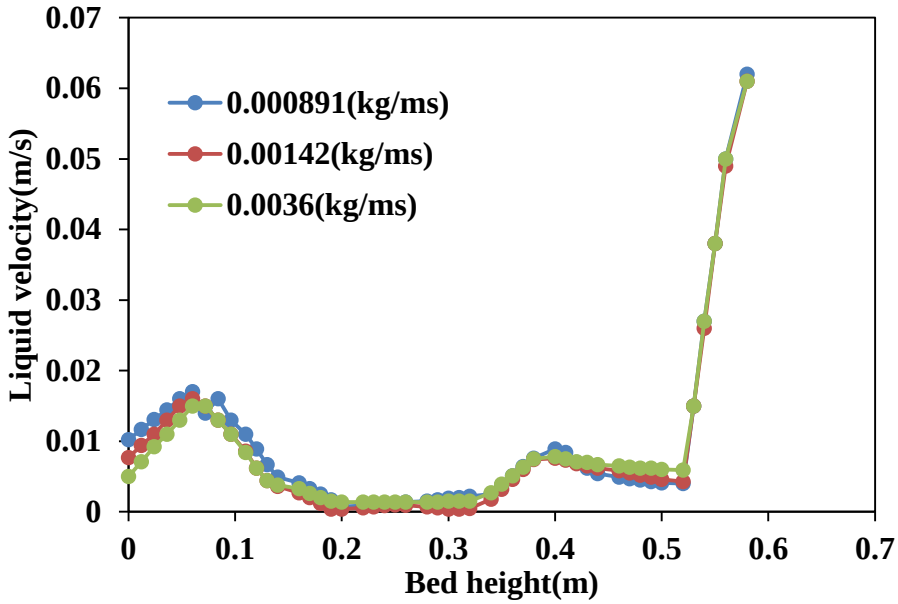

Fig. 4.36. Comparison of liquid velocity inside fluidized bed having different viscosity of liquid for 2D.

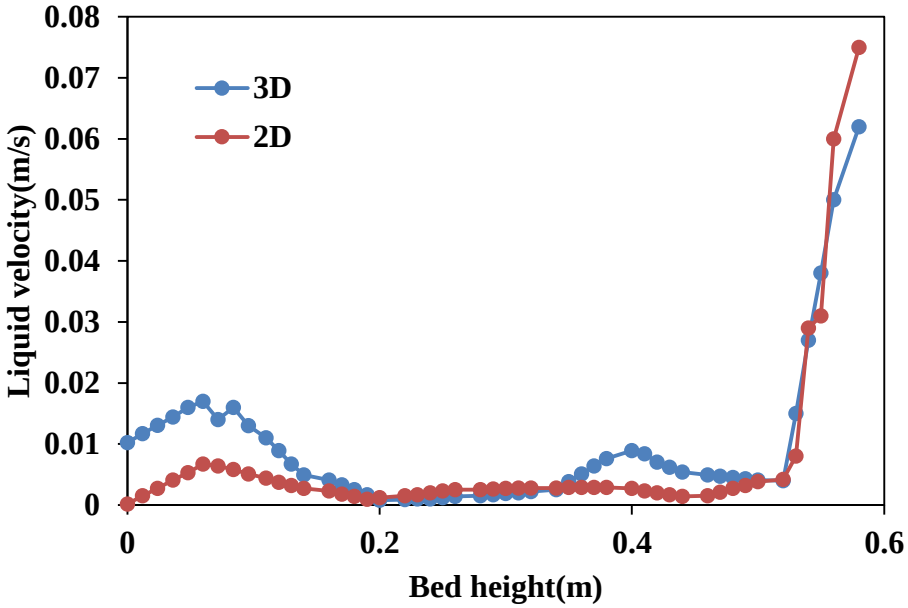

Fig. 4.37. Comparison of liquid velocity inside fluidized bed of liquid for 2D &3D.

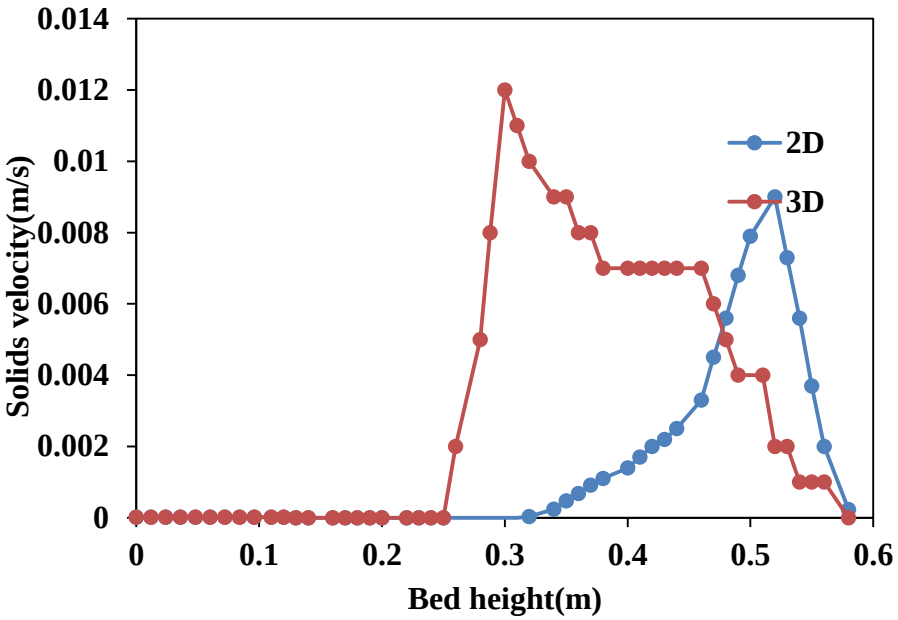

Fig. 4.38. Comparison of solids velocity inside fluidized bed with bed height under 2D &3D models

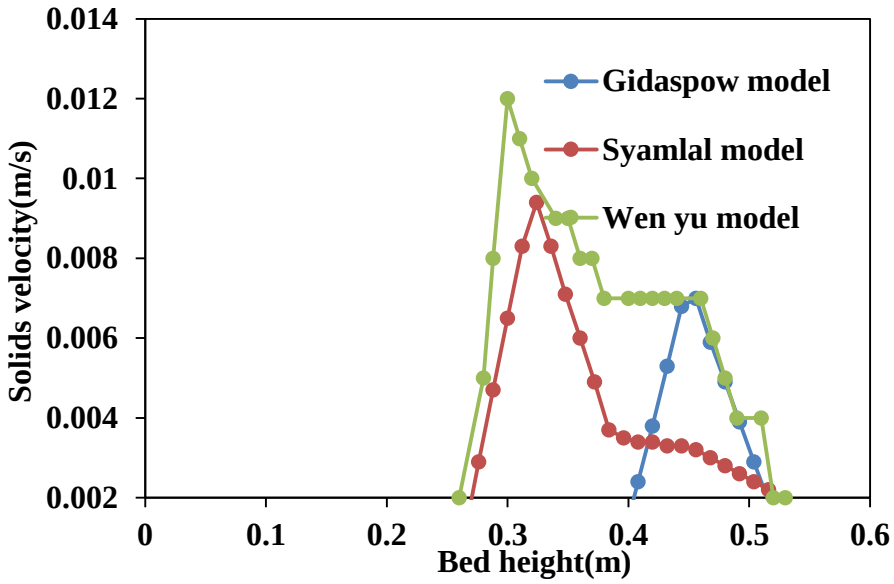

Fig. 4.39. Comparison of solids velocity inside fluidized bed with bed height under different drag models

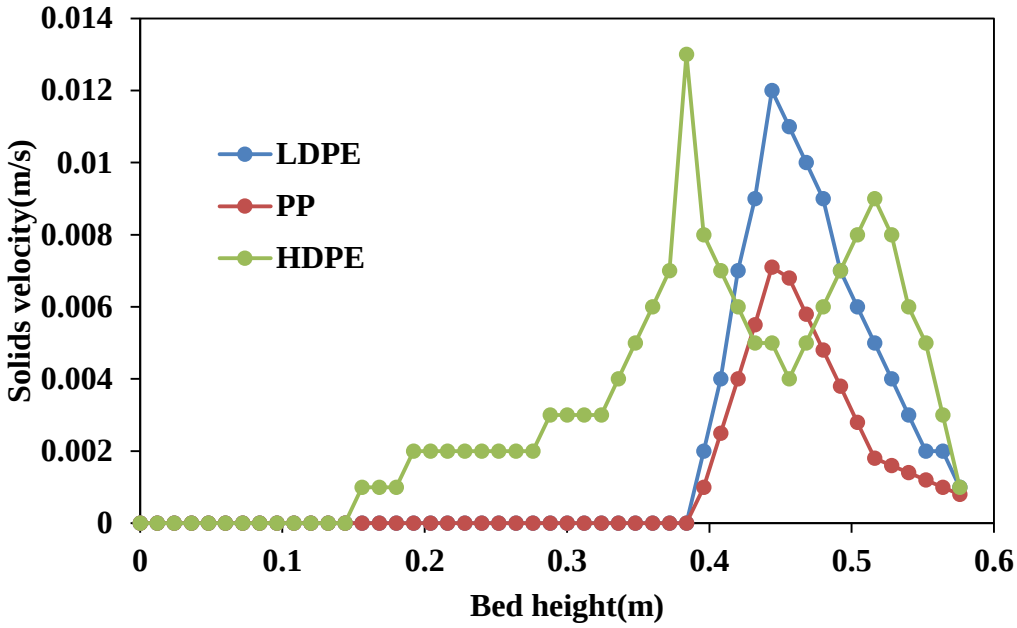

Fig 4.40 Comparison of solids velocity inside fluidized bed with bed height under different density of solids

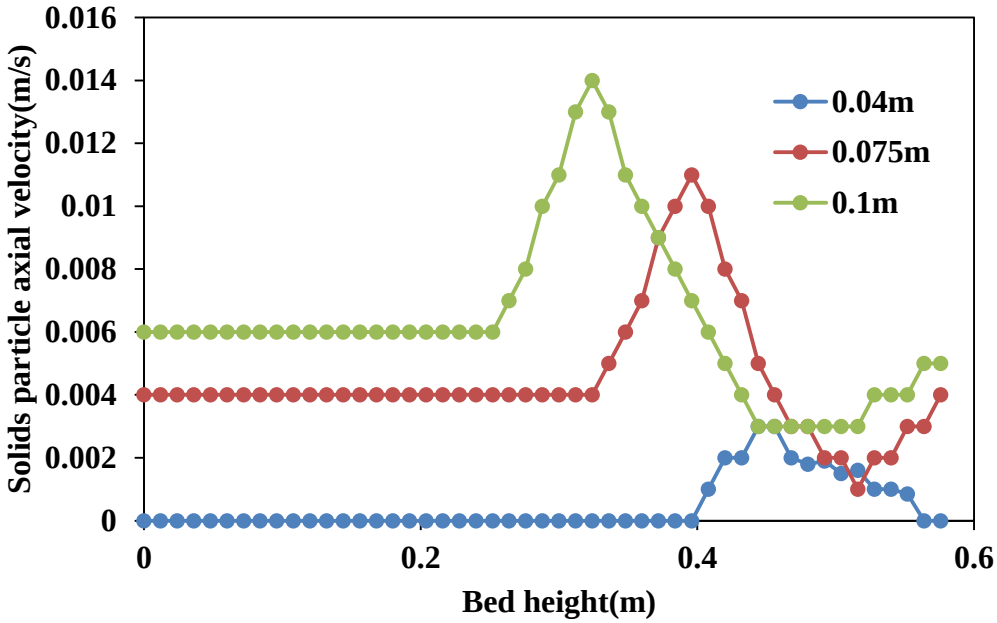

Fig 4.41 Comparison of solids velocity inside fluidized bed with bed height under different initial bed heights

From Fig. 4.37 indicated that the axial velocity in the 2D bed is less in magnitude and fluctuating type than in the 3D fluidized bed, as seen in the plot. This is owing to the bed's high level of discretization. Fig 4.39 shows comparison of solid velocity under different drag models. It is observed that wen-yu drag function give the better solids velocity profiles when compared to other two drag models. This is because wen-yu model is suitable for solid-liquid system. Fig 4.40 show the comparison of solids velocity profile under different density of solids along bed height. It is observed that higher density solids have more moving ability compared lower density of solids. It is because of buoyancy forces acting on the upward direction opposite to gravitational force. From fig.4.38, the solid particles are observed to be in to and fro motion on the plot, sometimes in the direction of liquid and solid flow and sometimes in the other way. The axial solid velocity is smaller in the bottom section of the fluidized section and increasing as we travel towards to the top of the bed, where it reaches maximum velocity, as shown in Fig. 4.41. This is due to greater liquid phase velocities with increasing bed height and decreased contact with the amount of solid particles. Solids at the bottom appear to have no motion.

4.1.2.7 Bed expansion:

The solid bed increases when the flow velocity exceeds the minimum fluidization velocity. With increasing fluid velocity, the expanded bed height gradually rises.

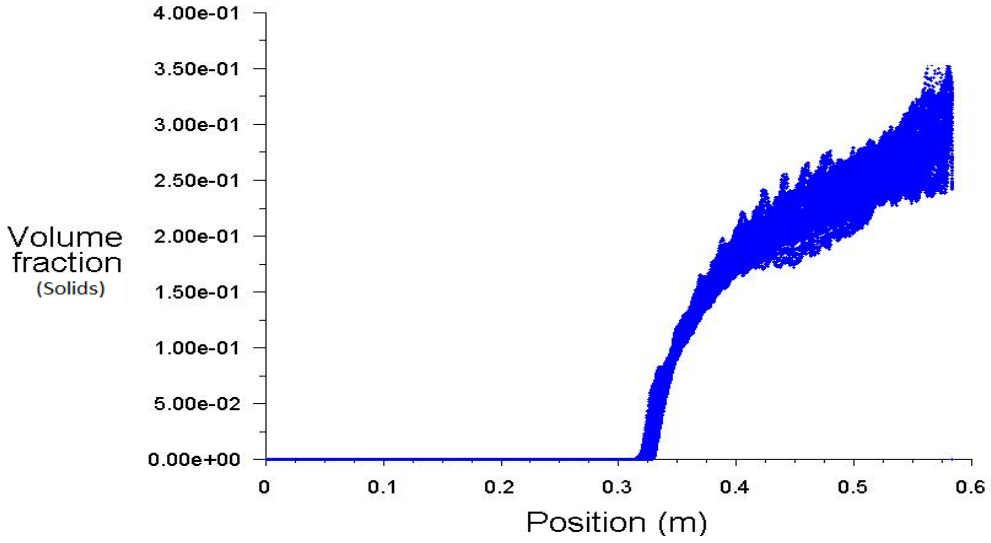

Fig. 4.42. XY plot of solid volume fraction

When liquid-solid inverse fluidization occurs, the bed expands as the liquid velocity (the main phase) increases to a large value, which is dependent on the relative velocity between the two phases. The XY plot of solid volume fraction w.r.t. axial direction from the base of the column is

used to determine the enlarged bed height in this study (as shown in Fig. 4.42). The height of the bed is defined as the point at which the solid volume fraction drops steeply to zero. The solid volume fraction in the bed (Fig. 4.43) shows that as the liquid velocity rises over the minimum fluidization velocity, the bed height rises steadily.

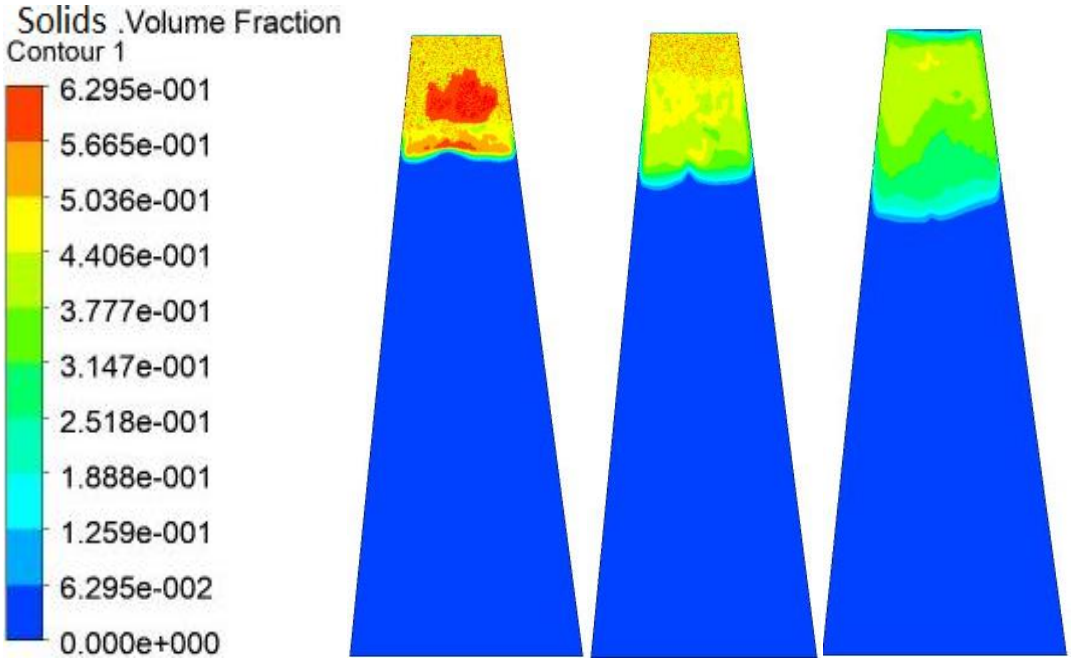

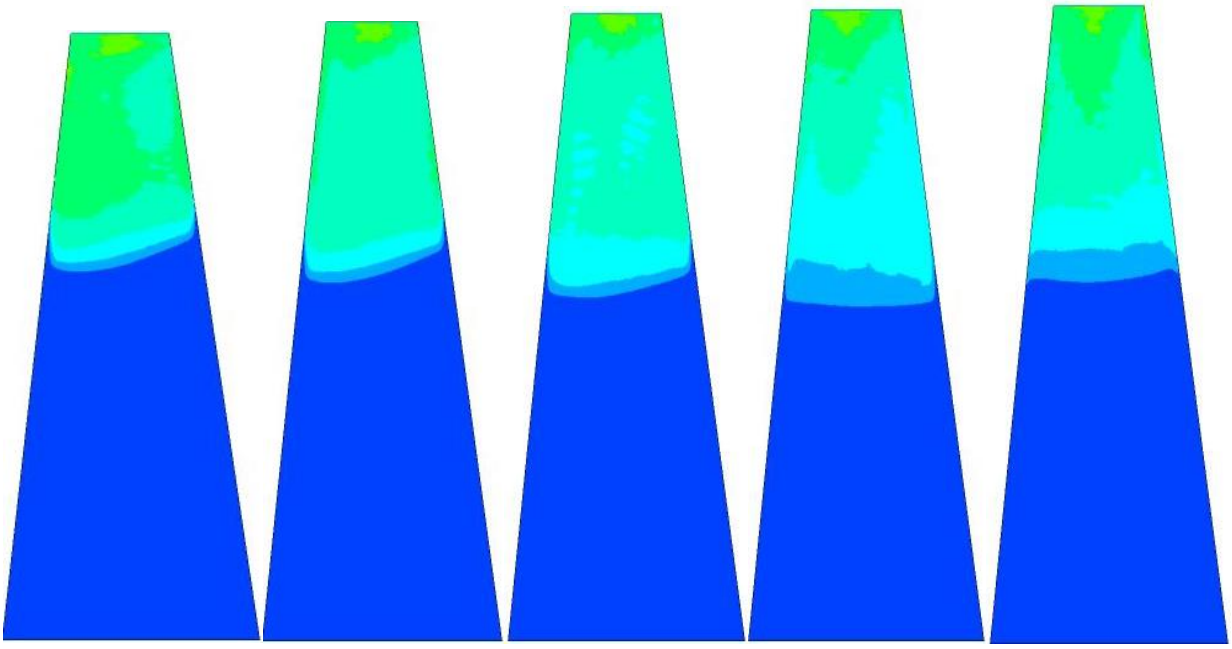

Fig. 4.43. Contour graphs of changes in solid volume fraction with variations in liquid velocity.

Fig. 4.44 indicated the profile of bed expansion of solid with liquid velocity at distinctive constant initial static bed heights. The plot shows that for a constant bed height, bed expansion increases as liquid velocity increases. Up to a modest level of liquid velocity, the bed expands more with more solids, while at a greater level of liquid velocity; the bed expands less with less solids same outcomes are provided by Nguyen et al (2011). Figure 4.45 present the data of a CFD simulation of bed expansion vs. liquid velocity for a fluidized bed with varying solid particle densities (i.e. 970 kg/m^3, 930 kg/ m^3 and 900 kg/m^3). It's obvious that the bed height rises as the density of the solid particles rises. Fig 4.46 presence the effect of bed expansion with liquid velocity under various conditions of liquid viscosity. It's obvious that the bed expansion rises for liquid viscosity with lower value this is due to the higher viscous nature in higher value of viscosity of liquid.

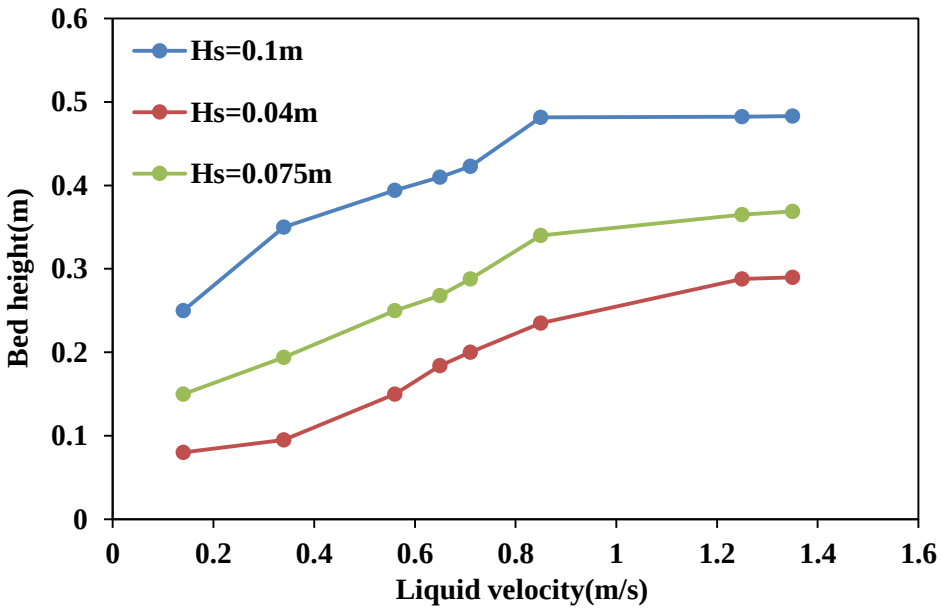

Fig. 4.44. CFD simulation outcomes of bed expansion performance of HDPE Polymer solids under different static bed heights in 3D fluidized bed at wen-yu drag model in 8 Deg angle bed.

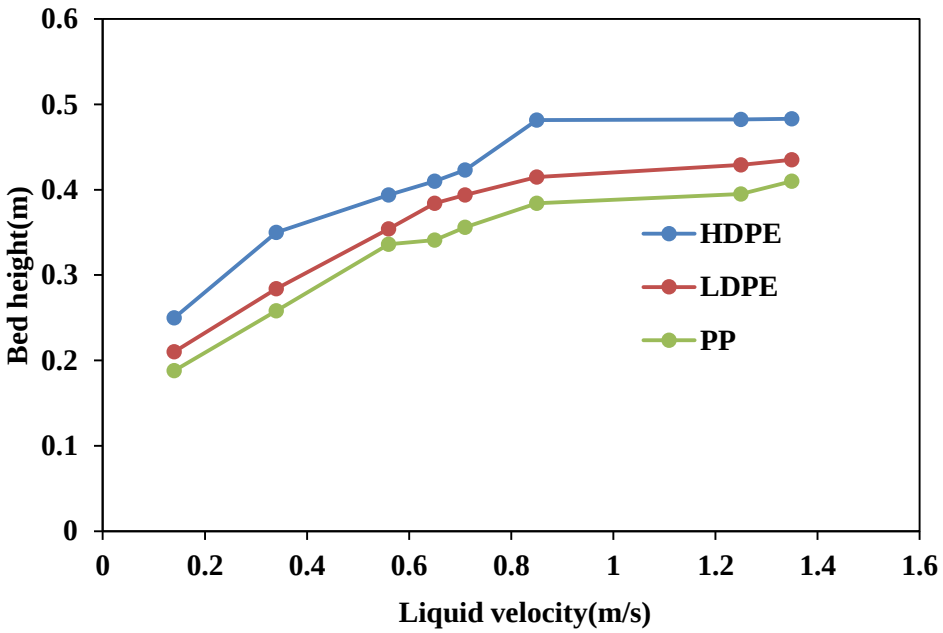

Fig. 4.45. CFD simulation outcomes of bed expansion performance under different density of polymer solids at initial bed height 0.1m in 3D fluidized bed at wen-yu drag model in 8^{o} angle bed.

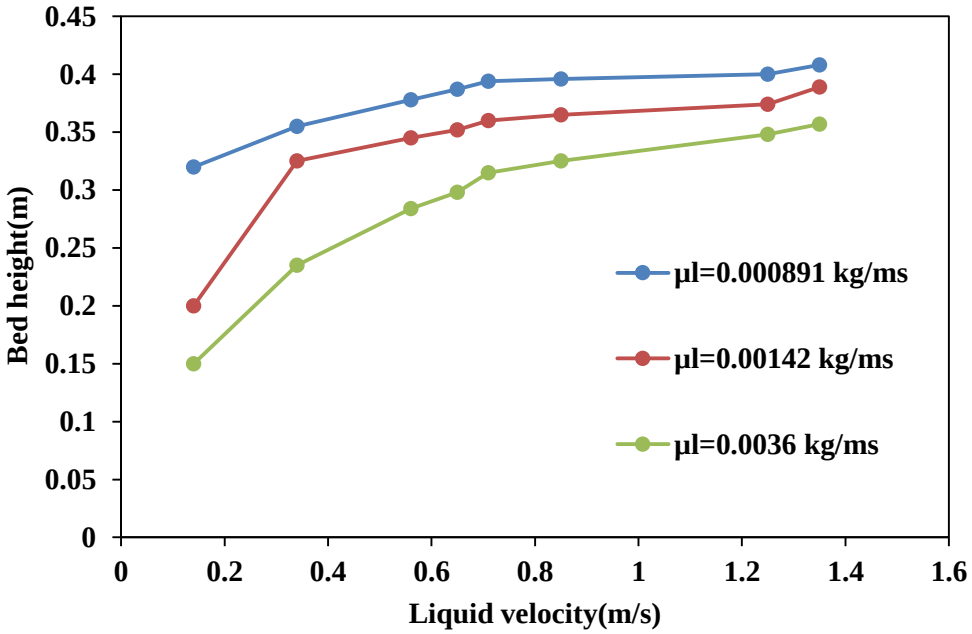

Fig. 4.46. CFD simulation result of bed expansion performance under different viscosity of liquid flow rates at initial bed height 0.0.075m in 3D fluidized bed at wen-yu drag model in 8 Deg angle bed.

4.1.2.8 Bed pressure drop:

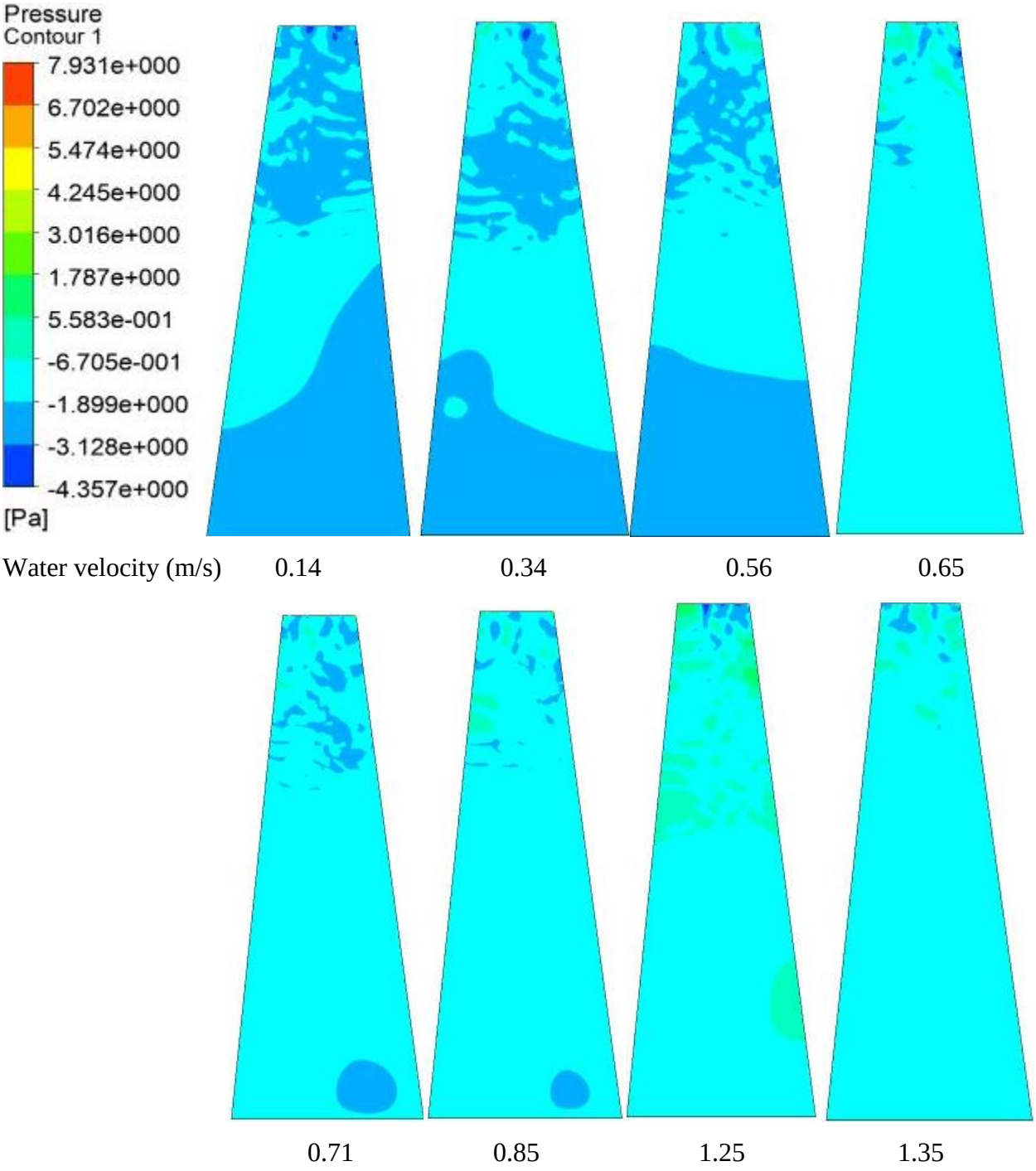

Fig. 4.47. Contour of bed pressure drop changing with liquid velocity in the inverse fluidized bed (2D).having at gidaspow drag model.

Fig. 4.47 indicated the contour of statics gauge pressure. The pressure is higher at the entrance and progressively decreases until it reaches zero at the outflow, as shown in the diagram.

Fig. 4.48 indicated the graph of bed pressure drop vs. superficial liquid velocity produced at various inlet values of liquid velocities after the minimum fluidization is obtained. The plot shows that when the surface liquid velocity is raised, the pressure drop increases under various drag models. From fig 4.49 it is find that the pressure drop raised with liquid velocity under different viscosity of liquid. For high viscosity of liquid the pressure drop is high compared to low viscosity of liquid. It is due to that higher resistance forces acting in higher viscosity nature liquids, for lift the particles with liquid we need force that purpose.

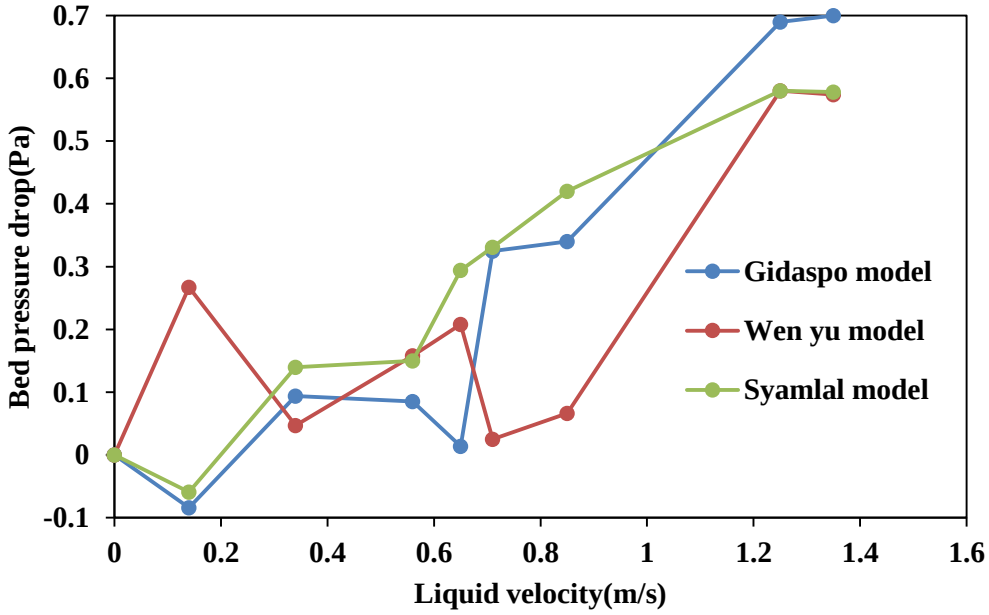

Fig. 4.48. Changing of bed pressure drop with liquid velocity profiles for 2D fluidized bed for HDPE solids under different drag models and at constant liquid viscosity 0.000891 kg/ms, HS = 0.1 m.

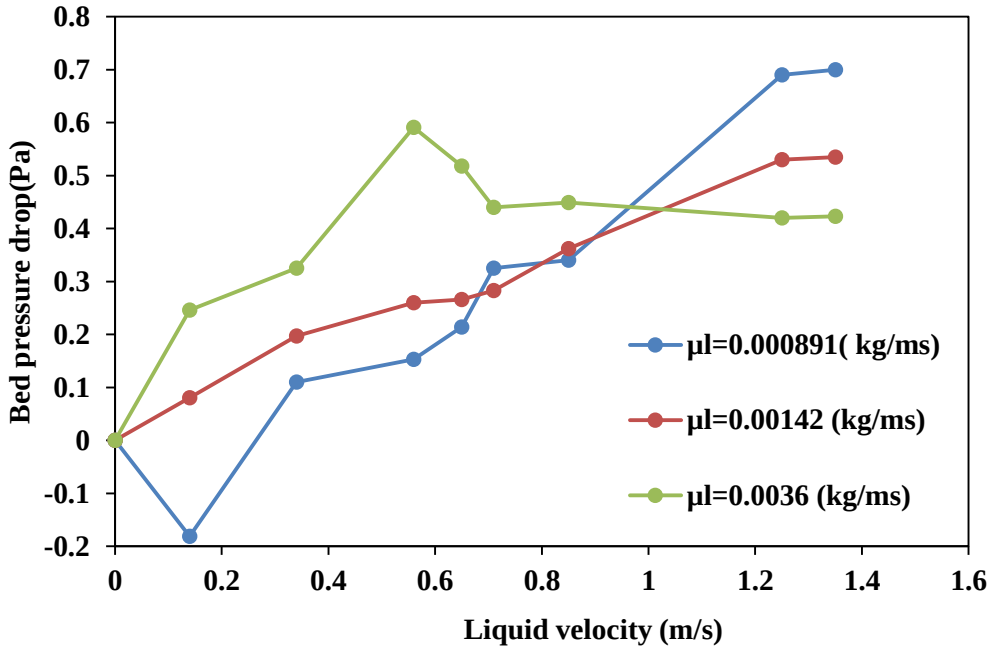

Fig. 4.49. Changing of bed pressure drop vs liquid velocity profiles for 2D fluidized bed for HDPE solids under different liquid viscosity at constant Gidaspow drag model, HS = 0.1 m.

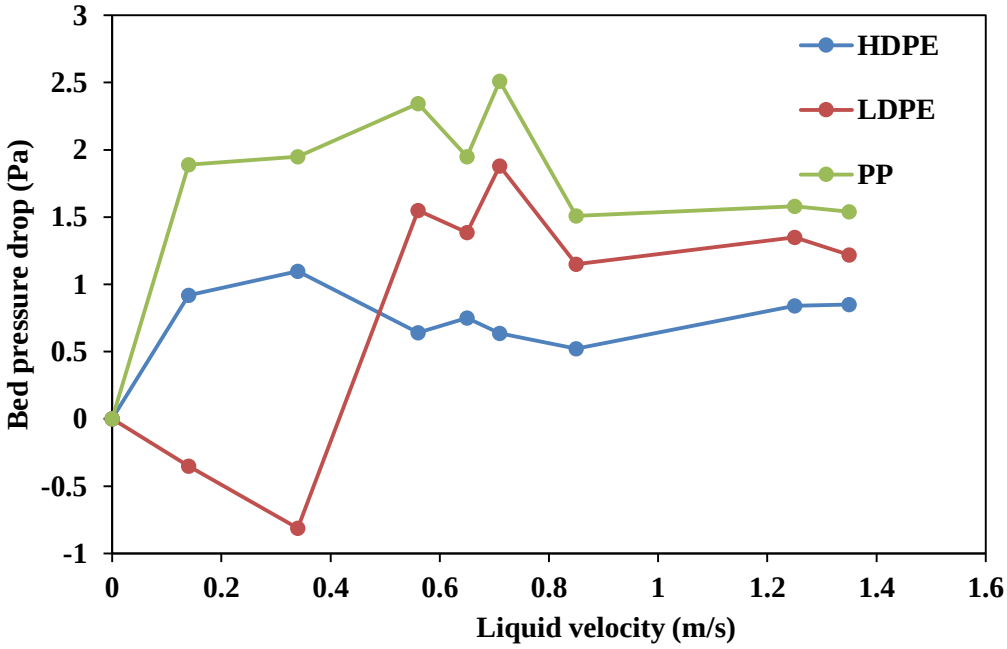

Fig. 4.50. Changing of bed pressure drop vs. liquid velocity profiles for 3D fluidized bed under different density of solids at constant liquid viscosity, wen-yu drag model and HS = 0.075 m.

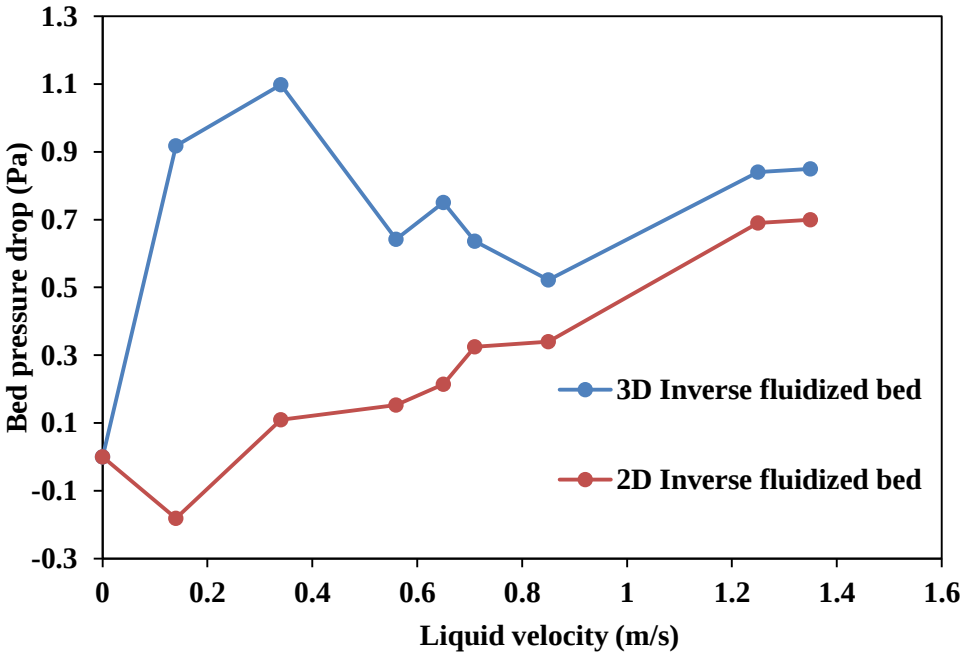

Fig. 4.51. Changing of bed pressure drop vs. liquid velocity profiles for HDPE Solids under different 2D&3D models at constant liquid viscosity, gidaspow drag model and HS = 0.1 m.

Fig. 4.50 indicated the changes of bed pressure drop vs. superficial liquid velocity for 2D fluidized bed having distributor of pore size 2 mm under different density of solid particles. The graphic shows that with constant bed height, the bed pressure increases as the liquid velocity increases. It is evident that for low density of solids has that higher pressure drop, it is due to the higher force required to lift the low density of solids from top to bottom of the bed. Fig. 4.40 indicated the comparison of bed pressure drop vs. superficial liquid velocity for constant static bed height 0.1 m. The figure demonstrates that the pressure drop of 3D fluidized bed with distributor finds higher with the 2D.of bed with distributor is seen in figure.

4.1.2.9 Solid granular temperature:

Since the solid phase is defined by the Kinetics Theory of Granular Flow (KTGF), the random element of solid particle velocities is represented by granular temperature (Goldhirsch, 2008). The temperature of the granules in a fluidized bed rises as the particle oscillation rises. For inlet liquid velocity 0.56 m/s and Hs 0.1m after quasi-steady is achieved, Fig. 4.52 displays the graphof axial

direction of the fluidized bed (i.e. height) vs. HDPE beads granular temperature.

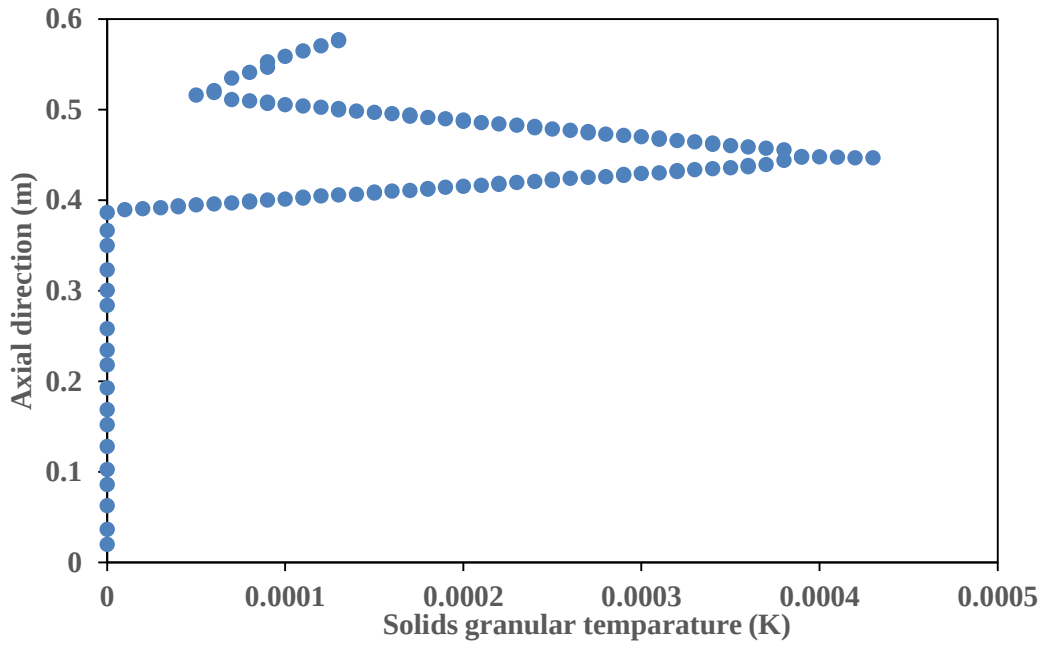

Fig. 4.52. Graph of fluidized bed axial direction vs. solid granular temperature of 3D inverse fluidized bed for liquid velocity 0.56 m/s and gidaspow model of initial height 0.1 m.

After quasi steady state is achieved, Fig. 4.53 depicts HDPE solids granular temperature vs. radial direction at various heights (0.1 m, 0.3 m, and 0.5 m) of the fluidized bed with superficial liquid velocity 0.56 m/s and gidaspow model at various physical simulation times. Granular temperature is evidently higher at the upper region of the inverse fluidized bed since a volume fraction of the solid particles is lower, causing the solid particle to oscillate, causing the temperature of the HDPE solids to rise. However, in the lower region, the volume percentage of solid particles is larger, reducing particle oscillation and resulting in a drop in granular temperature.

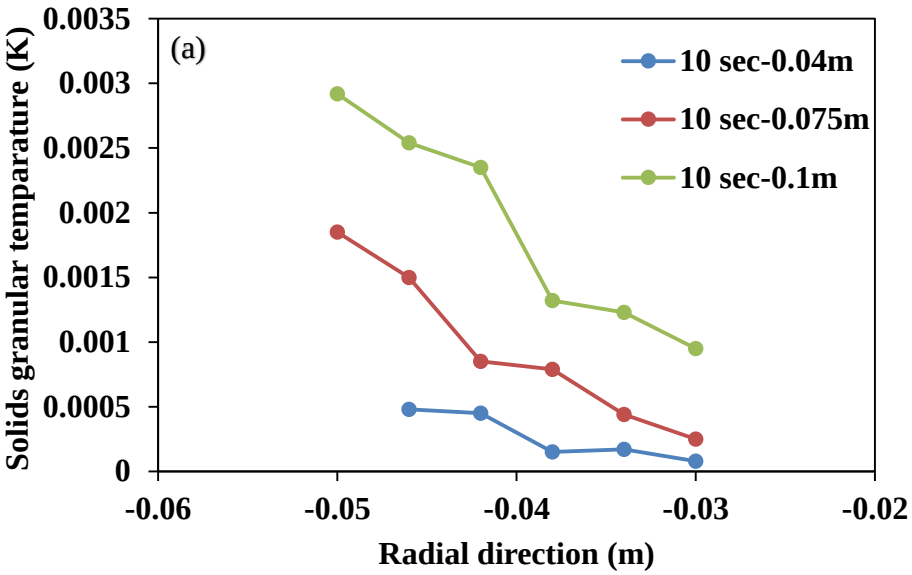
(a)
10 sec-0.04m
10 sec-0.075m
10 sec-0.1m
Solids granular temparature (K)
0.0035
0.003
0.0025
0.002
0.0015
0.001
0.0005
0
-0.06
-0.05
-0.04
-0.03
-0.02
Radial direction (m)

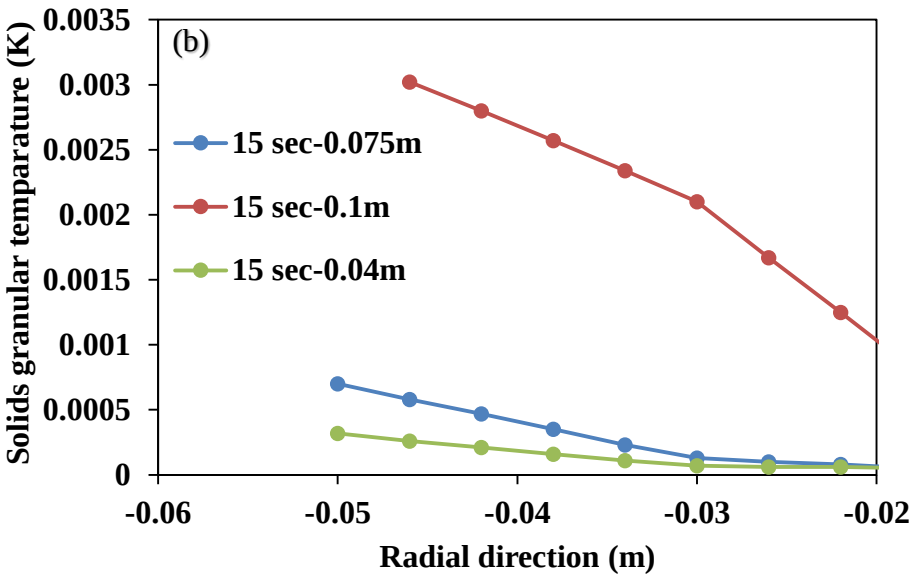
(b)
15 sec-0.075m
15 sec-0.1m
15 sec-0.04m
Solids granular temparature (K)
0.0035
0.003
0.0025
0.002
0.0015
0.001
0.0005
0
-0.06
-0.05
-0.04
-0.03
-0.02
Radial direction (m)

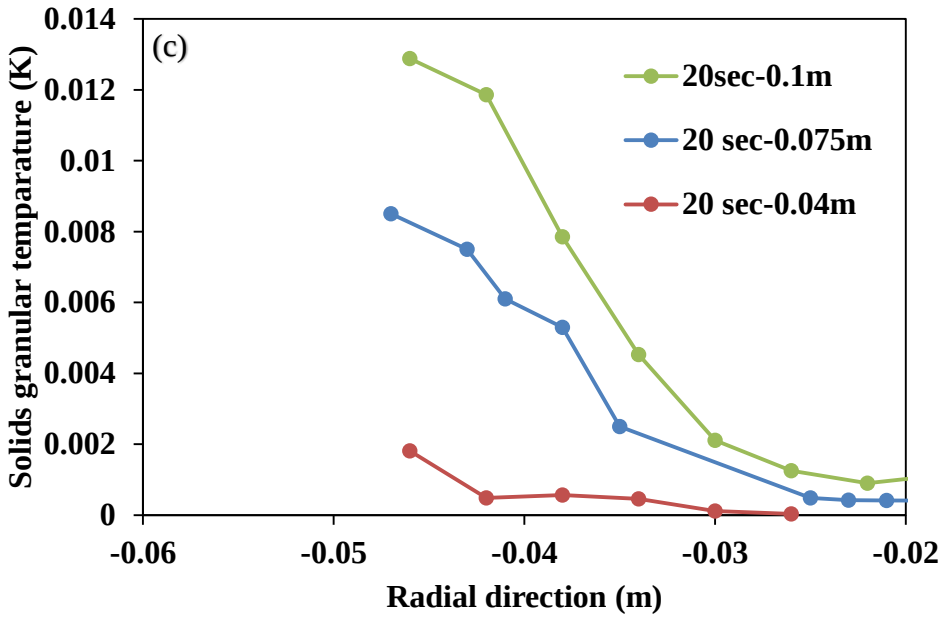
(c)
20sec-0.1m
20 sec-0.075m
20 sec-0.04m
Solids granular temparature (K)
0.014
0.012
0.01
0.008
0.006
0.004
0.002
0
-0.06
-0.05
-0.04
-0.03
-0.02
Radial direction (m)

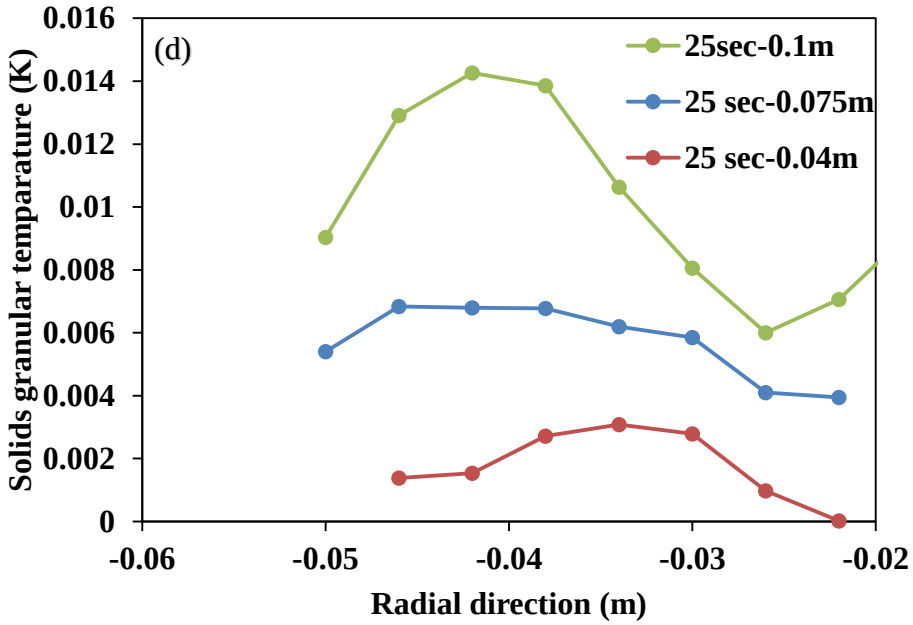
(d)
25sec-0.1m
25 sec-0.075m
25 sec-0.04m
Solids granular temparature (K)
0.016
0.014
0.012
0.01
0.008
0.006
0.004
0.002
0
-0.06
-0.05
-0.04
-0.03
-0.02
Radial direction (m)

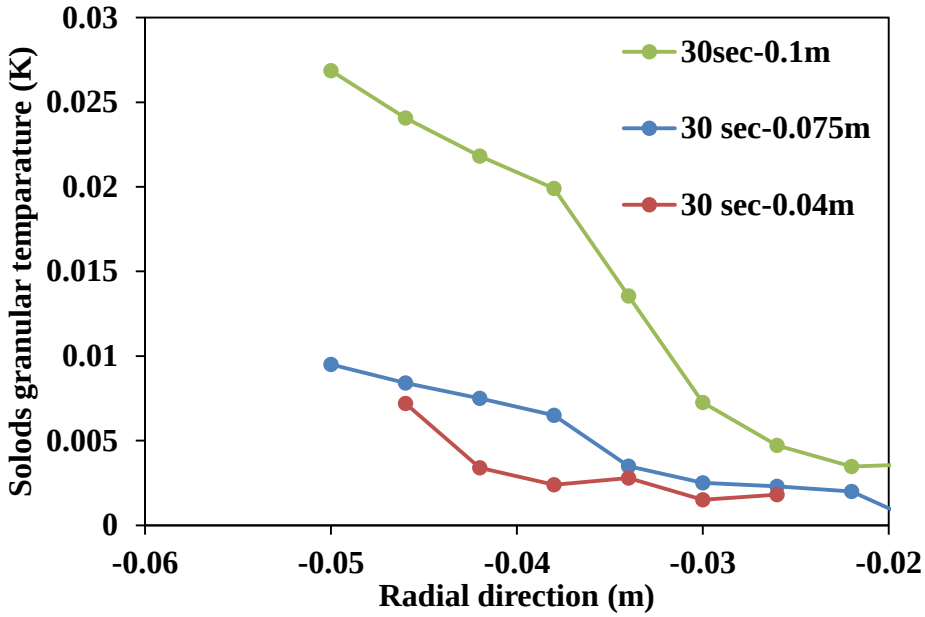

Fig. 4.53. Variability of solid granular temperature vs. radial direction of 3D fluidized bed heights of the fluidized under various initial bed heights and time intervals (a) 10, (b)15, (c)20,(d) 25 and (e)30 sec

4.2 RTD Studies by experimental and CFD results

RTD can be determined by performing tracer or stimulus-reaction tests, in which a tracer is injected promptly (a pulse input) at the channel of a stream framework, and its focus, *C (t)*, is estimated at the exit as an element of time. RTD investigation is commonly relevant to a stream framework with a one-channel stream where a tracer was injected; however, this limitation can be removed in the numerical simulation and the test for one-inlet, one-outlet stream framework by presenting a transporter liquid (water) with a stream rate. This decreases dead volumes inside the system and adequately makes the stream framework a one-bay, one-outlet framework as required, with essentially no stream aggravation. The exit concentration of the tracer, and solution of a blender, was estimated utilizing 0.0005N NaOH; the experiment of the tracer RTD was studied at various angles of the tapered inverse fluidized bed. The bed was patched with solids up to some height from the top with water flowing continuously from the top. After stable fluidization was reached, the (5ml) propionic tracer was injected into the bed within a short period. At the same time, the outlet mixer of water and tracer were collected in separate vessels at every 2 min time intervals.

4.2.1 Tracer

The residence time distribution (RTD) for the liquid (oxalic acid) can be determined easily and directly by the so-called "stimulus-response" technique. With this method, the RTD is experimentally obtained by injecting an inert liquid, called a tracer, into the inlet stream of liquid at time t = 0, and then measuring the tracer concentration in the effluent stream of the vessel as a function of time. According to Levenspiel (1972), "any material that can be detected and which does not disturb the flow pattern in the vessel can be used as tracer". Moreover, the tracer has to meet the following general characteristics:

1. It should be "miscible" in all proportions, and have physical properties similar to all liquids within the vessel under investigation. If the experiment involves more than one phase, then the tracer should stay in the phase of interest.
2. It has to be nonreactive and perfectly detectable even in very small concentrations.
3. The detection device and the tracer itself have to be unquestionably inexpensive.

The below described equations [Octave Levenspiel] were used to find the liquid tracer desired values.

The tracer concentration of the sample (*C(t)*) at any time (*t*) and mean residence time are calculated as follows [21]:

$$C(t) = \frac{M_{tracer}}{M_{total}} \tag{4.14}$$

$$E(t) = \frac{C(t)}{Area\ under\ the\ C(t)\ curve} \tag{4.15}$$

$$Mean\ residance\ time\ (\bar{t}) = \frac{\sum C_i t_i}{\sum C_i} \tag{4.16}$$

$$Varience\ (\sigma^2) = \frac{\sum C_i t_i^{\,2}}{\sum C_i} - (\bar{t})^2 \tag{4.17}$$

$$\sigma_\theta^2 = \frac{\sigma^2}{(\bar{t})^2} \tag{4.18}$$

For closed vessel the relation between the variance to D/UL -

$$\sigma_\theta^2 = 2\frac{D}{UL} - 2\left(\frac{D}{UL}\right)^2\left[1 - e^{-\left(\frac{UL}{D}\right)}\right] \tag{4.19}$$

Where *D*, *U* and *L* are the dispersion coefficient (m^2/s) of tracer, liquid velocity (m/s) and length (m) of tapered inverse fluidized bed, respectively.

4.2.2 Experimental details

The experiments are performed in a tapered inverse column that was made by using an acrylic sheet to measure the results in the reactor and indicated in Figure 4.54. Two different types of the tapered column angle (φ) was used and the geometrical dimensions are listed in Table 1. In the experiments, the three different density of solid materials (i.e., high-density polyethene (HDPE), polypropylene (PP) and beads with a density of 970, 930 and 900 kg/m^3, respectively), the propionic acid and water were used as a solid, tracer and liquid media, respectively. Water was continuously flowing into the fluidized bed while some amount of solid particles was kept in the bed. The bed materials were fluidized by a downward flow of water. To maintain a uniform flow of liquid and stop the escape of particles, distributor plates were installed at the top and bottom of the column and the liquid flow through these openings was controlled by valves. Water was pumped through a pipe connected with a liquid rotameter by a 1 horsepower motor pump to the top of the column. One small tap was mounted above the liquid distributor to inject the tracer. The physical properties of solid materials and operating conditions used in experiments also shown in Table 4.5.Three specific time indicators of liquid tracer within each angle of bed were of particular interest: residence time distribution, E (t), mean residence time, dispersion coefficient, and recirculation time, TR. Figures from fig.4.55 show concentration-time data obtained from the RTD experiments. From the data of a tracer concentration-time curves for both different angle of beds, nearly all the desired system parameters can be obtained. The design expert was utilized to investigate the predicted mean residence time distribution. τ_m =6.04

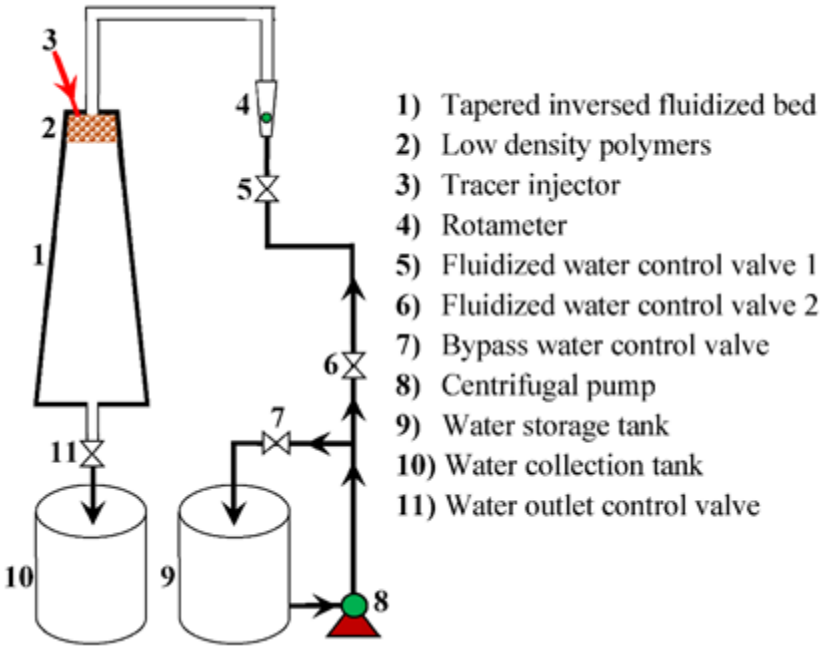

Figure 4.54: Schematic diagram of the tapered inverse fluidized bed.

Table 4.5: Geometrical dimensions, operating conditions, and physical properties of the liquid and solid phase.

Description	Value
Specification of tapered fluidized bed	
Column height (m)	0.59 and 0.59
Top diameter (m)	0.09 and 0.075
Bottom diameter (m)	0.25 and 0.22
Tapered angle, φ (^{o})	8 and 6.8
Solid-phase	
HDPE density (kg/m^3)	970
PP density (kg/m^3)	930
Beads density (kg/m^3)	900
HDPE diameter (m)	0.02
PP diameter (m)	0.025
Beads diameter (m)	0.035
Mass of solid, m_s (kg)	0.05; 0.08; 0.1
Initial bed height (m)	0.03; 0.04; 0.053
Liquid-phase	
Density (kg/m^3)	1000
Viscosity (Pas)	0.001
Liquid velocity, U (m/s)	0.133 - 0.341

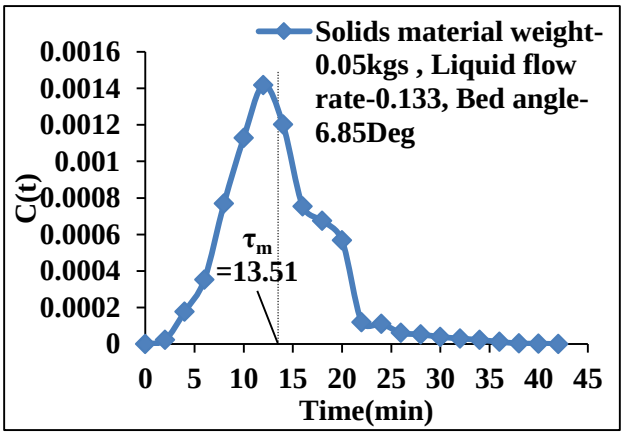

C (t) curve of experiment for HDPE

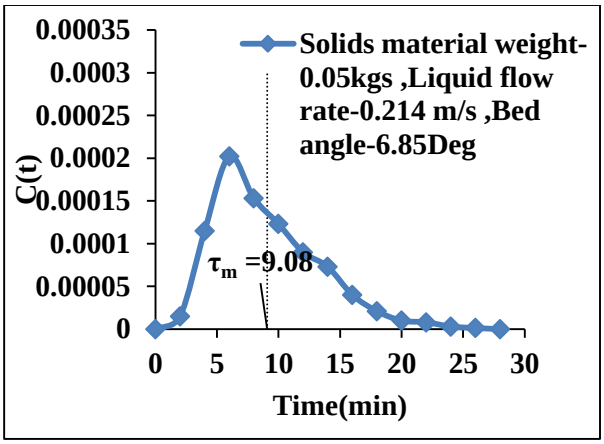

C (t) curve of experiment for HDPE

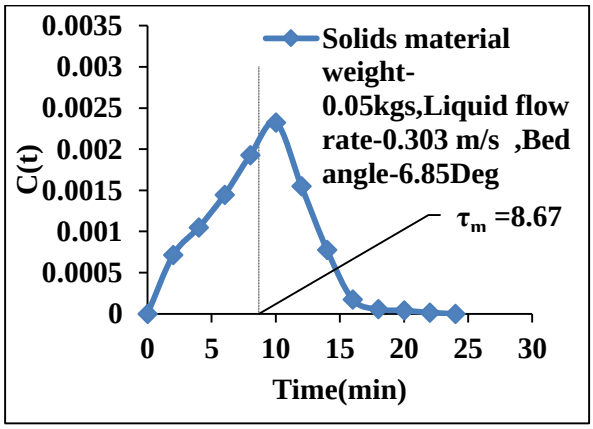

C (t) curve of experiment for HDPE

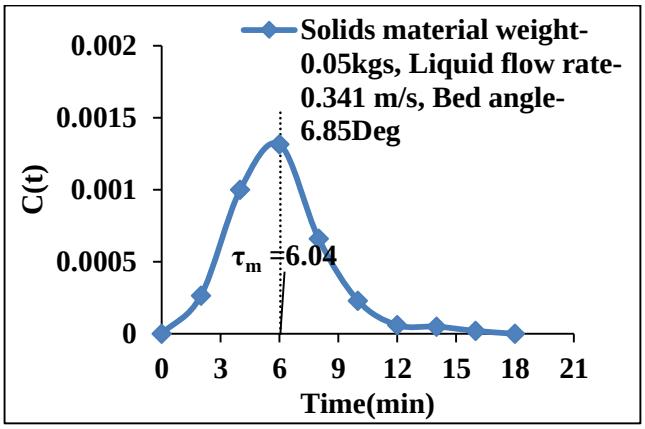

C (t) curve of experiment for HDPE

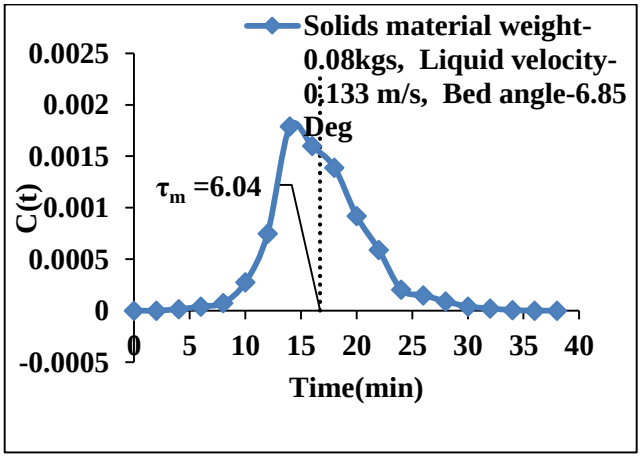

C (t) curve of experiment for HDPE

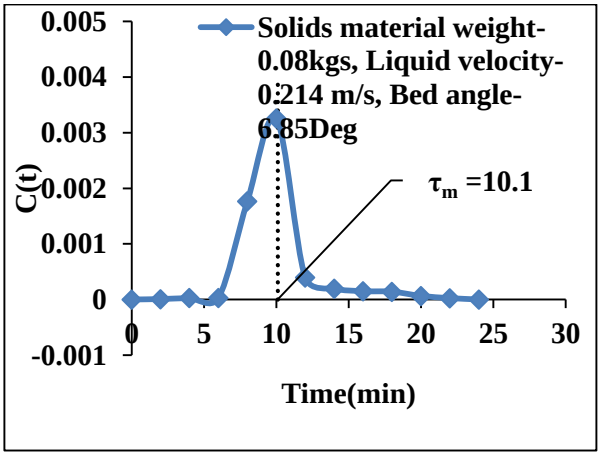

C (t) curve of experiment for HDPE

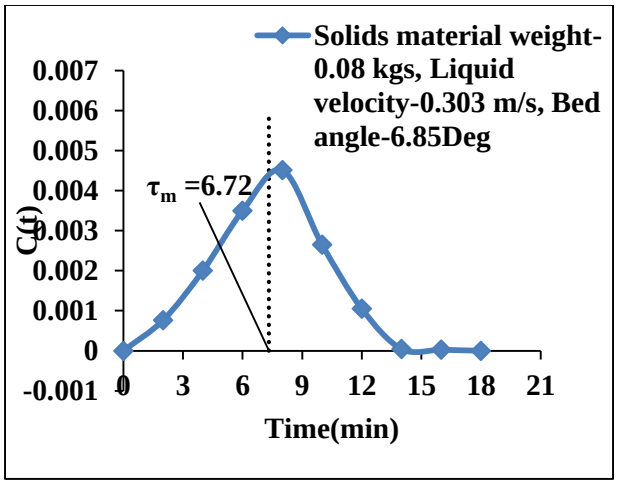

C (t) curve of experiment for HDPE

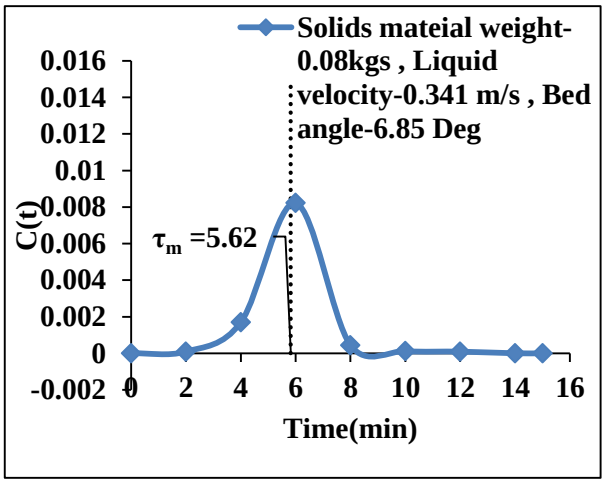

C (t) curve of experiment for HDPE

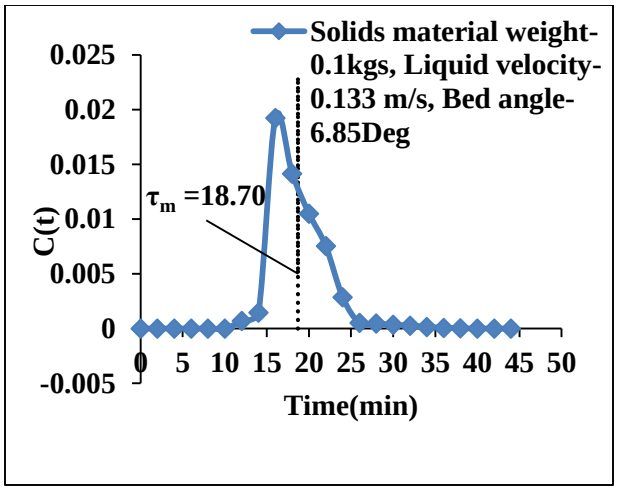

C (t) curve of experiment for HDPE

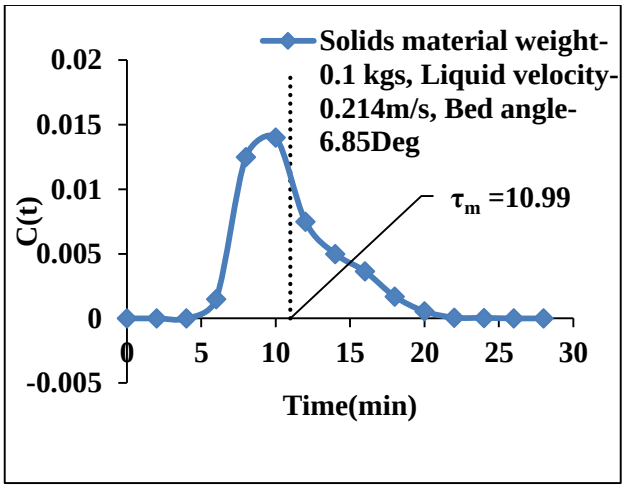

C (t) curve of experiment for HDPE

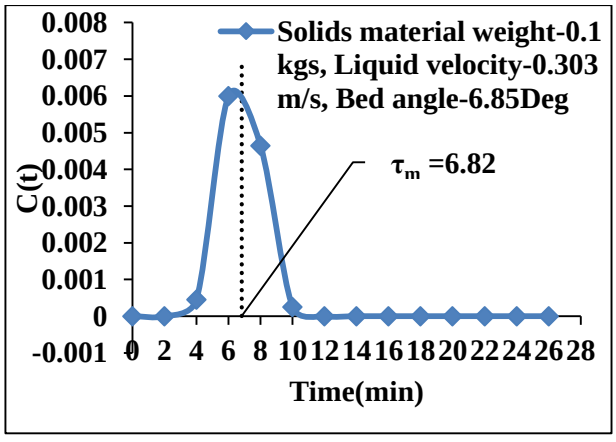

C (t) curve of experiment for HDPE

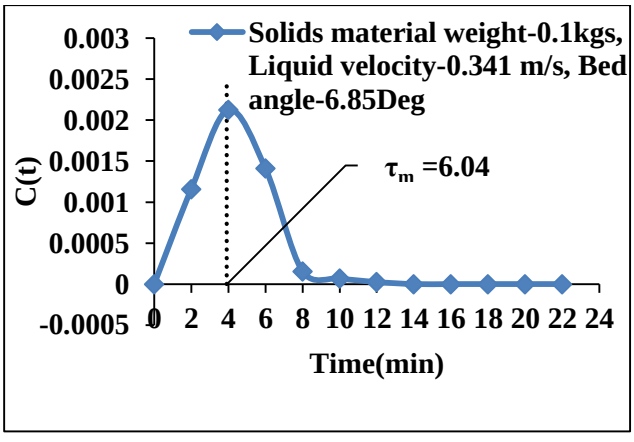

C (t) curve of experiment for HDPE

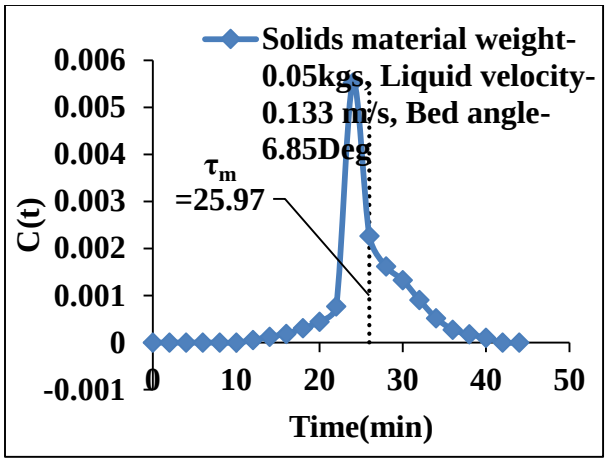

C (t) curve of experiment for Beads

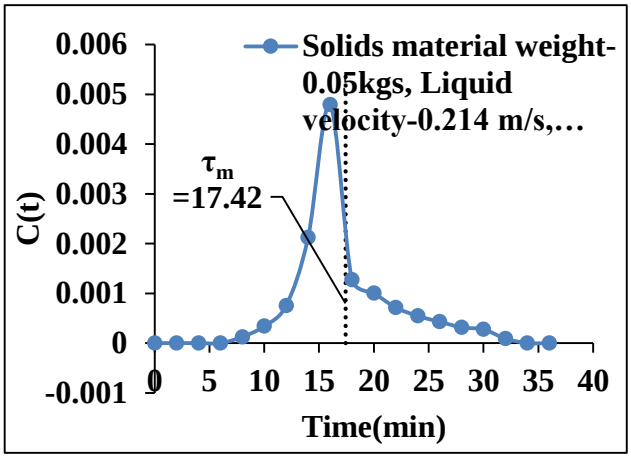

C (t) curve of experiment for Beads

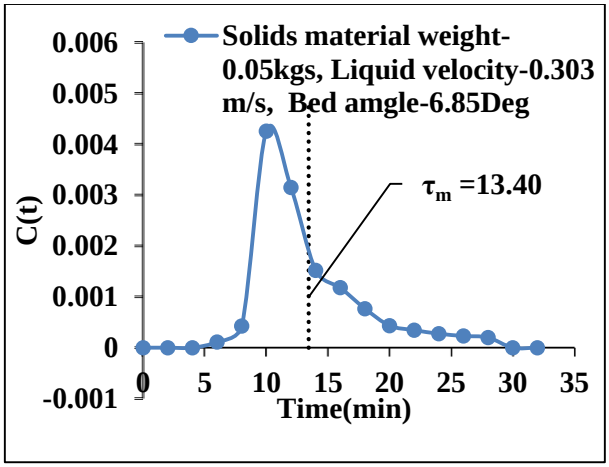

C (t) curve of experiment for Beads

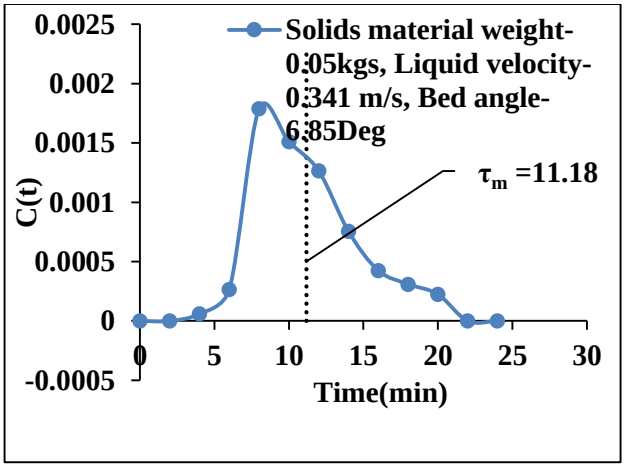

C (t) curve of experiment for Beads

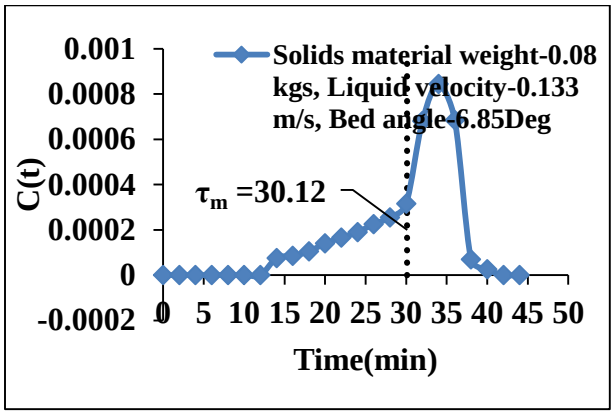

C (t) curve of experiment for Beads

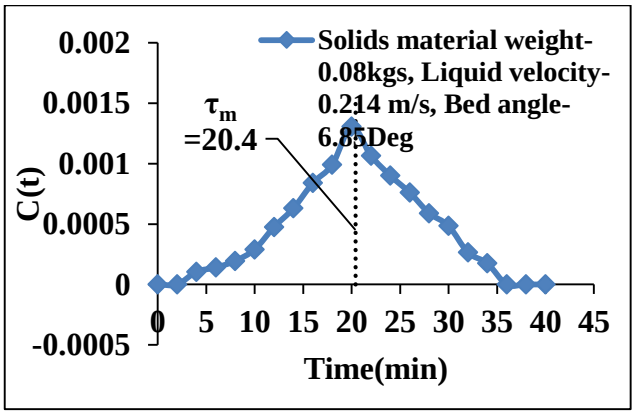

C (t) curve of experiment for Beads

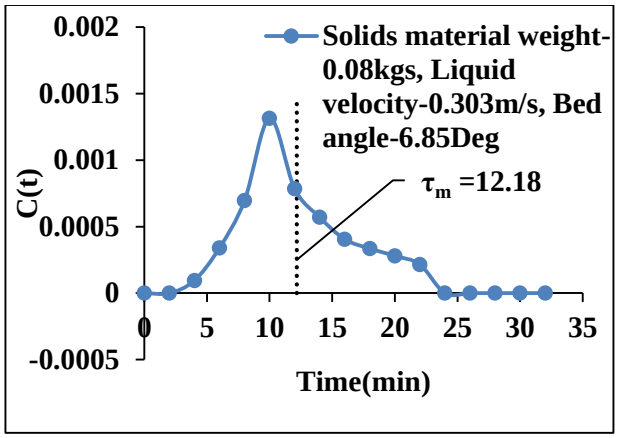

C (t) curve of experiment for Beads

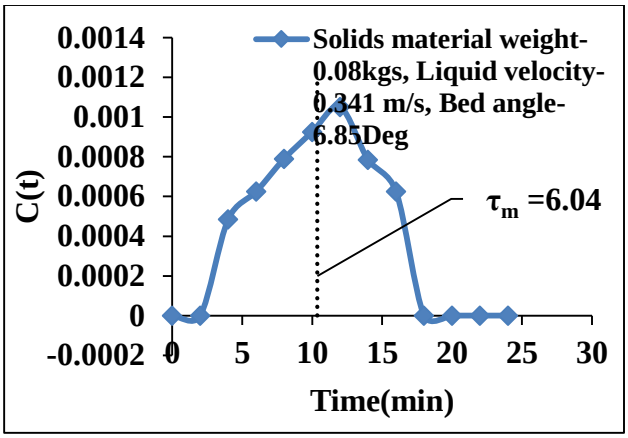

C (t) curve of experiment for Beads

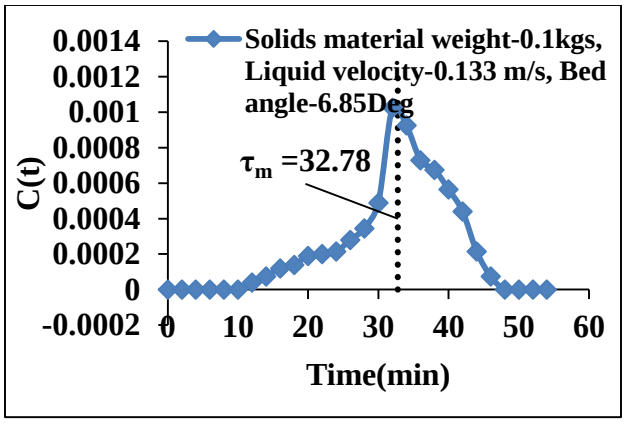

C (t) curve of experiment for Beads

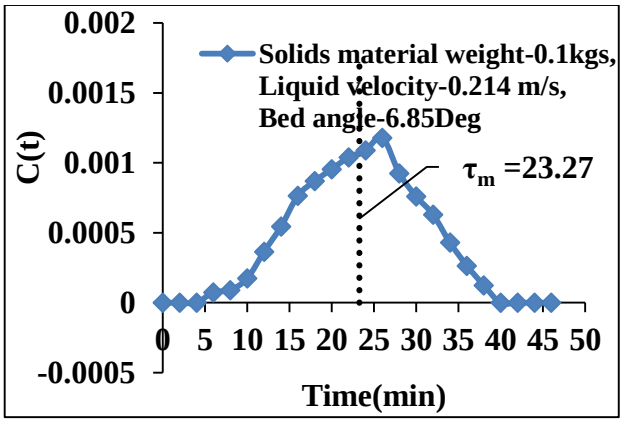

C (t) curve of experiment for Beads

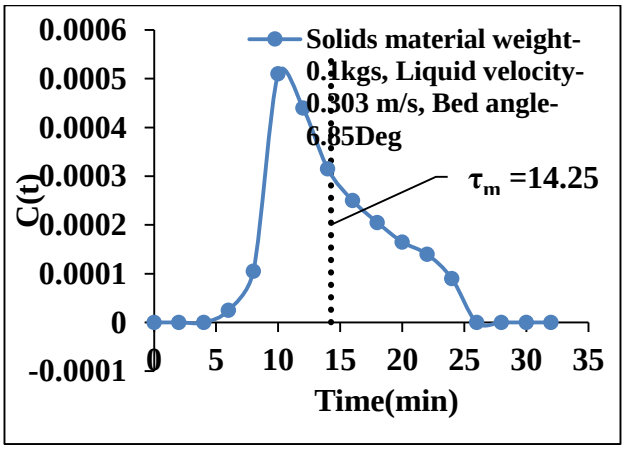

C (t) curve of experiment for Beads

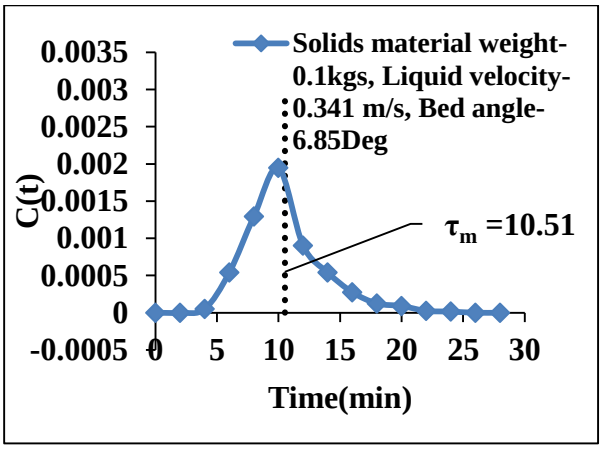

C (t) curve of experiment for Beads

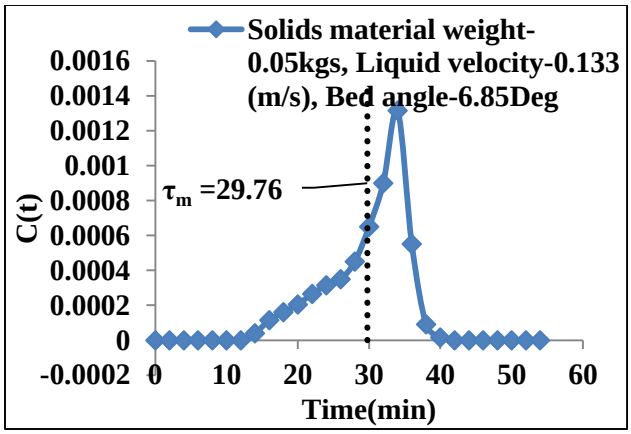

C (t) curve of experiment for PP

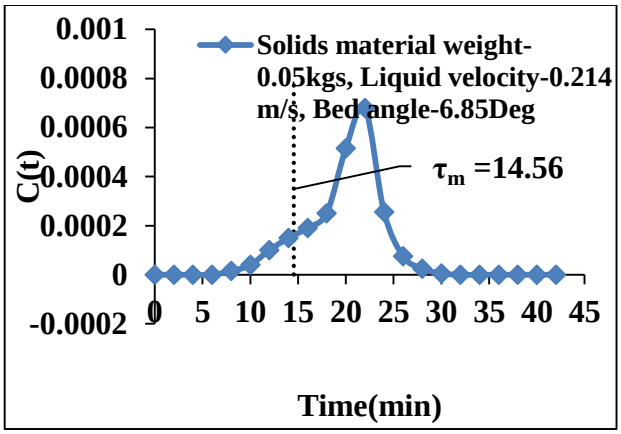

C (t) curve of experiment for PP

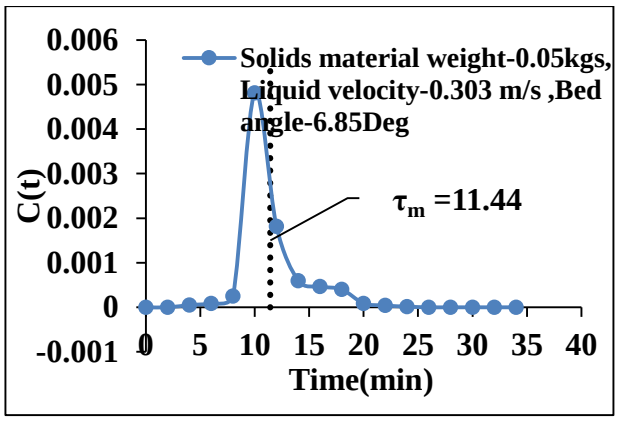

C (t) curve of experiment for PP

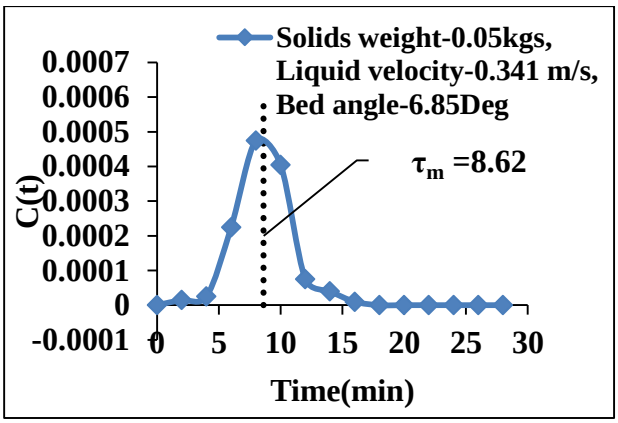

C (t) curve of experiment for PP

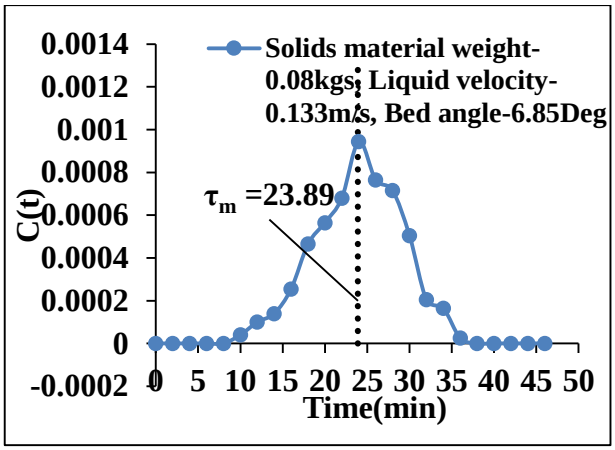

C (t) curve of experiment for PP

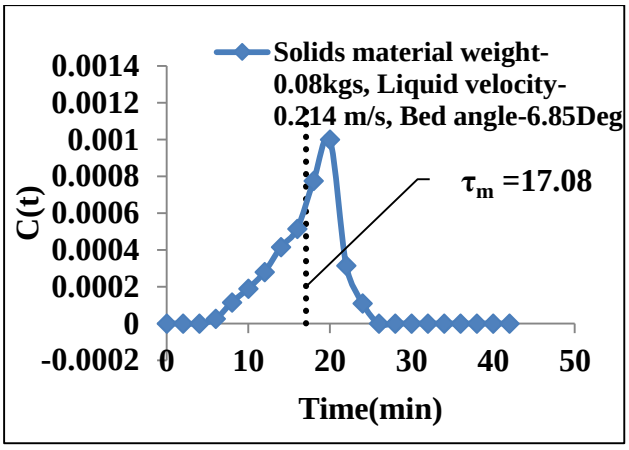

C (t) curve of experiment for PP

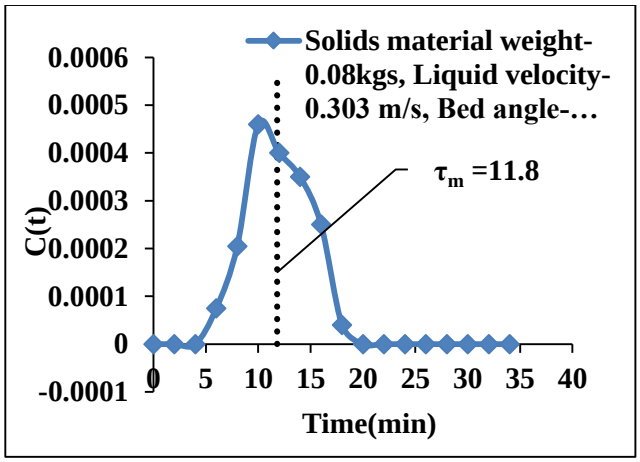

C (t) curve of experiment for PP

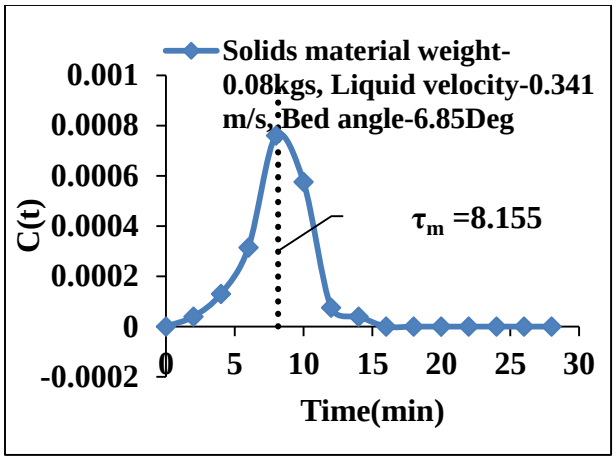

C (t) curve of experiment for PP

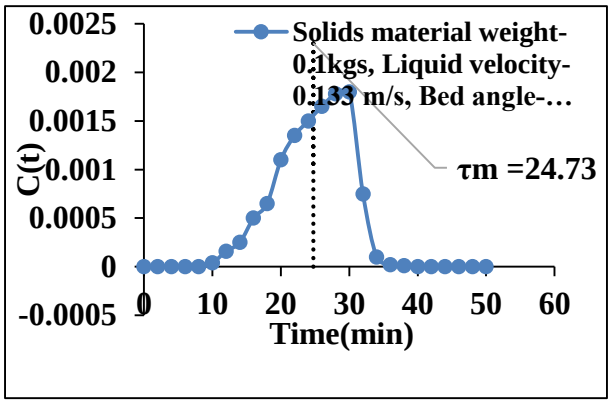

C (t) curve of experiment for PP

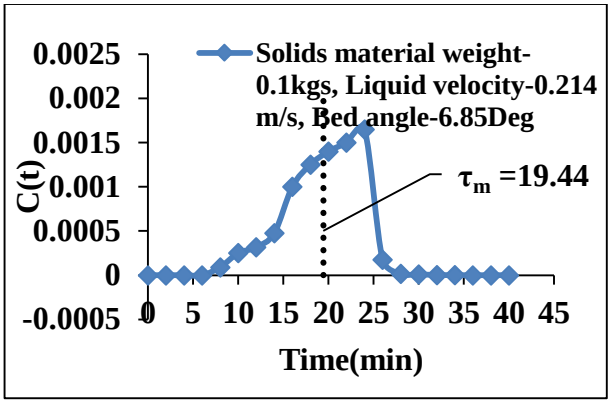

C (t) curve of experiment for PP

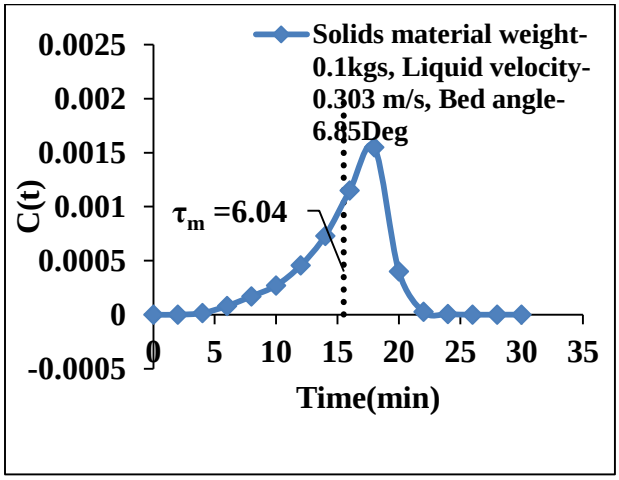

C (t) curve of experiment for PP

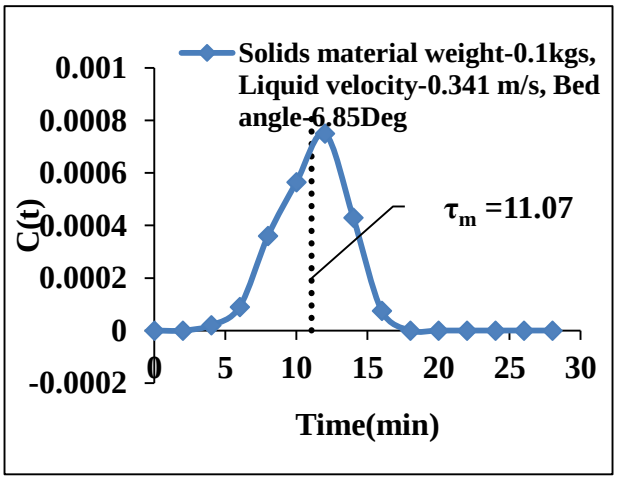

C (t) curve of experiment for PP

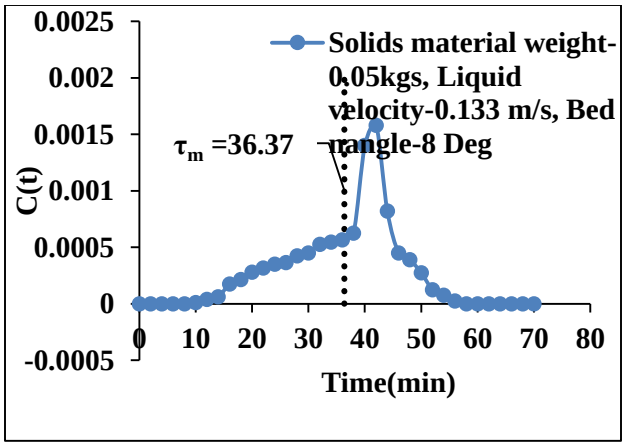

C (t) curve of experiment for HDPE

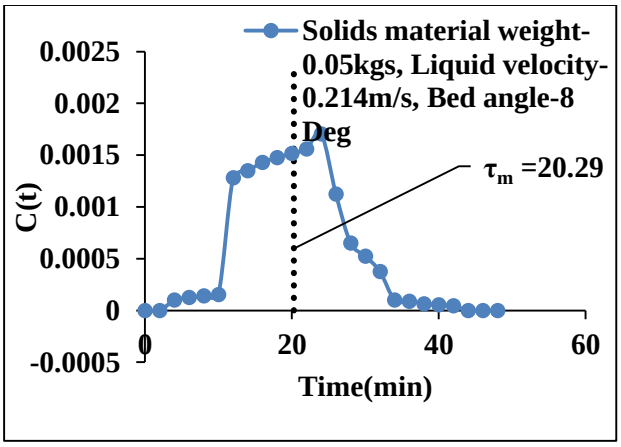

C (t) curve of experiment for HDPE

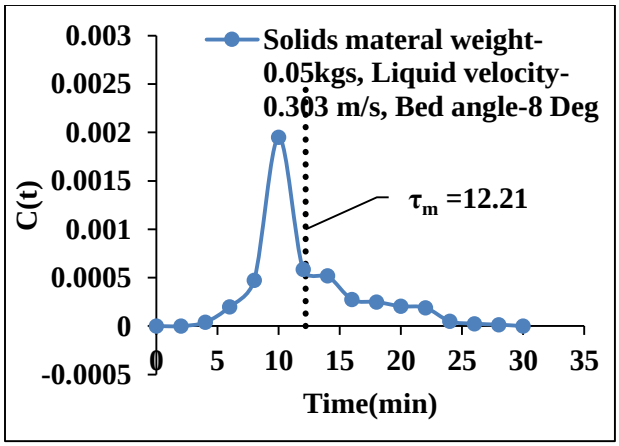

C (t) curve of experiment for HDPE

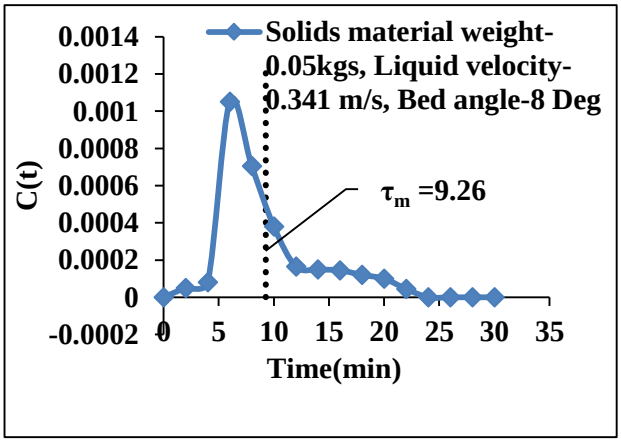

C (t) curve of experiment for HDPE

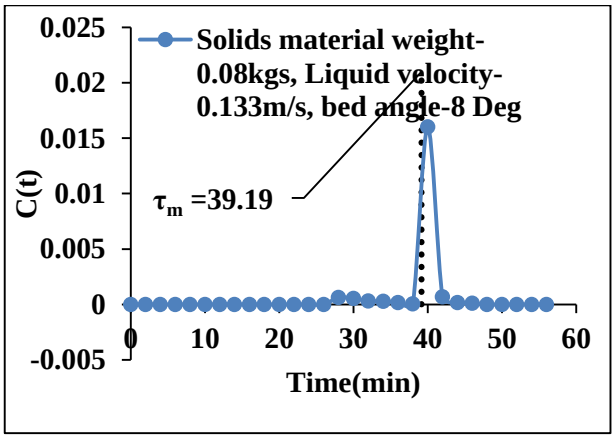

C (t) curve of experiment for HDPE

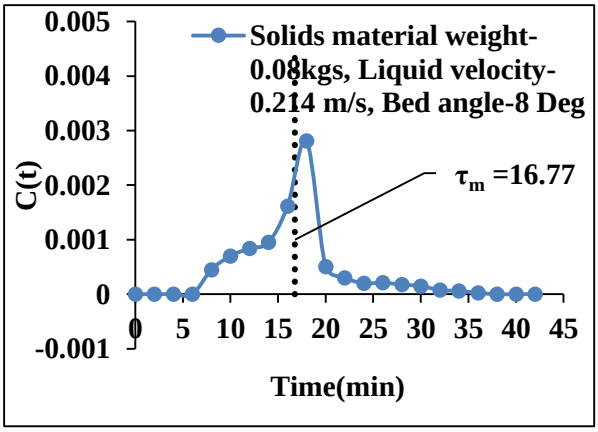

C (t) curve of experiment for HDPE

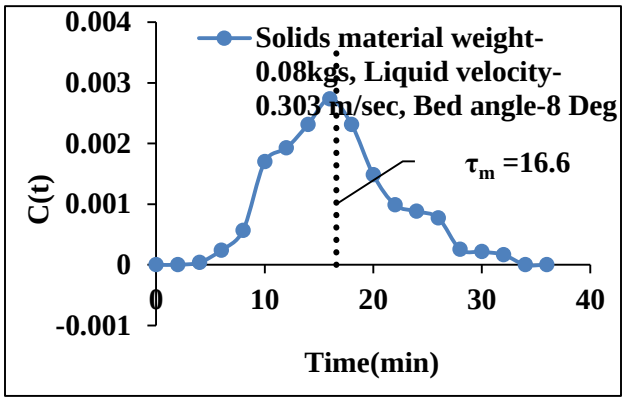

C (t) curve of experiment for HDPE

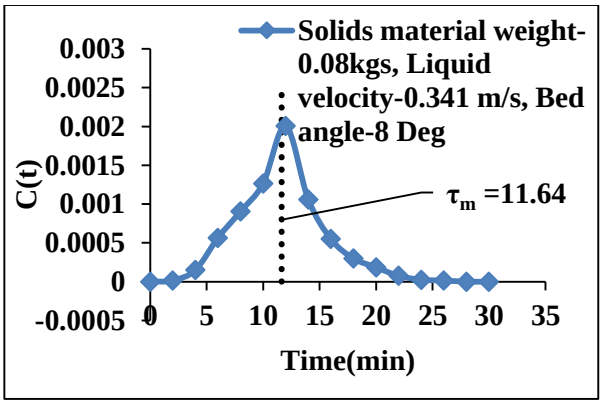

C (t) curve of experiment for HDPE

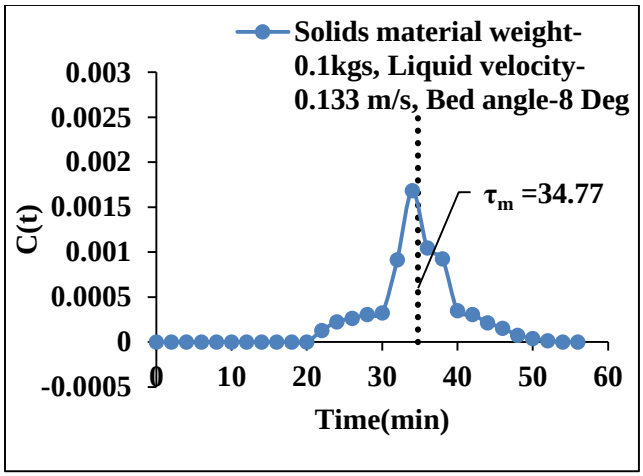

C (t) curve of experiment for HDPE

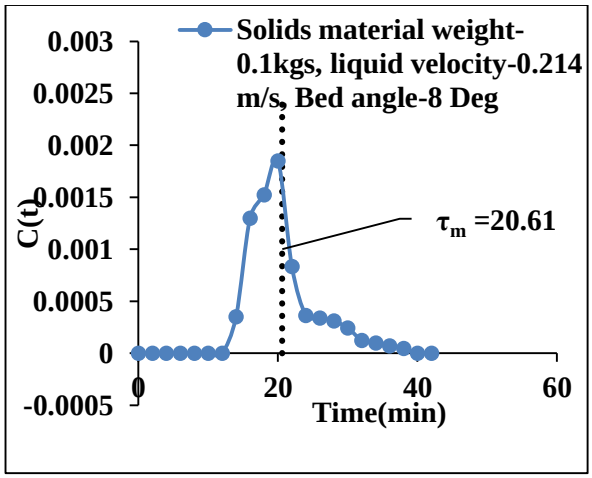

C (t) curve of experiment for HDPE

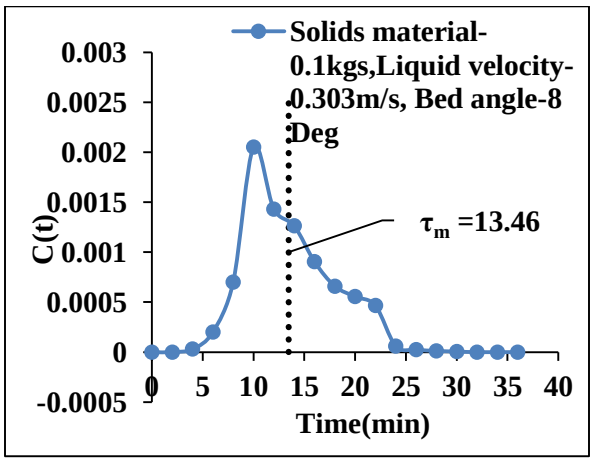

C (t) curve of experiment for HDPE

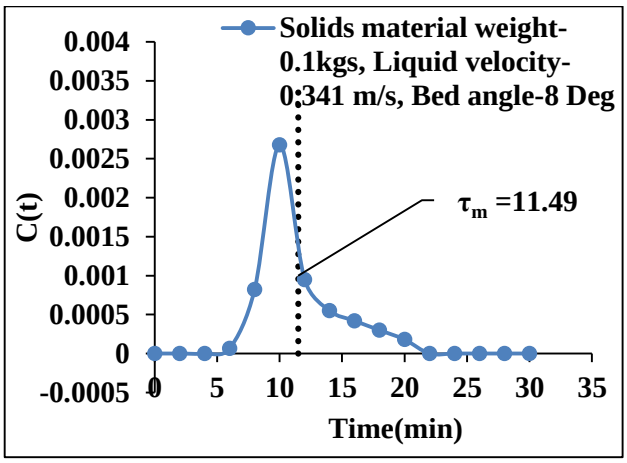

C (t) curve of experiment for HDPE

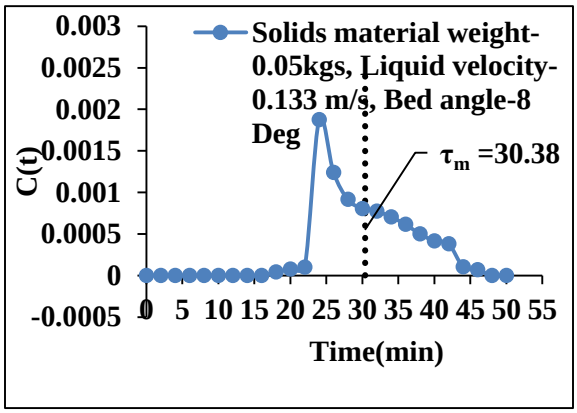

C (t) curve of experiment for Beads

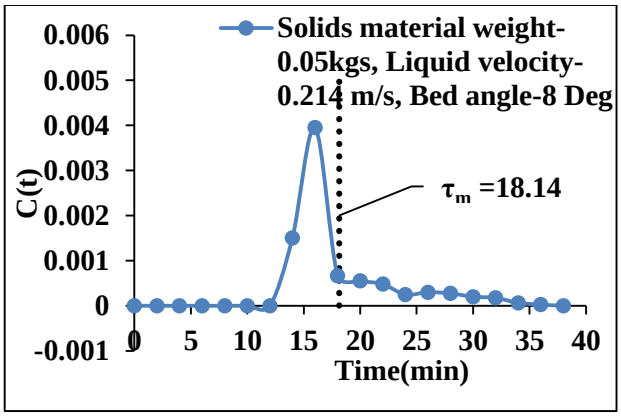

C (t) curve of experiment for Beads

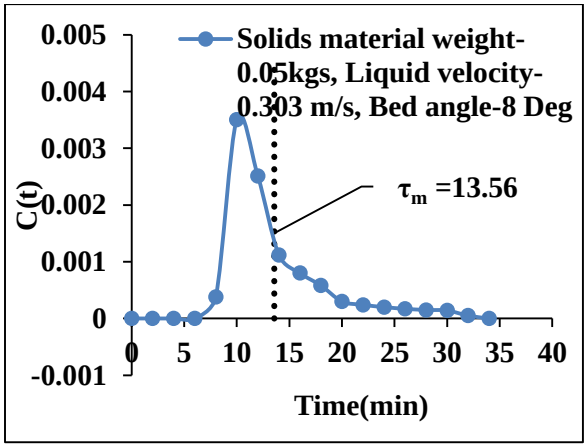

C (t) curve of experiment for Beads

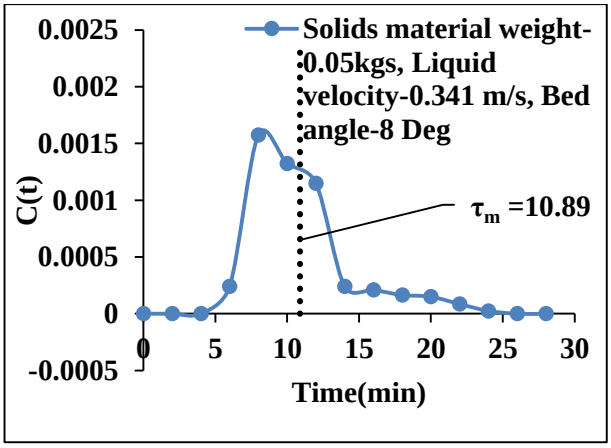

C (t) curve of experiment for Beads

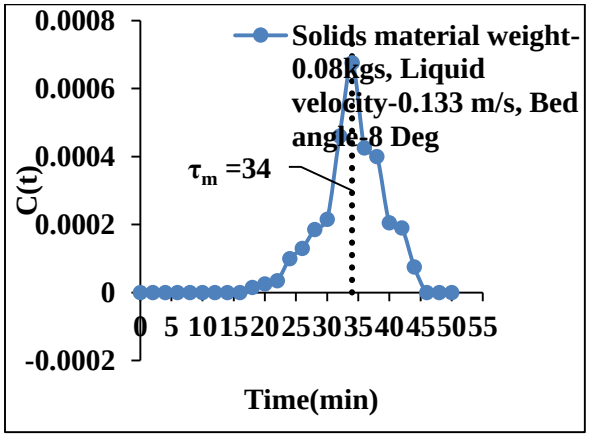

C (t) curve of experiment for Beads

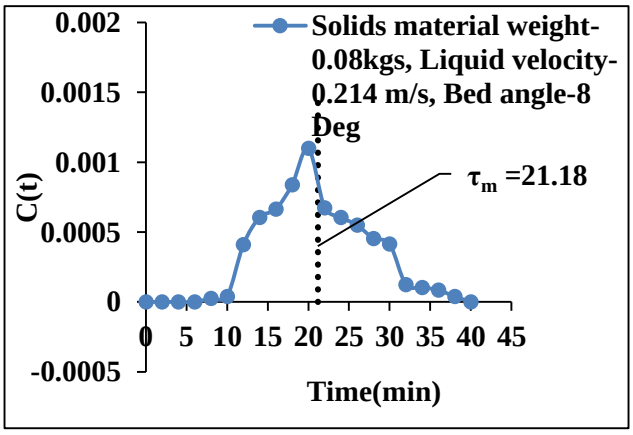

C (t) curve of experiment for Beads

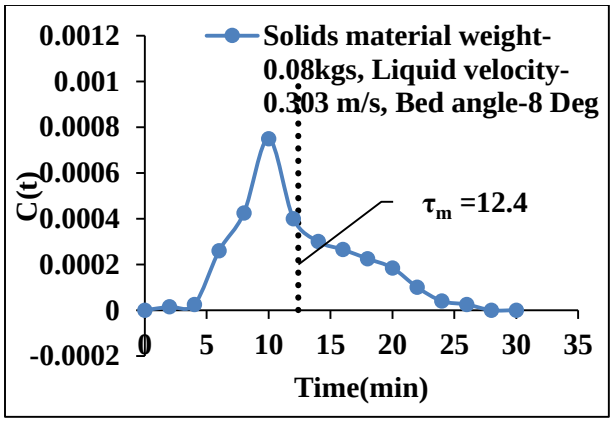

C (t) curve of experiment for Beads

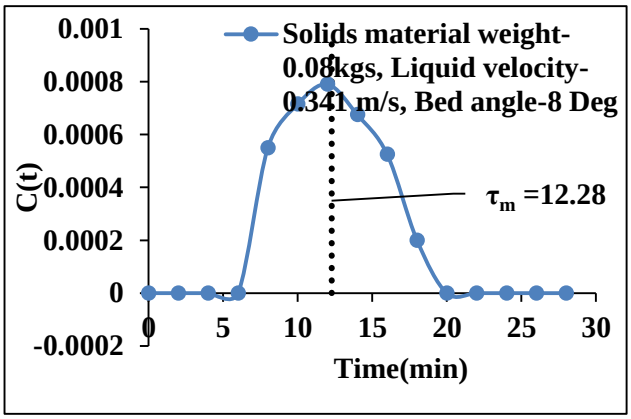

C (t) curve of experiment for Beads

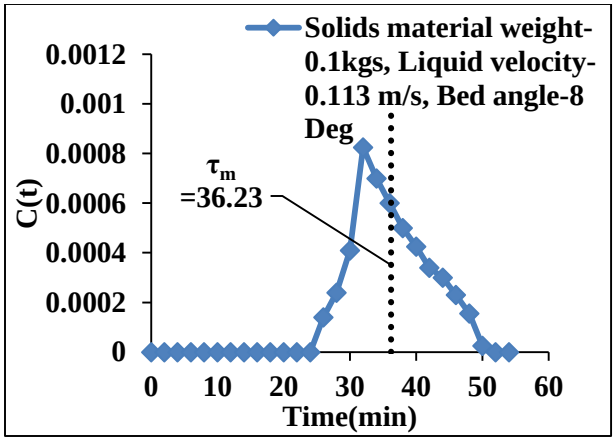

C (t) curve of experiment for Beads

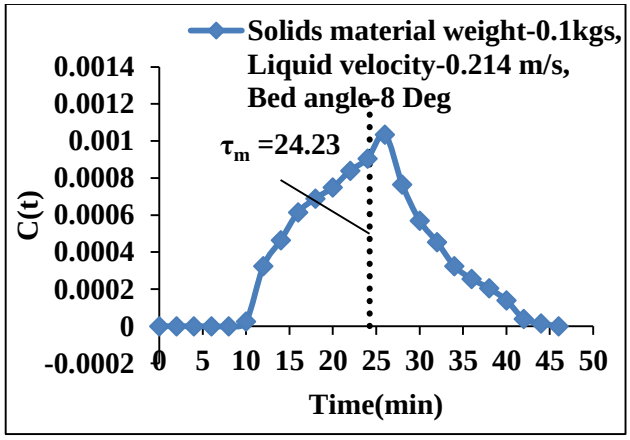

C (t) curve of experiment for Beads

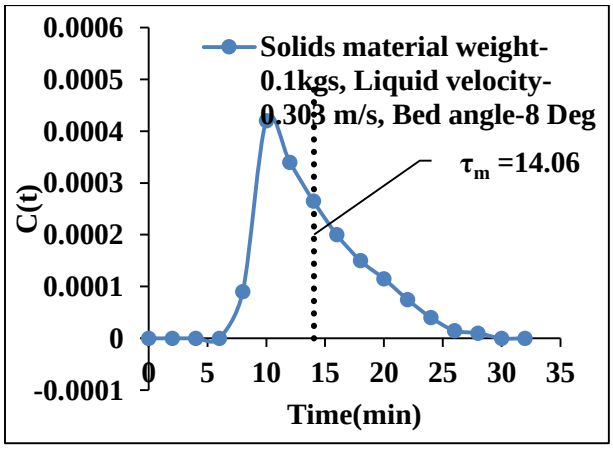

C (t) curve of experiment for Beads

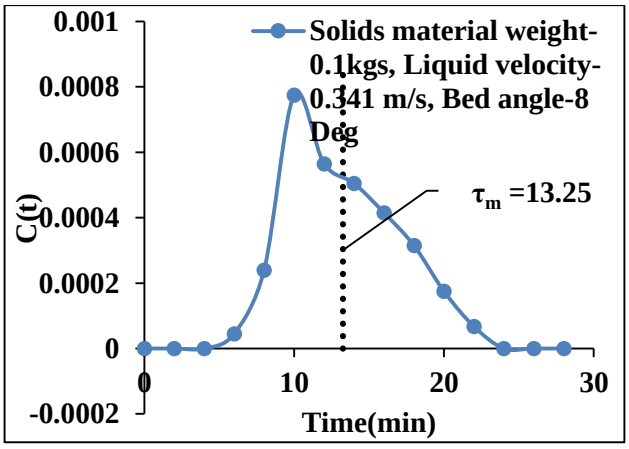

C (t) curve of experiment for Beads

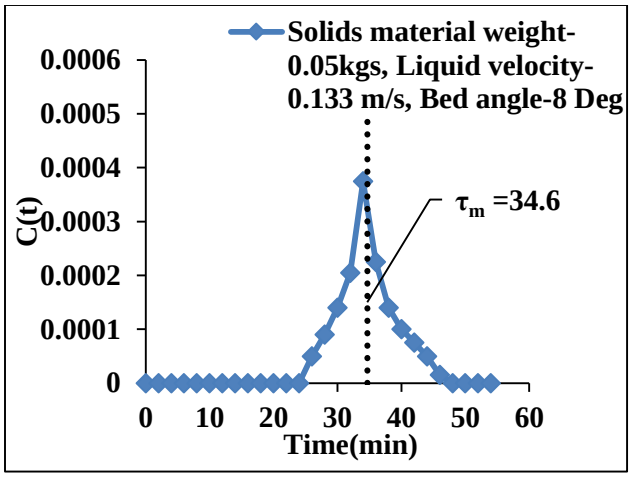

C (t) curve of experiment for PP

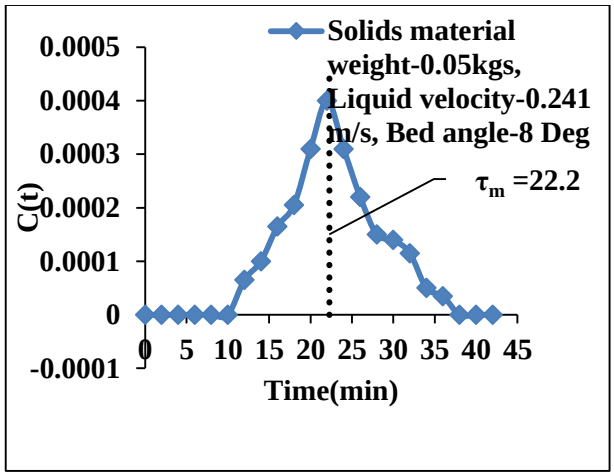

C (t) curve of experiment for PP

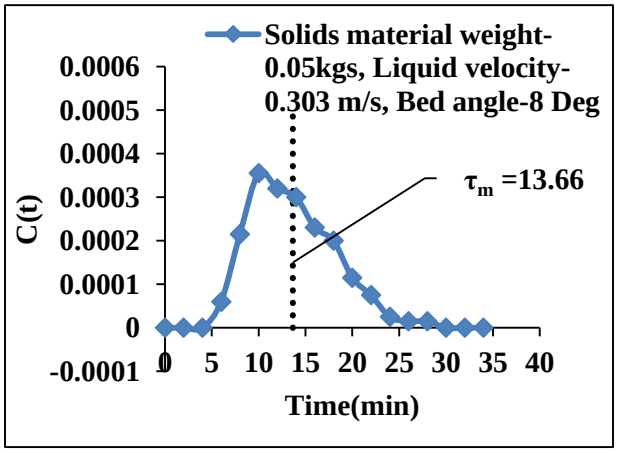

C (t) curve of experiment for PP

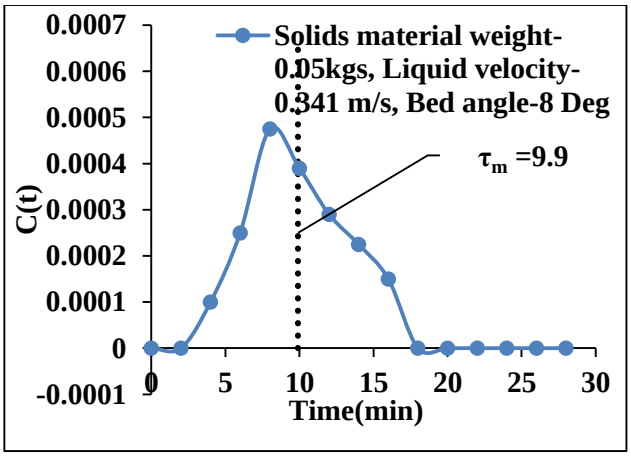

C (t) curve of experiment for PP

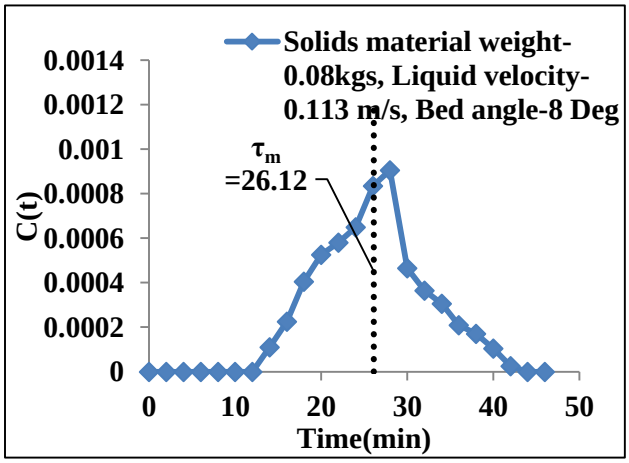

C (t) curve of experiment for PP

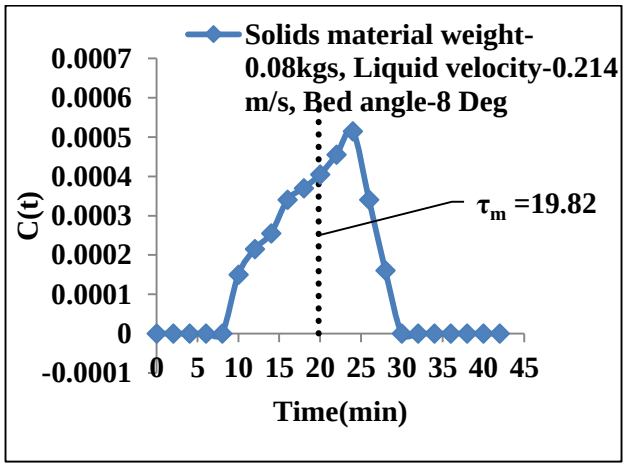

C (t) curve of experiment for PP

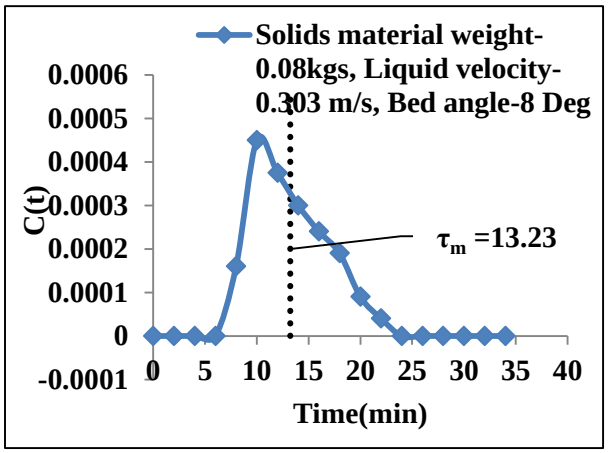

C (t) curve of experiment for PP

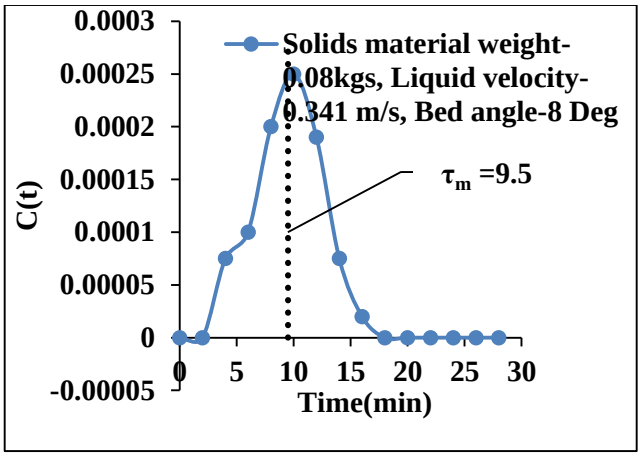

C (t) curve of experiment for PP

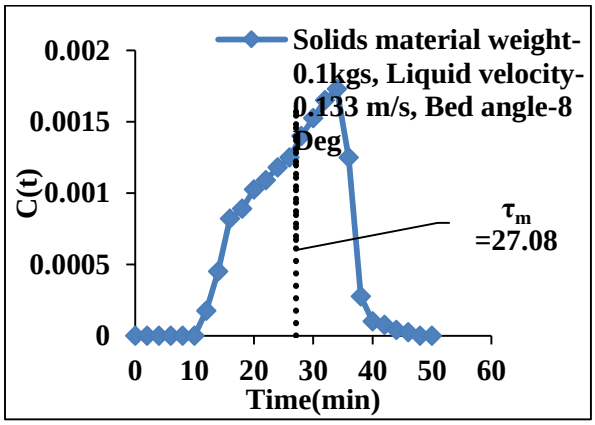

C (t) curve of experiment for PP

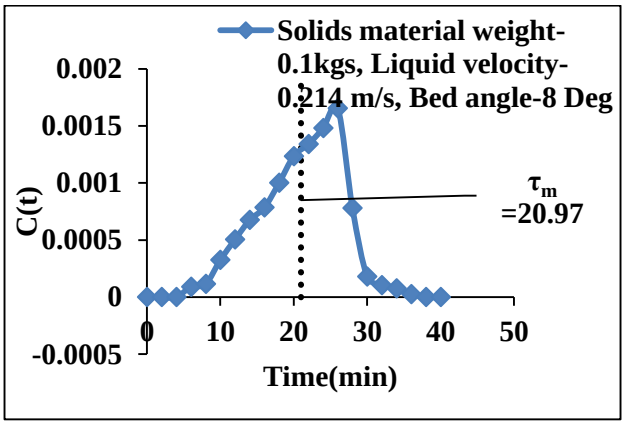

C (t) curve of experiment for PP

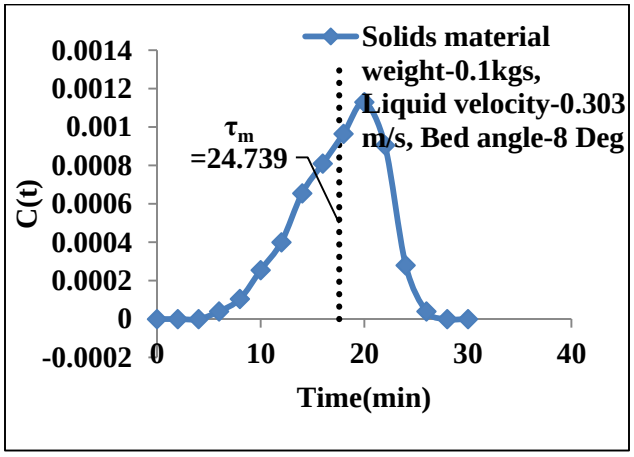

C (t) curve of experiment for PP

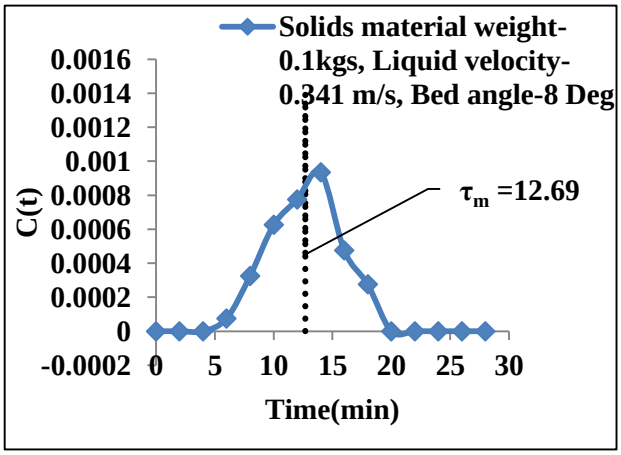

C (t) curve of experiment for PP

Figure 4.55 C (t) curves of experiments with time under different solids material weight, liquid velocity and bed angle

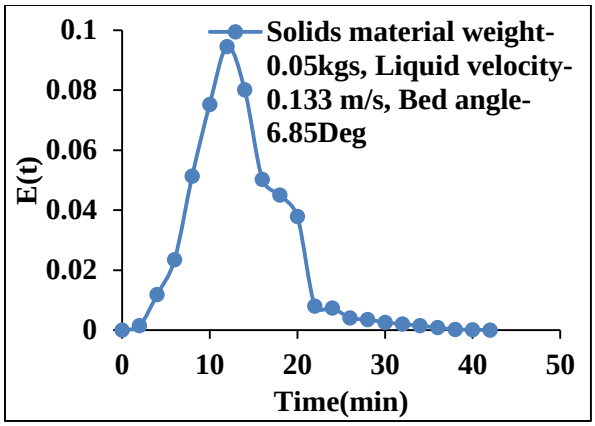

E (t) curve of experiment for HDPE

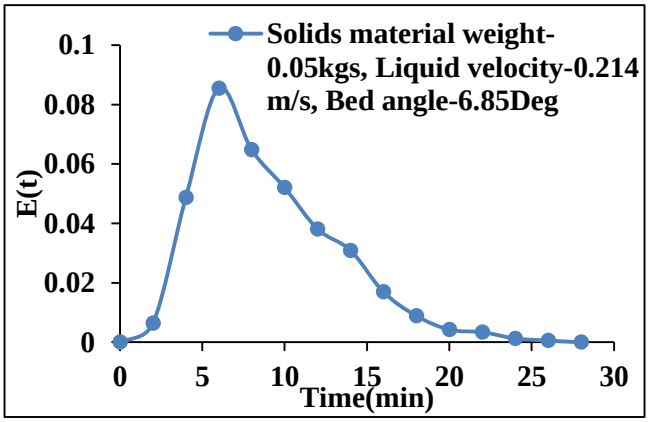

E (t) curve of experiment for HDPE

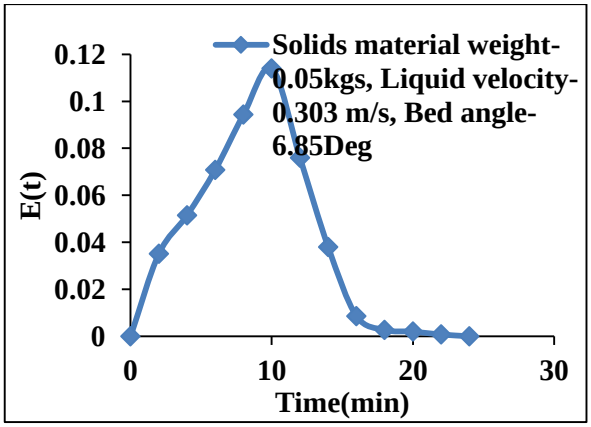

E (t) curve of experiment for HDPE

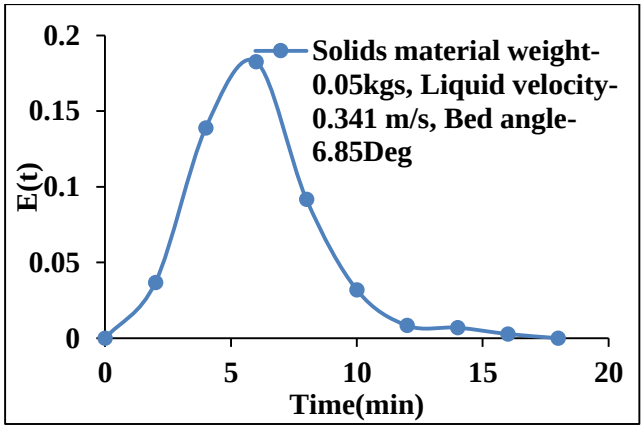

E (t) curve of experiment for HDPE

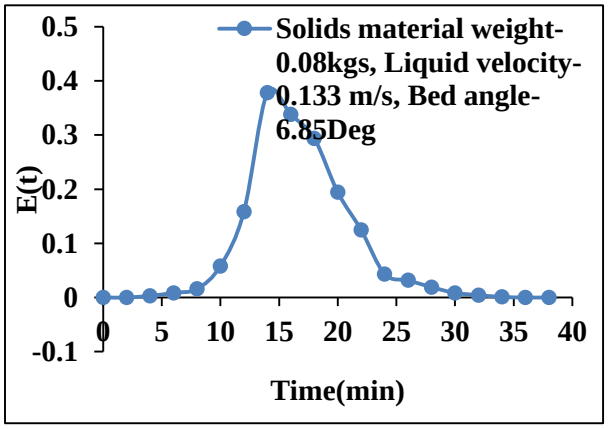

E (t) curve of experiment for HDPE

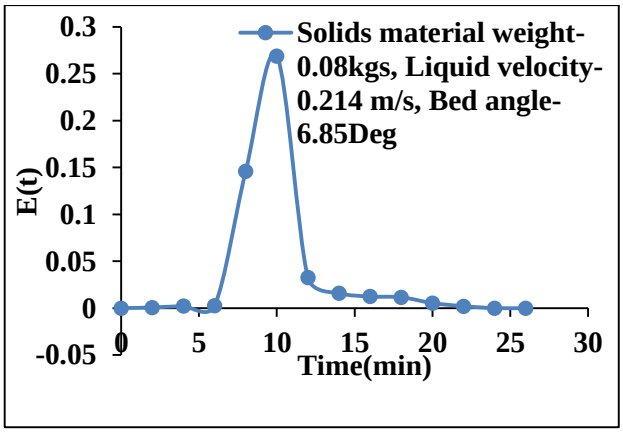

E (t) curve of experiment for HDPE

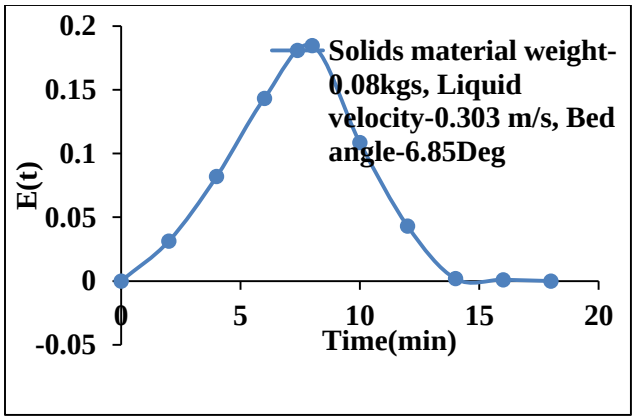

E(t)curve of experiment for HDPE

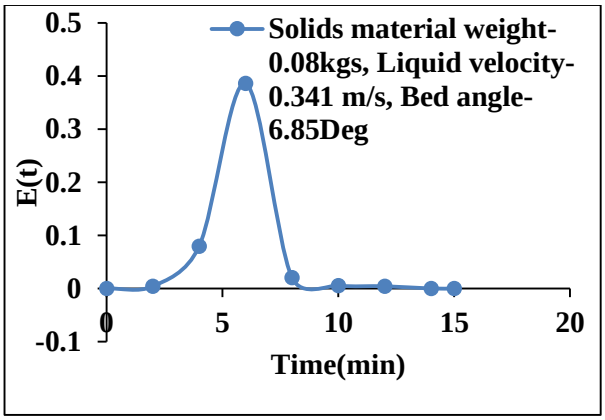

E (t) curve of experiment for HDPE

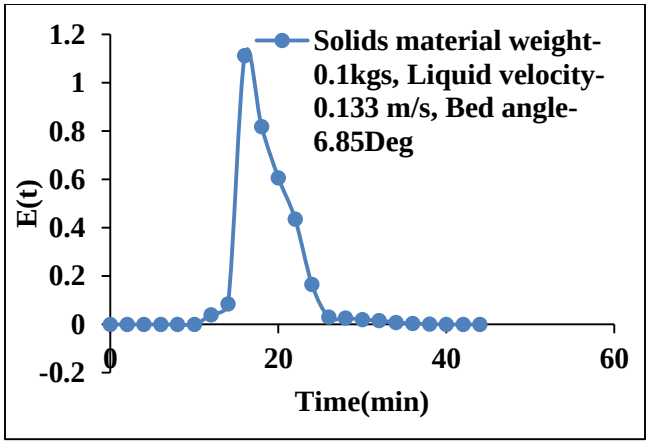

E (t) curve of experiment for HDPE

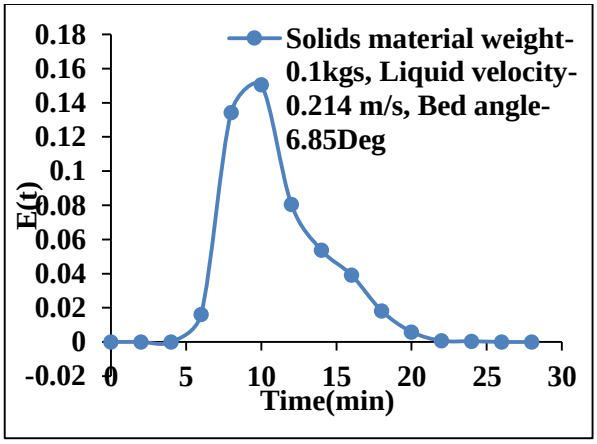

E (t) curve of experiment for HDPE

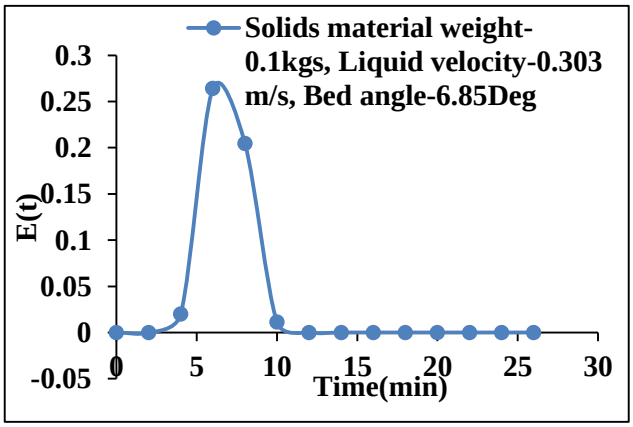

E (t) curve of experiment for HDPE

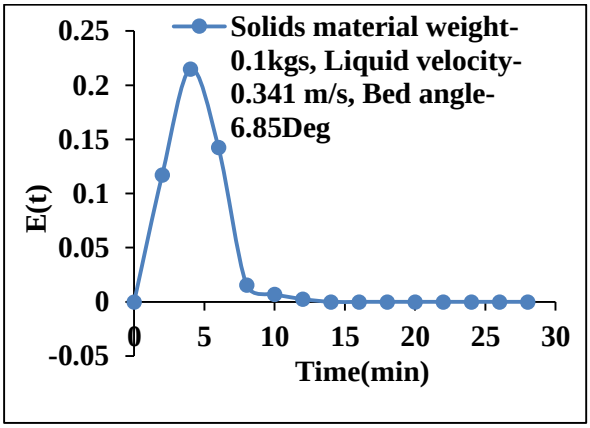

E (t) curve of experiment for HDPE

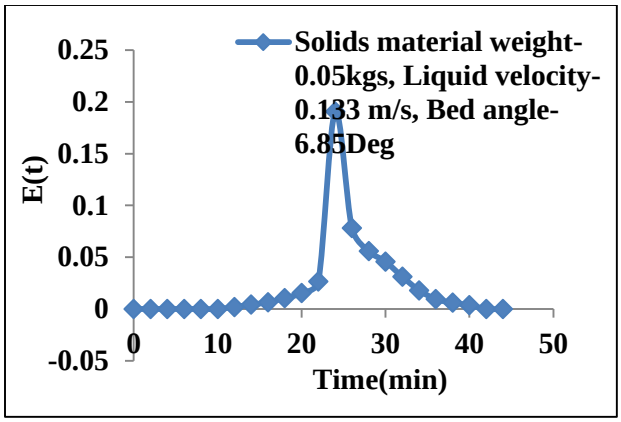

E (t) curve of experiment for Beads

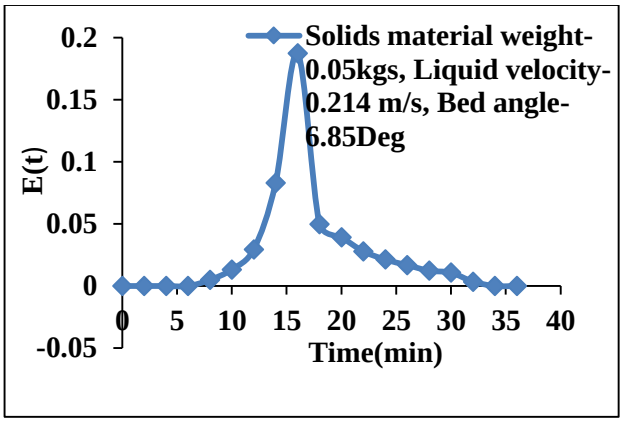

E (t) curve of experiment for Beads

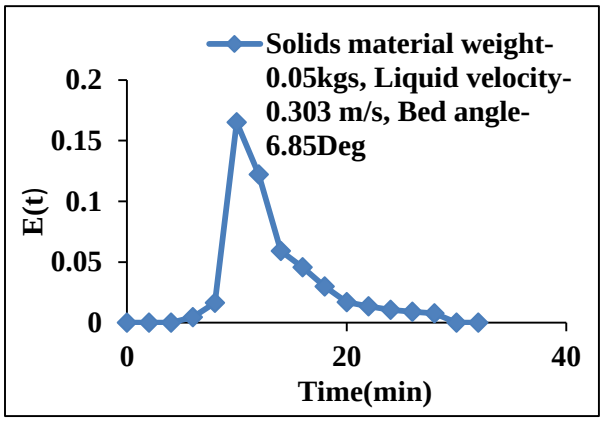

E (t) curve of experiment for Beads

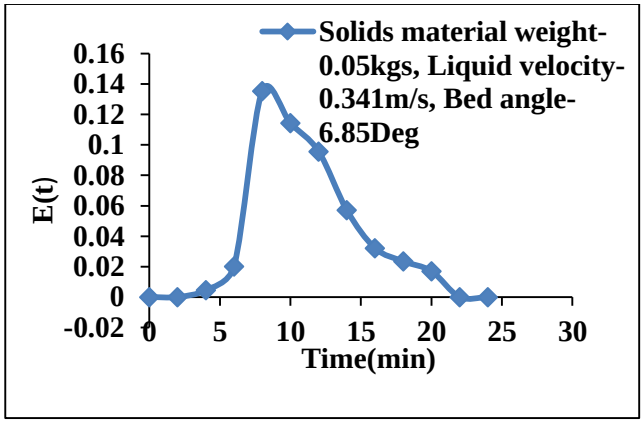

E (t) curve of experiment for Beads

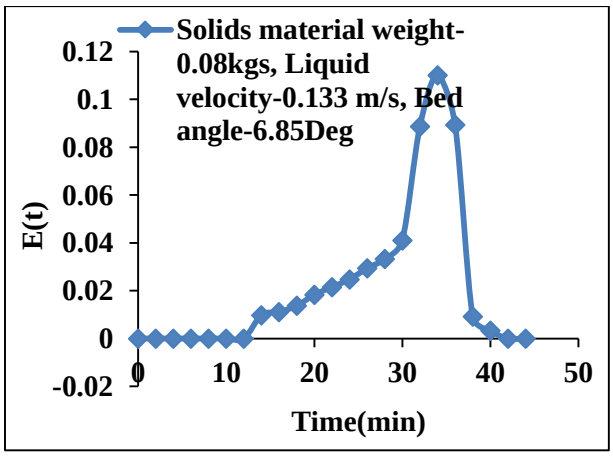

E (t) curve of experiment for Beads

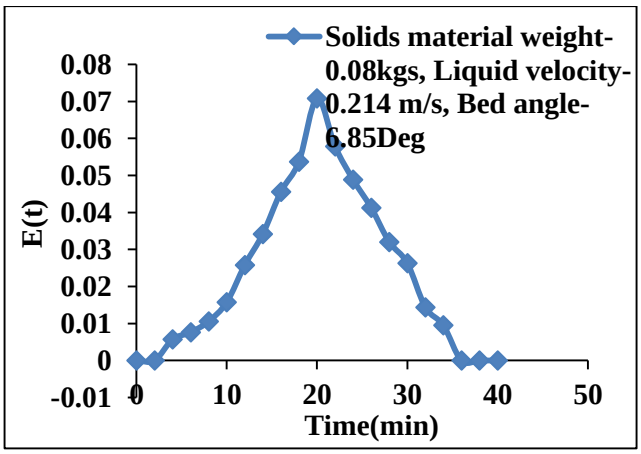

E (t) curve of experiment for Beads

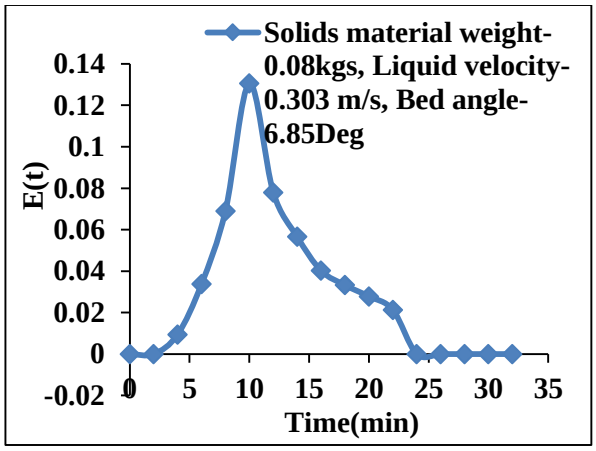

E (t) curve of experiment for Beads

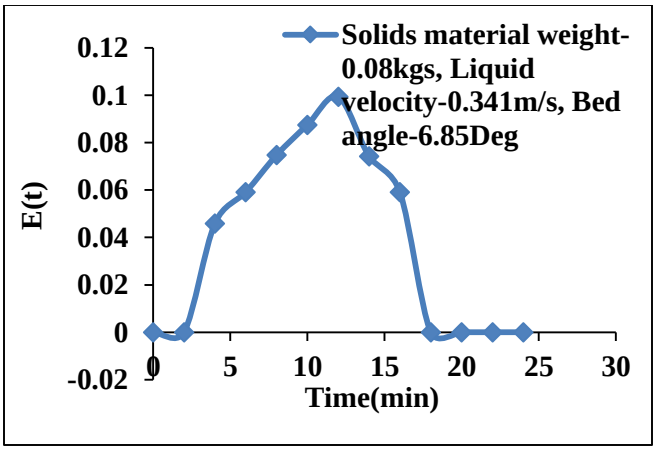

E (t) curve of experiment for Beads

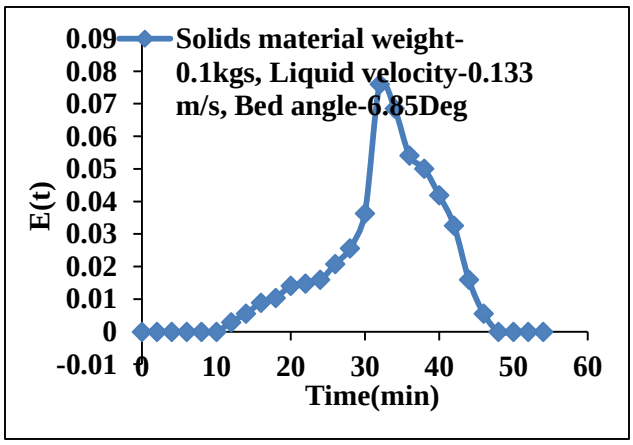

E (t) curve of experiment for Beads

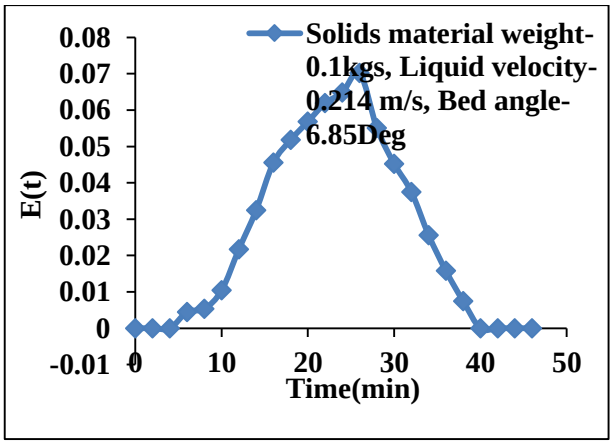

E (t) curve of experiment for Beads

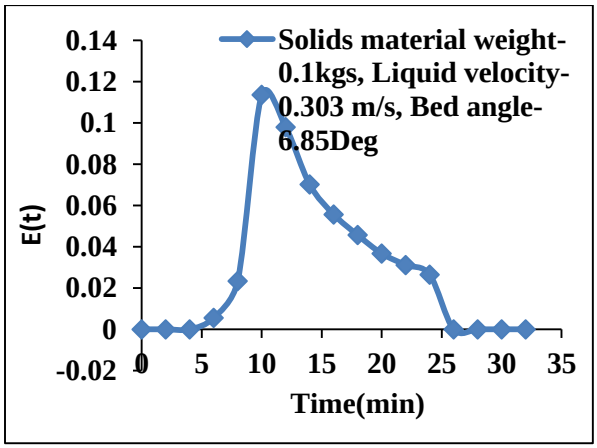

E (t) curve of experiment for Beads

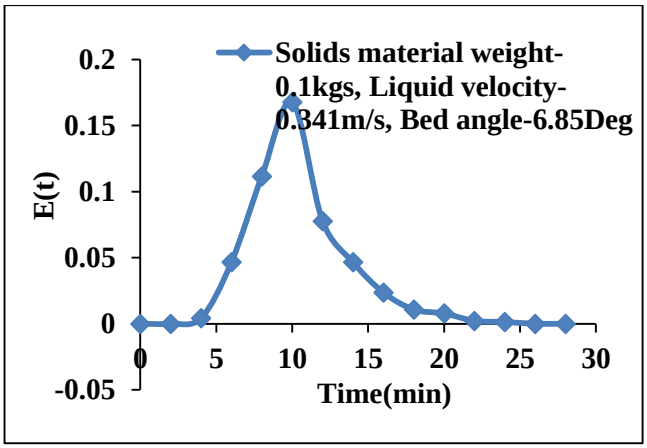

E (t) curve of experiment for Beads

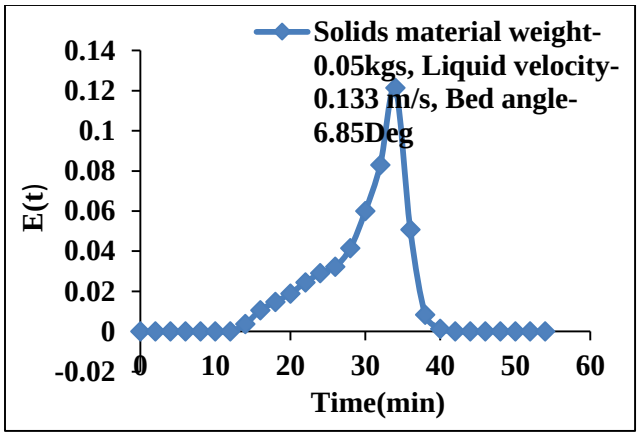

E (t) curve of experiment for PP

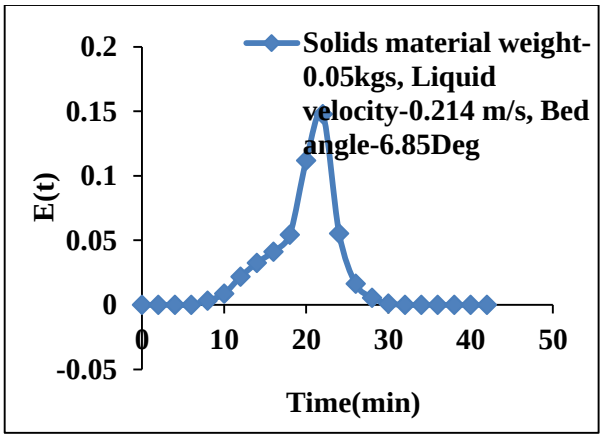

E (t) curve of experiment for PP

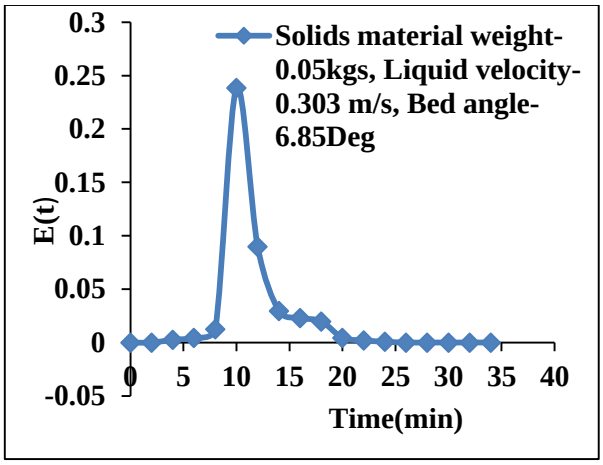

E (t) curve of experiment for PP

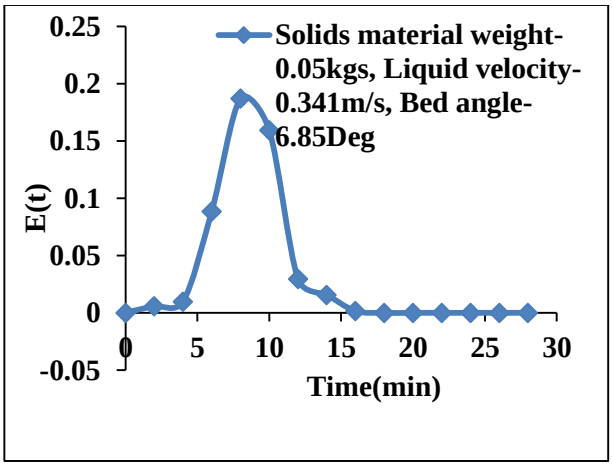

E (t) curve of experiment for PP

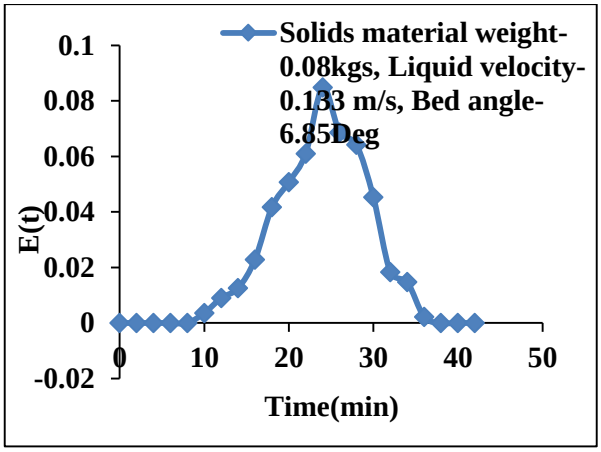

E (t) curve of experiment for PP

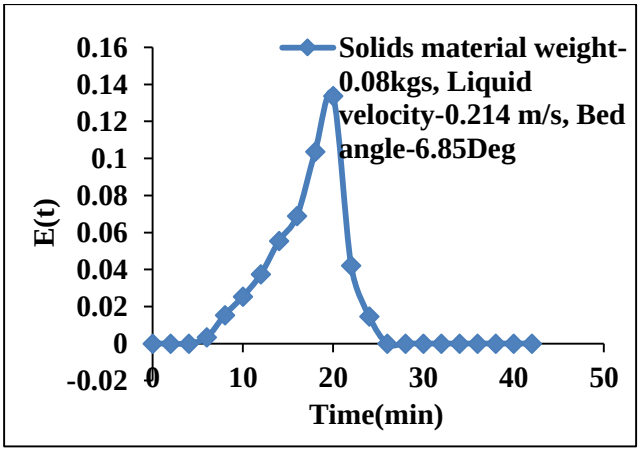

E (t) curve of experiment for PP

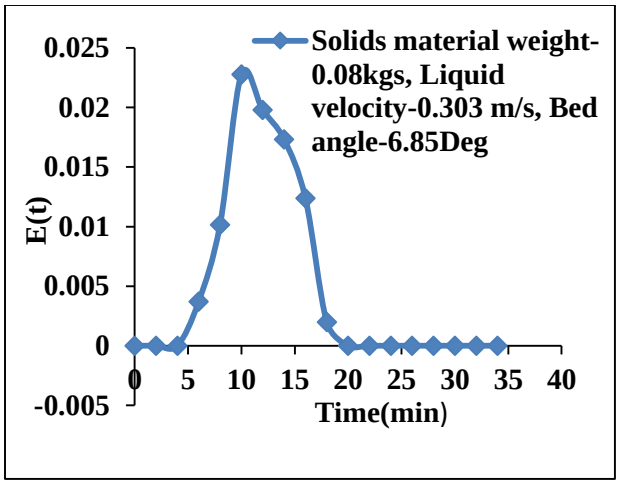

E (t) curve of experiment for PP

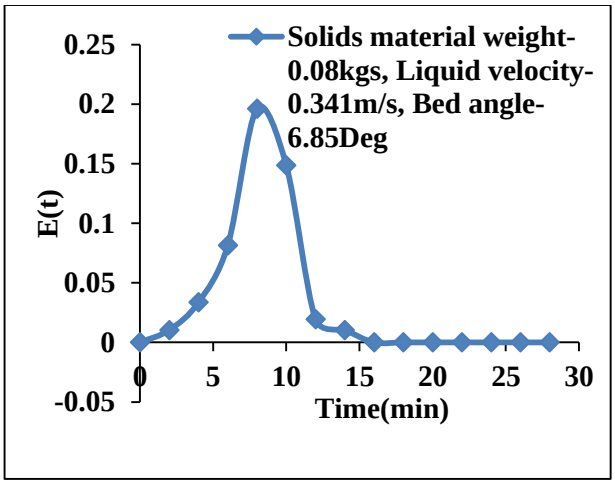

E (t) curve of experiment for PP

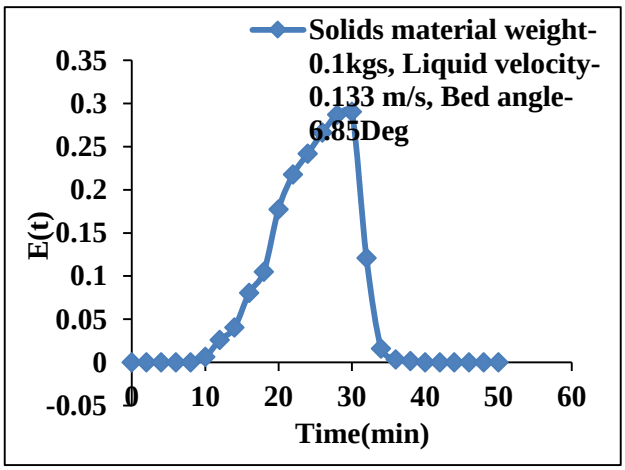

E (t) curve of experiment for PP

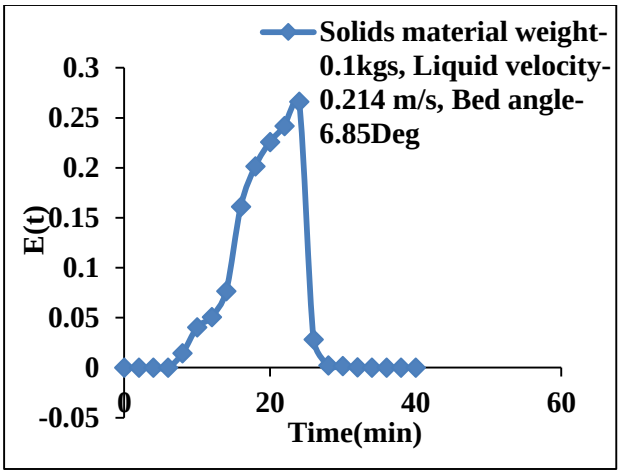

E (t) curve of experiment for PP

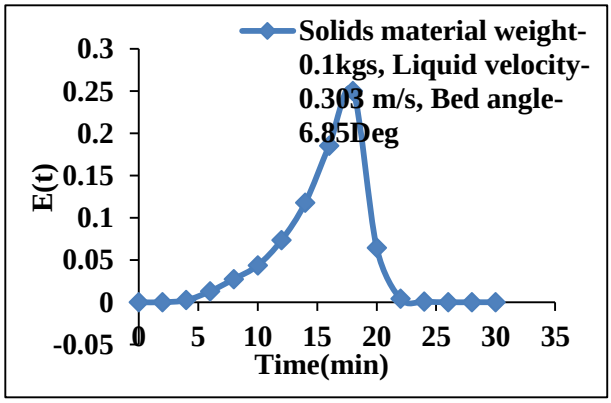

E (t) curve of experiment for PP

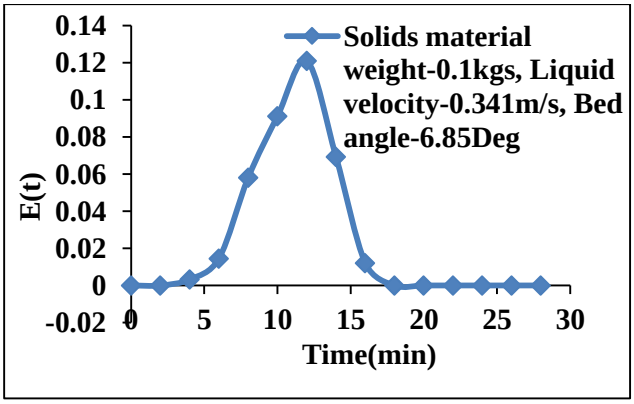

E (t) curve of experiment for PP

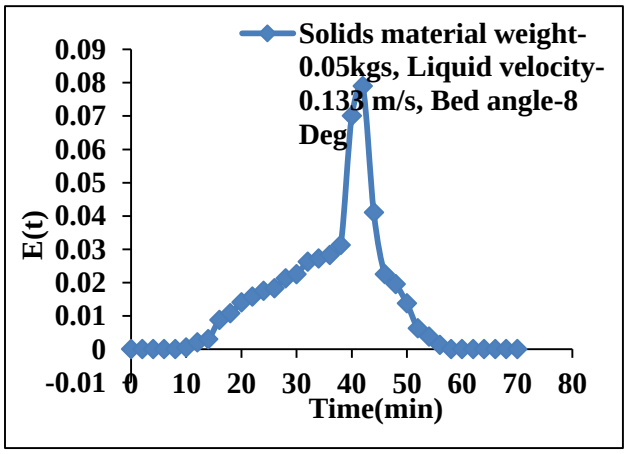

E (t) curve of experiment for HDPE

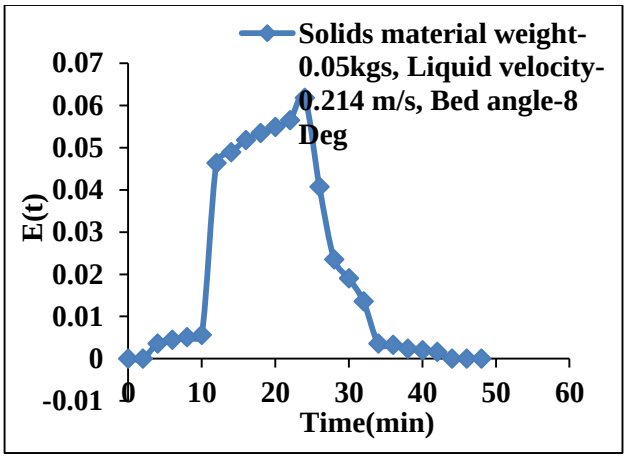

E (t) curve of experiment for HDPE

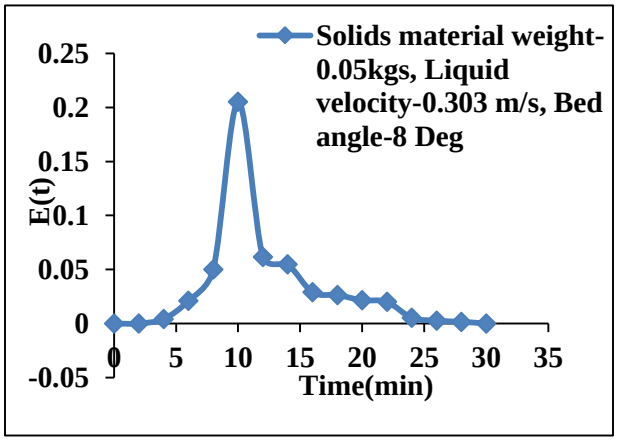

E (t) curve of experiment for HDPE

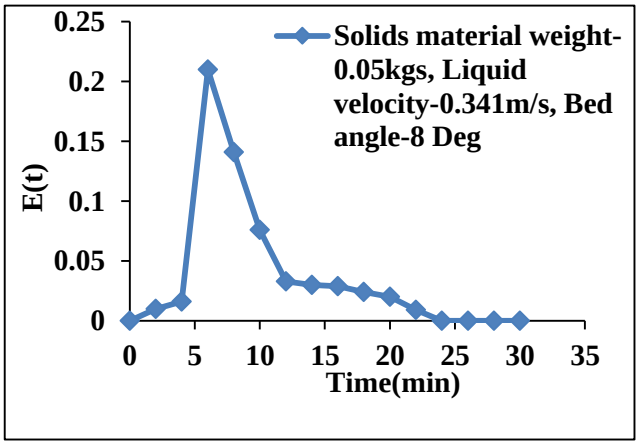

E (t) curve of experiment for HDPE

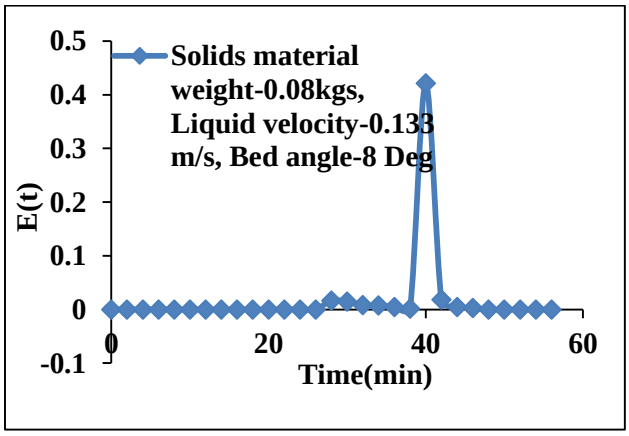

E (t) curve of experiment for HDPE

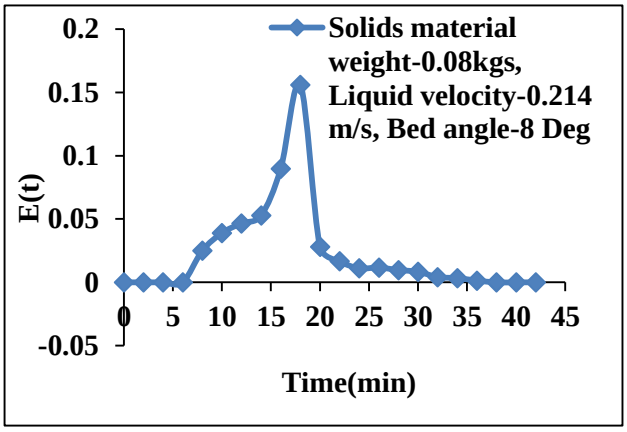

E (t) curve of experiment for HDPE

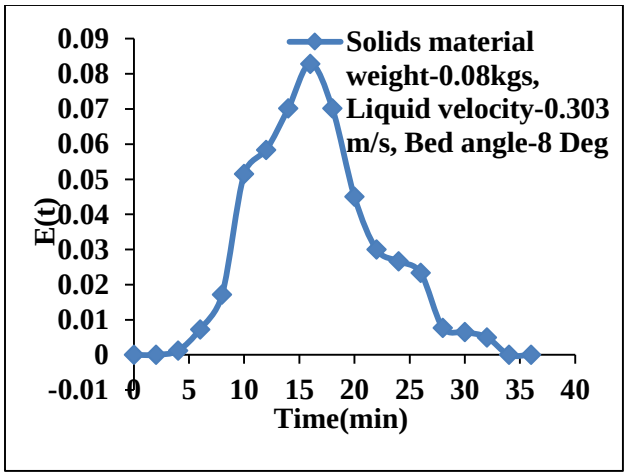

E (t) curve of experiment for HDPE

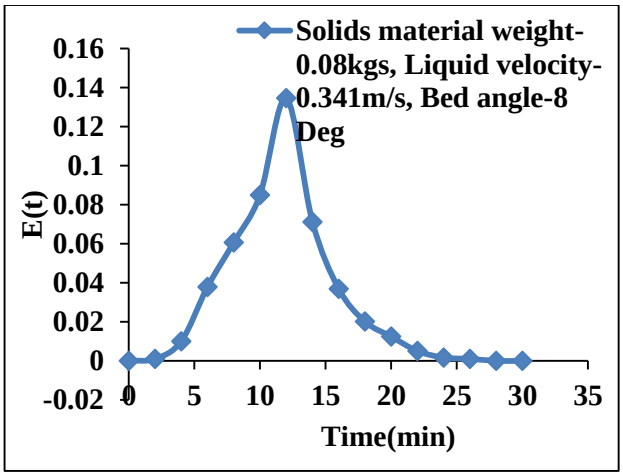

E (t) curve of experiment for HDPE

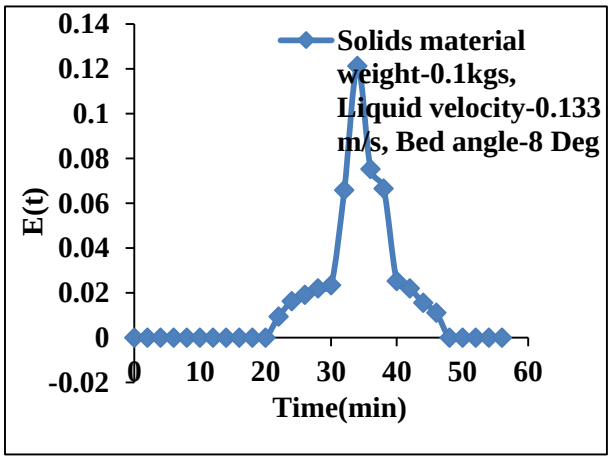

E (t) curve of experiment for HDPE

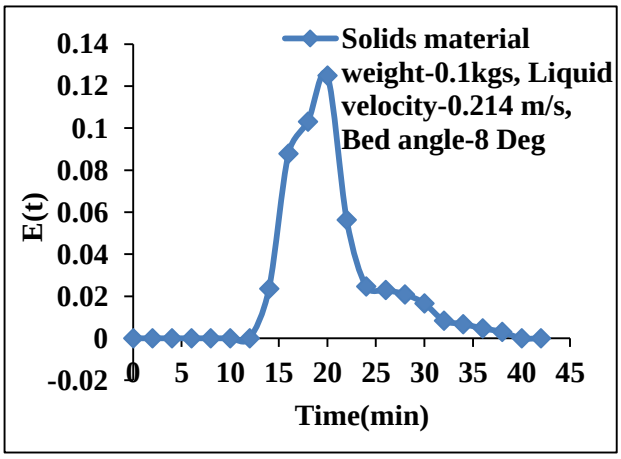

E (t) curve of experiment for HDPE

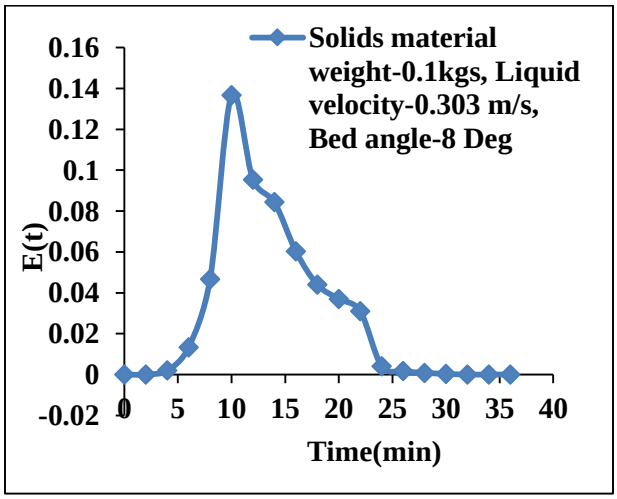

E (t) curve of experiment for HDPE

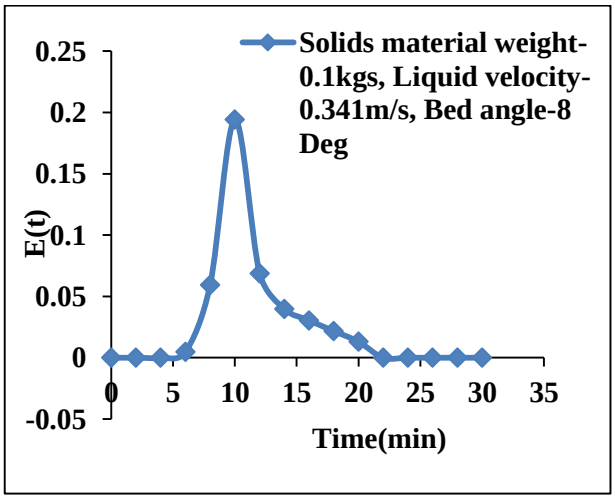

E (t) curve of experiment for HDPE

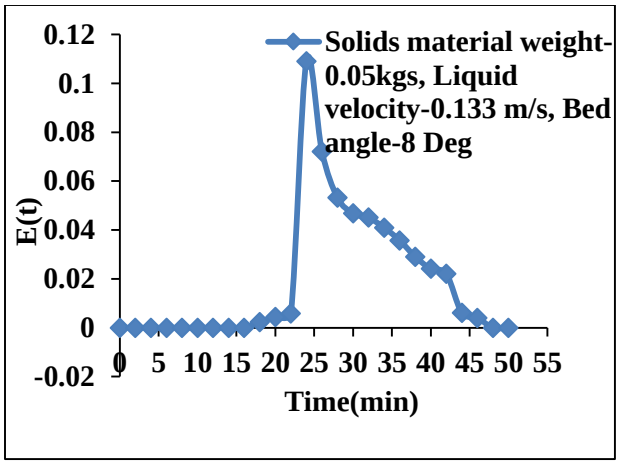

E (t) curve of experiment for Beads

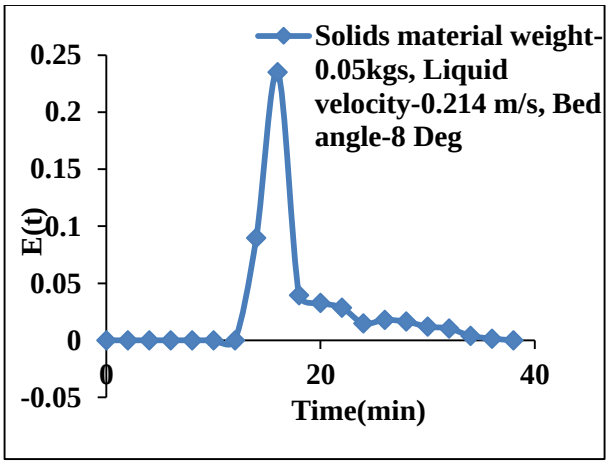

E (t) curve of experiment for Beads

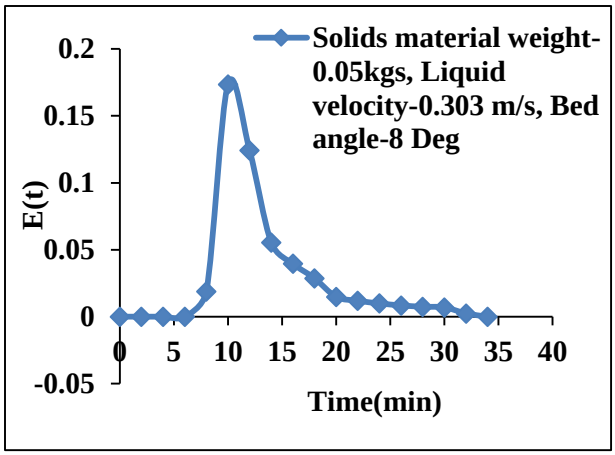

E (t) curve of experiment for Beads

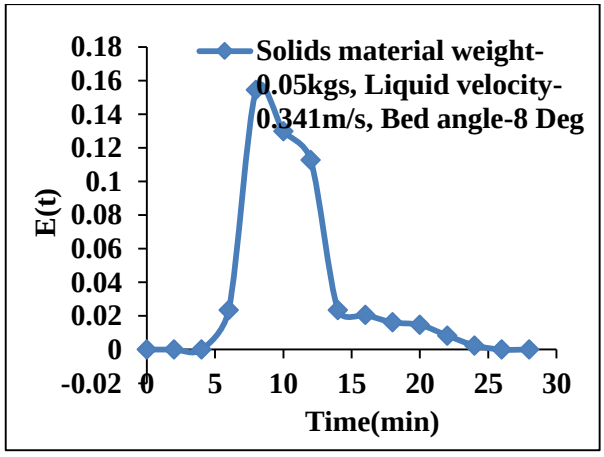

E (t) curve of experiment for Beads

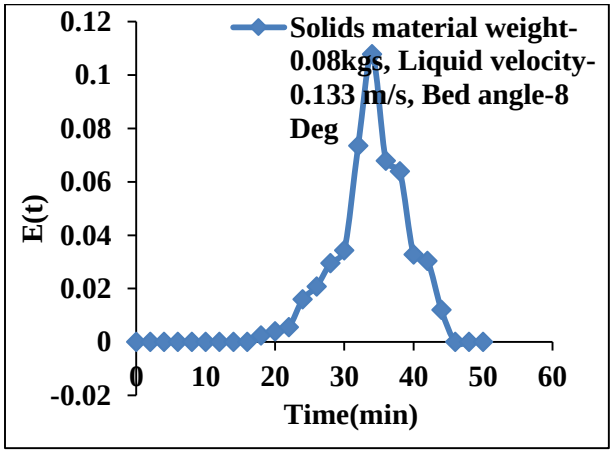

E (t) curve of experiment for Beads

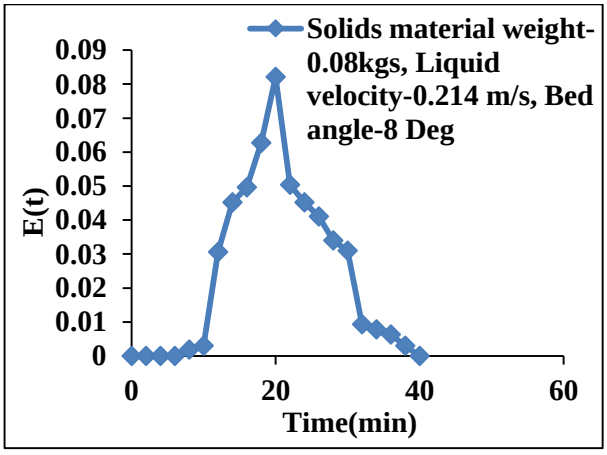

E (t) curve of experiment for Beads

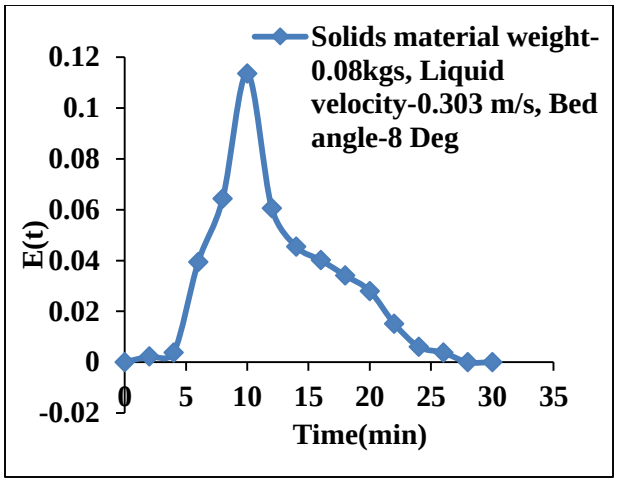

E (t) curve of experiment for Beads

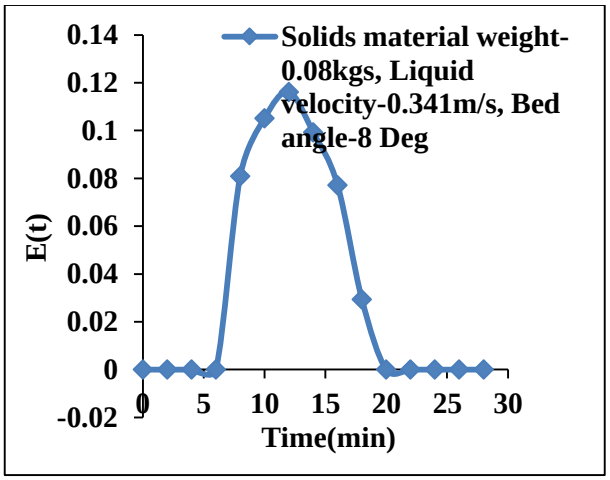

E (t) curve of experiment for Beads

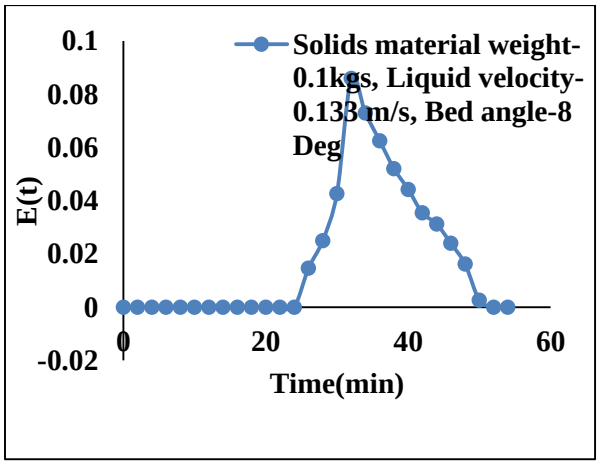

E (t) curve of experiment for Beads

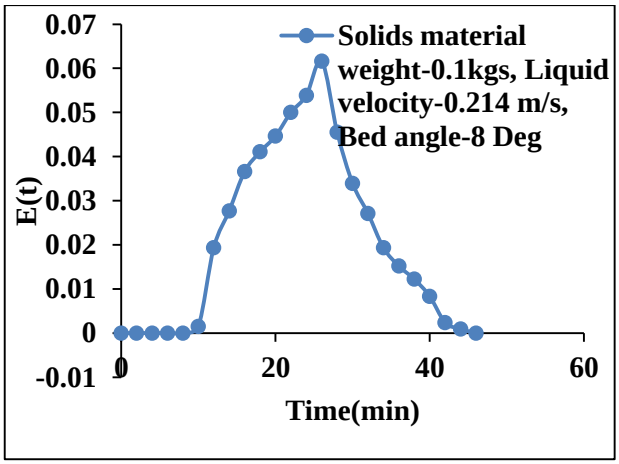

E (t) curve of experiment for Beads

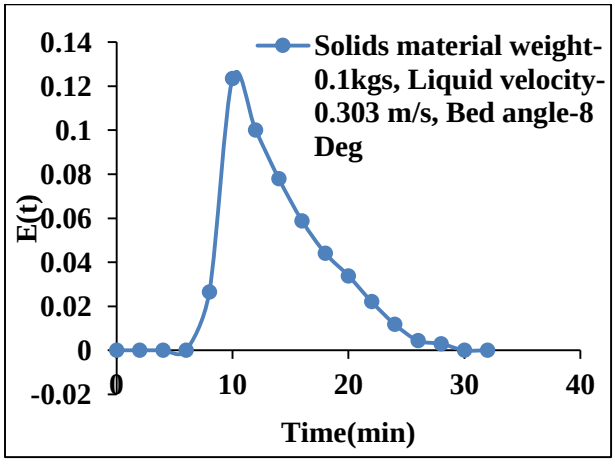

E (t) curve of experiment for Beads

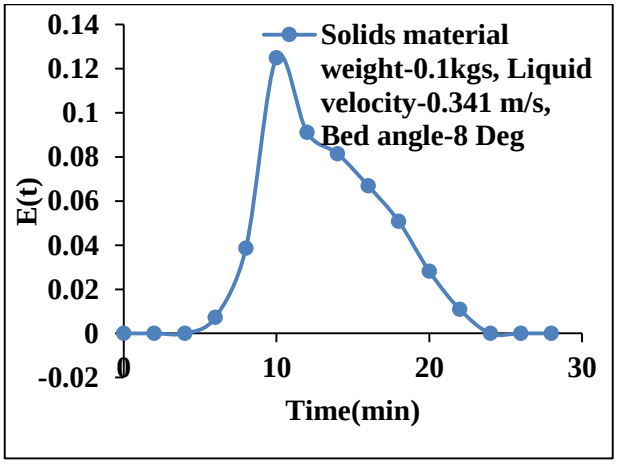

E (t) curve of experiment for Beads

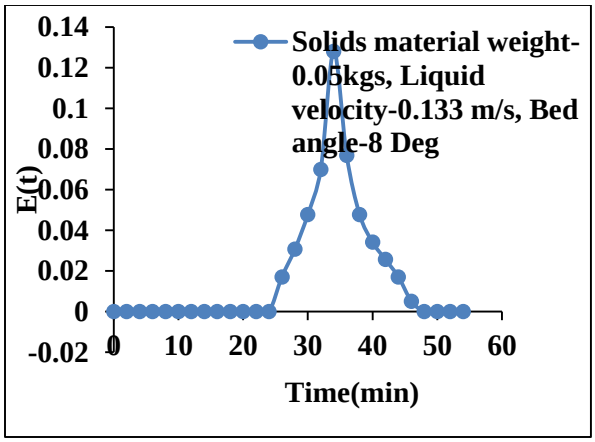

E (t) curve of experiment for PP

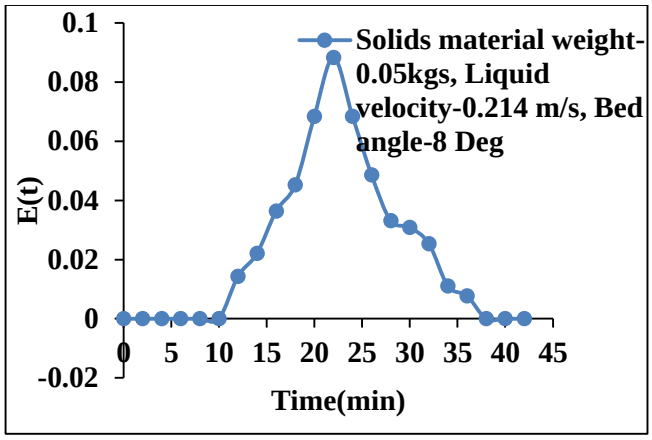

E (t) curve of experiment for PP

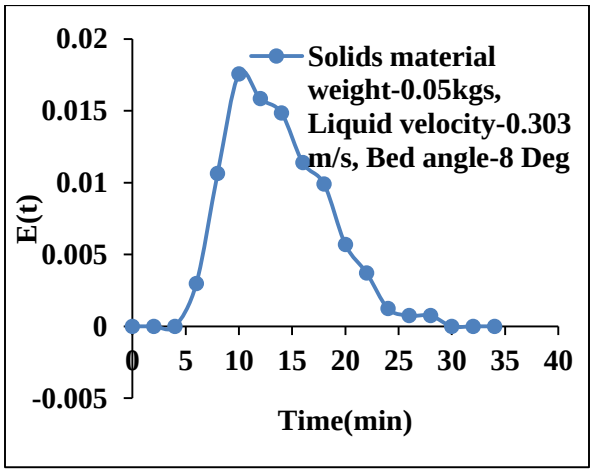

E (t) curve of experiment for PP

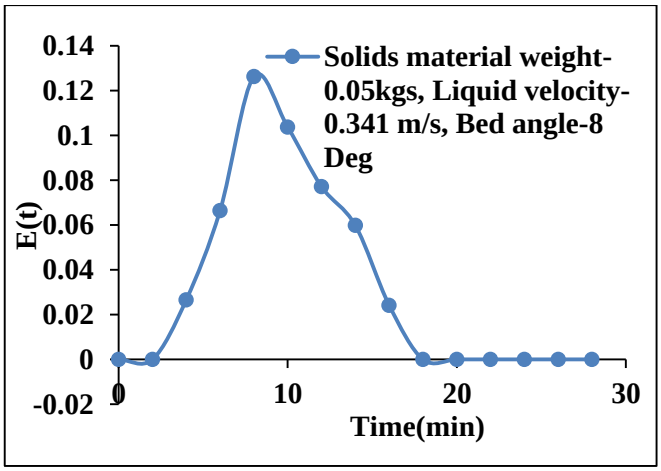

E (t) curve of experiment for PP

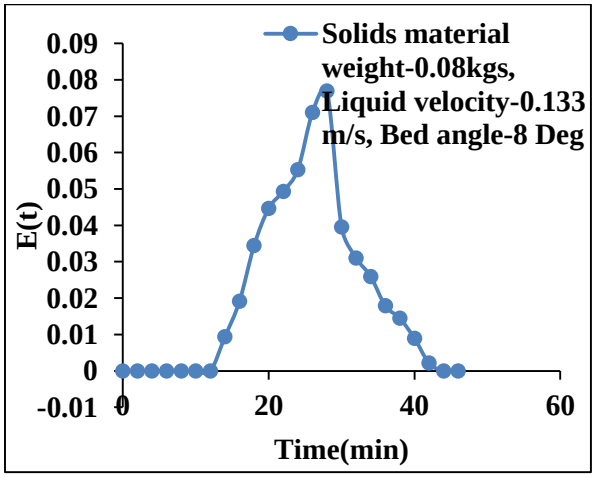

E (t) curve of experiment for PP

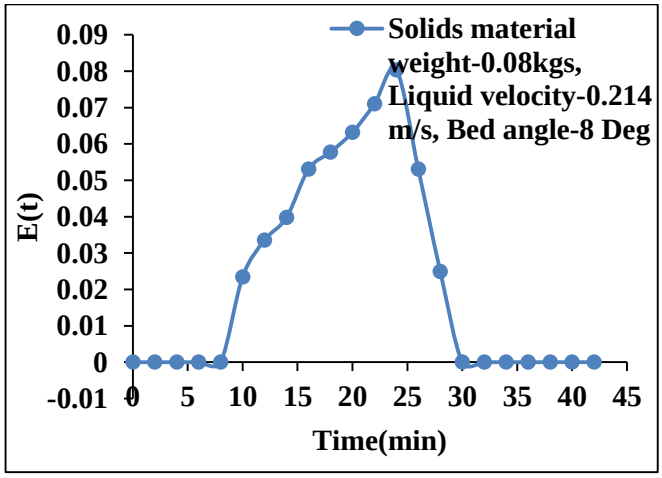

E (t) curve of experiment for PP

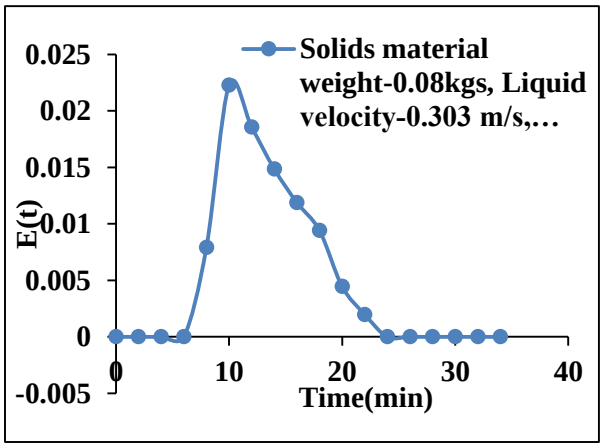

E (t) curve of experiment for PP

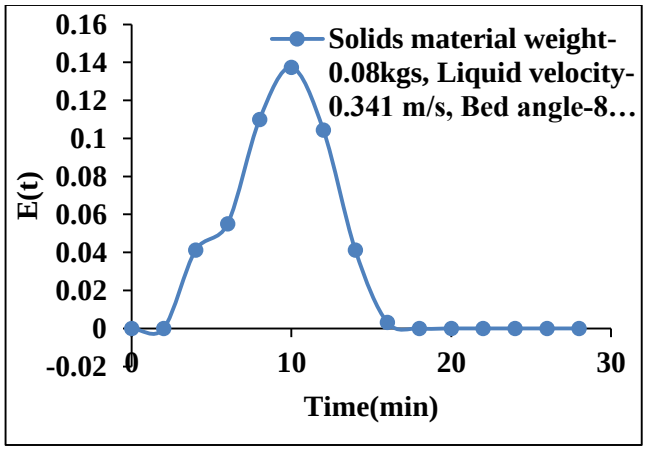

E (t) curve of experiment for PP

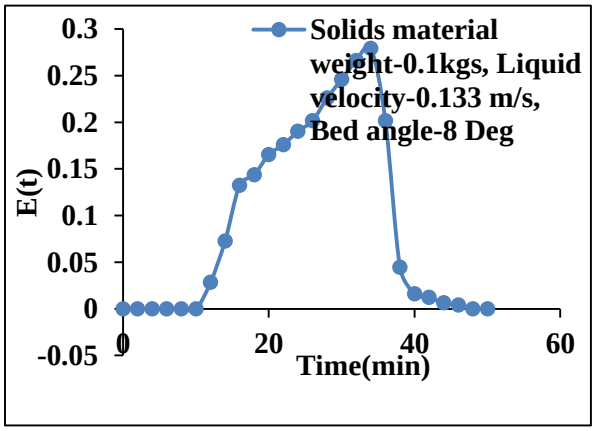

E (t) curve of experiment for PP

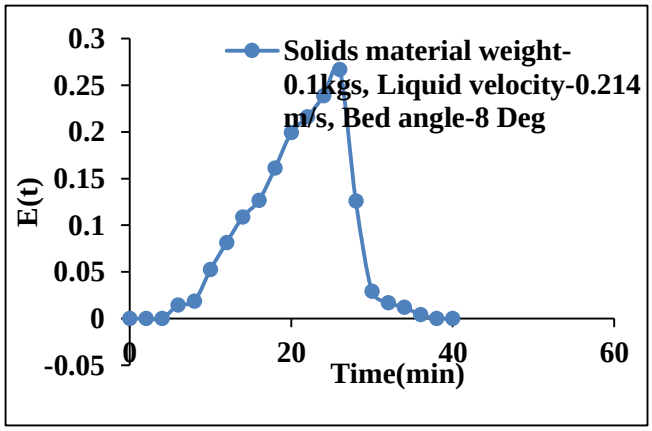

E (t) curve of experiment for PP

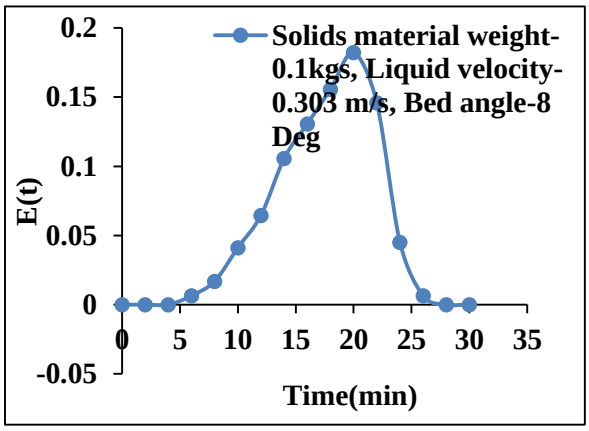

E (t) curve of experiment for PP

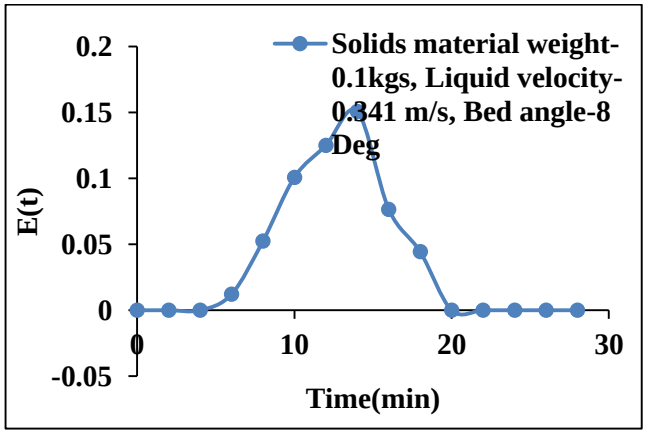

E (t) curve of experiment for PPFigure

4.56 E (t) curve of experiments with time under different solids material weight, liquid velocity and bed angle

4.2.3 Mean residence time

The mean residence time of tracer in a bed varied with liquid flow rate and bed tapered angle. The residence time versus the mass of solid for different liquid velocity is indicated in Figure 4.57. The mean residence time shows nearly constant with increasing solid materials and decreases with increasing liquid flow rate. Mass of solid has no impact on the mean residence time [34]. In addition, the relationship between liquid mean residence and the density of the solid is indicated in Figure 4.58. The mean residence time for all the lower density particles increases monotonically with increasing liquid flow rate. The effect of higher particle density on mean residence time is observed since a higher relative liquid velocity was required to suspend particles, hence the bed Voidage for heavy particles having a higher terminal velocity. As a result, more turbulence was produced, resulting in a greater amount of mixing.

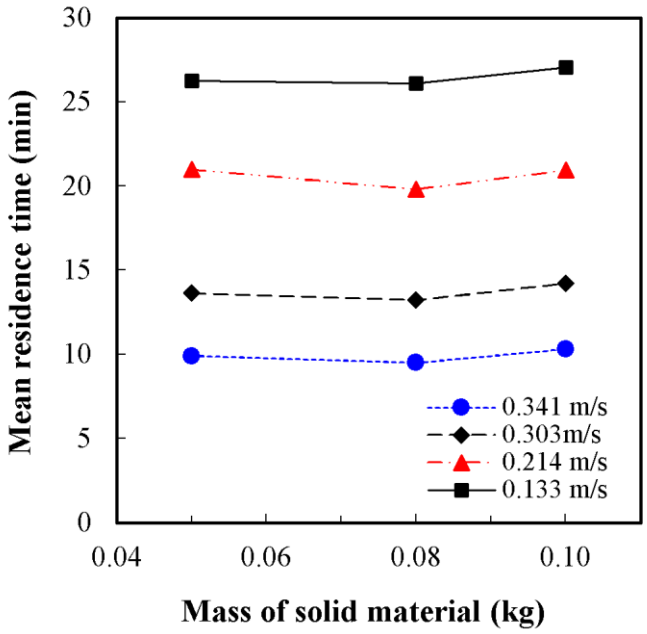

Figure 4.57: Mean residence time versus the mass of solid materials of HDPE for the different liquid velocity at $\varphi = 8^{o}$.

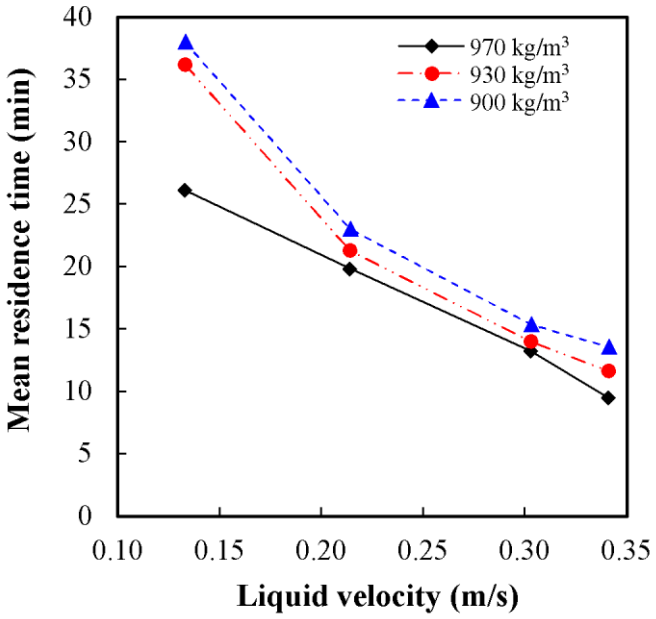

Figure 4.58: Mean residence time versus liquid velocity for different density of solid at initial solid mass, m_s = 0.08kg and φ = 8°.

4.2.4 Developing of Empirical model by using Surface Response Methodology (RSM):

Response surface methodology (RSM) is a gathering of scientific and measurable methods for observational model building. Through a careful outline of trials, the goal is to streamline a response (yield variable) that is impacted by a few input factors. The analysis is a progression of tests, called runs, in which changes are made in the information factors to recognize the purposes behind changes in the yield reaction. RSM was produced to demonstrate test reactions [35], and afterwards relocated into the display of numerical analyses. The difference is in the sort of error produced by the response. In the advancement of the models, all the levels of experimental parameters were kept independent in all the investigations. The levels of all process variables were specified based on the current task's experiments, and the level values of the individual parameters used in the experiments are shown in Table 4.6. Under various sets of investigating variables, the response of the mean residence of liquid tracer from the inverse tapered fluidized beds shows variation with different independent variables. Therefore, model (Eq. (4.20)) was developed to create the pattern in which experimental parameters affects the mean residence of the tracer.

$$\text{Mean residence time } (\bar{t}) = \begin{cases} 753.03 - 143.38A + 663.5B - 0.84C - 87.71D + 60.01AB + \\ 0.23AC - 22.40AD - 0.68BC - 2.67BD + 0.10CD \end{cases} \quad (4.20)$$

For the RSM data modelling, an inbuilt utility of the design expert package has been used in the current finding to derive the regression models in terms of various operating variables such as velocity, initial bed heights (material weights), the density of solids and various angles of reactors. This model equation was used to obtain the influence of operating variables on the mean residence time of tracer through the reactor. The confidence level of data was kept at 0.95 for mean residence time. The objective of the current task is to find the optimized input process variable data for the mean residence time of the tracer by utilizing the pulse technique. Experimental design equations were used to minimize the input process variables. The feasible data of the process variables for the ultimate output of the mean residence time was observed to be 0.341m/s, 0.05kg, 960kg/m^3, and 6.8^o as a liquid velocity, mass of solid, density and column angle, respectively. At such optimized points, the predicted and experimental outcomes were noted for mean residence time were 3.25 and 3.32, respectively. Figure 4.59 represents the response surface designed for the optimization of processes variables for the mean residence time utilizing the system. It can be seen that residuals errors were within ±7%. On the other hand, the comparison between the experimental and predicted results in mean residence time showed that there was approximately a 10 % difference. The parameters were analyzed in terms of numerical coefficients (see Table 4.7). Moreover, the results obtained from the model equation show that the mass of solid was affected very less compared to particle density and velocity of the liquid, while the angle of tapered inverse fluidized bed impacted the mean residence time of the liquid tracer. The experimental and predicted results of the mean residence time are shown in Figure 4.60; approximately, 10 % difference is found in the comparison between the experimental and predicted results.

Table 4.6: Symbols and levels of independent variables were used in response surface methodology

Symbol	Parameter	Unit	Level	Level			
				1	2	3	4
A	Velocity	m/sec	4	0.133	0.214	0.303	0.341
B	Solid mass	kg	3	0.05	0.08	0.1	
C	Particle density	kg/m^3	3	900	930	970	
D	Reactor Angle	degree	2	6.8	8		

Table 4.7: ANOVA table for response surface analysis

Source	Sum of square	F-value	P-value (Prob > F)
Model	4520.73	60.83	< 0.0001
A	3473.28	467.36	< 0.0001
B	13.97	1.88	0.1754
C	253.81	34.15	< 0.0001
D	448.44	60.34	< 0.0001
AB	0.71	0.096	0.7578
AC	21.00	2.83	0.0979
AD	84.75	11.40	0.0013
BC	11.58	1.56	0.2168
BD	0.078	0.011	0.9187
CD	231.43	31.14	< 0.0001

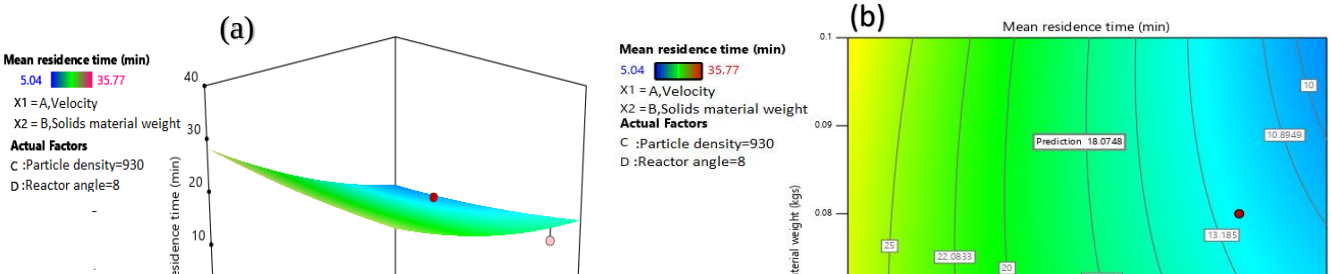

(b)

(d)

(g)

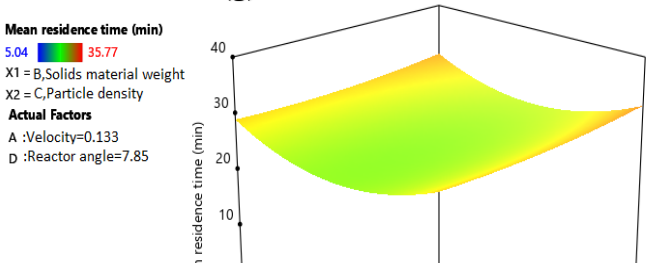
Mean residence time (min)
5.04 35.77
X1 = B,Solids material weight
X2 = C,Particle density
Actual Factors
A :Velocity=0.133
D :Reactor angle=7.85
40
30
20
10
Mean residence time (min)

(h)

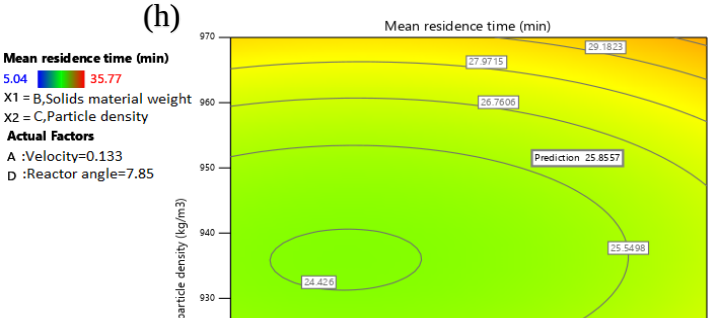
Mean residence time (min)
5.04 35.77
X1 = B,Solids material weight
X2 = C,Particle density
Actual Factors
A :Velocity=0.133
D :Reactor angle=7.85
Mean residence time (min)
970
960
950
940
930
Particle density (kg/m3)
29.1823
27.9715
26.7606
Prediction 25.8557
25.5498
24.426

Figure 4.59. Response surface graph indicating mutual interactions between the input variables to effect of mean residence time. (a) Solids material weight Vs Liquid velocity. (c) Particle density Vs Liquid velocity. (e) Reactor angle Vs Liquid velocity. (g) Particle density Vs Solids material weight. (i)Reactor angle Vs Solids material weight. (k) reactor angle Vs Particle density. And 7(b,d,f,h,j,L) are contour graphs.

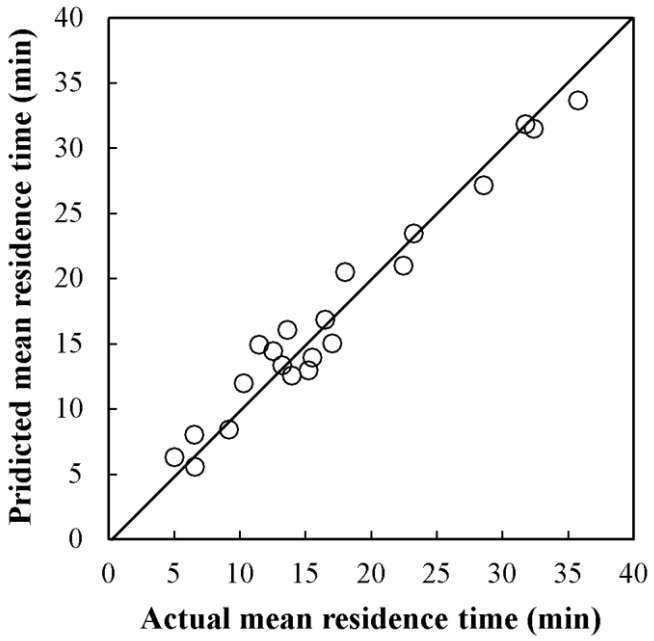

Figure 4.60: Comparison of experimental and predicted values of mean residence by RSM.

Optimization

Numerical analysis was used to perform further optimization. It is discovered that the best local maximum value is at air velocity of 0.329 m/s, initial material weight 0.065 kgs, particle density 958 kg/m3 and reactor angle 6.84 deg. Mean residence time obtained at these conditions is 3.25 min; the desirability for this is 1.00 (Fig. 4.61). Further, the mean residence time was verified with experimental results, which showed 3 min, conforming the agreement in those getting utilizing Optimal (custom) design. Thus it indicated that Optimal (custom) design can be utilizing effectively.

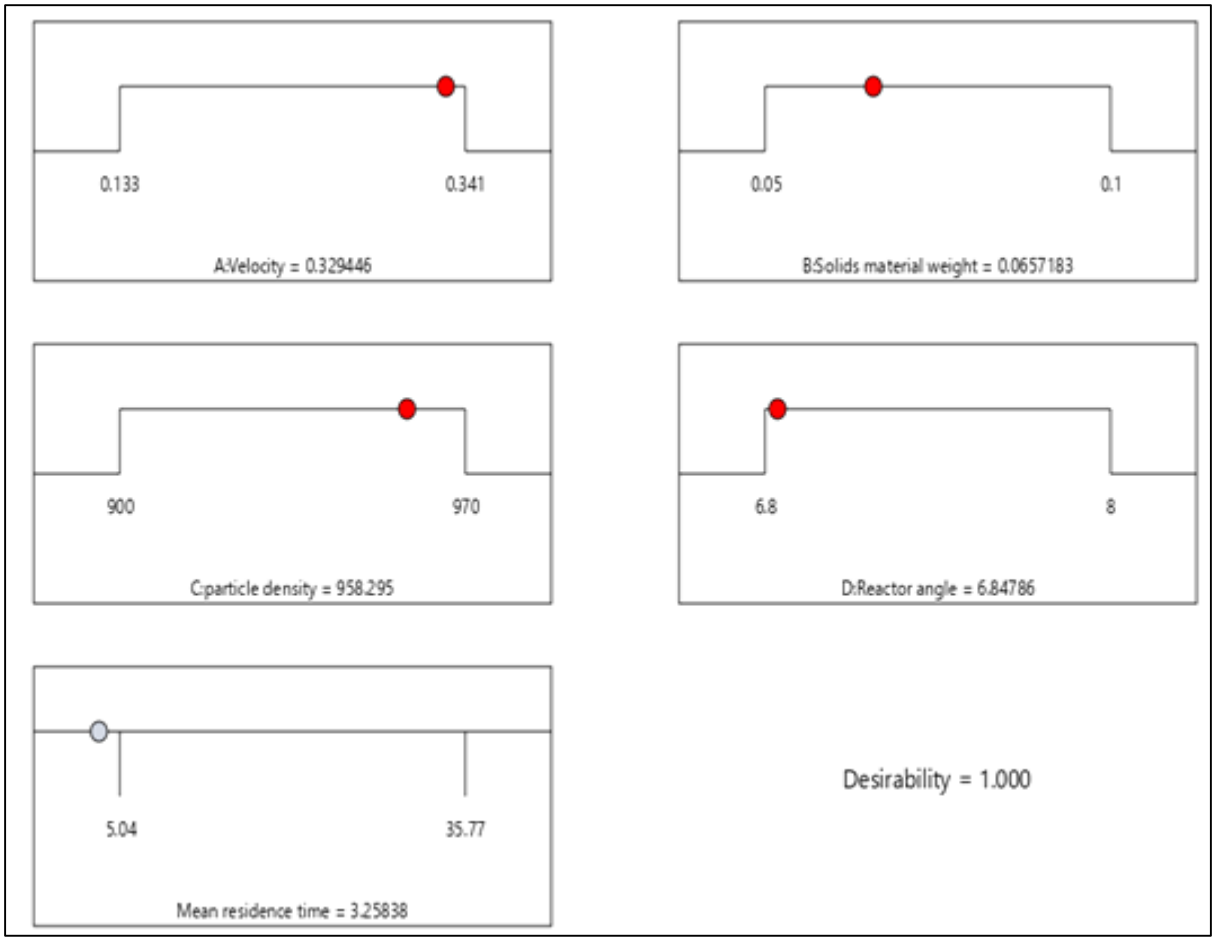

Fig. 4.61 Desirability ramp for numerical optimization obtained by software Design Expert®

4.2.5 Dispersion coefficient

The influence of solid mass and liquid velocity in the tracer axial dispersion coefficient was illustrated in Figure 4.62. The dispersion coefficient decreases with the increasing mass of solid because of less movement of particles in the bed, resulting in weak mixing of the liquid phase. With increasing the liquid velocity, the movement of particles intensifies in the bed, and the liquid in the bed is subjected to more vigorous turbulence, resulting in strong mixing of the liquid phase. Now comparing the experiment and simulation results, the dispersion coefficient showed the higher result for experimental cases. For example, of 0.133 m/s, up to 9% difference was obtained in the value of dispersion coefficient, while up to 25% difference was found for the higher liquid velocity cases. A monotonic increase of dispersion coefficient with increasing liquid velocity was also observed by researchers for classical liquid-solid fluidized beds [30-32].

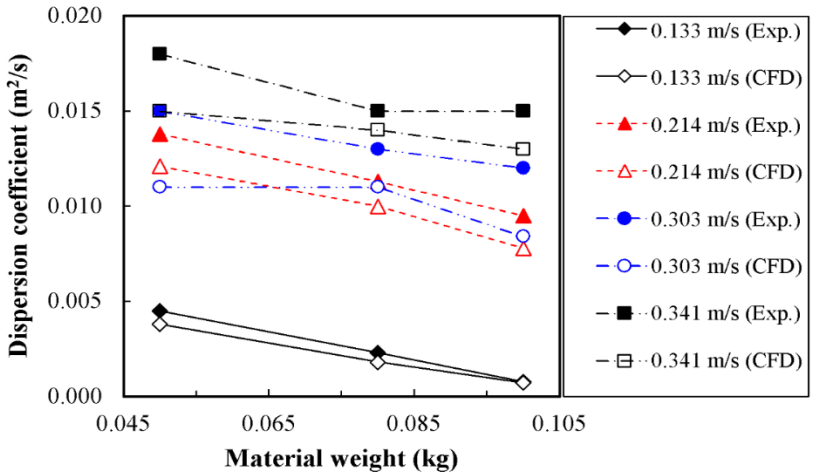

Figure 4.62: Dispersion coefficient with the mass of HDPE solid materials at $\varphi = 6.8^{o}$.

Figure 4.63 shows the dispersion coefficient versus liquid velocity for three different density of solids. The dispersion coefficient increases with increasing liquid velocity and particle density. It is noted that the bed Voidage was the same for all cases. The results indicate that at the same bed Voidage, heavy particles (970 kg/m^3) showed a higher value of dispersion coefficient. As expected, a higher relative liquid velocity was needed to maintain a stable bed Voidage for the heavy particle that typically has a higher terminal velocity. Therefore, higher turbulence was generated and led to a higher extent of mixing. In addition, there is a good agreement between the experiment and CFD results for the case of low liquid velocity (0.133 m/s). However, some deviation can be seen with increasing particle density. In CFD modelling, we considered the shape of particles as perfect spherical, so the liquid flow field can pass the spherical particles quiescently [33], in results a low dispersion coefficient in comparison to that of experimental data, in which perfect spherical particles was not considered.

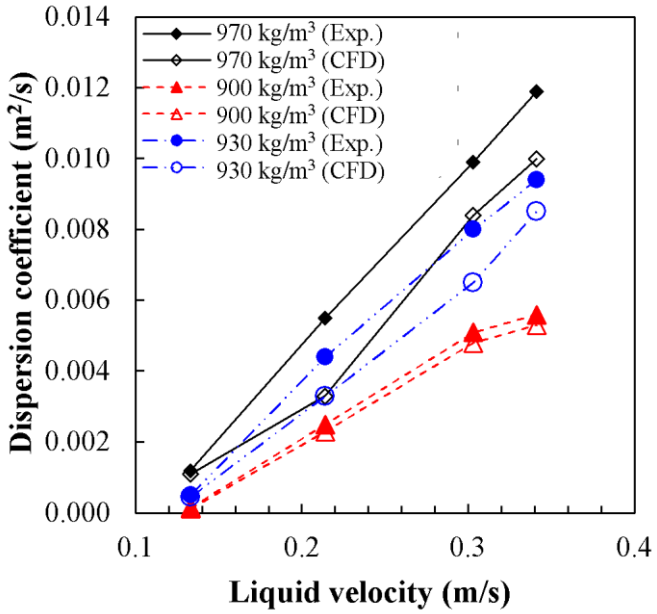

Figure 4.63: Dispersion coefficient versus liquid velocity for different density at initial solid mass, m_s = 0.08kg and φ = 6.8º.

4.2.6 CFD Model for RTD studies

In this study, RTD was analyzed by several numerical investigations with a full 3D Computational Fluid Dynamic model using FLUENT, while the used approach was based on (a) steady-state calculations of the flow velocity pattern and (b) transient calculations of RTD. The motion through the fluidic module of superimposed massless tracer particles was monitored using previously computed velocity fields. The pressure-based solver was utilized for the arrangement of the liquid stream and species transport, in which particular conditions were tackled in a successive way utilizing proper limit conditions and numerical calculations. The unfaltering state solution for the stream conditions was acquired by indicating as limit conditions: the mass stream rate at the inlet feeds, no-slip condition at the walls, and measure pressure of zero at the outlet of the arrangements. Utilizing the arrangement of enduring state liquid stream conditions, the tracer species condition was illuminated as a shaky reproduction, by determining zero diffusive transition as a limit condition at the walls and its solution was then utilized for RTD analysis. Species mass portions of one (for time t = 0 s at pulse inlet of tracer into water) were determined at the channel zone and kept up for resulting time steps. Utilizing the coordinated postprocessor, tracer focus information was obtained at the outlet from time-dependent nodal estimations of the mass fraction

of the tracer. Here, the Eulerian-Eulerian was used to study the RTD of liquid tracer in a 3D tapered inverse fluidized bed and the kinetic theory of granular flow (KTGF) was used for the solid phases. Besides the liquid phase, the solid phase was also like infiltrating continua in the model. The liquid (water) and tracer were assumed as the primary phase, whereas the single or particles phases were assumed as the secondary phase.

In the KTGF model, the irregular movement of the particle was assumed analogous to the motion of molecule in the liquid, was used to close the overseeing conditions for each solid phase. The equation of mass and momentum for the liquid, for single or paired molecule phases in addition to the solid phase, and fluctuating energy were summarized in Table 4.8 [22, 23]. It is known that the drag between liquid-solid phases was generally reliant on the stream behavior, therefore, an accurate definition of drag force is crucial for the correct simulation of tapered inverse fluidized bed RTD studies, which further influence the prediction of RTD.

In the present work, simulations were carried out to find the RTD (mass fraction and volumetric flow rate) behavior of liquid trace when the liquid tracer was injected for 30 s into the reactor. After reaching the steady-state condition, the simulation was run till the liquid tracer reached zero concentration for different velocity, bed heights and different densities of solid materials at different angles of the tapered inverse fluidized bed. The summary of simulation conditions is listed in Table 4.9. The mesh and 3D computational domain of the tapered inverse fluidization are shown in Figure 4.64a and 4.64b, respectively.

Table 4.8: Model equations in the CFD modelling for tapered inverse fluidized bed.

Description	***Continuity equation***	**Number**
Liquid phase	$\frac{\partial}{\partial t}\left(\alpha_L \rho_L\right)+\nabla.\left(\alpha_L \rho_L \vec{W}\right)=0$	(4.21)
Solid phase	$\frac{\partial}{\partial t}\left(\alpha_S \rho_S\right)+\nabla.\left(\alpha_S \rho_S \vec{V}\right)=0$	(4.22)
Balance equation for volume fraction	$\alpha_L+\alpha_S=1$	(4.23)
	Momentum equation	
Liquid phase	$\frac{\partial}{\partial t}\left(\alpha_L \rho_L \vec{W}\right)+\nabla.\left(\alpha_L \rho_L \vec{W}\vec{W}\right)=-\alpha_L \nabla P_L+\nabla.\bar{\bar{\tau}}_L+\alpha_L \rho_L \vec{g}+K_{LS}\left(\vec{V}-\vec{W}\right)$	(4.24)
Stress tensor of liquid phase	$\bar{\bar{\tau}}_L=-\frac{2}{3}\alpha_L \mu_L\left(\nabla \vec{W}\right)\bar{\bar{I}}+\alpha_L \mu_L\left(\nabla \vec{W}+\nabla \vec{W}^T\right)$	(4.25)
Solid phase	$\frac{\partial}{\partial t}\left(\alpha_S \rho_S \vec{V}\right)+\nabla.\left(\alpha_S \rho_S \vec{V}\vec{V}\right)=-\alpha_S \nabla P_S-\nabla P_S+\nabla.\bar{\bar{\tau}}_S+\alpha_S \rho_S \vec{g}+K_{LS}\left(\vec{W}-\vec{V}\right)$	(4.26)
Stress tensor of solid phase	$\bar{\bar{\tau}}_S=\alpha_S\left(\lambda_S-\frac{2}{3}\mu_S\right)\left(\nabla \vec{V}\right)\bar{\bar{I}}+\alpha_S \mu_S\left(\nabla \vec{V}+\left(\nabla \vec{V}\right)^T\right)$	(4.27)
	Constitutive equations of the granular flow	
Solid phase pressure [24]	$P_S=\alpha_S \rho_S \theta_S+2\rho_S\left(1+e_{SS}\right)\alpha_S{}^2 g_0 \theta_S$	(4.28)

Radial distribution function [25]

$$g_0 = \left[1-\left(\alpha_S/\alpha_{S,\max}\right)^{1/3}\right]^{-1} \tag{4.29}$$

Momentum exchange between liquid and solid [26]

$$K_{LS} = \begin{cases} \frac{3}{4} C_D \frac{\alpha_S \alpha_L \rho_L \left(\vec{V}-\vec{W}\right)}{d_S} \alpha_L^{-2.65} & for \quad \alpha_L > 0.8 \\ 150 \frac{\alpha_S (1-\alpha_L)\mu_L}{\alpha_L d_S^{\,2}} + 1.75 \frac{\alpha_S \rho_L \left(\vec{V}-\vec{W}\right)}{d_S} & for \quad \alpha_L \le 0.8 \end{cases} \tag{4.30}$$

Drag coefficient [26]

$$C_D = \begin{cases} \frac{24}{\alpha_L Re_S}\left[1+0.15\left(\alpha_L Re_S\right)^{0.687}\right] & for \quad Re_S \le 1000 \\ 0.44 & for \quad Re_S > 1000 \end{cases} \tag{4.31}$$

Reynolds number

$$Re_S = \frac{\rho_L d_S}{\mu_L}\left|\vec{V}-\vec{W}\right| \tag{4.32}$$

Total solid shear viscosity

$$\mu_S = \mu_{S,col} + \mu_{S,kin} + \mu_{S,fr} \tag{4.33}$$

Viscosity due to collisions [24]

$$\mu_{S,col} = \frac{4}{5}\alpha_S \rho_S d_S g_0 (1+e_{SS})\left(\frac{\theta_S}{\pi}\right)^{0.5} \tag{4.34}$$

Kinetic viscosity [27]

$$\mu_{S,kin} = \frac{\alpha_S \rho_S d_S \sqrt{\theta_S \pi}}{6(3-e_{SS})}\left[1+\frac{2}{5}(1+e_{SS})(3e_{SS}-1)\alpha_S g_0\right] \tag{4.35}$$

Viscosity due to friction [28]

$$\mu_{S,fr} = \frac{P_S \sin\varphi}{2\sqrt{I_{2D}}} \tag{4.36}$$

Stress deviator tensor	$I_{2D} = -\frac{1}{2}\overline{\overline{D}}:\overline{\overline{D}}$ and $\overline{\overline{D}} = \frac{1}{2}\left(\nabla\vec{V} + \nabla\vec{V}^{T}\right) - \frac{1}{3}\left(\nabla.\vec{V}\right)\overline{\overline{I}}$	(4.37)
Bulk viscosity of solid [24]	$\lambda_S = \frac{4}{3}\alpha_S\rho_S d_S g_0\left(1+e_{SS}\right)\left(\frac{\theta_S}{\pi}\right)^{0.5}$	(4.38)
Granular temperature due to solid random motion [24]	$\theta_S = \frac{1}{3}\vec{V}'.\vec{V}'$	(4.39)
Granular temperature conservation equation [29]	$\frac{3}{2}\left[\frac{\partial}{\partial t}\left(\alpha_S\rho_S\theta_S\right) + \nabla.\left(\alpha_S\rho_S\theta_S\vec{V}\right)\right] = \left(-P_S\overline{\overline{I}} + \overline{\overline{\tau}}_S\right):\nabla\vec{V} + \nabla.\left(k_{\theta_S}\nabla\theta_S\right) - \gamma_\theta + \phi_{LS}$	(4.40)
Energy diffusion coefficient for solid [26]	$k_{\theta_S} = \frac{150\rho_S d_S\left(\pi\theta_S\right)^{0.5}}{384\left(1+e_{SS}\right)g_0}\left[1+\frac{6}{5}\alpha_S g_0\left(1+e_{SS}\right)\right]^2 + 2\rho_S{\alpha_S}^2 d_S\left(1+e_{SS}\right)g_0\left(\frac{\theta_S}{\pi}\right)^{0.5}$	(4.41)
Collisional dissipation of the granular fluctuating energy [24]	$\gamma_\theta = \frac{12\left(1-{e_{SS}}^2\right)g_0}{d_S\sqrt{\pi}}\rho_S{\alpha_S}^2{\theta_S}^{\frac{3}{2}}$	(4.42)
Energy exchange between liquid and solid [28]	$\phi_{LS} = -3K_{LS}\theta_S$	(4.43)

Table 4.9: Setup of the CFD model settings

Description	Numerical value
Convergence criteria, discretization, and time step	
Convergence criteria (s)	0.001
Maximum iterations (s)	20
Time step size (s)	0.01
Discretization method	First order upwind scheme
Model precision	Double
Restitution coefficient for solid-wall collision, e_{sw} (-)	0.9
Operating pressure (Pa)	1.013×10^5
Granular viscosity (Pas)	Gidaspow [26]
Granular bulk viscosity (Pas)	Lun et al. [24])
Solid pressure (Pa)	Lun et al. [24]
Radial distribution (-)	Lun et al. [24]
Drag model	Gidaspow [26]
Restitution coefficient for solid-solid collision, e_{ss} (-)	0.9
Specularity coefficient, Φ (-)	No slip condition
Geometry and initial operating condition	
Fluidized bed reactor size (m)	0.59×0.25×0.09 and 0.59×0.22×0.75
Initial volume fraction of solid (-)	0.6
Liquid velocity (m/s)	0.133 - 0.341
Particle diameter (m)	0.02 - 0.035
Density of particle (kg/m^3)	900 - 970
Density of water (kg/m^3)	1000
Initial bed height (m)	0.03 - 0.055

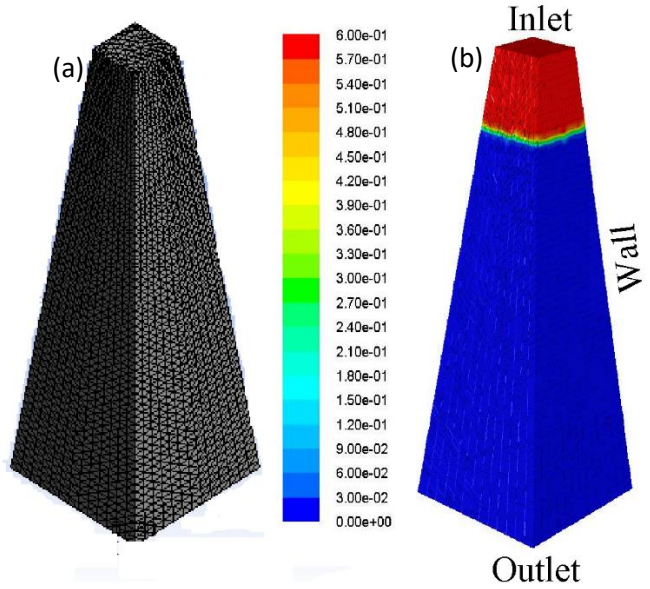

Figure 4.64: Schematic mesh (a) and 3D computational domain (b) of a tapered (φ = 6.8^o) inverse fluidized bed.

4.2.6.1 Grid study

A grid independence study was carried out using three different grid sizes such as coarse (elements of 3515), medium (elements of 19988) and fine (elements of 74157) grids with cells larger and closer than 10 times the particle diameter, respectively. Figure 4.65 shows the fluidized bed height versus time-averaged solids tracer mass fraction for the three grid sizes. Up to 0.2 m bed height, there are no considerable differences in the time-averaged mass fraction for all cases; after that, a significant difference can be seen in the results of coarse grid compared with the medium and fine grid results. Approximately 1% difference is obtained between the fine and medium grid. Therefore, the fine grid was adopted in the present numerical study.

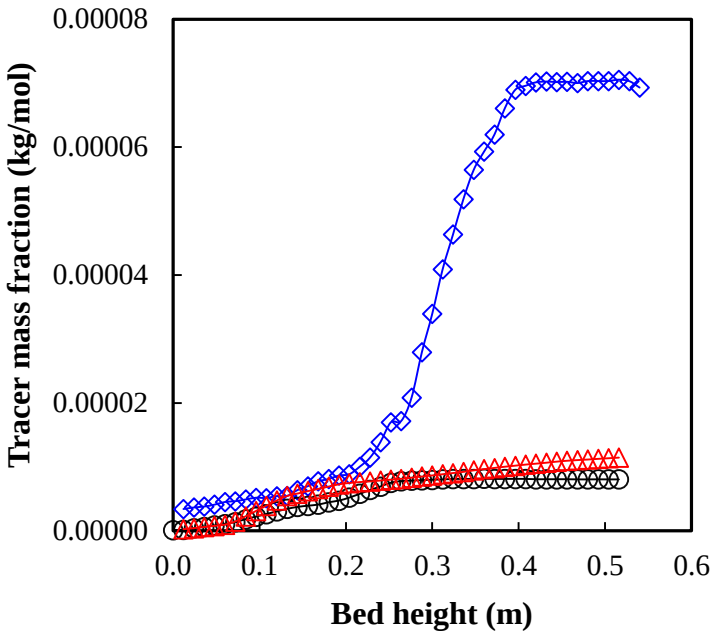

Figure 4.65: Axial profiles of the time-averaged tracer mass fraction for fine (circles), medium (triangles), coarse (diamonds) grid sizes versus bed height of HDPE material at U = 0.133 m/s, m_s = 0.08kg, φ = 8^o.

4.2.7 Mass fraction of tracer analysis using CFD

The contour results of mass fraction throughout the two tapered column angles for HPD, PP and beads for low (0.133 m/s) and high (0.314 m/s) liquid velocity cases are shown in Figure 4.66 and Figure 4.67. For the case of 0.133 m/s and HPD particle, the mass fraction throughout the 6.8^o (Figure 4.66a) shows flat profiles, while these profiles become incline with the increase of column angle 8^o (Figure 4.67a). For the case of high liquid velocity and particle of PP and Beads, the mass fraction profiles are not uniform. The quantitative results of mass fraction of tracer along with the height of the bed at 0.05kg, 0.08kg, and 0.10kg mass of PP materials for different liquid velocity are shown in Figure 4.68a -4.68c. In Figure 4.68a, at 0.05 kg PP solid materials, the mass fraction increases rapidly along with the bed height for a low liquid velocity of 0.133 m/s. There is a sudden rise up to 0.1 m bed height, after the bed height of 0.4 m is reached, the

mass fraction seems to achieve saturation as it is constant there inwards. For other velocities, the mass fraction remains unchanged. In Figure 4.68b (0.08 kg of PP), the mass fraction is found to be increased along with the bed height with the increase of lower liquid velocity in comparison to that of higher liquid velocity. Only at 0.314 m/s velocity, the mass fraction remains unchanged with the bed height. In Figure 4.68c (0.10 kg of PP), it is much clear that the liquid velocity significantly affects the mass fraction of the tracer along with the bed height. Additionally, the maximum mass fraction profile along the bed can be seen for the liquid velocity of 0.133 m/s, it means that this liquid velocity is an optimum liquid flow through the column.

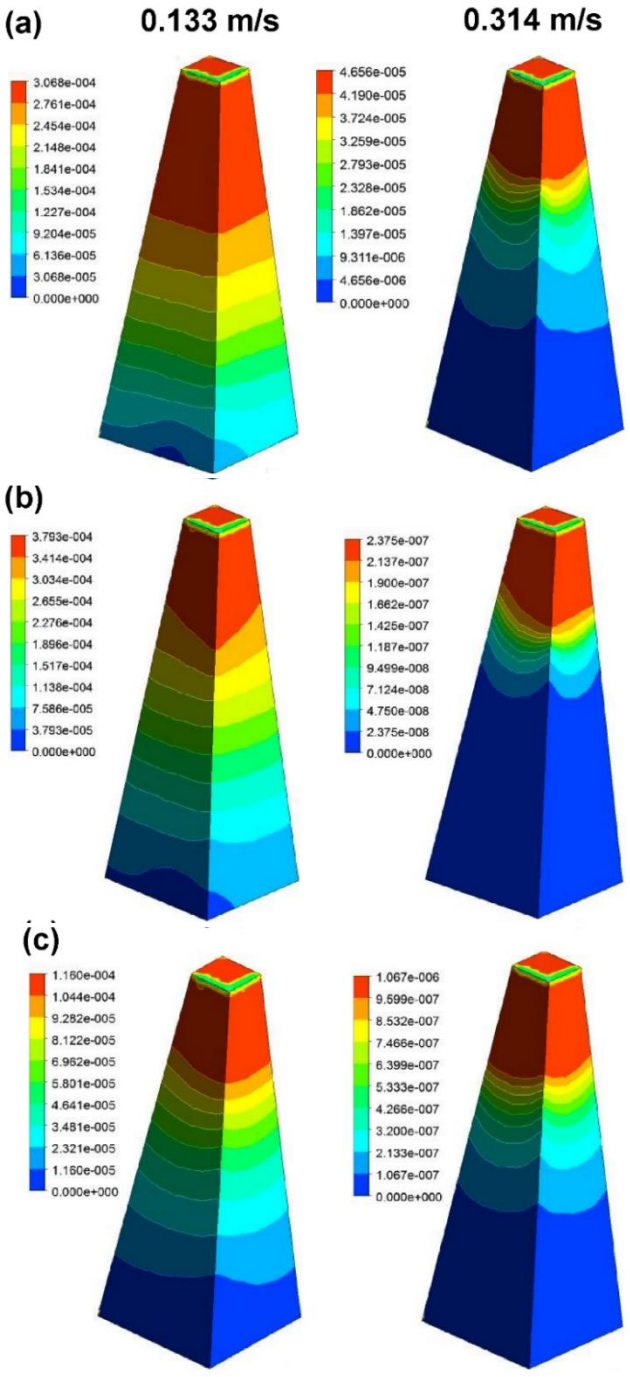

Figure 4.66: Mass fractions of tracer for (a) HPD, (b) PP, and (c) Beads for low (left column) and high (right column) velocity of liquid at φ = 6.8^{o} and m_s = 0.05kg.

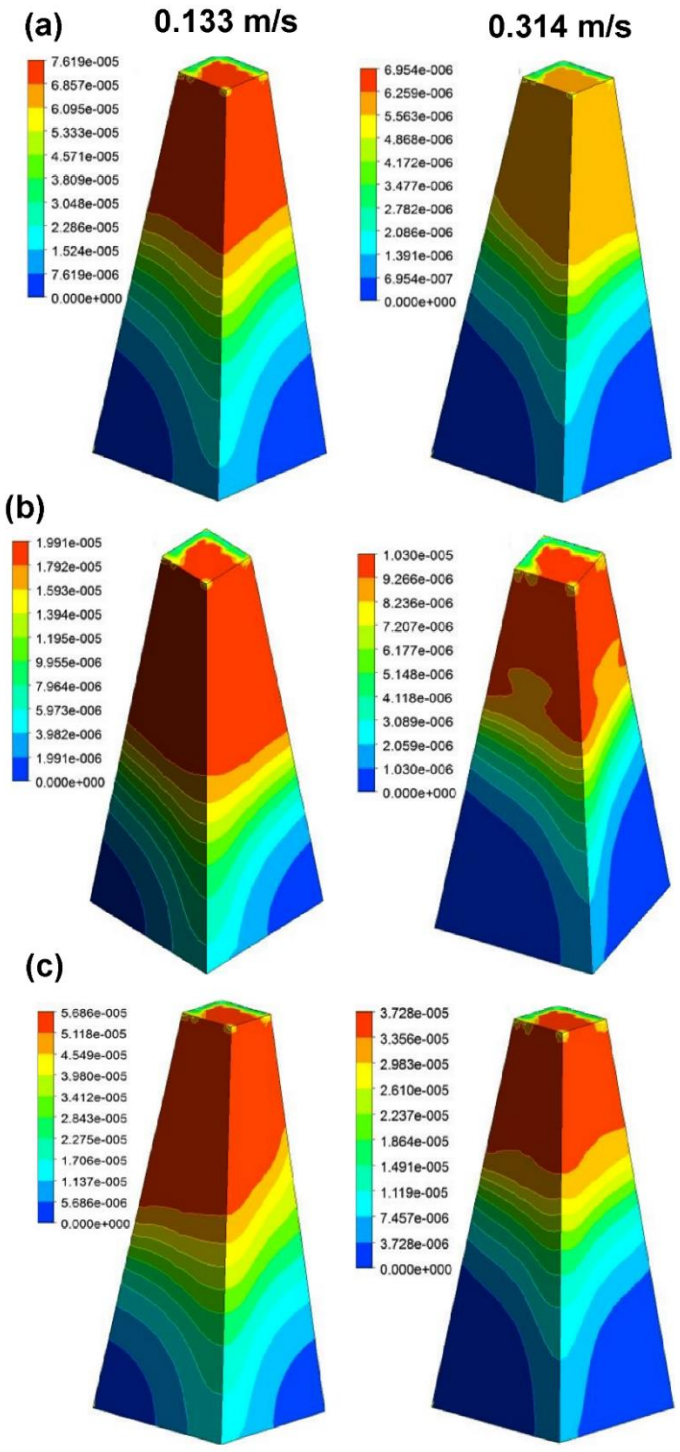

Figure 4.67: Mass fractions of tracer for (a) HPD, (b) PP, and (c) Beads for low (left column) and high (right column) velocity of liquid at $\varphi = 8^{o}$ and $m_s = 0.05$kg.

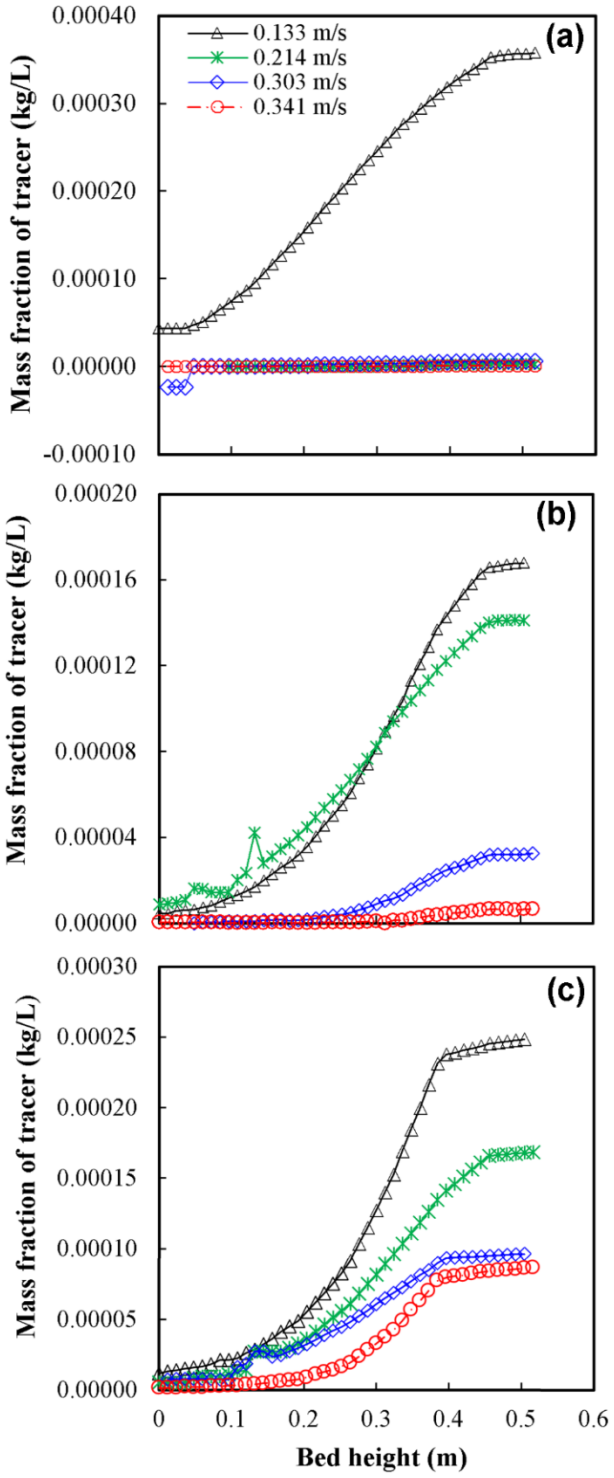

Figure 4.68: Mass fraction tracer along the height of the bed at (a) m_s = 0.05kg, (b) m_s = 0.08kg, and (c) m_s = 0.10kg PP solid materials for different liquid velocity at $\varphi = 8^o$.

The mass fraction results along the bed height for 0.05 to 0.1 kg solid are shown in Figure 4.69. For all cases, the mass fraction initially remains lower till the bed height of 0.2 m. When the bed height further increases, the mass fraction abruptly increases specifically for 0.10 kg. The mass fraction remains almost unchanged when the bed height reaches 0.35 m. For material weight is 0.08 kg, the rise in the mass fraction is significant but not as highly sensitive when material weight is 0.05 kg. With a material weight is 0.05 kg, the mass fraction slowly but steadily rises. In all these three cases, it is observed that after a certain bed height the mass fraction tries to become constant.

Figure 4.71 shows the mass fraction for increasing liquid velocity of 0.133 m/s to 0.341 m/s at 0.05 kg mass of HDPE solid. Here, it is observed that irrespective of any liquid velocity, the mass fraction upon reaching bed height of 0.3 m remains constant. The mass fraction starts increasing with increasing along with bed height, but the highest mass fraction is for the lowest liquid velocity and vice versa. In Figure 4.71, the mass fraction for two-column angles increasing with bed height is depicted. The trend is similar to preceding observations that the mass fraction increases up to a certain height and then remains constant. However, for the low angle of the column (6.8^o), the rise in mass fraction occurs at lower bed heights and for the higher column angle (8^o) the mass fraction rise is quite later. However, in the case of a low degree of the column angle, the steadiness is reached earlier than the high degree of the column angle.

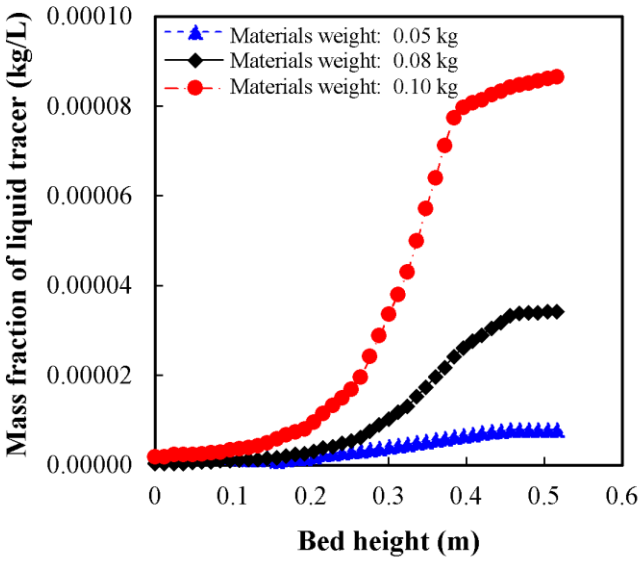

Figure 4.69: Mass fraction of tracer along bed height for the different mass of solid at U = 0.303 m/s and φ = 8^o.

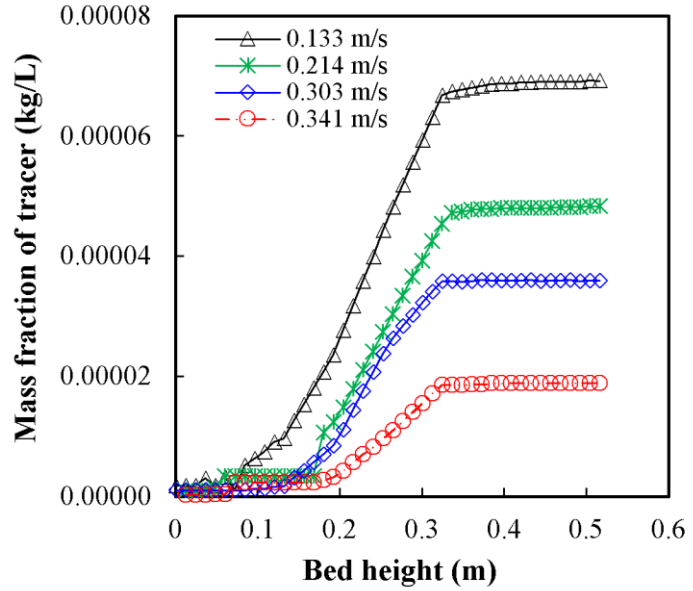

Figure 4.70: Mass fraction of tracer along with bed height for different liquid velocity with the mass of HDPE solid, m_s = 0.05kg and at φ = 8°.

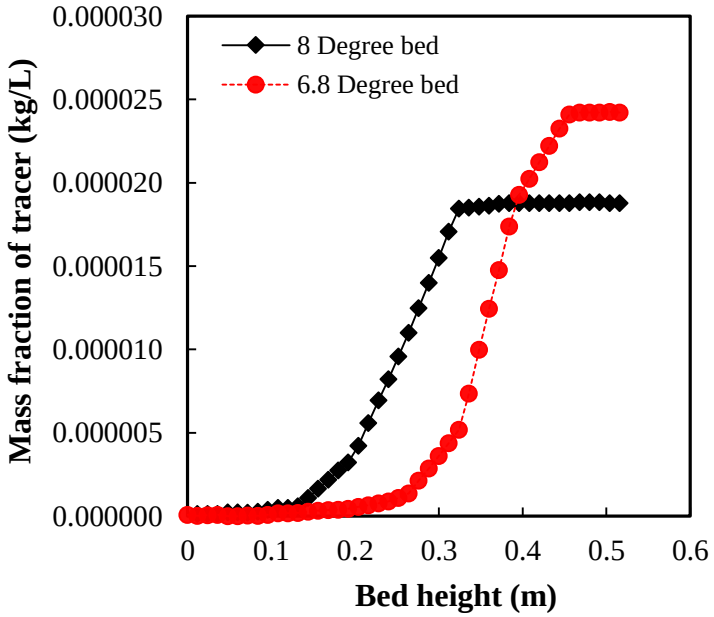

Figure 4.71: Mass fraction of tracer along bed height for the two different column angles at U = 0.133 m/s and mass of HDPE solid, m_s = 0.08kg.

4.3 Synthetic textile waste water treatment

Introduction

In this chapter, an adsorbent was selected based on removal efficiency for dye removal, COD removal, Turbidity removal, DO enhancement and then characterization analysis of the developed adsorbent was discussed in detail. The study was done for simultaneous removal of those contaminants and using coated raw wheat bran on Polypropylene (PP) as an adsorbent in batch mode was performed. In batch analysis, the central composite design (CCD) method of response surface methodology was utilized to find the impact of pH, initial concentration, adsorbent dose and air flow timing on removal efficiency of Dye removal, COD removal, and Turbidity removal and DO enhancement. However, adsorption isotherms and rate kinetics were also investigated.

4.3.1 Characterization of adsorbents

a. SEM analysis coupled with EDS

The Scanning electron micrograph (SEM) analyzer used for study of the surface morphology from SEM micrographs the image confirms that the sample exhibits the form of the coarse surface but after coated on the PP the surface becomes porous and homogeneous shown in Fig.4.72 (a–d). Particle aggregation has been disrupted and particles are uniformly dispersed, creating much surface area for adsorption. Further elementary measurement of the raw wheat bran and the coated wheat bran on PP was carried out with the help of EDS to measure its chemical distribution is observed in Fig. 4.73 (a, b). It was noted that they contain carbon and oxygen composition in cellulose was (49.40 and 50.60) wt % respectively. However, after coating the wheat bran on to PP, the carbon wt% increases to 58.53wt% the oxygen decreases to 38.94 wt% (Table 4.10).Wheat bran, resulting in a raise of carbon composition (Table 4.10) and the improvement of active adsorption sites. This develops the behavior of wheat bran extraction

b. **FTIR**

From the FTIR spectra of Fig. 4.74 (a, b), it was understood that both the wheat bran and the coated wheat bran on PP had equal trends, but the intensity of the absorption bands was varied. In the natural wheat bran, the peaks at 3400 cm^{-1} appeared the stretching vibration, suggesting the existence of cellulose. From the FTIR spectra of Fig.4.74 (a, b), it was understood that both the wheat bran and the coated wheat bran on PP had equal trends, however, the intensity of the absorption bands was varied. Similarly, the carboxyl group adsorption band at 1538 cm^{-1} was killed by coated wheat bran on PP. The peaks at 1157, 1241, 1024, and 1076 cm^{-1} indicate the existence of the C-O-C group in the natural wheat bran. Also, peaks at 860, 766, and 723 cm^{-1} have vanished in coated wheat bran on PP. There is a peak of 1657 cm^{-1} in the raw wheat bran due to the C = O group. The peaks are 1202 cm^{-1} and 1308 cm^{-1}, showing the presence of C-C and C - O groups in the coated wheat bran on PP.

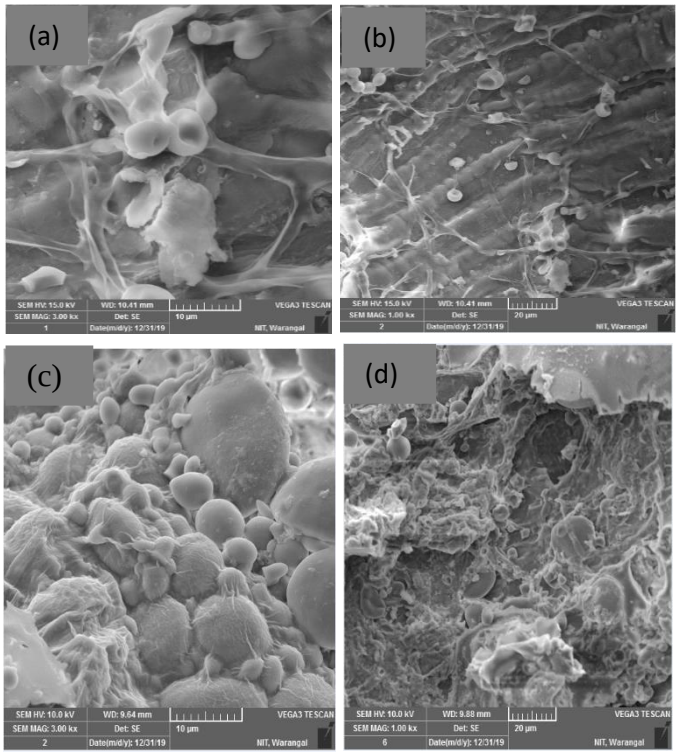

Fig. 4.72 SEM of (a) Raw wheat bran at 10 µm resolutions, (b) Raw wheat bran at 20 µm resolutions, (c) Coated raw wheat bran on PP at 10 µm resolutions, and (d) Coated raw wheat bran on PP at 20 µm resolution.

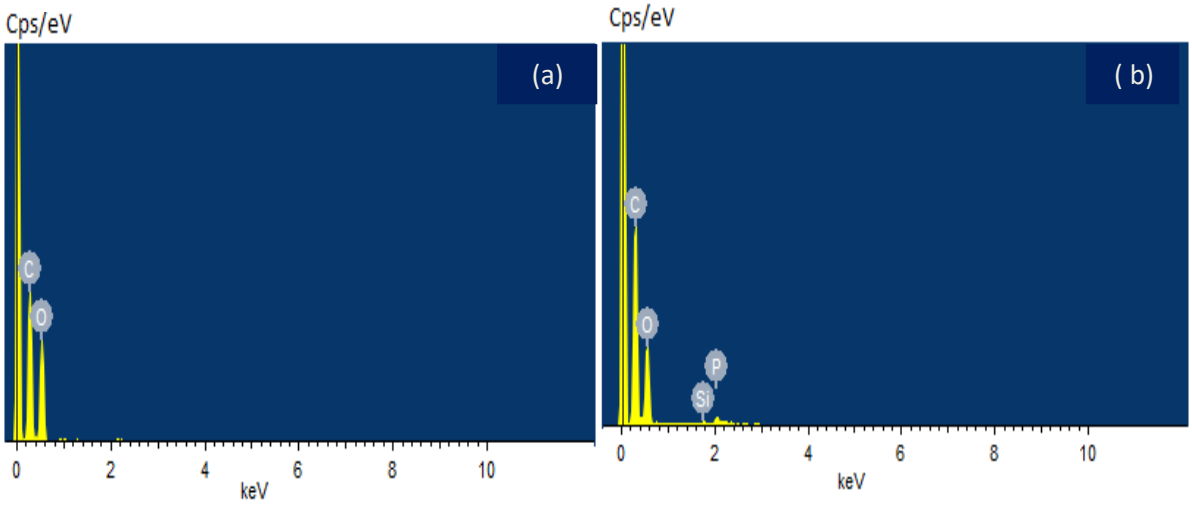

Fig.4.73 EDS spectra of the adsorbent (a) Raw wheat bran and (b) Raw wheat bran after coated on PP.

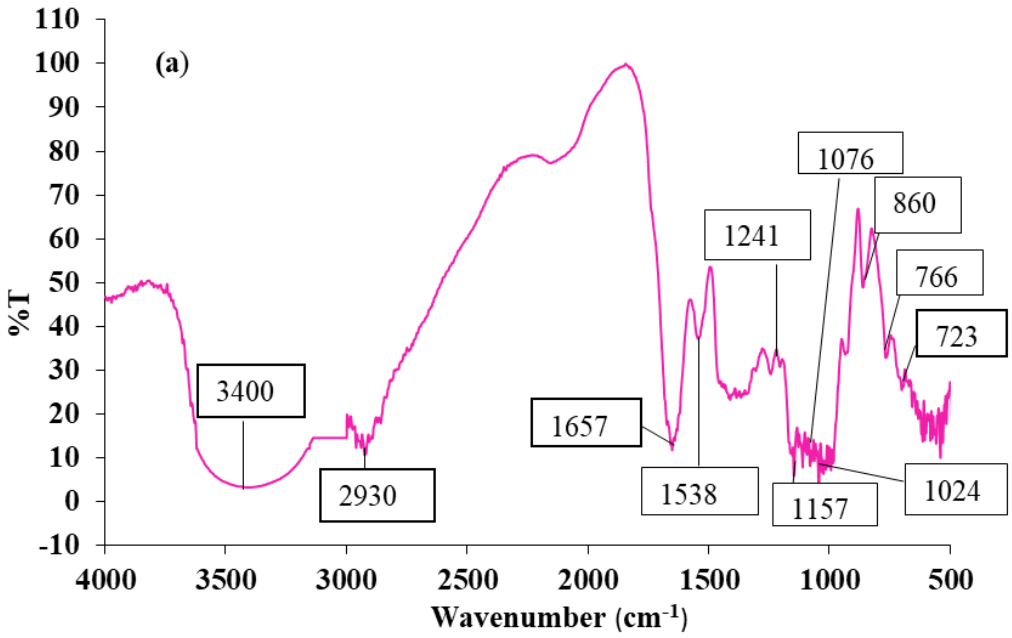

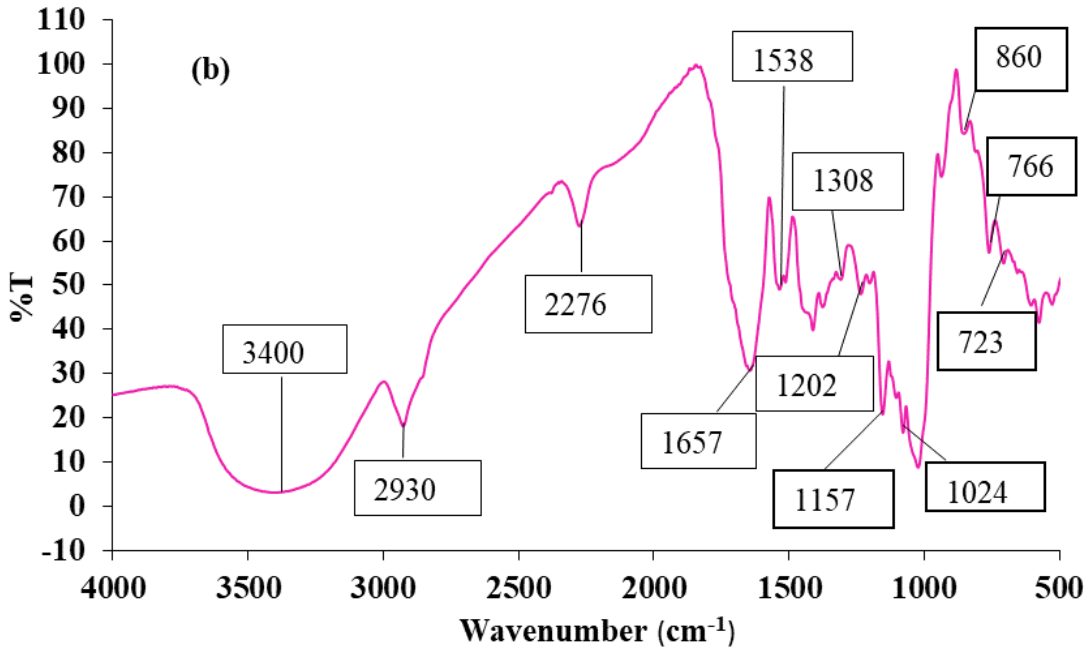

Fig. 4.74 FTIR analysis of (a) Raw wheat bran, and (b) Raw wheat bran after coated on PP

Table 4.10 Radical measurement of raw wheat bran and raw wheat bran after coated on PP.

Element	Raw wheat bran		Raw wheat bran after coating on Polypropylene	
	Weight%	Atomic%	Weight%	Atomic%
C	49.40	56.53	58.53	65.93
O	50.60	43.47	38.94	32.93
Si	x	x	0.66	0.32
P	x	x	1.87	0.82

4.3.2 Batch experiments

Batch experiments were performed for individual removals and dye using selected adsorbent based on design of experiments to optimise operating variables as an example initial concentration, air flow timing, adsorbent dose and pH for maximum removal of Dye removal, COD removal, and Turbidity removal and DO enhancement.

Table 4.11 Removal of Dye removals, COD removal, and Turbidity removal and DO enhancement at different parameter

For Dye removal %

Concentration (mg/lit)	Air flow contact time (hr) ,1.5grams, pH=1.6								
	4	8	12	16	20	24	28	32	36
100	56.71	64.85	68.28	73.5	75.1	77.21	82.4	83.98	88.15
200	43.54	54.18	67.51	69.18	72.5	74.61	76.18	77.41	79.12
350	38.17	46.22	56.42	60.10	66.1	69.18	72.21	73.84	76.14
450	33.12	43.14	51.19	54.17	55.1	58.25	61.12	65.13	68.7

For Dye removal %

Concentration (mg/lit)	Air flow contact time (hr) ,1.5grams, pH= 2.5								
	4	8	12	16	20	24	28	32	36
100	54.01	62.31	65.21	68.21	70.1	73.4	75.12	78.32	81.16
200	41.21	48.48	51.14	57.25	65.2	68.71	71.12	73.17	73.57
350	35.12	43.77	53.13	56.70	63.3	65.71	68.11	71.01	71.13
450	33.24	41.70	48.73	53.41	54.0	57.11	60.55	64.68	67.6

For Dye removal %

Concentration (mg/lit)	Air flow contact time (hr) ,1.5grams, pH= 3.3								
	4	8	12	16	20	24	28	32	36
100	53.27	61.34	64.32	67.55	69.2	72.23	74.68	76.23	78.71
200	36.18	47.57	50.57	55.23	64.2	67.41	69.91	72.54	72.95
350	34.12	41.37	52.31	55.31	62.2	64.11	67.59	69.21	70.21
450	32.16	40.11	46.25	52.21	53.1	56.17	59.34	63.13	66.3

For Dye removal %

Concentration (mg/lit)	Air flow contact time (hr) ,1.5grams, pH=5								
	4	8	12	16	20	24	28	32	36
100	51.31	58.13	63.2	66.84	68.5	73.5	73.5	74.5	76.8
200	35.68	45.68	48.69	53.65	63.8	66.87	68.92	71.64	75.32
350	33.25	38.96	51.74	53.84	59.1	62.58	65.32	67.32	73.85
450	30.58	38.56	45.24	49.23	51.2	55.32	58.69	62.35	65.3

For Dye removal %

Concentration (mg/lit)	Air flow contact time (hr) ,1.5grams, pH=8.5								
	4	8	12	16	20	24	28	32	36
100	50.23	55.36	62.57	65.32	67.4	71.62	72.1	73.6	75.95
200	33.65	44.32	47.85	52.87	62.4	65.21	67.95	70.58	73.85
350	32.65	37.65	50.23	52.85	58.6	61.23	64.17	66	69.58
450	29.35	37.28	38.42	47.36	51.2	54.23	57.36	61.23	64.3

For Dye removal %

Concentration (mg/lit)	Air flow contact time (hr) ,5.6grams, pH=1.6								
	4	8	12	16	20	24	28	32	36
100	59.71	66.85	71.28	75.5	77.1	79.21	83.21	88.98	93.25
200	45.65	58	69.34	73	75.3	76.84	78.54	79.35	83.54

350	41.23	48.32	61.35	63.20	68.2	73.21	75.34	78.32	79.24
450	35.24	45.27	55.21	58.17	60.1	63.25	65.2	68.34	75.1

For Dye removal %

Concentration (mg/lit)	Air flow contact time (hr) ,5.6grams, pH= 2.5								
	4	8	12	16	20	24	28	32	36
100	56.01	64.21	68.33	71.21	73.1	75.32	78.11	81.13	89.32
200	44.11	50.49	53.24	59.89	68.1	74.25	75.84	77.25	81.17
350	38.33	46.15	52.35	58.36	67.2	73.71	73.25	76.01	77.34
450	36.14	45.65	51.13	57.35	65.0	68.21	70.23	73.68	75.3

For Dye removal %

Concentration (mg/lit)	Air flow contact time (hr) ,5.6grams, pH= 3.3								
	4	8	12	16	20	24	28	32	36
100	55.63	63.34	66.32	70.55	71.2	74.23	76.68	79.23	86.71
200	42.18	49.17	52.51	58.13	67.1	69.41	73.91	76.54	79.15
350	37.2	45.37	51.31	57.31	66.2	72.11	73.35	75.21	75.31
450	35.23	44.13	49.15	55.21	63.1	66.17	69.34	72.13	74.3

For Dye removal %

Concentration (mg/lit)	Air flow contact time (hr) ,5.6grams, pH=5								
	4	8	12	16	20	24	28	32	36
100	54.11	62.21	65.21	69.14	69.5	74.5	76.15	78.15	85.1
200	41.18	48.68	51.19	57.15	66.8	68.87	72.92	75.14	78.12
350	36.25	44.96	52.74	56.84	65.1	68.18	72.12	74.12	74.15
450	34.58	43.56	48.24	54.23	61.2	65.32	67.69	68.15	73.1

For Dye removal %

Concentration (mg/lit)	Air flow contact time (hr) ,5.6grams, pH=8.5								
	4	8	12	16	20	24	28	32	36
100	53.13	61.16	63.57	68.12	68.4	73.12	75.1	77.6	83.15
200	38.65	47.32	50.85	55.87	65.4	67.21	71.15	74.18	74.85
350	35.65	43.65	51.23	55.85	64.6	67.23	71.17	73	73.58
450	33.35	42.28	46.42	53.36	60.2	64.23	65.36	66.23	74.3

For Dye removal %

Concentration (mg/lit)	Air flow contact time (hr) ,10grams, pH=1.6								
	4	8	12	16	20	24	28	32	36
100	76.71	84.85	88.28	94	95.4	97.11	97.4	97.86	98.05
200	75.54	84.28	87.71	93.68	94.7	96.71	97.28	97.61	97.82
350	65.57	84.28	96.44	96.50	96.6	96.68	97.15	97.27	97.27
450	68.79	83.74	94.19	94.97	95.2	95.25	95.29	95.43	95.7

For Dye removal %

Concentration (mg/lit)	Air flow contact time (hr) ,10grams, pH= 2.5								
	4	8	12	16	20	24	28	32	36
100	71.05	81.4	85.42	88.25	90.4	91.4	91.94	92.68	93.6
200	69.55	80.48	84.82	87.54	89.8	90.71	91.22	92.17	92.97
350	32.82	42.77	76.25	79.70	84.3	84.71	86.9	87.31	87.57

450	63.97	87.70	89.73	91.41	92.0	93.11	93.55	93.68	94.7

For Dye removal %

Concentration (mg/lit)	Air flow contact time (hr) ,10grams, pH= 3.3								
	4	8	12	16	20	24	28	32	36
100	58.57	71.14	85.42	86.25	88.2	91.14	92.48	93.11	93.71
200	56.28	70.57	84.57	85.71	87.6	90.54	91.91	92.54	93.05
350	32.82	42.77	76.25	79.70	84.3	84.71	86.9	87.31	87.57
450	28.36	39.36	70.27	76.09	83.8	83.57	84.71	84.85	85.8

For Dye removal %

Concentration (mg/lit)	Air flow contact time (hr) ,10grams, pH=5								
	4	8	12	16	20	24	28	32	36
100	75.71	88.57	90	92	92.2	92.82	93.42	94	94.85
200	86.25	87.54	88.48	90.4	91	92.11	92.74	93.4	93.8
350	31.14	36.28	61.28	72.85	76.6	79.55	83.68	83.36	83.32
450	49.79	67.07	74.02	75.13	77.2	85.77	86.21	86.04	86.0

For Dye removal %

Concentration (mg/lit)	Air flow contact time (hr) ,10grams, pH=8.5								
	4	8	12	16	20	24	28	32	36
100	62.28	75.6	79.11	85.42	87.9	88.42	89.114	90.28	91.14
200	55.71	70.22	72.82	84.74	87.6	87.91	88.42	89.88	90.42
350	20.28	41.63	60.66	69.98	80.6	77.07	86.15	89.27	89.30
450	19.63	37.18	58.42	65.50	74.1	76.66	78.28	79.2	81.5

For COD removal %

Concentration (mg/lit)	Air flow contact time (hr) ,1.5grams, pH=1.6								
	4	8	12	16	20	24	28	32	36
100	68.5	74.6	79.1	85.18	86.9	88.4	89.51	90.6	93.3
200	66	73.38	80.16	81.01	82.2	82.50	82.753	83	83.58
350	62.61	70.92	71.41	72.66	73.6	74.18	75.31	75.71	75.96
450	10.87	29.13	31.18	32.13	35.6	45.11	53.36	59.13	68.13

For COD removal %

Concentration (mg/lit)	Air flow contact time (hr) ,1.5grams, pH= 2.5								
	4	8	12	16	20	24	28	32	36
100	50.6	53.15	58.12	65.15	67.3	71.16	74.34	79.11	83.15
200	48.76	51.15	55.61	62.07	64.5	65.92	66.69	67.58	67.34
350	30.07	43.84	45	45.55	51.2	60.07	63.615	64.92	66.44
450	23.5	38.2	43.1	45.3	51.5	61.5	62.18	63.6	65.1

For COD removal %

Concentration (mg/lit)	Air flow contact time (hr) ,1.5grams, pH= 3.3								
	4	8	12	16	20	24	28	32	36
100	48.3	51.5	56.3	61.84	66.5	70.6	72.84	76.5	80.6
200	46.38	50.76	53.92	61.15	62.5	64.65	65.692	66.64	66.88
350	26.15	42.56	43.46	44.38	48.8	55.89	61.769	62.32	65.07
450	8.907	17.76	19.98	23.92	33.5	55.90	58.6	60.30	62.07

For COD removal %

Concentration (mg/lit)	Air flow contact time (hr) ,1.5grams, pH=5								
	4	8	12	16	20	24	28	32	36
100	38.9	41.38	47.84	56.15	62.0	67.46	69.692	71.16	78.61
200	44.3	48.46	52.30	58.29	61.7	63.53	64.292	65.04	66.12
350	25.6	41	41	42	46.5	55	58.3	61.5	63.9
450	1.284	15.52	18.75	21.87	22.3	27.35	47.046	50.52	58.90

For COD removal %

Concentration (mg/lit)	Air flow contact time (hr) ,1.5grams, pH=8.5								
	4	8	12	16	20	24	28	32	36
100	36.5	40.6	45.5	55	60	65.4	68.25	70.8	76.1
200	21.23	23.30	26.07	27.69	28.6	34.76	43.538	62.38	64.8.
350	12.76	20.46	23.07	25.69	26.9	31.23	41.538	60.69	61.84
450	0.723	10.53	14.38	18.30	21.0	25.92	41.307	50.53	56.61

For COD removal %

Concentration (mg/lit)	Air flow contact time (hr) ,5.6grams, pH=1.6								
	4	8	12	16	20	24	28	32	36
100	70.5	76.6	81.1	87.18	89.9	90.4	91.51	93.6	95.1
200	68	75.38	83.16	84.01	85.2	86.50	88.85	89	92.58
350	65.61	72.92	73.41	75.66	77.6	78.18	79.31	81.53	83.96
450	13.87	31.13	33.18	35.13	38.6	48.11	57.36	63.13	73.13

For COD removal %

Concentration (mg/lit)	Air flow contact time (hr) ,5.6grams, pH= 2.5								
	4	8	12	16	20	24	28	32	36
100	55.36	57.15	63.12	68.15	71.3	73.26	76.34	81.11	86.35
200	51.76	57.15	59.61	65.07	66.5	68.92	73.69	71.58	73.34
350	38.07	46.84	48	51.55	55.2	65.07	69.615	71.92	79.14
450	15.5	30.2	45.1	43.3	51.5	61.5	62.18	63.6	65.1

For COD removal %

Concentration (mg/lit)	Air flow contact time (hr) ,5.6grams, pH= 3.3								
	4	8	12	16	20	24	28	32	36
100	53.3	55.5	62.3	66.84	69.5	72.6	75.41	78.3	83.1
200	48.18	53.76	56.92	63.15	65.5	67.65	68.692	69.64	71.88
350	35.15	45.56	46.16	49.18	51.8	63.19	67.769	70.32	75.07
450	13.90	25.76	30.98	35.92	38.5	58.90	60.6	61.10	63.07

For COD removal %

Concentration (mg/lit)	Air flow contact time (hr) ,5.6grams, pH=5								
	4	8	12	16	20	24	28	32	36
100	41.9	45.38	55.84	58.15	65.0	71.46	73.692	76.16	81.61
200	46.3	51.46	55.30	61.29	64.7	65.53	67.292	69.04	70.12
350	32.6	43	45	48	50.5	61	65.3	68.5	73.1
450	1.284	18.52	21.75	33.87	37.3	56.35	58.046	59.52	62.76

For COD removal %

Concentration (mg/lit)	Air flow contact time (hr) ,5.6grams, pH=8.5								
	4	8	12	16	20	24	28	32	36
100	38.5	43.6	53.5	56	63	68.4	71.25	73.8	80.1
200	28.23	33.30	41.07	48.69	51.6	55.76	58.538	66.38	68.8.
350	35.76	41.46	44.07	46.69	47.9	48.23	51.538	62.69	65.84
450	0.923	13.53	17.38	20.30	23.0	27.92	43.307	52.53	61.61

For COD removal %

Concentration (mg/lit)	Air flow contact time (hr) ,10grams, pH=1.6								
	4	8	12	16	20	24	28	32	36
100	70.5	76.6	83.4	86.58	88.9	89.4	90.51	92.6	95
200	68	75.38	82.76	83.01	83.2	83.50	83.753	84	84
350	64.61	72.92	73.41	73.66	74.1	75.38	76.123	76.61	76.86
450	11.87	21.23	24.18	27.13	41.6	54.21	63.753	71.13	74.83

For COD removal %

Concentration (mg/lit)	Air flow contact time (hr) ,10grams, pH= 2.5								
	4	8	12	16	20	24	28	32	36
100	51.6	56.87	63.71	67.67	69.7	75.6	76.912	81.71	85.67
200	50.76	58.15	60.61	63.07	65.5	66.76	67.507	68	68.24
350	31.07	45.84	46	46.15	53.2	63.07	64.615	65.92	68.44
450	25	41	45	46.	52	62.5	63.58	64.5	67.5

For COD removal %

Concentration (mg/lit)	Air flow contact time (hr) ,10grams, pH= 3.3								
	4	8	12	16	20	24	28	32	36
100	50.5	55.5	62.3	66.84	68.5	73.6	75.84	80.5	83.6
200	48.38	53.76	58.92	63.15	66.5	66.65	66.692	67.64	68.15
350	28.15	44.56	45.46	45.38	51.8	58.89	62.769	64.32	66.07
450	9.907	18.76	20.98	24.92	34.5	57.90	60.6	61.30	63.07

For COD removal %

Concentration (mg/lit)	Air flow contact time (hr) ,10grams, pH=5								
	4	8	12	16	20	24	28	32	36
100	40.92	43.38	48.84	58.15	63.0	70.46	71.692	73.16	81.61
200	46	52.46	56.30	61.29	65.7	66.53	66.292	67.04	67.92
350	27.6	43	44	45	48.5	57	60.3	63.5	65.9
450	1.284	16.52	19.75	23.87	27.3	29.35	49.046	51.52	60.90

For COD removal %

Concentration (mg/lit)	Air flow contact time (hr) ,10grams, pH=8.5								
	4	8	12	16	20	24	28	32	36
100	38.5	42.6	47.5	57	62	68.4	70.25	72.8	78.6
200	22.23	24.30	28.07	28.69	29.6	35.76	44.538	63.38	65.8.
350	13.76	21.46	24.07	26.69	28.9	32.23	43.538	62.69	63.84
450	0.923	11.53	15.38	20.30	23.0	26.92	42.307	51.53	58.61

For Turbidity removal %

Concentration	Air flow contact time (hr) ,1.5grams, pH=1.6

(mg/lit)	4	8	12	16	20	24	28	32	36
100	85.75	87.31	88.14	88.58	89.5	91.54	91.74	92.85	93
200	83.5	86.1	87.1	87.86	88.8	89.1	90	90.3	91
350	76.3	78.1	80.1	81.35	82.6	83	83.75	84	86.1
450	73.5	75.5	76.3	76.89	77.1	78.4	79.5	80.7	82

For Turbidity removal %

Concentration (mg/lit) — Air flow contact time (hr) ,1.5grams, pH= 2.5

	4	8	12	16	20	24	28	32	36
100	86.2	89.1	89.5	89.93	90.7	91.8	92	92.9	93.5
200	84.7	88.2	89.3	90.66	90.1	90.8	91.85	92	92.3
350	78.6	79.1	80.6	82.54	83.4	84.7	86.54	87.4	91.2
450	49.6	53.2	57.2	62	67.1	73	78.33	83.2	85.3

For Turbidity removal %

Concentration (mg/lit)	4	8	12	16	20	24	28	32	36
100	87.1	89.5	89.8	90	90.9	92.1	92.54	93	93.8
200	85.5	88.7	90.1	90.74	90.5	91	91.94	92.5	92.5
350	82.1	83.1	83.5	83.87	85.2	88.1	88.87	90.4	92
450	55.6	61.6	63.2	66.16	68.4	71.1	82.14	83.7	91.6

For Turbidity removal %

Concentration (mg/lit) — Air flow contact time (hr) ,1.5grams, pH=5

	4	8	12	16	20	24	28	32	36
100	88.5	91.4	92.8	91.21	93.1	94	94.5	94.9	95
200	87.1	90.1	91.3	92.57	93.1	93.5	94.3	95.8	94.8
350	85.1	85.6	87.2	89.55	91.6	93	94.15	94.2	94.3
450	61.7	65.4	71.7	75.33	77	78.4	83.54	86.8	92

For Turbidity removal %

Concentration (mg/lit) — Air flow contact time (hr) ,1.5grams, pH=8.5

	4	8	12	16	20	24	28	32	36
100	89.4	92.4	93.2	94.15	94.8	94.9	95.14	95.8	96.7
200	88.2	91.2	92.1	93.16	94	94.1	95	95.1	95.6
350	86	87.5	89	90.51	92.5	93.8	94.57	95	95.3
450	71.7	75.8	83.1	86.88	90.3	92.0	94.2	94.5	95

For Turbidity removal %

Concentration (mg/lit) — Air flow contact time (hr) ,5.6grams, pH=1.6

	4	8	12	16	20	24	28	32	36
100	86.15	88.11	90.14	91.58	92.8	93	93.35	93.85	94.1
200	84.5	87.1	89.1	90.86	91.8	92.5	93	93.5	93.8
350	77.3	79.1	81.1	82.35	83.6	84.5	84.81	85.3	88
450	74.5	77.5	78.3	79.89	80.1	82.4	83.54	84.6	86.1

For Turbidity removal %

Concentration (mg/lit) — Air flow contact time (hr) ,5.6grams, pH= 2.5

	4	8	12	16	20	24	28	32	36

100	87.5	89.6	90.3	92.5	92.8	93.4	93.66	93.9	94.3
200	85.7	89.2	90.3	91.66	92	92.5	92.68	92.7	93.9
350	79.6	80.1	81.7	83	84.1	85	87.24	88.1	92
450	52.6	55.1	59.3	64	66.1	68.1	79.4	85.1	88

For Turbidity removal %

Concentration (mg/lit)	Air flow contact time (hr) ,5.6grams, pH= 3.3								
	4	8	12	16	20	24	28	32	36
100	89.3	90.5	91	93.41	93.6	94	94.54	95.1	95.5
200	86.1	89.7	90.3	91.74	92.5	92.8	93.94	94.5	94.6
350	83.1	85.1	87.5	89.87	90.2	91.2	92	92.5	93
450	57.6	63.6	65.2	67.24	70	72.1	84.14	86.7	92

For Turbidity removal %

Concentration (mg/lit)	Air flow contact time (hr) ,5.6grams, pH=5								
	4	8	12	16	20	24	28	32	36
100	89.5	92.4	93.8	94.21	94.3	94.5	94.87	95	95.9
200	88.1	91.1	92.3	94.57	94.6	94.6	94.65	95.8	94.9
350	87.1	88.6	90.2	91.55	91.6	92.1	92.58	93	93.4
450	63.7	66.4	68.7	69.33	71	72.4	73.15	74.5	78.5

For Turbidity removal %

Concentration (mg/lit)	Air flow contact time (hr) ,5.6grams, pH=8.5								
	4	8	12	16	20	24	28	32	36
100	90.1	91.4	93.3	94.5	94.7	94	95.25	96	96.9
200	89.2	90.2	91.1	92.16	93.1	93.5	94.65	94.8	95.8
350	87	88.5	89.5	91.51	91.6	92.1	92.58	93	93.6
450	73.7	77.8	85.1	88.1	88.8	93.5	93.68	93.7	94.2

For Turbidity removal %

Concentration (mg/lit)	Air flow contact time (hr) ,10grams, pH=1.6								
	4	8	12	16	20	24	28	32	36
100	95.75	97.31	98.54	98.88	99	99.54	99.74	99.85	99.91
200	95.6	96.9	98.1	98.86	98.8	98.9	98.99	99	99.1
350	95.1	96.5	97.9	98.73	98.8	98.8	98.88	99.0	99.4
450	41.1	46.3	52.2	57	60.6	63.3	67	72.2	76.6

For Turbidity removal %

Concentration (mg/lit)	Air flow contact time (hr) ,10grams, pH= 2.5								
	4	8	12	16	20	24	28	32	36
100	68.1	75.1	78.3	80.54	89.7	91.4	92	93.7	95.8
200	66.6	72.2	76.3	79.66	85.1	90.7	91.77	93.2	94.3
350	63.6	70.2	75.6	77.14	79.5	87.7	89.54	91.4	92.5
450	49.6	53.2	57.2	62	67.1	73	78.33	83.2	85.3

For Turbidity removal %

Concentration (mg/lit)	Air flow contact time (hr) ,10grams, pH= 3.3								
	4	8	12	16	20	24	28	32	36
100	67.5	74.3	77.8	79.84	88	90.5	91.84	93.5	95

200	65.5	71.7	76.1	78.	87.7	89.8	91.57	93.2	94.3
350	62.5	66	73	75	85.3	87.4	88.54	90.4	91.7
450	57.6	60.6	68.2	70.66	78.4	79.7	84.44	87.7	91.1

For Turbidity removal %

Concentration (mg/lit)	Air flow contact time (hr) ,10grams, pH=5								
	4	8	12	16	20	24	28	32	36
100	87.5	93.4	93.8	94.21	94.3	94.8	95.4	96.9	97
200	86.1	92.1	93.3	93.57	94.2	94.5	96.3	96.8	96.9
350	86.1	86.6	87.4	90.55	93.6	95	95.7	96.0	96.6
450	62.7	67.4	73.7	79.33	83	87.4	91.61	92.2	92.4

For Turbidity removal %

Concentration (mg/lit)	Air flow contact time (hr) ,10grams, pH=8.5								
	4	8	12	16	20	24	28	32	36
100	88	94	94.2	94.55	94.8	95	95.68	97	97.5
200	86.2	92.2	93.5	93.76	94.4	94.6	96.62	96.9	97
350	85.5	88	89.1	91.21	94.1	94.5	95.81	96	96.2
450	72.7	77.8	85.1	89.88	92.3	94.0	95.2	96.1	96.5

For DO enhancement %

Concentration (mg/lit)	Air flow contact time (hr) ,1.5grams, pH=1.6								
	4	8	12	16	20	24	28	32	36
100	61	63.5	65.2	64	63.2	64.3	68.35	78	83.1
200	58.6	60.4	62.2	62.35	63.2	64.54	65.712	73	82.6
350	55.5	58.87	63.75	71.37	72.6	74.87	81.5	92.37	93.5
450	3.49	3.89	4.232	4.616	4.79	5.096	5.566	67.34	6.5

For COD removal %

Concentration (mg/lit)	Air flow contact time (hr) ,1.5grams, pH= 2.5								
	4	8	12	16	20	24	28	32	36
100	56.5	58.1	60.1	65.47	68.1	69.4	73	75.1	76.3
200	55.6	57.6	57.44	64.36	66.8	68.4	71.2	66	67.56
350	43.75	41.62	40	38.75	32.5	31.37	30.625	30	29.75
450	51.6	56.87	63.71	67.67	69.7	75.6	76.912	81.71	85.67

For DO enhancement %

Concentration (mg/lit)	Air flow contact time (hr) ,1.5grams, pH= 3.3								
	4	8	12	16	20	24	28	32	36
100	58.3	61.4	71.8	73.64	75.1	76.8	77.41	78.4	86.6
200	56.92	63.4	70	72.4	74.9	75.22	76.5	76.2	84.31
350	53	55	61.25	63.55	65.2	73.5	75	78.62	82.75
450	46.8	51	60.2	58.84	61.5	71.2	72.636	75.63	80.6

For DO enhancement %

Concentration (mg/lit)	Air flow contact time (hr) ,1.5grams, pH=5								
	4	8	12	16	20	24	28	32	36
100	57.2	66.4	61.8	63.6	65	66.4	68.1	72.1	85.7
200	50.8	56.8	61.4	63.8	64.3	65.12	67.3	71.3	84.54

350	4.32	55.15	61.15	70.2	71.1	73.15	75.15	80.5	82.62
450	46.5	53.2	58	65.3	66.4	71.2	73.12	76.12	81.5

For DO enhancement %

Concentration (mg/lit)	Air flow contact time (hr) ,1.5grams, pH=8.5								
	4	8	12	16	20	24	28	32	36
100	20.5	32.6	38.1	40.5	43.6	46.3	49.15	51.3	61.1
200	13.55	30.15	36.12	38.12	41.7	46.3	48.15	48.5	60.35
350	12.13	27.37	33.5	37.25	40.7	42.5	46.15	48.15	58.12
450	9.2	25.6	25.32	32.2	34.2	37	33.5	40.5	38.62

For DO enhancement %

Concentration (mg/lit)	Air flow contact time (hr) ,5.6grams, pH=1.6								
	4	8	12	16	20	24	28	32	36
100	61.5	64.5	66.2	64.5	64.8	65.3	69.35	79.5	84.1
200	59.6	61.4	63.2	65.35	66.3	67.68	67.85	74.5	83.6
350	56.5	58.87	65.75	73.37	74.6	76.15	82.5	93.15	94.5
450	5.49	4.89	5.232	5.716	6.79	7.096	8.566	68.54	69.5

For DO enhancement %

Concentration (mg/lit)	Air flow contact time (hr) ,5.6grams, pH= 2.5								
	4	8	12	16	20	24	28	32	36
100	57.5	59.1	62.1	67.54	69.1	70.4	74.5	76.1	78.3
200	56.6	58.6	59.56	66.36	68.8	69.4	73.2	67	68.56
350	44.75	43.62	44	39.75	33.5	35.37	33.625	35	36.75
450	53.6	57.87	64.71	69.67	71.7	77.6	78.912	82.31	87.67

For DO enhancement %

Concentration (mg/lit)	Air flow contact time (hr) ,5.6grams, pH= 3.3								
	4	8	12	16	20	24	28	32	36
100	60.3	64.4	75.8	76.64	77.1	77.8	78.41	79.4	87.6
200	58.92	65.4	71.5	73.4	75.9	77.22	77.5	78.2	85.31
350	54	56.5	62.25	64.55	66.2	72.5	76.5	79.62	83.75
450	48.8	52.5	62.2	59.84	62.5	73.2	73.636	78.63	82.6

For DO enhancement %

Concentration (mg/lit)	Air flow contact time (hr) ,5.6grams, pH=5								
	4	8	12	16	20	24	28	32	36
100	58.2	67.4	68.8	65.6	66.8	67.4	69.1	73.1	86.7
200	52.8	57.8	62.4	64.8	66.3	66.12	68.3	73.3	85.54
350	5.32	57.15	62.15	73.2	75.1	76.15	77.15	81.5	83.62
450	47.5	54.2	59.5	66.3	68.4	73.2	75.12	77.12	83.5

For DO enhancement %

Concentration (mg/lit)	Air flow contact time (hr) ,5.6grams, pH=8.5								
	4	8	12	16	20	24	28	32	36
100	22.5	34.6	39.1	42.5	45.6	48.3	51.15	53.3	63.1
200	15.55	32.15	38.12	40.12	43.7	48.3	50.15	51.5	61.35
350	13.13	29.37	35.5	39.25	43.7	45.5	48.15	50.15	62.12

450	10.2	27.6	28.32	33.2	38.2	39	35.5	42.5	45.5

For DO enhancement %

Concentration (mg/lit)	Air flow contact time (hr) ,10grams, pH=1.6								
	4	8	12	16	20	24	28	32	36
100	62	65	67	68.5	69	70.2	71.35	79.5	88.1
200	61.6	63.4	65.2	64.35	66.2	66.54	68.712	78	87.6
350	60.5	61.87	66.75	73.37	74.6	76.87	83.5	94.37	95.5
450	4.49	4.89	5.232	5.616	5.79	6.096	6.566	7.344	7.5

For DO enhancement %

Concentration (mg/lit)	Air flow contact time (hr) ,10grams, pH= 2.5								
	4	8	12	16	20	24	28	32	36
100	56.5	58.1	60.1	65.47	68.1	69.4	73	75.1	76.3
200	55.6	57.6	57.44	64.36	66.8	68.4	71.2	66	67.56
350	43.75	41.62	40	38.75	32.5	31.37	30.625	30	29.75
450	51.6	56.87	63.71	67.67	69.7	75.6	76.912	81.71	85.67

For DO enhancement %

Concentration (mg/lit)	Air flow contact time (hr) ,10grams, pH= 3.3								
	4	8	12	16	20	24	28	32	36
100	61.5	67.4	73.8	75.64	77.1	78.8	79.41	80.4	88.6
200	60.92	66.4	72	74.4	76.9	77.22	78	79.2	86.31
350	55	57	62.25	65.75	67.2	74.5	76	80.62	84.75
450	49.8	54	61.2	63.84	65.5	73.2	73.636	77.63	81.6

For DO enhancement %

Concentration (mg/lit)	Air flow contact time (hr) ,10grams, pH=5								
	4	8	12	16	20	24	28	32	36
100	55.2	59.4	63.8	65.6	66	68.4	69.7	74.1	88.7
200	51.8	58.8	62.4	64.8	65.8	66.92	68.4	73.2	86.54
350	49.12	57.25	63.75	71	73.3	74.75	77.25	82.5	85.62
450	48	54	60	66	68.4	73.2	75.6	80.4	84

For DO enhancement %

Concentration (mg/lit)	Air flow contact time (hr) ,10grams, pH=8.5								
	4	8	12	16	20	24	28	32	36
100	21.5	33.6	40.1	41.5	45.6	49.3	51.2	53.7	63.5
200	16.87	32.25	38.12	40.62	44.7	48	49.625	51	62.12
350	14.25	29.37	35.5	39.25	41.7	44.5	48.375	49.37	60.62
450	10.2	27.6	28.32	34.2	34.2	39	40.125	42	40.62

4.3.3.1 Design of experiments

Design of experiments was employed in this study to optimize operating conditions and removal efficiency, and four parameters were included, including initial concentration (100-450mg/L), pH (1.6-8.9), and adsorbent dose (1.5-10g) and air flow timing (4-36 hrs) (Table 4.12).The central composite design (CCD) technique of response surface methodology was applied to measure the impact of these variables on removal percent Dye, COD, Turbidity and DO enhancement. The usage of CCD has the advantage of allowing complex response functions to be determined with only a few combinations of variables (Muthukumar et al., 2003). Each was subjected to a total of 29 experiments in this study.

Table 4.12 CCD operation factors and their levels.

Factor coded values	Levels		Responses
	Low	High	
pH	1.6	8.9	COD Removal(mg/l), Turbidity Removal(mg/lit), Dye removal(mg/lit), DO enhancement (mg/lit).
Initial concentration(mg/l)	100	450	
Adsorbent dose(g/l)	1.5	10	
Air flowing time(hr)	4	36	

4.3.3.2. Statistical analysis

An effective fit of the model should be obtained to optimize the response surface. A suitable model is needed due to its eliminating of poor results. The actual and predicated adsorption graphs for cod, turbidity, dye removal, and DO increase are observed in Fig. 4.75 (a, b, c, d), respectively. In Fig. 4.75, the actual R^2 value and the adjusted R^2 value were found to be 0.9786 and 0.9571 for COD, 0.9575 and 0.9151 for turbidity, and 0.9526 and 0.9352 for dye and DO, respectively. Also, the value of R^2 investigates the fitness of the model. In this present investigation, the R^2 value indicates that there is the best agreement with regression models to achieve good results.

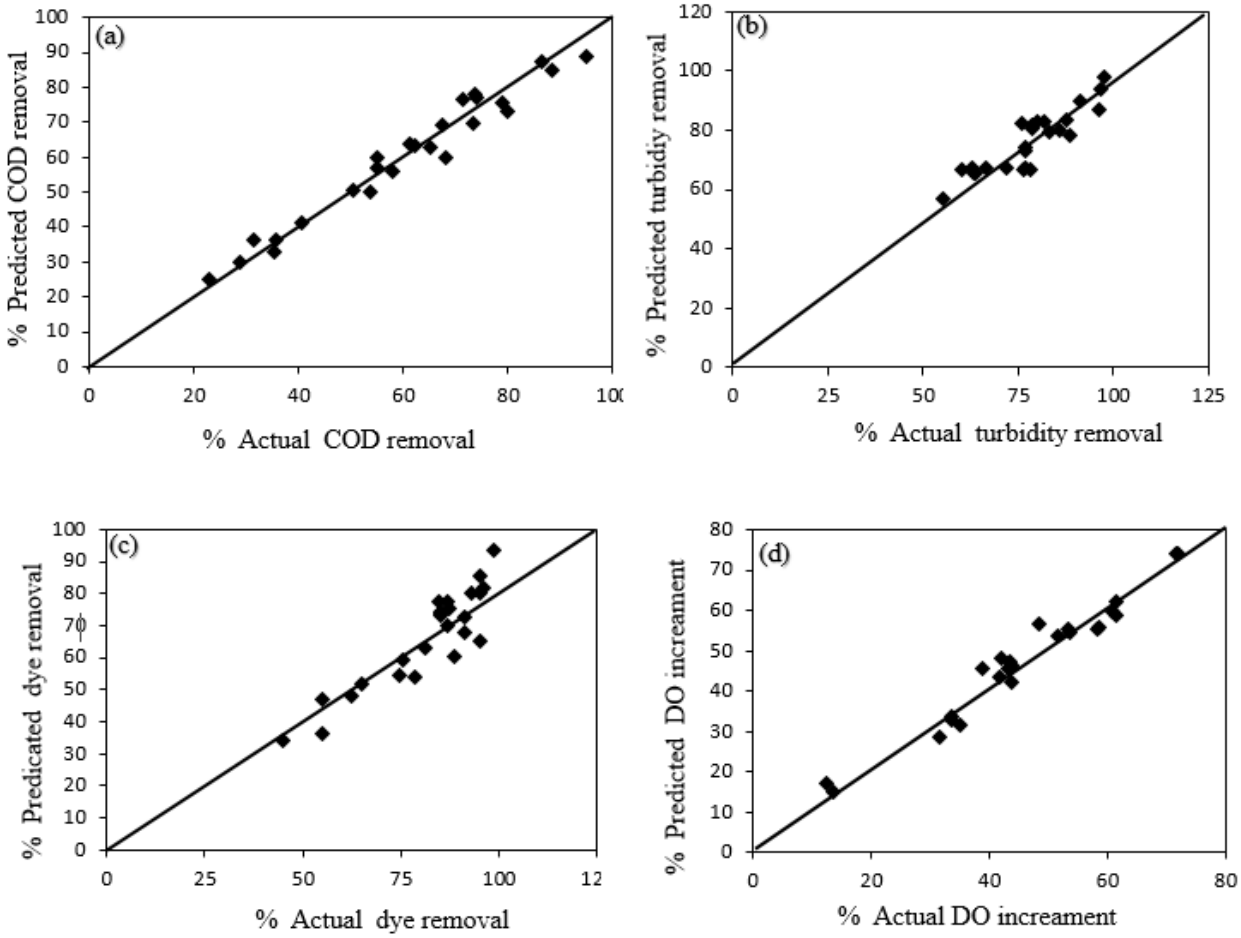

Fig. 4.75 Actual and predicted graphs for (a) COD, (b) Turbidity, (c) Dye removal efficiency, and (d) Increment efficiency of DO

Not only R^2, but the fitness of the obtained model equations was also justified by utilizing residuals. The normality of the residuals can be measured by utilizing normal probability graphs. The residuals represented in Figure 4.76 were indicated against the anticipated data. Better outcomes can be indicated in Figure 4.77.

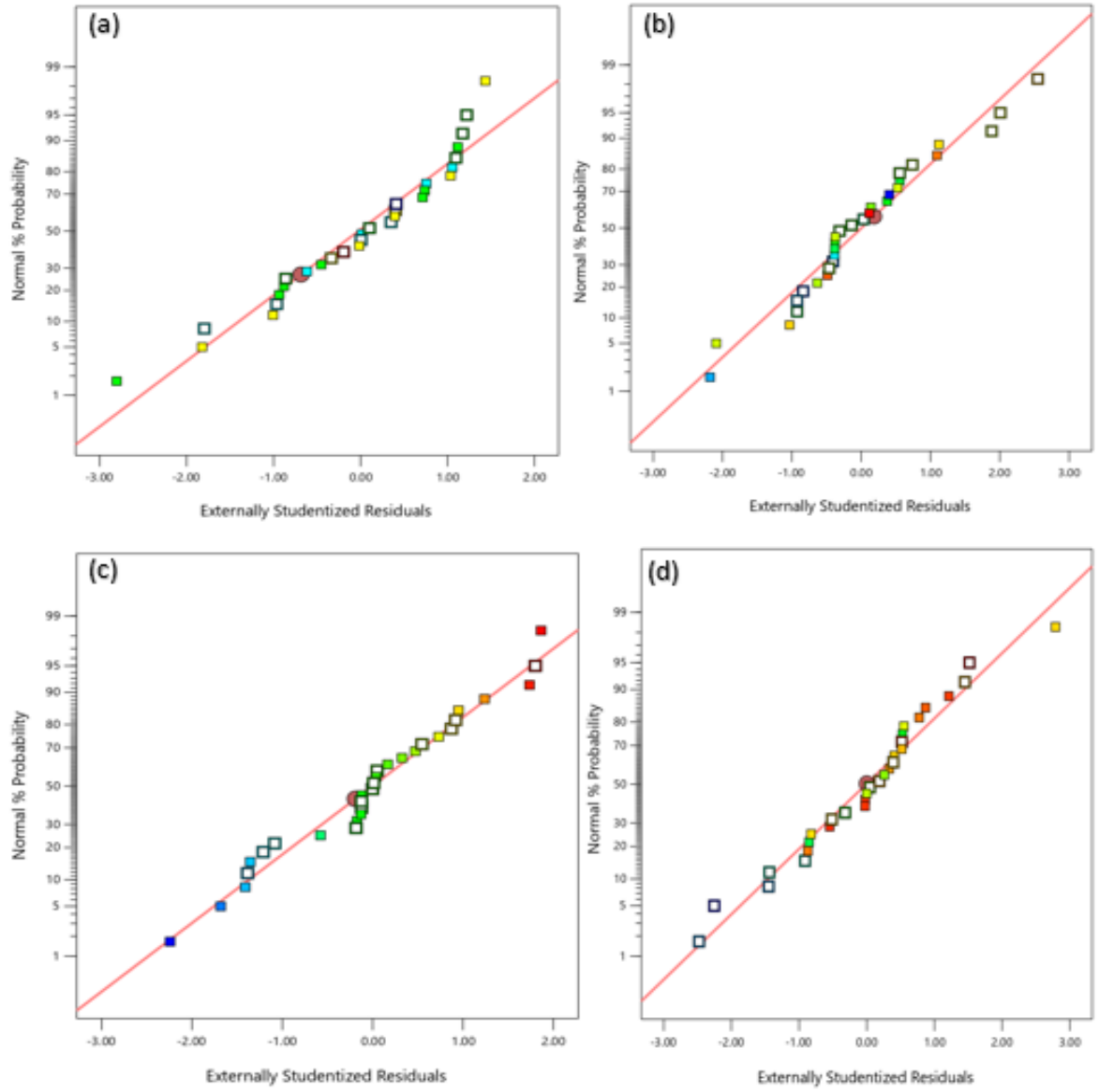

Fig. 4.76 Normal % probability and standardized residual plot for (a) COD (b) DO (c) Turbidity (d) Dye uptake capacity of adsorbent

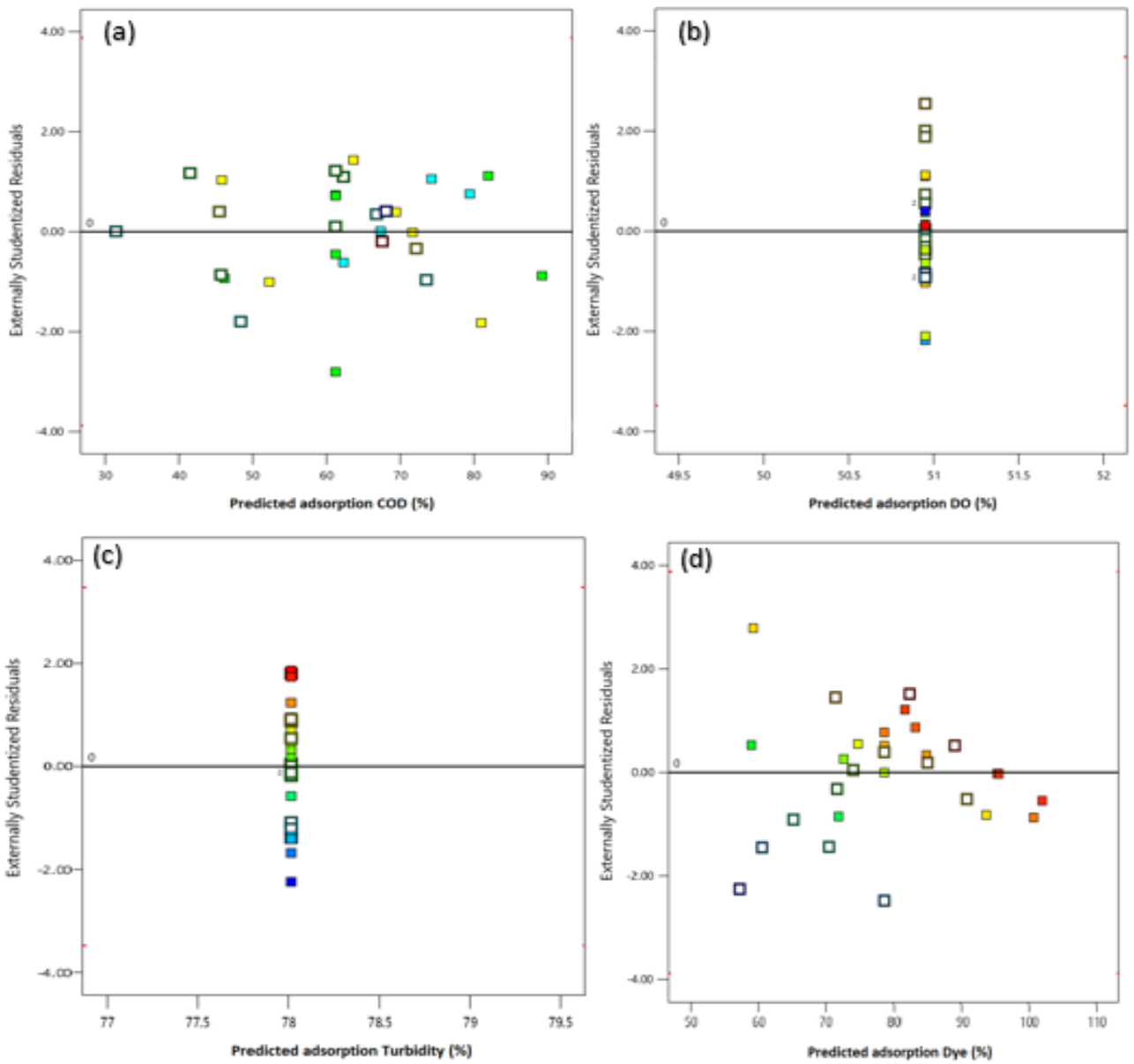

Fig. 4.77 The standardized residuals and predicted response plot for (a) COD (b) DO (c) Turbidity (d) Dye uptake capacity of adsorbent

4.3.3.3. Analysis of variance

The below-mentioned 2nd-order polynomial model Eqn.(4.44),(4.45),(4.46), and (4.47) are derived from the present investigations and show the correlation among COD, turbidity, dye removal (R) efficiency, and DO increase (I) efficiency with unconstrained parameters (A, B, C, D).

$$R_{COD} = -1.0 + 22.6A + 0.007B + 4.88C - 1.5D - 1.123A^2 + 0.000208B^2 + 0.66C^2 - 0.0203D^2 - 0.0305AB - 1.453AC + 0.354AD - 0.0033BC + 0.0032BD - 0.182CD \quad (4.44)$$

$$R_{turbidity} = 57.9 + 6.25A - 0.038B + 0.21C - 0.38D - 0.124A^2 + 0.000269B^2 + 0.389C2 + 0.0107D^2 - 0.018AB - 0.041AC - 0.005AD - 0.0092BC + 0.00088BD - 0.030CD \quad (4.45)$$

$$R_{Dye\ removal} = 106.9 + 0.1A + 0.054B - 10.9C - 3.01D - 0.353A^2 + 0.000069B^2 + 0.753C^2 + 0.0160D^2 - 0.0213AB + 1.112AC + 0.229AD - 0.0081BC + 0.00428BD - 0.039CD \quad (4.46)$$

$$I_{DO} = 58.9 + 7.9A + 0.027B - 1.94C - 1.58D - 1.289A^2 - 0.000082B^2 - 0.004C^2 + 0.0095D^2 - 0.0163AB + 1.059AC + 0.149AD + 0.0003BC + 0.00388BD - 0.149CD \quad (4.47)$$

Table 4.13 Analysis of variance (ANOVA) of COD, Turbidity, Dye removal and DO

Source	Sum of squares					F Value			
	COD	Turbidity	Dye	DO	df	COD	Turbidity	Dye	DO
Model	11346.9	2025.82	5643	5396.4	14	18.34	20.49	21.58	22.65
A, pH	202.6	22.78	378.8	192.8	1	10.34	15.08	0.54	0.33

B, Initial concentration	18.4	157.14	125.1	216.2	1	8.03	17.53	0.18	15.36
C, Dose	26.2	389.77	75.9	96	1	0.04	11.31	0.11	5.16
D, Air flow time	1379.9	24.0	145.8	128.1	1	2.29	10.08	0.21	0.22
AB	1522.2	538.89	741.4	435.8	1	12.52	11.81	1.06	0.74
AC	2033.1	1.59	1189.7	1079.8	1	13.37	0.08	1.70	11.82
AD	1709.0	0.36	715.3	304.5	1	2.83	9.00	1.02	0.51
BC	24.8	185.50	145.2	0.2	1	0.04	20.62	0.21	20.00
BD	332.5	24.55	573.5	472.6	1	0.55	13.08	0.82	5.80
CD	614.5	17.88	28.7	413.3	1	1.02	0.06	0.04	0.70
A^2	1193.8	14.44	117.9	1572	1	1.98	0.05	0.17	2.65
B^2	215.6	362.85	23.5	33.8	1	0.36	1.22	0.03	0.06
C^2	772.5	263.87	987.9	0.00	1	1.28	0.88	1.14	0.00
D^2	143.5	39.83	89.9	31.8	1	0.24	0.13	0.13	0.05
Residuals	245	375	300	113	12				
Lack of fit	469	415	314	390	10	0.26	4.55	0.36	0.26
Pure Error	317	150	303	120	2				

Table 4.13 displays ANOVA for a quadratic surface response model. Model F values for COD, turbidity, dye, and DO are 18.34, 20.49, 21.58, and 22.65, and this value tests how well the variables represent the variance in mean results. It indicates that only these operating conditions are suitable for COD, turbidity, dye removal, and DO increment.

4.3.4. Impact of input variables

The issues of operation factors on the removal of COD, turbidity, dye and DO enhancement have been explained along by the supporting of 3-dimensional Fig. 4.78 (a–f), Fig. 4.79 (a)–(f), Fig. 4.80 (a)–(f), and Fig. 4.81 (a)-(f).

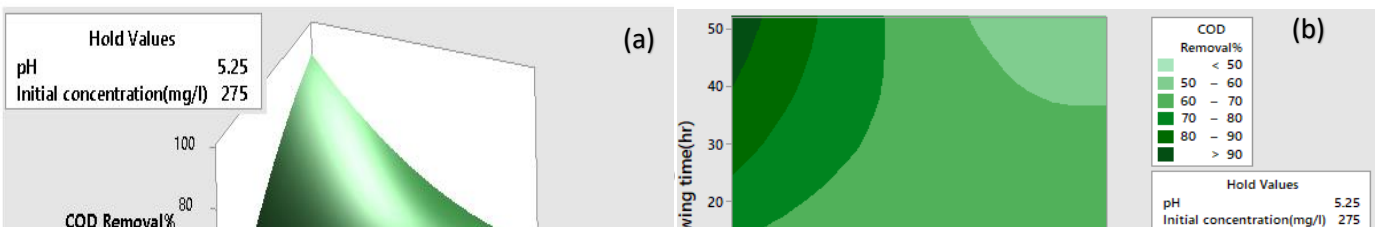

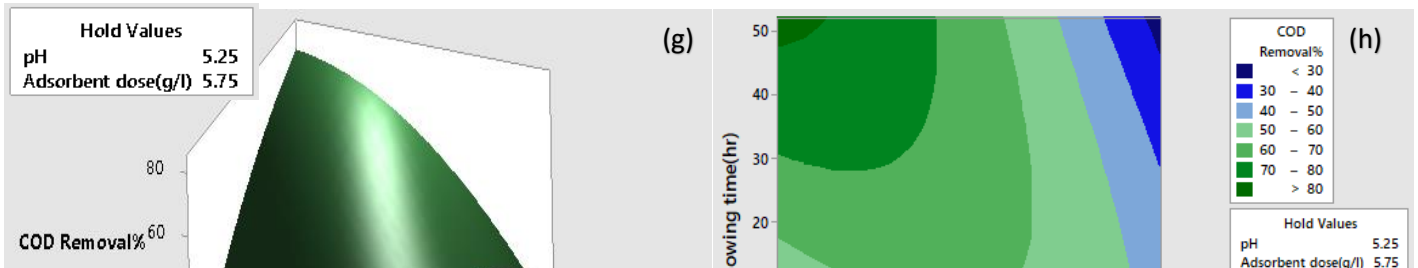
Hold Values
pH 5.25
Adsorbent dose(g/l) 5.75
COD Removal%
80
60
(g)
50
40
30
20
owing time(hr)
COD
Removal%
< 30
30 – 40
40 – 50
50 – 60
60 – 70
70 – 80
> 80
(h)
Hold Values
pH 5.25
Adsorbent dose(g/l) 5.75

Fig. 4.78 Response surface graphs for combined effect of (a) adsorbent dose and airflow timing, (c) Initial dye concentration and Adsorbent dose, (e) Air flow timing and pH, (g) Initial concentration and Air flow timing, (i) Adsorbent dose and pH, and (k) Initial dye concentration and pH, 4.74 (b, d, f, h, j, l) are contour plots on removal efficiency of COD.

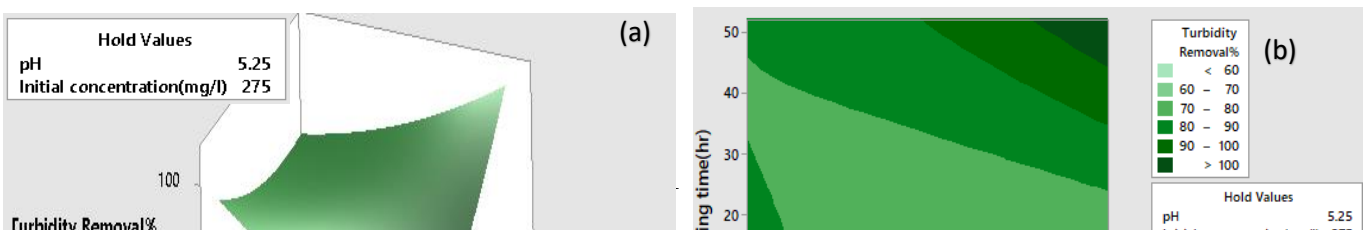

Hold Values	
pH	5.25
Initial concentration(mg/l)	275

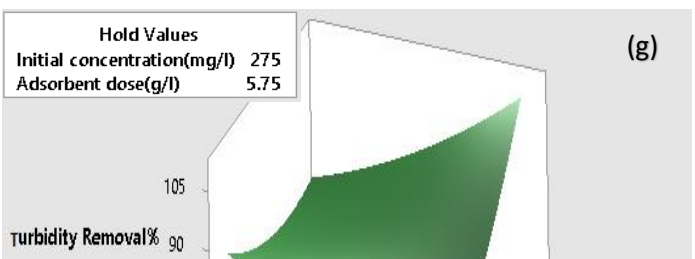

(g)

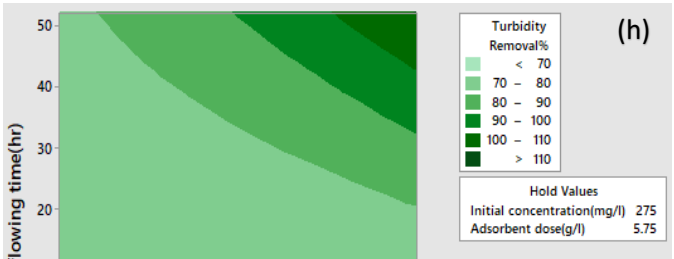

(h)

Fig. 4.79 Response surface graphs for combined effect of (a) adsorbent dose and airflow timing, (c) Initial dye concentration and Air flow timing, (e) Initial concentration of dye and Adsorbent dose, (g) pH and Air flow timing, (i) Initial dye concentration and pH, and (k) Adsorbent dose and pH, 4.75 (b, d, f, h, j, l) are contour plots on removal efficiency of turbidity.

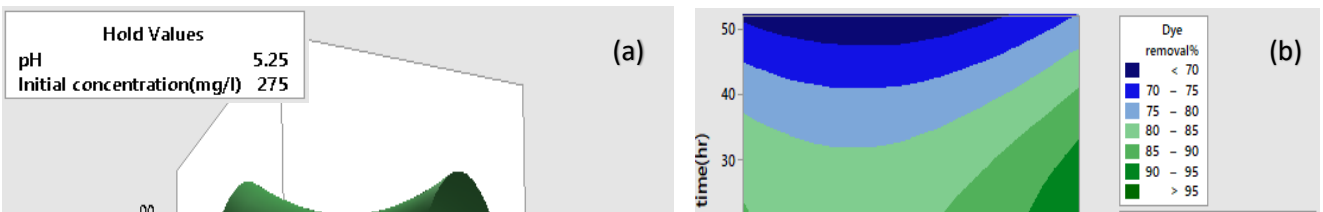

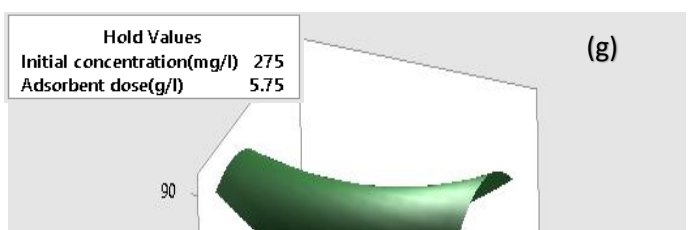
Hold Values
Initial concentration(mg/l) 275
Adsorbent dose(g/l) 5.75
90
(g)


50
40
30
20
g time(hr)
Dye removal%
< 60
60 – 65
65 – 70
70 – 75
75 – 80
80 – 85
85 – 90
> 90
(h)

Fig. 4.80 Response surface graphs for combined effect of (a) adsorbent dose and airflow timing, (c) Initial dye concentration and Air flow timing, (e) Initial concentration of dye and Adsorbent dose, (g) pH and Air flow timing, (i) Adsorbent dose and pH, and (k) Initial dye concentration and pH, 4.76(b, d, f, h, j, l) are contour plots on removal efficiency of dye.

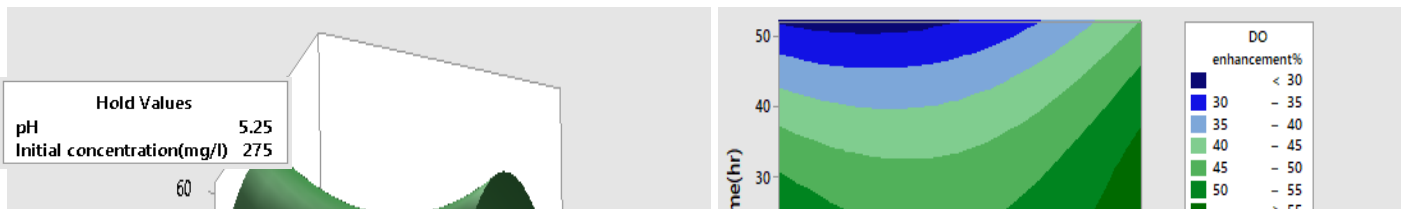

Hold Values	
pH	5.25
Adsorbent dose(g/l)	5.75

Hold Values	
Initial concentration(mg/l)	275
Air flowing time(hr)	20

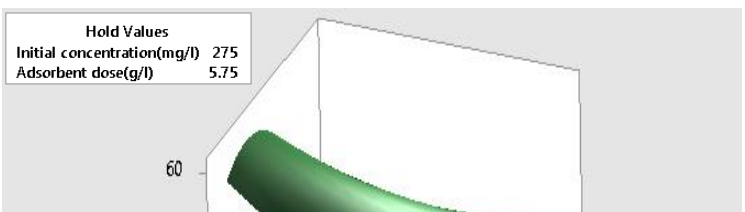

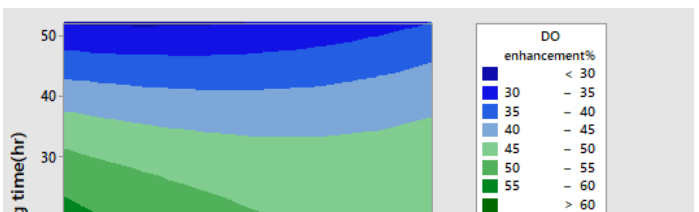

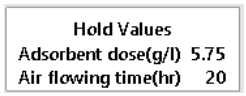

Fig.4.81 Response surface graphs for combined effect of (a) adsorbent dose and airflow timing, (c) Initial dye concentration and Air flow timing, (e) pH and Adsorbent dose, (g) pH and Air flow timing, (i) Adsorbent dose and initial dye concentration, and (k) Initial dye concentration and pH, 4.77(b, d, f, h, j, l) are contour plots on increasing efficiency of DO.

4.3.5 Optimization

Numerical analysis was used to accomplish more such optimization. It is discovered that the best local maximum value exists is at pH of 5.31, initial dye concentration 334.5 mg/L, adsorbent dose 5.2 gram and air flow timing 32.82hr. At these conditions, the removal efficiency is 68.83% for COD, 81.404% for Dye and for 91.31% for Turbidity and 95.16% for DO enhancement; the desirability for these heavy metals is 1.00 (Fig. 4.82). Furthermore, experimental results demonstrated elimination efficiencies of 68 %, 81 %, 91.3 %, and 95.16 % for COD, Dye, Turbidity, and DO, respectively, which were consistent with those, obtained using the CCD design. As a result, it demonstrates that CCD design may be employed efficiently.

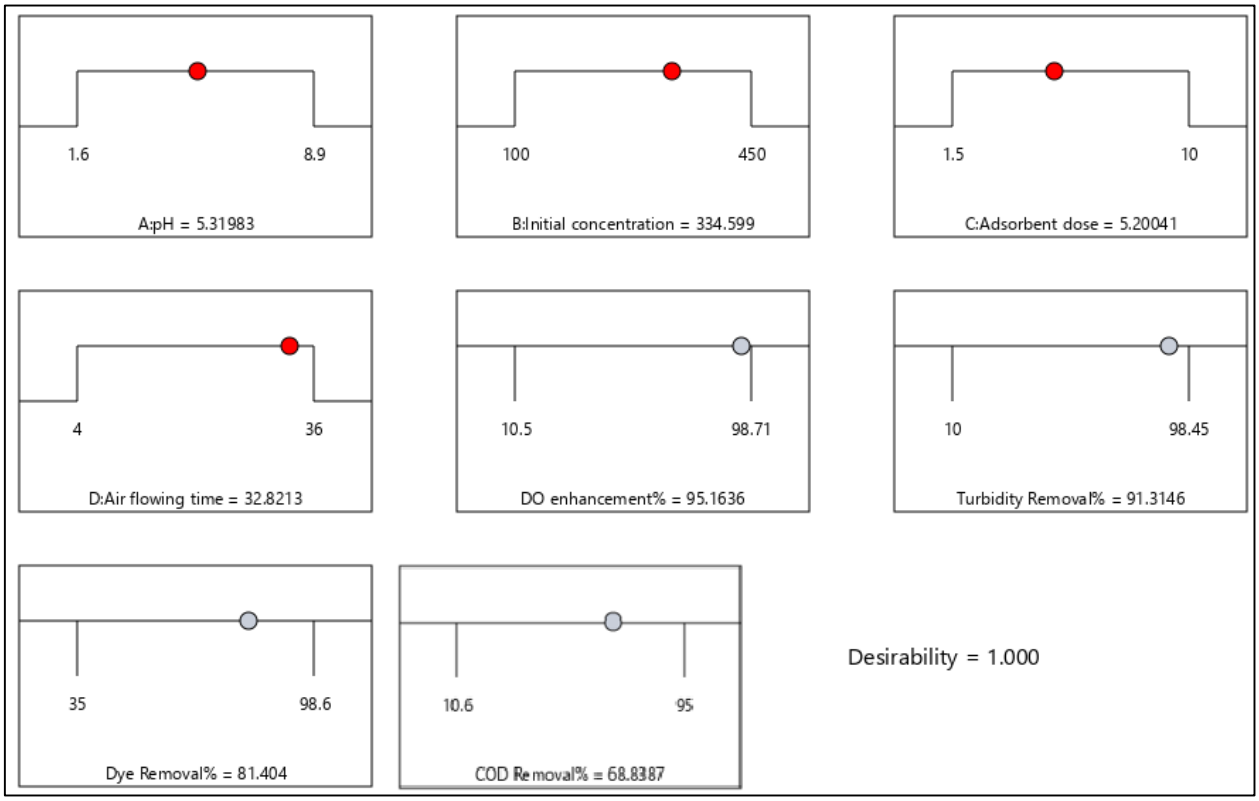

Fig. 4.82 Desirability ramp for numerical optimization obtained by software Design Expert®

The Effect of concentration

The effect of increasing dye initial concentration on removal efficiency of COD is more as observed in Fig. 4.78 (a, b, c, d), it is observed that the rejection efficiency of COD decreases with increasing of initial dye concentration, it has more effect on the rejection of turbidity and dye both are observed in ANOVA investigations. Thus the increasing percentage of DO decreases with increasing dye concentration. These are because the long settling time is required to enhance the reduction percentages

The Effect of the adsorbent dose

Increasing adsorbent dose the rejection of COD, turbidity, dye, and DO enhance sites are also increased at varying adsorption doses from 1.5 g L^{-1} to 10 g L^{-1}. This is because of much number of exchange reaction sites for an effective reduction method of organic composition in the effluent. In the Fig. 4.78 (a, c, e), Fig. 4.79 (b, d, f), Fig. 4.80 (a, c, e) and Fig. 4.81 (b, d, f), it is clear that at an initial adsorbent dose of 1.5 g L^{-1} the rejection efficiency is very less it is due to the less surface area and less adsorption activated sites are present for adsorption of COD, turbidity, dye, and DO. But on increasing adsorption dose the present sites are increased for adsorption. Thus the removal efficiency is increased from low adsorbent dose to high adsorbent dose.

The effect of pH

The experiments were done at various pH ranges between 1.6 to 8.9.From Fig.4.78 (d, e, f), Fig. 4.79 (a, b, c), Fig. 4.80 (d, e, f), and Fig. 4.81 (c, d, e), it is observed that by increasing the pH the rejection efficiency of COD, dye, and turbidity is decreased and at low pH the rejection efficiency is increased it is due to the in acidic pH, adsorbent brings negatively charged organic matters in the effluent, which means that the percentage of COD, turbidity, and dye at the high level of pH positive charged ions in effluent they are decreased on the surface of the adsorbent and become insoluble which negatively affected treated processes and rejected the effluents. For DO at high pH, it is increased certain level after that it is decreased it is due to activated sites are saturated on the adsorbent surface.

The Effect of airflow timing

From the Fig. 4.78 (a, b, d), Fig. 4.79 (c, e, f), Fig.4.80 (a, b, d), and Fig. 4.81 (a, c, f), it is clear that by increasing the aeration timing into the effluent, the rejection efficiency of effluents in the wastewater is increased because the interaction of wastewater on the surface of adsorbent was increased so that removal efficiency was high and at initial aeration time the poor mixing occurred so the interaction is less between the wastewater on the surface of adsorbent. At high aeration time, the birding flocculation mechanism of adsorbent enhances the compact nature and strength of flocculation, which affects the treatment processes significantly.

4.4. Equilibrium modeling

In our analysis, the models Langmuir, Freundlich, and Temkin were utilized to analyze adsorption data (Table 4.14). Langmuir isotherm is focused on the premise that adsorption happens at the same position as the adsorbent, so no more adsorption happens before the adsorbent locations have been filled. Nevertheless, Freundlich isotherm is used on heterogeneous surfaces and multilayer adsorption. Temkin isotherm demonstrates the effects of adsorption heat that decreases linearly with coverage of adsorbent and adsorbate interactivity.

The importance of adsorption energy also gives details are either the adsorption mechanism is of a chemical or physical nature. Fig. 4.83 (a – d) shows the equilibrium data for Freundlich, Langmuir, and Temkin isotherm fitting for COD, turbidity removal, and DO increment. Isotherm and R^2 values are shown in Table 4.15. It is concluded that the adsorption isotherms of Temkin and Langmuir are well suited for the removal of COD and turbidity.

Table 4.14. Isotherm models

Isotherms	parameters
Freundlich $\ln q_e = \ln K_f + \frac{1}{n}\ln C_e$	k_f: measure of adsorption capacity q_e: equilibrium sample uptake (mg/g) n: adsorption intensity C_e: equilibrium concentration (mg/l)
Langmuir $\frac{1}{q_m} = \frac{1}{q_0} + \frac{1}{q_0 K_L}\frac{1}{c_e}$	k_L: the Langmuir constant (L/mg), qm: maximum adsorption capacity (mg/g),
Temkin $q_e = B\ln K_T + B\ln C_e$,$B = \frac{RT}{b_T}$	R (8.314 J/(mol K)): the gas constant T (K): the absolute temperature b_T (J/mol): Temkin constant k_T (L/mg): the Temkin constant related to the equilibrium binding energy

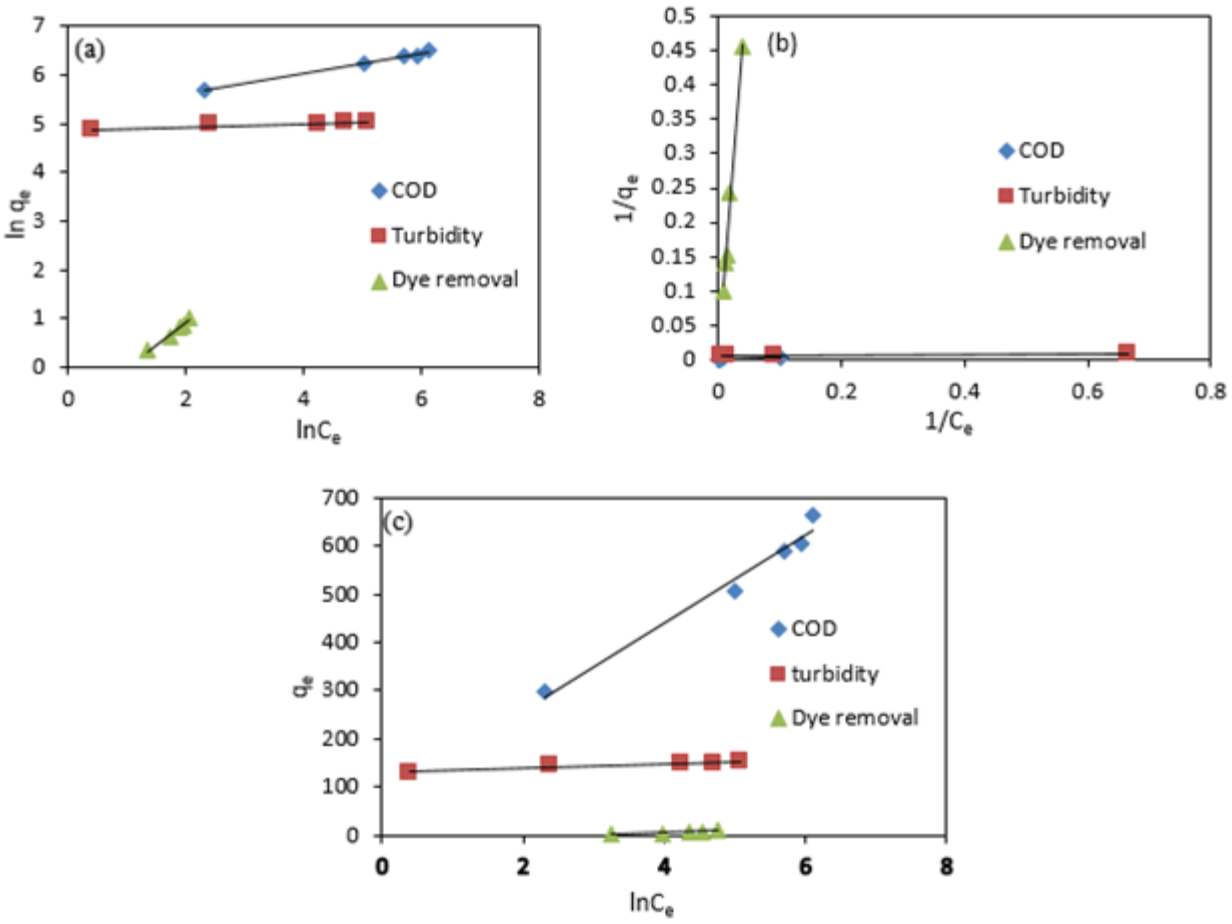

Fig. 4.83 Isotherm plots of (**a**) Freundlich, (**b**) Langmuir, and (**c**) Temkin for adsorption of COD, turbidity, and dye removal at optimum conditions

Table 4.15 Kinetic variables for adsorption of COD, turbidity, and dye removal on wheat bran at optimum conditions.

	Freundlich isotherm			Langmuir			Temkin			
	K_f	n	R^2	q_m	K_L	R^2	B	K_T	b_T	R^2
Dye removal	0.6828	1.11	0.97	116	0.0074	0.98	1.55	4.19	1571	0.98
COD	1.65	4.9	0.99	625	0.091	0.96	1.58	4.38	1562	0.97
Turbidity	1.58	3.56	0.98	149	4.194	0.97	4.49	4.85	550	0.97

4.5 Kinetic modelling

The investigation of adsorption kinetics explains the solvent uptake rate and obviously, this rate regulates the residence time of adsorbate uptake at the solid sample interface. The kinetics of the COD reduction, Turbidity removal, DO enhancement and dye removal on adsorbent were studied utilizing pseudo-first-order and pseudo-second-order by Hamadi et al. (2001). The adsorption

kinetics of the immobilized CS-MT was studied at different initial dye concentrations ranging from 20 to 320 mg L−1. The best kinetic fit for the adsorption of MO dye onto the immobilized CS-MT was pursued using the non-linearized equation of the Lagergren's pseudo-first-order and Ho's pseudo-second-order kinetic models as summarized by Bahrudin et al. (2020), The pseudo-first-order model (PFO) and pseudo-second-order model (PSO) were used to investigate the adsorption kinetics of MB dye on ATRL surface by Jawad et al. (2018).

4.5.1 Pseudo-first order equation

The rate of adsorption is directly proportional to the number of vacant sites when considering reversible binding contaminants and adsorption on active sites present on the adsorbent surface. The equation of pseudo-first-order was expressed by Eqn. 4.48

$$\frac{dq}{dt} = k_1 (q_e - q_t) \quad (4.48)$$

Where q_t and q_e are the adsorption capacity at time t and equilibrium, respectively (mg/g).

k_1 is the rate constant (min^{-1}). Integrating and implementing the above equation boundary conditions from t = 0 to t = t, and q_t = 0 to $q_t = q_t$, the integrated form of Eqn.4.48 becomes

$$\log (q_e - q_t) = \log (q_e) - \frac{k_1 t}{2.303} \quad (4.49)$$

Eqn. 4.49 is applies to the experimental results. The rate constant in this model was investigated by the slope of the graph of ln ($q_e - q_t$) over time (t)

4.5.2 Pseudo second order equation

In this model, it was considered that capability of adsorption of adsorbate on the adsorbent surface is affected by chemical forces, instead of physical attrition forces.

Non-linear form of the model is given as Eqn. (4.50)

$$\frac{dq}{dt} = k_2 (q_e - q_t)^2 \quad (4.50)$$

Upon integration with boundary conditions from $q_t = 0$ at $t = 0$, $q = q_t$ at $t = t$, the above equation **(**Eqn.4.50) Reduces to

$$\frac{t}{q_t} = \frac{1}{k_2 q_e^2} + \frac{t}{q_e} \qquad (4.51)$$

From Eqn (4.51) where q_t and qe are the adsorption capacities at time t, and at equilibrium respectively (mg/l). k_2 is the rate constant (g/mg.min).The rate constant can be investigated for different dye and COD concentrations according to the graph of t/q_t versus t.

From Table 4.16, it is observed that pseudo-second order kinetic model has greater value of R^2 as compared to that for pseudo-first order kinetic model. Theoretical value of qe for COD, dye and Turbidity removal are determined to be closer to experimental value (qe (exp)) for the case of pseudo-second order rate kinetics (Fig. 4.84 (a—c); Fig. 4.85 (a—c); Fig. 4.86 (a—c); Fig. 4.87 (a—c); ; Fig 4.88 (a—c))

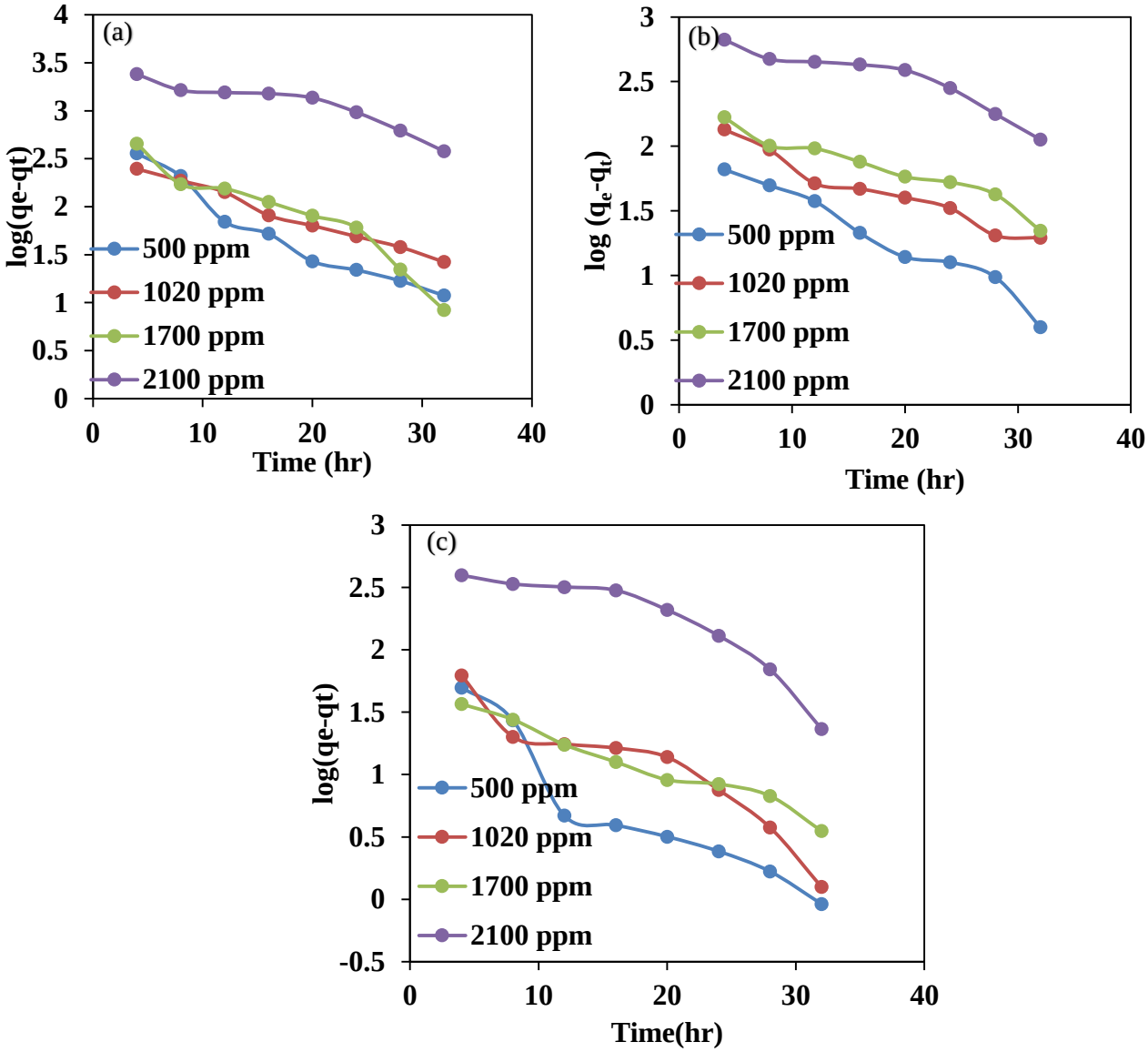

Fig. 4.84 Pseudo-first order kinetic plots for adsorption of COD at (a) 1.5 g/L (b) 5.6 g/L(c) 10 g/L under pH 1.6.

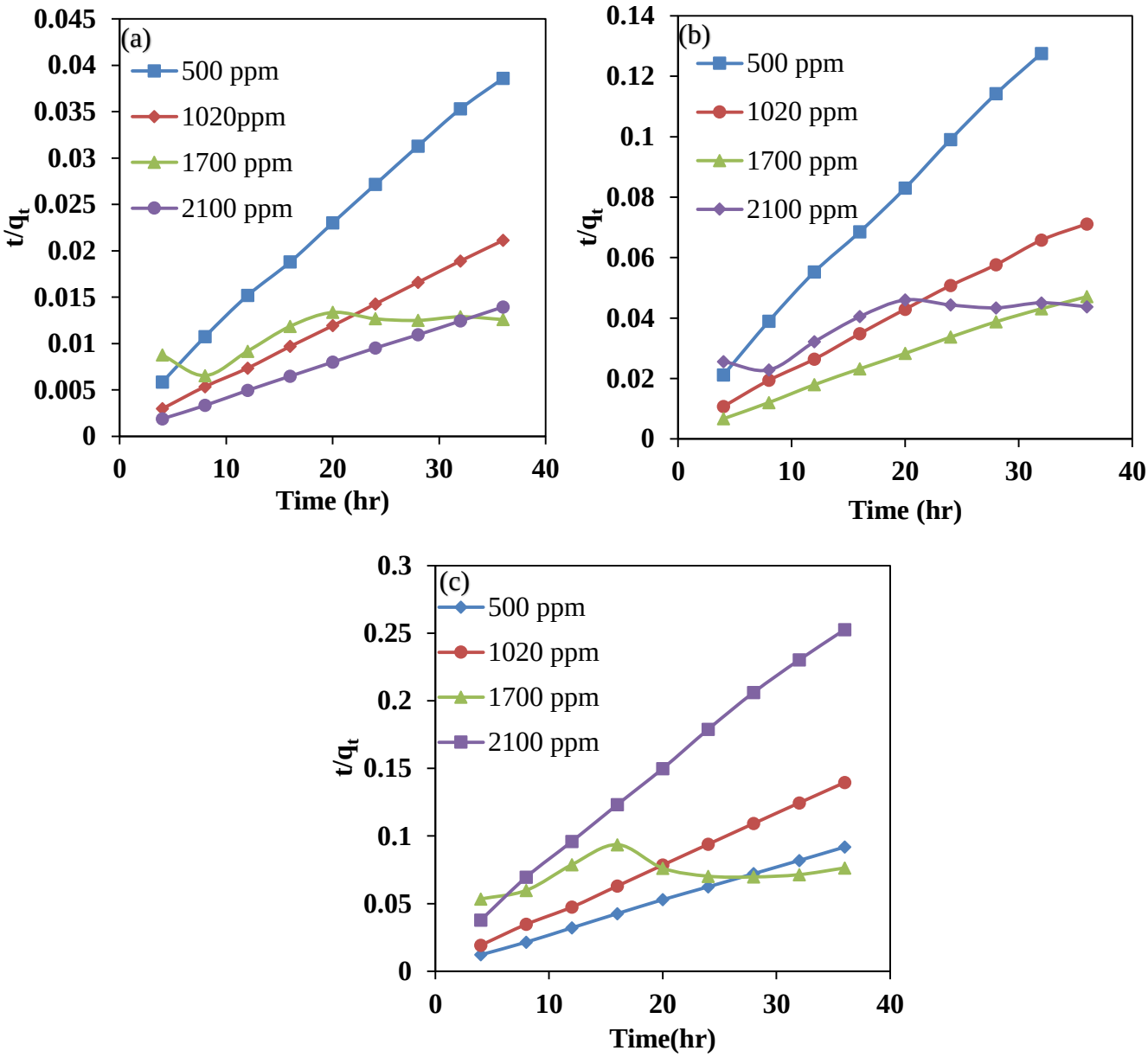

Fig. 4.85 Pseudo-second order kinetic plots for adsorption of COD at (a) 1.5 g/L (b) 5.6 g/L(c) 10 g/L under pH 1.6.

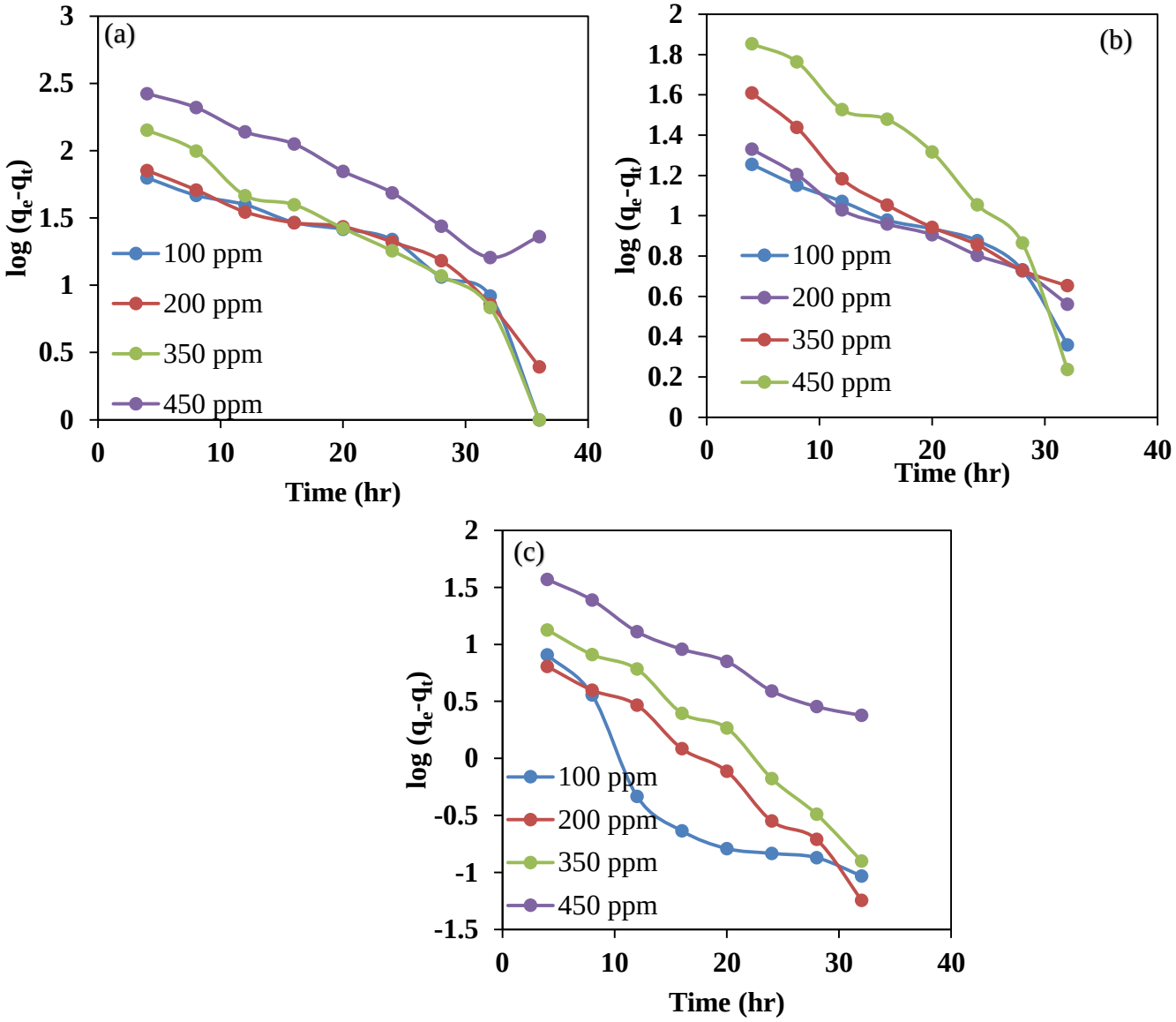

Fig. 4.86 Pseudo-first order kinetic plots for adsorption of Dye at (a) 1.5 g/L (b) 5.6 g/L(c) 10 g/L under pH 1.6.

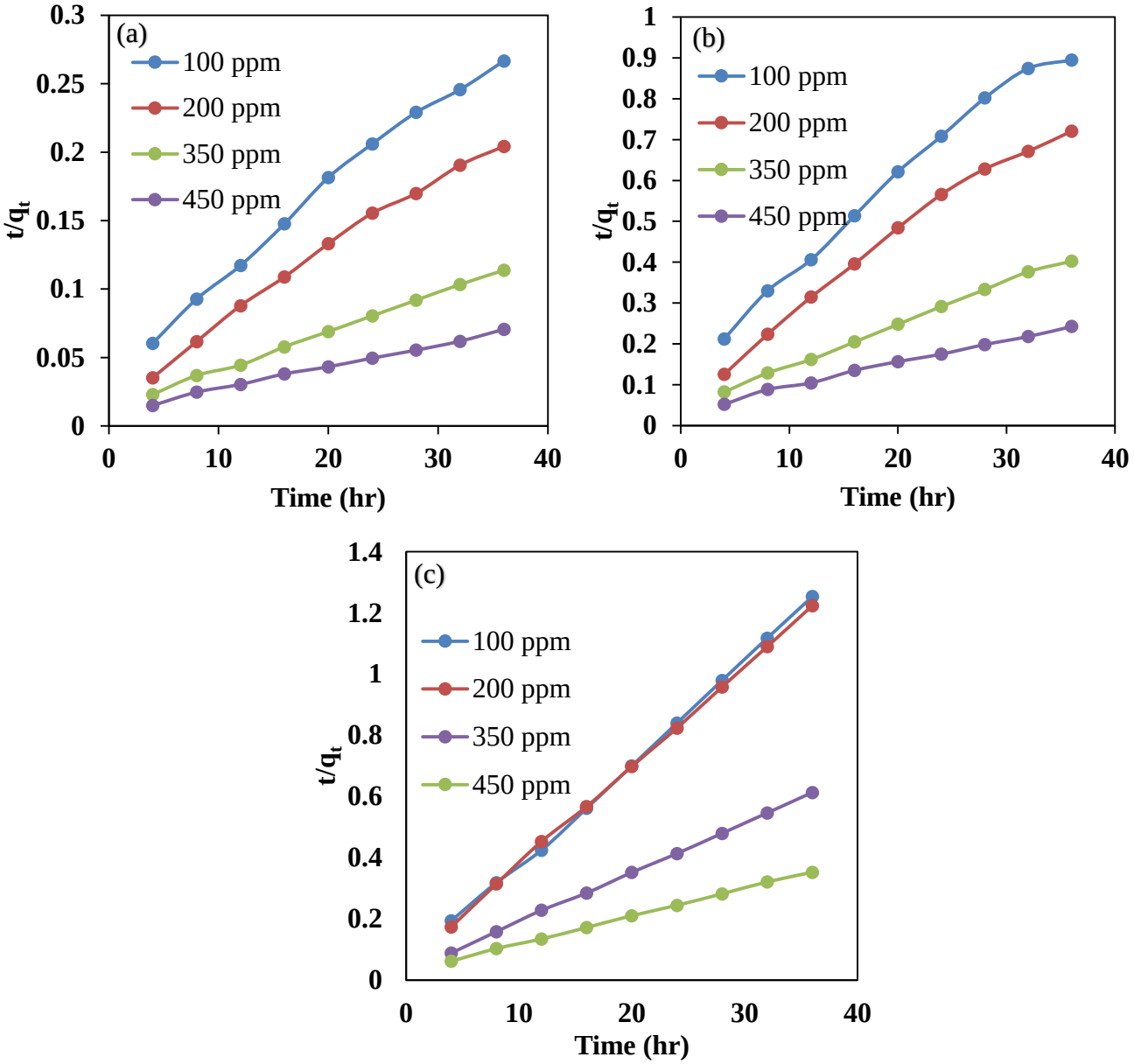

Fig. 4.87 Pseudo-second order kinetic graphs for adsorption of Dye at (a) 1.5 g/L (b) 5.6 g/L(c) 10 g/L under pH 1.6.

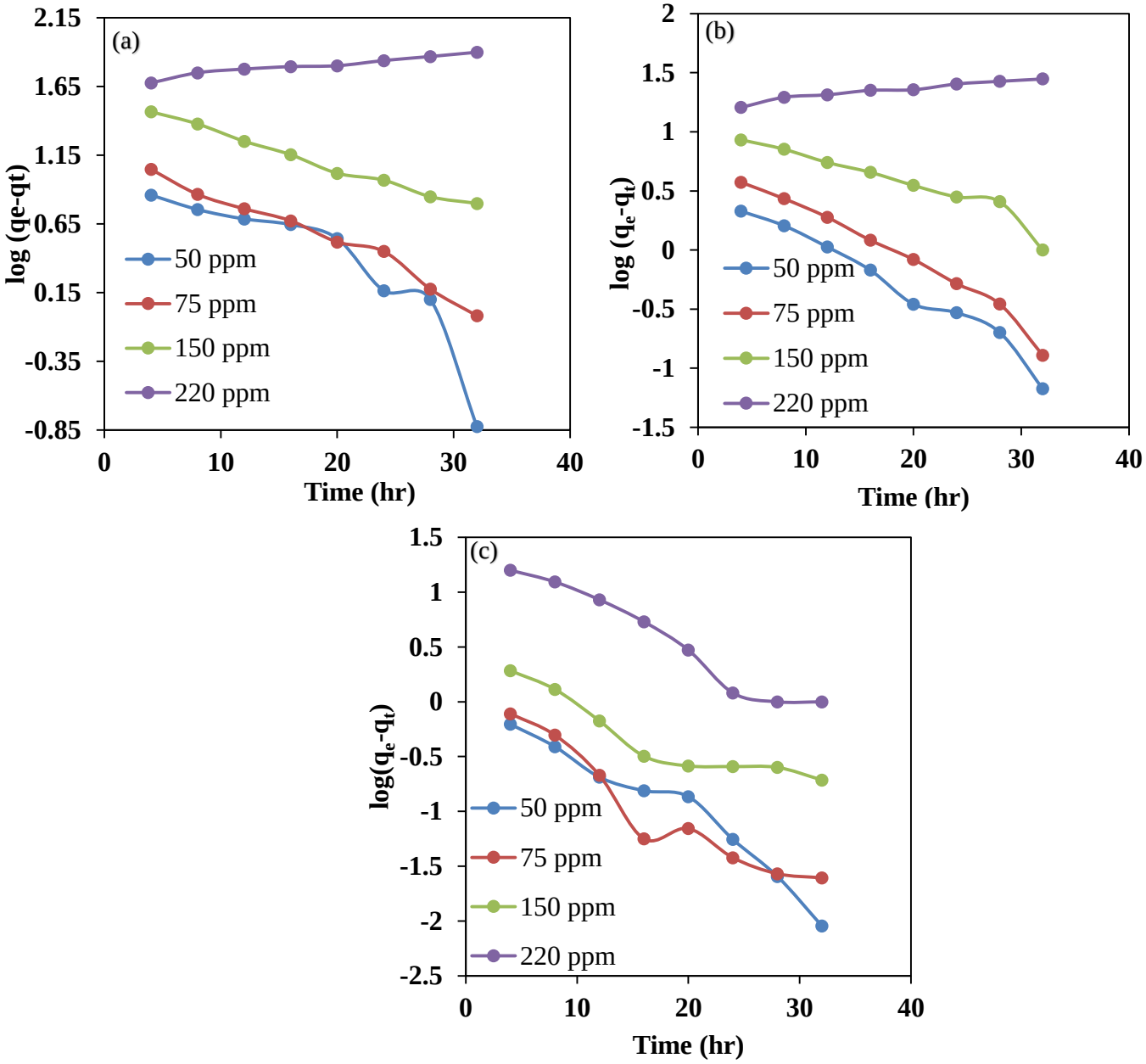

Fig. 4.88 Pseudo-first order kinetic plots for adsorption of Turbidity at (a) 1.5 g/L (b) 5.6 g/L(c) 10 g/L under pH 1.6.

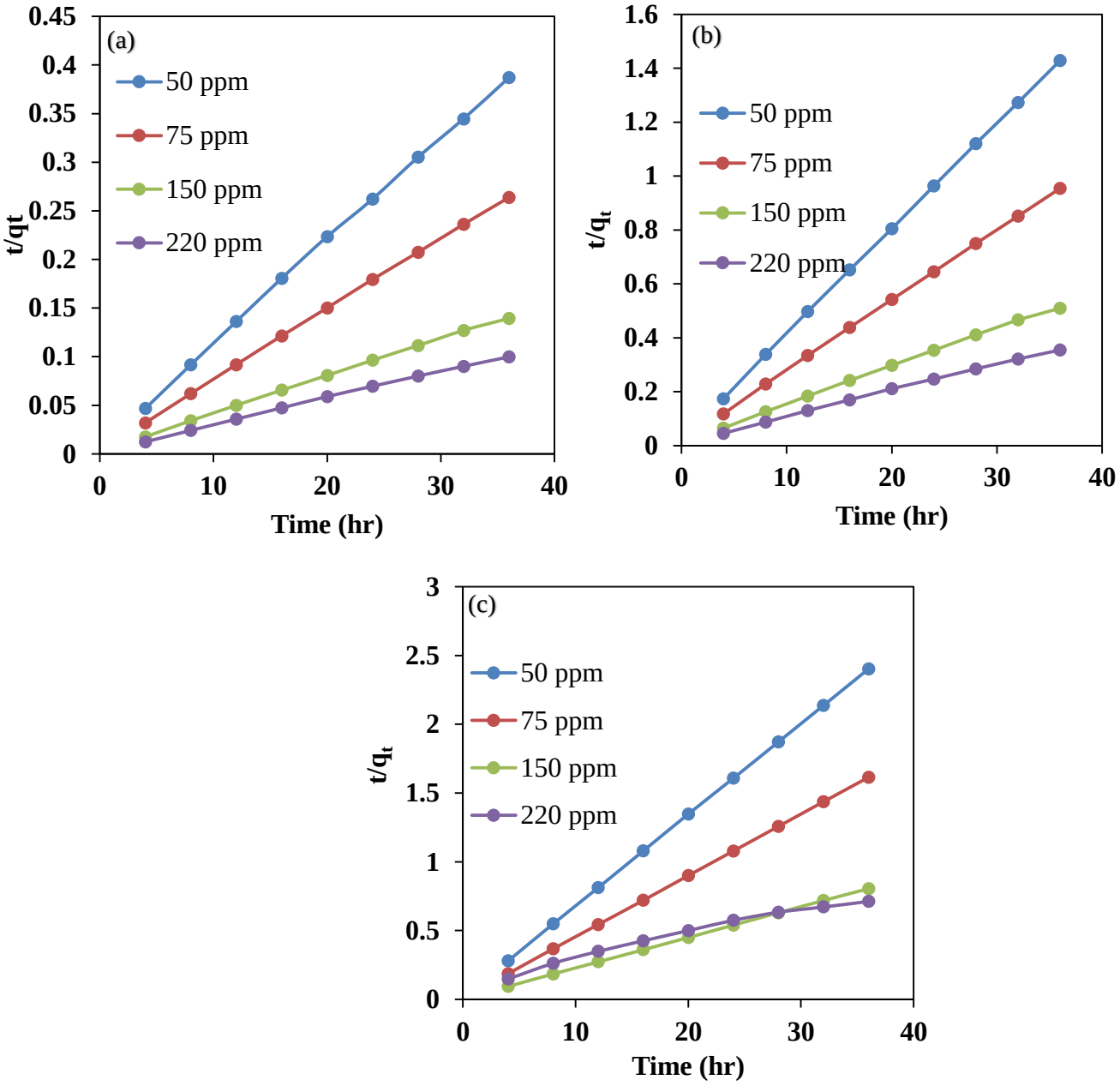

Fig. 4.89 Pseudo-second order kinetic plots for adsorption of Turbidity at (a) 1.5 g/L (b) 5.6 g/L(c) 10 g/L under pH 1.6.

Table 4.16 Kinetic variable for adsorption of COD, dye and turbidity on wheat bran at optimum conditions [pH = 1.6, Adsorbent loading = 5.5 g/L]

	Co (ppm)	**Q_{exp}**	**Pseudo first order**			**Pseudo second order**		
			K_1	Q_{cal}	R^2	K_2	Q_{cal}	R^2
COD	500	214.68	0.066	165	0.97	5.58*10^-4	219	0.98
	1020	428.18	0.041	323	0.99	2.43*10^-4	434	0.98
	1700	559	0.0043	263	0.917	5.73*10^-4	526	0.98
	2100	801	0.025	800	0.99	1.38*10^-5	1250	0.95
Dye	100	45.58	0.00561	19.95	0.97	0.00719	44.04	0.99
	200	82.22	0.095	84.52	0.97	0.0018	94.33	0.99
	350	140.47	0.15	199.5	0.99	7.15*10^-5	172.41	0.99
	450	182.39	0.063	131	0.97	5.93*10^-4	215	0.99
Turbidity	50	25.20	0.116	4.07	0.96	0.063	25.57	0.99
	75	37.71	0.113	6.96	0.973	0.014	41.81	0.99
	150	70.71	0.066	12.30	0.918	0.0146	69.93	0.99
	220	71.73	0.017	16.43	0.947	0.015	71.96	0.99

CHAPTER - 5
CONCLUSIONS AND RECOMMENDATIONS FOR FUTURE WORK

5.1 Conclusions

The conclusions of this study are as follows:

1. The experimental outcome showed that the decrease in bed pressure changes with the overview of solids (i.e., initial bed height), solid density, and angle of bed and liquid velocity and liquid viscosity but it is not a function of particle size.
2. Due to variance in liquid volume fractions, it is challenging to measure the bed pressure drop for the liquid-solid system as it varies with liquid velocities.
3. The bed stays packed until it reaches the minimum fluidization velocity.
4. The less amount of particles only began to move at the minimum fluidization velocity.
5. When the experiment is repeated, this behavior becomes more severe. Conducted by changing a certain fluid velocity keeping the other constant. The minimum fluidization velocity (U_{Lmf}) is not a function of initial static bed height but a function of particle size. The bed expansion ratio is independent on the initial bed height but a depended on particle size, solids density and liquid velocity.
6. The minimum fluidization velocity in depended upon the initial bed height.
7. The minimum fluidization velocity falls as particle density increases. It's also been discovered that for lower particle density, the height at which the bed reaches minimum fluidization is higher.
8. The minimum fluidization velocity was higher for high apparent viscosity of liquids and lower for low apparent viscosity of liquids, and the minimum fluidization velocity depended on the angle of fluidized beds, diameter, and density of solids.
9. The heat transfer coefficient increases with increasing liquid velocity in two-phase, tapered inverse fluidized bed.
10. The heat transfer coefficient was higher for high-density particles (HDPE) than for low-density particles (LDPE) and (PP).
11. The heat transfer coefficient reached its maximum value with increasing particle density.
12. The bed expansion ratio was higher for high temperatures and decreased by increasing the liquid viscosity. The bed expansion ratio also depends on the density of solids and the angle of beds.
13. The bed Voidage increased with increasing liquid velocity, while the Reynolds number depends on the diameter of particles. The volume of solids increased with increasing liquid velocity and varied with initial bed heights. From the design expert software, the bed expansion ratio was found to depend on almost all the independent parameters.
14. The Eulerian multiphase model was used to do a CFD simulation on the hydrodynamics of a two-phase tapering inverse fluidized bed. Inside the fluidized part of the fluidized bed model, the distribution of volume percentage of the two phases. The simulation findings also show that the velocity of water and polymer particles fluctuates considerably.

15. It is assumed that the bed will expand as the fluid flow rate increases. In addition, when compared to lower static bed heights, higher static bed heights extend higher.
16. The bed expansion behavior with changes in liquid velocity derived from CFD simulation has somewhat confirmed the experimental results. The bed expansion increased with liquid velocity in the experimental results, however the bed expansion decreased slightly in the CFD simulation. For the operating conditions, the CFD simulation showed a robust circulation pattern, which is consistent with the findings of previous researchers. The excellent agreement with CFD simulation and experimental data for the range of current operating variables proves that the Eulerian multiphase granular flow technique can forecast the current effectiveness of a liquid-solid tapered inverse fluidized bed.
17. By changing the restitution coefficient (0.85, 0.9, 0.95 and1.0) between the solid-solid and Specularity coefficient (0.5, 1.0) interaction between the solid-wall there was a lot of effect on the behavior of hydrodynamics of inverse fluidized bed.
18. At different restitution coefficients, there were dissimilar results of solid volume fraction along the lateral distance and distance and lateral velocity of particles along the lateral distance of different bed heights.
19. We found that most of the effect is at e_{ss}=0.99 and 0.95 due to that at this interaction, collisions between them high and elaborated kinetic energy between them and we get desired results compared with other restitution coefficients.
20. In addition, bed height, Voidage profiles by simulated results and experimental results almost the same.
21. By developing a three-dimensional Eulerian-Eulerian process coupling with KTGF, the effect of the drag models on the hydrodynamic behavior of liquid-solid flow in a tapered inverse fluid bed was studied.
22. The solid's volume fraction, particle velocity and Voidage at various liquid velocities were evaluated for different drag models and bed angles. It was observed that with the order of models like Wen-yu > Gidaspow > Syamlal obrain and bed angles like 8<6.8, more, and big bubbles are formed in the bed. The predicted time averaged axial profile velocity and tangential particle velocity were determined. Additionally, the bed expansion results were compared with experimental results, and reasonably good agreement was obtained using the experimental data that were found at Wen-yu drag model.
23. The results of the CFD modelling of bed expansion of low density solid particles are quite similar to the experimentally generated results. The bed pressure decrease calculated using CFD simulation matches the experimental measurements very well. The pressure drop and bed expansion figures show that the drag model employed in the CFD simulation accurately reproduced the two-phase (liquid-solid) phenomena. By comparing the three-dimensional

and two-dimensional models, we observed that three-dimensional model get the good results than the two-dimensional model.

24. Mean residence time and mass fraction of tracer in a laboratory-scale liquid-solid tapered inverse fluidized bed were investigated by using both experimentally and three-dimensional computational fluid dynamics modelling. The influence of liquid velocity, the angle on tapered beds, the mass of solid particles and its density on mean residence time, dispersion coefficient and mass fraction of tracer were examined. The key findings are summarized as follows:
    a) The dispersion coefficient increased sharply with increasing velocity of the liquid, while a gradual increase was found for the different mass of solid materials. The estimated time-averaged dispersion coefficient using simulation agrees reasonably well with our experimental data.
    b) The trend of the mean residence time of tracer was almost flat for the different mass of solid materials, while a decreasing value in mean residence time was observed with increasing liquid velocity and density of solid materials. Finally, a new empirical model was developed to estimate the mean residence time.
    c) The mass fraction profiles along the bed height increased with the decreasing liquid velocity and the lower values in the mass fraction are found by comparing with the higher velocity of the liquid. For heavy materials weight, the mass fraction showed higher results than that of the weight of the light material, while the low degree of tapered angle showed the higher mass fraction in values.
25. The outcomes in this study presents that modified wheat bran is an effective adsorbent for Dye, COD, and Turbidity removal and DO enhancement. The optimum operating conditions for maximum adsorption were obtained by statistical analysis as given below:
    a. The optimum adsorption conditions for dye removal by raw wheat bran, which is coated on PP, initial dye concentration 100 mg/L, pH 1.6, room temperature, air flow timing 28hr and adsorbent dose 10 g/100 mL at which 99.55% Dye removal was obtained.
    b. The optimum adsorption conditions for COD removal by raw wheat bran, which is coated on PP, initial dye concentration 100 mg/L, pH 1.6, room temperature, air flow timing 28hr and adsorbent dose 10 g/100 mL at which 98.56% COD removal was obtained.
    c. The optimum adsorption conditions for Turbidity removal by raw wheat bran, which is coated on PP, initial dye concentration of 100 mg/L, pH 8.5, room

temperature, air flow timing 28 h and adsorbent dose 10 g/100 mL at which 98.03% Turbidity removal was obtained.

d. The optimum adsorption conditions for DO enhancement by raw wheat bran, which is coated on PP, initial dye concentration of 100 mg/L, pH 8.5, room temperature, air flow timing 28hr and adsorbent dose 10 g/100 mL at which 99.55% DO enhancement was obtained. Therefore, the order of maximum adsorption capacity for heavy metal removal is Turbidity Removal > Dye removal > COD Removal>DO enhancement.

36. Out from results, this has been observed that dye starting concentration, air flow timing, and pH have the most important effect on the removal effectiveness of dye removal. Adsorbent dose, pH and initial concentration played a significant effect on the removal efficiency of COD. Initial dye concentration and adsorbent have the most significant effect of Turbidity removal. Initial concentration, pH, Air flow timing played significant effect on enhancement efficiency of DO.
37. The equilibrium data fitted well with both Temkin isotherms and Langmuir with the maximum adsorption capacity of 4.33 mg/g for COD, 9.0 mg/g for Dye, and 3.37mg/g for Turbidity.
38. The adsorption followed the pseudo-second order model for all the pollutants.

Different aspects of Research Work Carried out:

- Experiments have determined the hydrodynamic characteristics of two-phase tapered inverse fluidized beds with solid particles of low density.
- An adsorbent from raw wheat bran was prepared and coated on low density PP by using binder.
- The modified adsorbent was characterized for SEM, EDS and FTIR.

5.2 Recommendations for future work

The following works are recommended for future scope of research

1. Detailed study on Hydrodynamics, RTD in three phase tapered inverse fluidized bed and CFD as well as Design expert simulations can be done to observe the desired outcomes.
2. Adsorbent can be further modified by attaching various functional groups such as amino groups, hydroxyl groups that can enhance the adsorption efficiency.

3. The continuous adsorption and regeneration can also be studied in three phase systems in tapered inverse fluidized bed.

REFERENCES

1. Y.Peng, L.T.Fan, Hydrodynamic characteristics of fluidization in liquid-solid tapered beds, Chemical Engineering Science 52 (14) (1997) 2277 – 2290.
2. Allen, C. M. and Taylor, E. A.Trans (1923), Amer. Soc. Mech. Engrs, Vol. 45, pp.285.
3. M. Olazar, M.J. San Jose, A.T.J. Aguayo, M. Arandes, J.Bilbao, Ind. Eng. Chem. Res. 31 (1992) 1784–1792.
4. M.Olazer, M.J.San Jose, A.T.Aguayo, J.M.Arandes, J.Bilbao, Pressure drop in conical spouted beds, The Chemical Engineering Journal 51 (1993) 53 – 60.

5. N.I. Gelperin, E.N. Einstein, E.N. Gelperin, S.D. Lvova, Khim.I Tekin. Topl. I Masel. 5 (8) (1960) 51.
6. Y. Nishi, Kagaku kogaku Ronbunshu 5 (1979) 202–204.
7. M. Kwauk, Fluidization 1993 91–100, Science and Press, NewYork.
8. Y.F. Shi, Y.S. Yu, L.T. Fan, Incipient fluidization condition for a tapered fluidized bed, Ind. Eng. Chem. Fundam. 23 (1984) 484–489.
9. K.C. Biswal, T. Bhowmik, G.K. Roy, Prediction of minimum fluidization velocity for gas–solid fluidization of regular particles in conical vessels, Chem. Eng. J. 30 (1985) 57–62.
10. K.C. Biswal, T. Bhowmik, G.K. Roy, Prediction of pressure drop for a conical fixed bed of spherical particles in gas–solid systems, Chem. Eng. J. 29 (1984) 47–50.
11. A.E. Gorshtein, I.P. Mukhlenov, Hydraulic resistance of a fluidized bed in a cyclone without a grate. II. Critical gas rate corresponding to the beginning of a jet formation, Zh. Prikl. Khim. (Leningrad) 37 (1964) 1887–1893.
12. S. Jing, Q. Hu, J.Wang, Y. Jin, Fluidization of coarse particles in gas–solid conical beds, Chem. Eng. Process. 39 (2000) 379–387.
13. J. Shan, C. Guobin, M.Fan, B.Yu, W. Jingfu, J. Yong, Fluidization of fine particles in conical beds, Powder Technology 118 (2001) 271 – 274.
14. F.Depypere, J.G.Pieters, K.Dewettinck, Expanded bed height determination in a tapered fluidized bed reactor, Journal of Food Engineering 67 (2005) 353 – 359.
15. H.G.Kim, I.O.Lee, U.C.Chung and Y.H.Kim, Fluidization characteristics of iron ore fines of wide size distribution in a cold tapered gas-solid fluidized bed, ISIJ International 40(2000)16-22.
16. S.Chiba,T.Chiba,A.W.Nienow and H.Kobayashi, The critical fluidization velocity, bed expansion and pressure-drop profiles of binary particle mixtures, Powder Technology,22(1979)255-269. 74
17. K.Noda, S.Uchida, T.Makino and H.Kamo, Critical fluidization velocity of binary particles with large size ratio, Powder Technology, 46(1986) 149-154.
18. D.Bai, Y.Masuda, N.Nakagawa and K.Kato, Hydrodynamic behavior of a binary solids fluidized bed, Journal of Chemical Engineering of Japan, 29(1996) 211-216.
19. V.Thonglimp, N.Hiquily and C.Laguerie, Vitesse minimale de fluidization et expansion des couches de mélanges de particules solids fluidisees par un gaz, Powder Technology 39(1984) 223-239.
20. J.Rincon, J.Guardiola, A.Romero and G.Ramos, Predicting the critical fluidization velocity of multicomponent systems, Journal of Chemical Engineering of Japan, 27(1994)177-181.

21. R.Deiva Venkatesh, J.Chaouki, D.Klvana, Fluidization of cryogel in a conical column, Powder technology 89(1996) 179-186.
22. M.Olazer,R.Aguado,M.J.San Jose,S.Alvarez,J.Bilbao, Critical spouting velocity for the pyrolysis of scrap tyres with sand in conical beds, Powder Technology,165(2006) 128-132.
23. J.Li, B.Yang, G.Cheng, Affinity adsorption and hydrodynamic behavior in a tapered-bed of upward flow, Biochemical Engineering Journal 15(2003) 185-192.
24. W.R.A.Goossens, G.L.Dumont, G.L., Spaepen, Fluidization of binary mixtures in the laminar flow region, Chem.Eng.Prog.Symp.Ser. 67(1971) 38-45.
25. D.S.Povrenovic, D.E.Hadzismajlovic, Z.B.Grbavcic, D.V.Vukovic, Critical fluid flow rate, pressure drop and stability of a conical spouted Bed, The Canadian Journal of Chemical Engineering 70 (1992) 216 – 222.
26. G.R.Caicedo, M.G.Ruiz, J.J.P.Marques, J.G.Soler, Critical fluidization velocities for gas solid 2D beds, Chemical Engineering and Processing 41 (2002) 761 – 764.
27. Babu, S. P., Leipsiger, S., Lee, B. S., Weil, S. A. (1973), 'Solids mixing in batch operated tapered bed and non- tapered gas fluidized beds'. Fluidized Bed Fundam. Appl. AIChE Symp.Ser.69, 49-57.
28. Biswal K.C., Sahu, S., Roy, G. K. (1982), 'Prediction of fluctuation ratio for gas solid fluidization of regular particles in conical vessels', The Chemical Engineering Journal, 23, 97- 100.
29. Biswal.K.C, Samal, B. B., Roy, G. K. (1984), 'Dynamics of gas-solid fluidization of regular particles in conical vessels', The Journal the IE (India), Vol. 65, CH-1, 15 -17. 75
30. Biswal K.C. and Roy, G. K. (1985), 'Prediction of fluctuation ratio for gas-solid fluidizations of irregular particles in conical vessels'. The Journal of the IE (India), Vol. 65, CH2, 57-62.
31. Maruyama T.and Koyanagi T (1993). 'Fluidization in tapered vessels'. The Chemical Engineering Journal.51, 121-128.
32. C.D. Scott, C.W. Hancher, Use of a tapered fluidized bed as a continuous bioreactor, Biotechnol. Bioeng. 18 (1976) 1393–1403.
33. K. Ridgway, The tapered fluidized bed—a new processing tool, Chem. Process. Eng. 6 (1965) 317–321.
34. S.P. Babu, S. Leipsiger, B.S. Lee, S.A.Weil, Solids mixing in batch operated tapered bed and non-tapered gas fluidized beds, Fluidized Bed Fundam.Appl. AIChE, Symp. Ser. 69 (1973) 49–57.
35. T. Maruyama, H. Sato (1991)," Liquid fluidization in conical vessels", Chem. Eng.J. 46 15– 21.

36. T. Koloini, E.J. Farkas, Fixed bed pressure drop of a liquid fluidization in tapered or conical vessels, Can. J. Chem. Eng. 51 (1973) 499–502.
37. Y.F. Shi, Y.S. Yu, L.T. Fan, Incipient fluidization condition for a tapered fluidized bed, Ind. Eng. Chem. Fundam. 23 (1984) 484–489.
38. K.C. Biswal, T. Bhowmik, G.K. Roy, Prediction of minimum fluidization velocity for gas–solid fluidization of regular particles in conical vessels, Chem. Eng. J. 30 (1985) 57–62.
39. K.C. Biswal, T. Bhowmik, G.K. Roy, Prediction of pressure drop for a conical fixed bed of spherical particles in gas–solid systems, Chem. Eng. J. 29 (1984) 47–50.
40. R.K. Singh, A. Suryanarayana, G.K. Roy (1992), "Prediction of minimum velocity and minimum bed pressure drop for gas–solid fluidization in conical conduits", Can. J. Chem. Eng. 70 185–189.
41. J. Shan, C. Guobin, M. Fan, B. Yu,W. Jingfu, J. Yong, Fluidization of fine particles in conical beds, Powder Technol. 118 (2001) 271–274. 76
42. G. Narsimhan, On generalized expression for prediction of minimum fluidization velocity, AIChE J. 11 (1965) 550–554.
43. J. Li, B. Yang, G. Cheng, Affinity adsorption and hydrodynamic behavior in a tapered-bed of upward flow, Biochem. Eng. J. 15 (2003) 185–192.
44. D.S. Povrenovic, D.E. Hadzismajlovic, Z.B. Grbavcic, D.V. Vukovic, Minimum fluid flow rate, pressure drop and stability of a conical spouted bed, Can. J. Chem. Eng. 70 (1992) 216–222.
45. G.R. Caicedo, M.G. Ruiz, J.J.P. Marqu´es, J.G. Soler, Minimum fluidization velocities for gas–solid 2D beds, Chem. Eng. Process. 41 (2002) 761–764.
46. Fluent Inc.,"Fluent 6.1 UDF Manual" (2003a)
47. Fluent Inc.,"Fluent 6.1 user guide" (2003b)
48. R. Escudiéa, N. Epsteina, J.R. Gracea, H.T. Bi. Effect of particle shape on liquid-fluidized beds of binary (and ternary) solids mixtures: segregation vs. mixing, Journal of Chemical Engineering Science 61 (2006) 1528 – 1539.
49. K.C. Biswal, T. Bhowmik, G.K. Roy, Prediction of minimum fluidization velocity for gassolid fluidization of regular particles in conical vessels, Chem. Eng. J. 30 (1985) 57–62.
50. Maureen A. Howley, Benjamin J. Glasser. Hydrodynamics of a uniform liquid-fluidized bed containing a binary mixture of particles, Chemical Engineering Science 57 (2002) 4209 – 4226.
51. Trambouze, P., Euzen, J., 2004. Chemical Reactor, from Design to Operation. Technip, Paeis.

52. F. Depypere, J.G. Pieters, K. Dewettinck, Expanded bed height determination in a tapered fluidised bed reactor, Journal of Food Engineering 67 (2005) 353–359
53. N. Epstein, B.B. Pruden, Liquid fluidization of binary particle mixtures—III Stratification by size and related topics, Chemical Engineering Science 54 (1999) 401—415.
54. Jena, H.M., 2009. Hydrodynamic of Gas-Liquid-Solid Fluidized and Semi-Fluidized Beds, PhD thesis. National Institute of Technology, Rourkela
55. Rupesh K. Reddy, Jyeshtharaj B. Joshi, CFD modeling of solid–liquid fluidized beds of mono and binary particle mixtures, Chemical Engineering Science 64 (2009) 3641 – 3658.
56. S. Barghi, C.L. Briens, M.A. Bergougnou, Mixing and segregation of binary mixtures of particles in Liquid–solid fluidized beds, Powder Technology 131 (2003) 223– 233.
57. Renzo Di Felice, Hydrodynamics of liquid solid fluidization, Chemical Engineering Science, Vol. 50, No, 8, pp. 1213-1245,1995.
58. B. Formisani and R. Girimonte, Experimental Analysis of the Fluidization Process of Binary Mixtures of Solid, Dipartimento di Ingegneria Chimica e die Materiali, Università della Calabria
59. M.G. Rasul, V. Rudolph, F.Y. Wang, Particles separation using fluidization techniques, Int. J. Miner. Process. 60 2000 163–179
60. R. Escudiéa, N. Epsteina, J.R. Gracea, H.T. Bi. Effect of particle shape on liquid-fluidized beds of binary (and ternary) solids mixtures: segregation vs. mixing, Journal of Chemical Engineering Science 61 (2006) 1528 – 1539 63
61. Maureen A. Howley, Benjamin J. Glasser, Hydrodynamics of a uniform liquid-fluidized bed containing a binary mixture of particles, Chemical Engineering Science 57 (2002) 4209 – 4226.
62. Sankarshana Talapuru, J S N Murthyy, S Nandanaz, Phani Kiran S V G R, V Rameshy, Hydrodynamic Characteristics of Liquid-Solid Fluidization of Binary Mixtures in Tapered Beds, 2010 ECI Conference on The 13th International Conference on Fluidization - New Paradigm in Fluidization Engineering.
63. S. Barghi, C.L. Briens, M.A. Bergougnou, Mixing and segregation of binary mixtures of particles in Liquid–solid fluidized beds, Powder Technology 131 (2003) 223– 233.
64. N. Epstein, B.B. Pruden, Liquid fluidization of binary particle mixtures—III Stratification by size and related topics, Chemical Engineering Science 54 (1999) 401—415.
65. A.K. Mukherjee, B.K. Mishra, Experimental and simulation studies on the role of fluid velocity during particle separation in a liquid–solid fluidized bed, Int. J. Miner. Process. 82 (2007) 211–221

66. M.G. Rasul, V. Rudolph, M. Carsky, Segregation in binary and ternary liquid fluidized beds, Powder Technology 126 (2002) 116– 128
67. Fan, L.S., Muroyama, K., Chern, S.H., 1982. Hydrodynamic characteristics of inverse fluidization in liquid–solid and gas–liquid–solid systems. The Chemical Engineering Journal 24, 143-150.
68. Bruno Formisani, Rossella Girimontey, Tiziana Longoz, The Fluidization Pattern of DensitySegregating Two-Solid Beds, 2007 ECI Conference on The 12th International Conference on Fluidization - New Horizons in Fluidization Engineering
69. Y.Peng, L.T.Fan, Hydrodynamic characteristics of fluidization in liquid-solid tapered beds, Chemical Engineering Science 52 (14) (1997) 2277 – 2290
70. K. Ganesh Palappan, P.S.T. Sai, Studies on segregation of binary mixture of solidsin a continuous fast fluidized bed Part I. Effect of particle density, Chemical Engineering Journal 138 (2008) 358–366
71. Paola Lettieri , Renzo Di Felice , Roberta Pacciani , Olumuyiwa Owoyemi, CFD modeling of liquid fluidized beds in slugging mode, www.elsevier.com/locate/powtec, Powder Technology 167 (2006) 94–103
72. Rupesh K. Reddy, Jyeshtharaj B. Joshi, CFD modeling of solid–liquid fluidized beds of mono and binary particle mixtures, Chemical Engineering Science 64 (2009) 3641 – 3658.
73. R. Panneerselvam, S. Savithri, G.D. Surender, CFD based investigations on hydrodynamics and energy dissipation due to solid motion in liquid fluidised bed, Chemical Engineering Journal 132 (2007) 159–171 29. Luca Mazzei, PaolaLettieri, CFD simulations of expanding/contracting homogeneous fluidized beds and their transition to bubbling, Chemical Engineering Science 63 (2008) 5831- 5847
74. Shuyan Wang, Xiaoqi Li, Yanbo Wu, Xin Li, Qun Dong, and Chenghai Yao, Simulation of Flow Behavior of Particles in a Liquid-Solid Fluidized Bed, Ind. Eng. Chem. Res. 2010, 49, 10116–10124
75. Long Fan, John Gracey, Norman Epsteinz, CFD Simulation of a Liquid-Fluidized Bed of Binary Particles, 2010 ECI Conference on the 13th International Conference on Fluidization - New Paradigm in Fluidization Engineering
76. Jack T. Cornelissena, Fariborz Taghipoura, Renaud Escudiea, Naoko Ellisa, John R. Grace, CFD modelling of a liquid–solid fluidized bed, Chemical Engineering Science 62 (2007) 6334 – 6348
77. Olumuyiwa Owoyemi, Paola Lettieri, A CFD Study into the Influence of the Particle-Particle Drag Force on the Dynamics of Binary Gas Solid Fluidized Beds, Department of

Chemical Engineering, University College London, Torrington Place, London, WC1E 7JE, UK.

78. Olumuyiwa Owoyemi, Luca Mazzei, and Paola Lettieri, CFD Modeling of Binary-Fluidized Suspensions and Investigation of Role of Particle–Particle Drag on Mixing and Segregation, AIChE J, 53: 1924–1940, 2007
79. Fariborz Taghipour, Naoko Ellis, Clayton Wong, Experimental and computational study of gas–solid fluidized bed hydrodynamics, Chemical Engineering Science 60 (2005) 6857 – 6867
80. G.R. Kumar Reddy And J.B. Joshi, CFD Simulation of Fluid-Particle and Particle-Particle Interaction in Packed and Fluidized Beds, Institute of Chemical Technology, Matunga, Mumbai400 019, INDIA 65
81. Matteo Chiesaa, Vidar Mathiesenb, Jens A. Melheimc, Britt Halvorsend, Numerical simulation of particulate flow by the Eulerian–Lagrangian and the Eulerian–Eulerian approach with application to a fluidized bed, Computers and Chemical Engineering 29 (2005) 291–304
82. Scott Cooper, Charles J. Coronella T, CFD simulations of particle mixing in a binary fluidized bed, Powder Technology 151 (2005) 27– 36
83. Joshi J. B., Vitankar, V. S., Dhotre, M. T., 2002. A low Reynolds number k–e model for the prediction of flow pattern and pressure drop in bubble column reactors. Chemical Engineering Science 57, 3235 – 3250
84. Mitra-Majumdar, D., Farouk, B., Shah, Y. T., 1997. Hydrodynamic modeling of three-phase flows through a vertical column. The Chemical Engineering Science 52, 4485–4497
85. Li, Y., Zhang, J., Fan, L. S., 1999. Numerical simulation of gas–liquid–solid fluidization systems using a combined CFD–VOF–DPM method, bubble wake behavior. Chemical Engineering Science 54, 5101–5107 42. Andre Bakker, Introduction to CFD, Applied Computational Fluid Dynamics,
86. Wen Y. Soung, Bed Expansion in Three-phase Fluidization, Ind. Eng. Chem. Process Des. Dev., Vol. 17, No. 1, 1978 33
87. H.M. Jenaa, B.K. Sahoo, G.K. Roya, B.C. Meikap, Characterization of hydrodynamic properties of a gas–liquid–solid three-phase fluidized bed with regular shape spherical glass bead particles, Chemical Engineering Journal (2008)
88. Haibo Yu and Bruce E. Rittmann, Predicting Bed Expansion and Phase Holdups for three Phase Fluidized-Bed Reactors with and Without Biofilm, Wat. Res. Vol. 31, No. 10. pp. 2604- 2616, 1997

89. X Hu, The segregation in the binary-solid liquid fludized bed, Chemical Engineering Technology, 25 (2002) 9
90. R. Panneerselvam, S.Savithri, G.D.Surender, CFD simulation of hydrodynamics of gas–liquid–solid fluidised bed reactor, Chemical Engineering Science 64 (2009) 1119-1135
91. Huilin Lu, ShuyanWang,Yunhua Zhao, LiuYang, Dimitri Gidaspow, Jiamin Ding, Prediction of particle motion in a two-dimensional bubbling fluidized bed using discrete hard-sphere model, Chemical Engineering Science 60 (2005) 3217 – 3231
92. Zhang Wei, A Review of Techniques for the Process Intensification of Fluidized Bed Reactors, Chinese Journal of Chemical Engineering, 17(4), 688 – 702, 2009.
93. M.C. Ruzicka et.al, Smart RTD for multiphase flow systems, chemical engineering research and design 9 0, 1739–1749, 2 0 1 2.
94. T.E. Baldock et.al, settling velocity of sediments at high concentrations, Coastal Engineering, 51, 91–100, 2004.
95. J. Martin, N. Rakotomalala, and D. Salin, Accurate determination of the sedimentation flux of concentrated suspensions, Phys. Fluids, 7, No.10, 2510 – 2512, 1995.
96. By Renzo Di Felice and Ralf Kehlenbeck, Sedimentation Velocity of Solids in Finite Size Vessels, Chem. Eng. Technol. 23, No.12, 1123 – 1126, 2000.
97. Ju-Sheng Huang et.al, Comparative bioparticle and hydrodynamic Characteristics of conventional and tapered anaerobic fluidized-bed bioreactors, J Chem Technol Biotechnol, 75, 269 – 278, 2000.
98. Yan-Fu Shi, Y. S. Yu, and L. T. Fan, Incipient Fluidization Condition for a Tapered Fluidized Bed, Ind. Eng. Chem. Fundamentals., 23, No. 4, 484 – 489, 1984.
99. T.M. Gernon and M.A. Gilbertson, Segregation of particles in a tapered fluidized bed, Powder Technology, 231, 88 –101, 2012.
100. Howard Littman, Solids Mixing in Straight and Tapered Fluidized Beds, A.1.Ch.E. Journal, 94, No.10, 924 – 929,1964.
101. D.C. Sau et al., Minimum fluidization velocities and maximum bed pressure drops for gas – solid tapered fluidized beds, Chem. Eng. Journal, 132, 151–157, 2007.
102. G. Kwant et.al, Particle mixing and separation in a binary solids floating fluidized bed, Powder Technology, 82, 279-291, 1995.
103. Sun Liyan et.al, Prediction of flow behavior of particles in a tapered bubbling fluidized bed using a second - order moment-frictional stresses model, Chem. Eng. Sci., 84, 170 – 181, 2012.
104. Hassan Basirat Tabrizi et.al, Pulsating flow effect on the segregation of binary particles in a gas – solid fluidized bed, Powder Technology, 264, 570 – 576, 2014.

105. Yong Chen et.al, Development of a new type of thermo gravimetric analyser with a mini-tapered fluidized bed. Effect of fluidization of particles on the stability of the system, Chem. Eng. Journal, 68, 7 - 9, 1997.
106. Leila Boumehdi Toumi et.al, Wet Granulation of Cereal Grains in a Tapered Fluidized Bed, Chem. Eng. Transactions, 32, 2149 – 2154, 2013.
107. Manon Van de Velden et.al, Solids mixing in the riser of a circulating fluidized bed, Chem. Eng. Sci., 62, 2139 – 2153, 2007.
108. V. Idakiev and L. Morl, Study of residence time of disperse materials in continuously operating fluidized bed apparatus, Journal of Chemical Technology and Metallurgy, 48, 5, 451 - 456, 2013.
109. M. Prasad Babu and Y. Pydi Setty, Residence Time Distribution of Solids in a Fluidized Bed, The Canadian Journal of Chem. Eng., 81, 118 – 123, 2003.
110. Danckwerts, P. V., Chem. Eng. Sci., 2, 1, 1953.
111. Couderc, J.P., Incipient fluidization and particulate systems. In: Davidson, J.F., Clift, R., Harrison, D. (Eds.), Fluidization. Academic Press, New York, 1– 46, 1985.
112. Fan L - S., Summary paper on fluidization and transport phenomena. Powder Technology 88, 245–253, 1996.
113. Di Felice, R, Hydrodynamics of liquid fluidization, Chem. Eng. Sci., 50,N0.8, 1213-1245, 1995.
114. Bolton, L. W., & Davidson, J. F., Recirculation of particles in fast fluidized risers. In P. Basu & J. F. Large (Eds.), Circulating fluidized bed technology II (pp. 139–146). Oxford: Pergamon Press, 1988.
115. Kunii, D., & Levenspiel, O., Entrainment of solids from fluidized beds II operation of fast fluidized bed. Powder Technology, 61, 193–206, 1990.
116. Yang, W. C., A model for dynamics of circulating fluidized bed loop. In P. Basu & J. F. Large (Eds.), Circulating fluidized bed technology II (pp. 181– 192). Oxford: Pergamon Press, 1988.
117. Liang, W- G et al., Radial non-uniformity of flow structure in a liquidsolid Circulating fluidized bed, Chem. Eng. Sci., 51, 2001-2010, 1996.
118. K. Mitsutania, J.R. Grace and C.J. Lim, Residence time distribution of particles in a continuous liquid–solid classifier, Chem. Eng. Sci., 60, 2703 – 2713, 2005. 117
119. Umang Trivedi, Amarjeet Bassi and Jing-Xu (Jesse) Zhu, Continuous enzymatic Polymerization of phenol in a liquid- solid circulating fluidized bed, Powder Technol., 169, 61-70, 2006.
120. Levenspiel O, (1972), Chemical Reaction Engineering, Wiley, New York.

121. Grace, J. R., Avidan, A. A., Knowlton, T. M., Eds. Circulating Fluidized Beds; Blackie Academic and Professional: London, U.K., 1997.
122. R´egis Andreux et.al, Hydrodynamic and solid residence time distribution in a circulating fluidized bed: Experimental and 3D computational study, Chem. Eng. and Processing 47, 463–473, 2008.
123. Samir S Chapadgaonkar and Y Pydi Setti, Residence time distribution of solids in fluidized bed, Indian Journal of Chemical Technology, 6,100-106, March 1999.
124. Felix Donat et.al, Use of a Chemical-Looping Reaction to Determine the Residence Time Distribution of Solids in a Circulating Fluidized Bed, Energy Technol. 4, 1230 – 1236, 2016.
125. Youg Jin, et.al, Liquid dispersion in gas – liquid – solid circulating fluidized beds, Chem. Eng. Journal, 70, 9-14, 1998.
126. Kai Zhang, Axial solid concentration distribution in tapered and cylindrical bubble columns, Chemical Engineering Journal, 86, 299–307, 2002.
127. J S N Murthy et.al, hydrodynamic characteristics of liquid-solid Fluidization of binary mixtures in tapered beds, Refereed Proceedings, the 13th International Conference on Fluidization - New Paradigm in Fluidization Engineering, Engineering Conferences International Year 2010. 118
128. Lu Gan, Xiaofeng Lu and Quanhai Wang, Experimental and theoretical study on hydrodynamic characteristics of tapered fluidized beds, Advanced Powder Technology, 25, 824–831, 2014.
129. Jing Shan et.al, Fluidization of fine particles in conical beds, Powder Technology, 118, 271–274, 2001.
130. Goran N. Jovanovic et.al, magnetically assisted liquid–solid fluidization in normal and microgravity conditions: experiment and theory, Powder Technology 148, 80–91, 2004.
131. Asghar Molaei Dehkordi et.al, Steam reforming of methane in a tapered membrane - Assisted fluidized - Bed reactor: Modeling and simulation, Int. J. Hydrogen Energy, 3 6, 4 9 0 - 5 0 4, 2011.
132. Hideya Nakamura et.al, Numerical analysis of fluid flow and particle entrainment in a novel tapered rotating fluidized bed, Chemical EngineeringScience116, 725–733, 2014.
133. L.T.Fan and Yimin Peng, Hysteresis in liquid-solid tapered fluidized beds, Chem.Eng.Sci.50, no.16, 2669-2671, 1995.
134. L.T.Fan and Yimin Peng, Hydrodynamic characteristics of fluidization in liquid-solid tapered beds, Chem.Eng.Sci.52, no.14, 2277-2290, 1997.

135. Zhu Jiahua and XIA Sulan, Study on Liquid-Phase Axial Dispersion in Converging Taper Liquid-Solid Fluidized Beds, Chinese J. Of Chem.Eng., 8(2), 134-139, 2000.
136. George H. Webster and Joseph J. Perona, Liquid Mixing in a Tapered Fluidized Bed, AICHE Journal, 34, no.8,1398-1402, 1988. 119
137. Jing-Xu Zhu and Wu-Geng Liang, A core-annulus model for the radial flow structure in a liquid-solid circulating fluidized bed (LSCFB), Chem.Eng.Journal, 68, 51-62, 1997.
138. JSN Murthy et.al, Residence Time Distribution in Semi-Fluidized Beds, IE(I) Journal-CH, 71, 42-43, 1990.
139. R Di Felice, Hydrodynamics of liquid fluidisation, Chemical engineering science, 50(8), 1213-1245, 1995. [31] Domenico Sanfilippo, Dehydrogenations in fluidized bed: Catalysis and reactor engineering, Catalysis Today 178, 142– 150, 2011.
140. Chunyi Li et.al, Catalytic cracking of n-heptane under activation of lattice oxygen in a circulating fluidized bed unit, Chemical Engineering Journal 172, 410– 417, 2011.
141. G. Ruoppolo et.al, Biomass gasification in a catalytic fluidized reactor with beds of different materials, Chemical Engineering Journal 154, 369– 374, 2009.
142. George Nakhla et.al, Simultaneous carbon and nitrogen removal with enhanced bio particle circulation in a Circulating Fluidized Bed Biofilm Reactor, Chemical Engineering Journal, 181– 182, 35 – 44, 2012.
143. Jalal Abedi et.al, A comprehensive mathematical model for biomass gasification in a bubbling fluidized bed reactor, Fuel, 89, 3650–3661, 2010.
144. J.-X Zhu and Jing Xu, Experimental study on solids concentration distribution in a two-dimensional circulating fluidized bed, Chemical Eng. Sci. 65, 5447–5454, 2010. 120
145. R. Veneman et.al, Continuous CO2 capture in a circulating fluidized bed using supported amine sorbents, Chemical Engineering Journal, 207–208, 18–26, 2012.
146. Todd Pugsley and Shayan Karimipour, Study of gas streaming in a deep fluidized bed containing Geldart's Group A particles, Chem. Eng. Sci., 65, 3508–3517, 2010.
147. Zhengbiao Peng et.al, Experimental study on drop formation in liquid– liquid fluidized bed, Chem. Eng. Sci. 64, 1249 – 1259, 2009.
148. J.-X. Zhu et.al, Application of electrical resistance tomography on liquid–solid two-phase flow characterization in an LSCFB riser, Chem. Eng. Sci., 64, 2851 – 2858, 2009.
149. George Nakhla et.al, Impact of worm predation on pseudo-steady-state of the circulating fluidized bed biofilm reactor, Bioresource Technology 128, 281–289, 2013.
150. R. Sundaresan & Ajit Kumar Kolar, Axial heat transfer correlations in a circulating fluidized bed riser, Applied Thermal Engineering 50, 985 – 996, 2013.

151. B.C. Meikap et.al, Hydrodynamics of a multi-stage counter-current fluidized bed reactor with down-comer for amine impregnated activated carbon particle system, Advanced Powder Technology, 28, 854–864, 2017. 121
152. F. Depypere et.al, expanded bed height determination in a tapered fluidised bed reactor, Journal of Food Engineering, 67, 353 – 359, 2005.
153. Marianthi Ierapetritou et.al, Characterizing continuous powder mixing using residence time distribution, Chem. Eng. Sci., 66, 417–425, 2011.
154. Jyeshtharaj B. Joshi et.al, Liquid phase axial mixing in solid–liquid circulating multistage fluidized bed: CFD modelling and RTD measurements, Chem. Eng. Journal 191, 475 – 490, 2012.
155. Martin Martinov et.al, Liquid flow residence time in a fibrous fixed bed reactor with recycle, Bioresource Technology, 101, 1300–1304, 2010.
156. F. Berruti et.al, measuring and modelling residence time distribution of low density solids in a fluidized bed reactor of sand particles, Chem. Eng. Sci., Vol. 43, No. 4, 739-748,1988.
157. Marianthi Ierapetritou et.al, Characterizing continuous powder mixing using residence time distribution, Chem. Eng. Sci., 66, 417–425, 2011.
158. Mayank Kashyap and Dimitri Gidaspow, Measurements of Dispersion Coefficients for FCC Particles in a Free Board, Ind. Eng. Chem. Res., 50, 7549–7565, 2011.
159. G.Weickert et.al, Fluidization behavior in a circulating slugging fluidized bed reactor. Part I: Residence time and residence time distribution of polyethylene solids, Chem. Eng. Sci., 62, 2522 – 2534, 2007.
160. Marianthi G. Ierapetritou et.al, A review of the Residence Time Distribution (RTD) applications in solid unit operations, Powder Technology 228, 416–423, 2012. 122
161. A.T. Harris et.al, A novel method for measuring the residence time distribution in short time scale particulate systems, Chem. Eng. Journal, 89, 127–142, 2002.
162. X. S. Wang and M. J. Rhodes, Determination of particle residence time at the walls of gas fluidized beds by discrete element method simulation, Chem. Eng. Sci., 58, 387 – 395, 2003.
163. A.T. Harris et.al, Particle residence time distributions in circulating "fluidized beds, Chem. Eng. Sci., 58, 2181 – 2202, 2003.
164. Jing-Xu (Jesse) Zhu et.al, (Gas-) Liquid-Solid Circulating Fluidized Beds and their Potential Applications to Bioreactor Engineering, The Canadian Journal of Chemical Engineering, 78, 82-94, February 2000.
165. Masoud et.al, Heat Transfer of Liquid/ Solid Fluidized Beds for Newtonian and Non-Newtonian Fluids, Iran. J. Chem. & Chem. Eng., Vol. 23, No. 1, 119-129, 2004.

166. Sunun Limtrakul et.al, Solids motion and holdup profiles in liquid fluidized beds, Chem. Eng. Sci., 60, 1889 – 1900, 2005.
167. Guodong Jin, Multi-scale modelling of gas–liquid–solid three-phase fluidized beds using the EMMS method, Chem. Eng. Journal, 117, 1–11, 2006. 123
168. Majid Khanali et.al, Study of Residence Time Distribution of Rough Rice in a Plug Flow Fluid Bed Dryer, International Journal of Adv. Sci. and Tech., 48, 103-114, 2012.
169. Anuj Srivastava and Sankaran Sundaresan, Role of wall friction in Fluidization and standpipe flow, Powder Technology 124, 45– 54, 2002.
170. W. Zhang and Y. Tung, Radial voidage profiles in fast fluidized beds of different diameters, Chem. Eng. Sci., 46, No 12, 3045 – 3052, 1991.
171. T. Renganathan and K. Krishnaiah, Voidage characteristics and prediction of bed expansion in liquid–solid inverse fluidized bed, Chem. Eng. Sci., 60, 2545 – 2555, 2005.
172. V.V.Basava Rao, T.Bala Narsaiaha and B.V. Reddy, Prediction of Falling Solids Film Thickness near the Wall in Circulating Fluidized Bed Risers, International Journal of Chem. Eng. and Applications, 2, No. 2, 84-90, 2011.
173. Jing-Xu Zhu et.al, Flow characteristics of the liquid–solid circulating fluidized bed, Powder Technology, 90, 95 –102, 1997.
174. P Natarajan et.al, Holdup and solids circulation rate in liquid-solid fluidized bed, Indian journal of Chemical Technology, 13,247-254, 2006.
175. Boaz Habib and Mohammed Farid, Heat transfer and operating conditions for freeze concentration in a liquid–solid fluidized bed heat exchanger, Chemical Engineering and Processing 45, 698–710, 2006. 124
176. Jianzhong Yang and Albert Renken, A generalized correlation for equilibrium of forces in liquid–solid fluidized beds, Chemical Engineering Journal, 92, 7–14, 2003.
177. Jyeshtharaj B. Joshi et.al, Solid-Liquid Circulating Multistage Fluidized Bed: Hydrodynamic Study, Ind. Eng. Chem. Res., 48, 4592–4602, 2009.
178. Binay K. Dutta and Suman Bhattacharyya, On Mixing and Segregation in Binary Solid-Liquid Fluidized Beds, Ind. Eng. Chem. Res., 43, 7129-7136, 2004.
179. Shuyan Wang et.al, Simulation of Flow Behavior of Particles in a LiquidSolid Fluidized Bed, Ind. Eng. Chem. Res., 49, 10116–10124, 2010.
180. Miryan Cassanello et.al, Solids mixing in Gas-Liquid-Solid Fluidized beds: Experiments and Modelling, Chem. Eng. Sci., 51, No.10, 2011-2020, 1996.
181. J. Zhou, J. R. Grace et.al, Voidage profiles in a circulating fluidized bed of square cross-section, Chem. Eng. Sci., 49, No.19, 3217-3226, 1994.

182. Jing-Xu (Jesse) Zhu et.al, Continuous Protein Recovery from Whey Using Liquid-Solid Circulating Fluidized Bed Ion-Exchange Extraction, Biotechnology and Bioengineering, 78, NO. 2,157-163, 2002.
183. Jinfu Wang et.al, Fluidization of coarse particles in gas–solid conical beds, Chemical Engineering and Processing 39, 379–387, 2000.
184. Dandan Zhou et.al, Minimum fluidization velocity of a three – phase conical fluidized bed in comparison to a cylindrical fluidized bed, Ind. Eng. Chem. Res., 48, 27-36, 2009.
185. Jing Shan et.al, Fluidization of fine particles in conical beds, Powder Technology, 118, 271–274, 2001. [99]
186. Ronald W. Missen, Charles A. Mims and Bradley A. Saville, Introduction to Chemical Reaction Engineering and Kinetics, John Wiley & Sons, Inc., 1999.
187. Chao Li et.al, Numerical study of the particle residence time and flow characters in an Opposed Multi-Burner gasifier, Powder Technology, 286, 64–72, 2015.
188. Shantanu Roy et.al, A method for estimating the solids circulation rate in a closed-loop circulating fluidized bed, Powder Technology, 121, 213–222, 2001.
189. Laurence A. Belfiore, Transport Phenomena for Chemical Reactor Design, John Wiley & Sons, Inc., Publication, 2003.
190. Bolun Yang et.al, Affinity adsorption and hydrodynamic behavior in a tapered-bed of upward flow, Biochemical Engineering Journal, 15, 185 – 192, 2003.
191. Rangasamy Parthiban et.al, Anaerobic tapered fluidized bed reactor for starch wastewater treatment and modeling using multilayer perceptron neural network, Journal of Environmental Sciences, 19, 1416–1423, 2007.
192. Jianjun Dai and John R. Grace, Biomass screw feeding with tapered and extended sections, Powder Technology 186, 56 – 64, 2008.
193. Chun – Sheng and Ju – Sheng Huang, Bio Particle characteristics of tapered anaerobic fluidized – bed Bioreactors, Wat. Res., 30, No.1, 233 - 242, 1996. 128
194. W.O. Filtvedt et.al, Review: Development of fluidized bed reactors for silicon production, Solar Energy Materials & Solar Cells, 94, 1980 – 1995, 2010.
195. J.G. Pieters et.al, Comparison and evaluation of interphase momentum exchange models for simulation of the solids volume fraction in tapered fluidized beds, Chem. Eng. Sci., 65, 3100 – 3112, 2010.
196. Bo – Lun Yang et.al, Hydrolysis of O – nitrophenyle – β – D – galactoside by an enzyme immobilized on perfluorocarbon in a tapered column reactor, Colloids and Surfaces B: Bio interfaces, 10, 127 – 135, 1998.

197. D.T.K. Dora et.al, Hydrodynamics of gas – solid fluidization of a homogeneous ternary mixture in a conical bed: Prediction of bed expansion and bed fluctuation ratios, Particuology, 11, 681– 688, 2013. [111] D.C. Sau et.al, Minimum fluidization velocity at elevated temperature in tapered fluidized bed, Chemical Engineering and Processing, 47, 2391– 2394, 2008.
198. Yin Wang et.al, Rarefaction wave propagation in tapered granular columns, Chem. Eng. Sci., 71, 32 – 38, 2012.
199. D.C. Sau et.al, Correlations for critical fluidization velocity and maximum bed pressure drop for heterogeneous binary mixture of irregular particles in gas – solid tapered fluidized beds, Chem. Eng. and Processing, 47, 2386 – 2390, 2008.
200. D.C. Sau et.al, Prediction of critical fluidization velocity and maximum bed pressure drop for binary mixture of irregular particles in gas – solid tapered fluidized beds, Chem. Eng. and Processing, 47, 2114 – 2120, 2008. 129
201. Benjapon Chalermsinsuwan et.al, CFD modeling of tapered circulating fluidized bed reactor risers: Hydrodynamic descriptions and chemical reaction responses, Chem. Eng. and Processing, 49, 1144 – 1160, 2010.
202. Hossein Askaripour and Asghar Molaei Dehkordi, Effects of initial static bed height on fractional conversion and bed pressure drop in tapered – in and tapered – out fluidized bed reactors, International Journal of Multiphase Flow, 79, 50 – 61, 2016.
203. Richardson, J.F., Zaki, W.N., 1954. Sedimentation and fluidization: Part 1. Transactions of the Institution of Chemical Engineers 32, 35 – 53.
204. Alvarado-Lassman A, Rustrián E, García-Alvarado MA, et al (2008) Brewery wastewater treatment using anaerobic inverse fluidized bed reactors. Bioresour Technol 99:3009–3015 . doi: 10.1016/j.biortech.2007.06.022
205. Wang D, Silbaugh T, Pfeffer R, Lin YS (2010) Removal of emulsified oil from water by inverse fluidization of hydrophobic aerogels. Powder Technol 203:298–309 . doi: 10.1016/j.powtec.2010.05.021
206. Rajasimman M, Karthikeyan C (2009) Performance of inverse fluidized bed bioreactor in treating starch wastewater. Front Chem Eng China 3:235–239 . doi: 10.1007/s11705-009-0020-0
207. Sokół W, Woldeyes B (2011) Evaluation of the Inverse Fluidized Bed Biological Reactor for Treating High-Strength Industrial Wastewaters. Adv Chem Eng Sci 01:239–244 . doi: 10.4236/aces.2011.14034
208. Krishnaiah K, Guru S, Sekar V (1993) Hydrodynamic studies on inverse gas-liquid-solid fluidization. Chem Eng J 51:109–112 . doi: 10.1016/0300-9467(93)80017-I

209. Cho YJ, Park HY, Kim SW, et al (2002) Heat transfer and hydrodynamics in two- and three-phase inverse fluidized beds. Ind Eng Chem Res 41:2058–2063 . doi: 10.1021/ie0108393
210. Il Lee K, Mo Son S, Yeong Kim U, et al (2007) Particle dispersion in viscous three-phase inverse fluidized beds. Chem Eng Sci 62:7060–7067 . doi: 10.1016/j.ces.2007.08.024
211. Karamanev DG, Nikolov LN (1992) Bed Expansion of Liquid-Solid Inverse. 38:1916–1922
212. Sabarunisha Begum S, Radha K V. (2014) Hydrodynamic behavior of inverse fluidized bed biofilm reactor for phenol biodegradation using Pseudomonas fluorescens. Korean J Chem Eng 31:436–445 . doi: 10.1007/s11814-013-0260-z
213. Renganathan T, Krishnaiah K (2004) Liquid phase mixing in 2-phase liquid-solid inverse fluidized bed. Chem Eng J 98:213–218 . doi: 10.1016/j.cej.2003.08.001
214. Scott CD, Hancher CW, Shumate SE (2013) A Tapered Fluidized Bed as a Bioreactor. Enzym Eng XVIII:255–261 . doi: 10.1007/978-1-4757-5163-5_29
215. Rasteh M, Farhadi F, Bahramian A (2015) Hydrodynamic characteristics of gas-solid tapered fluidized beds: Experimental studies and empirical models. Powder Technol 283:355–367 . doi: 10.1016/j.powtec.2015.06.002
216. Kumar U, Agarwal VK (2017) Simulation of 3D gas–solid fluidized bed reactor hydrodynamics. Part Sci Technol 35:1–13 . doi: 10.1080/02726351.2015.1119227
217. Wang S, Sun J, Yang Q, et al (2014) Numerical simulation of flow behavior of particles in an inverse liquid-solid fluidized bed. Powder Technol 261:14–21 . doi: 10.1016/j.powtec.2014.04.017
218. Abdelmotalib HM, Youssef MAM, Hassan AA, et al (2016) Influence of the specularity coefficient on hydrodynamics and heat transfer in a conical fluidized bed combustor. Int Commun Heat Mass Transf 75:169–176 . doi: 10.1016/j.icheatmasstransfer.2016.04.018
219. Rao BJM, Rao KVNS, Ranga Janardhana G (2017) CFD analysis of hydrodynamic studies of a bubbling fluidized bed. Int J Mech Prod Eng Res Dev 7:341–350 . doi: 10.24247/ijmperddec201738
220. Solli K-A, Agu C (2017) Evaluation of drag models for CFD simulation of fluidized bed biomass gasification. Proc 58th Conf Simul Model (SIMS 58) Reykjavik, Iceland, Sept 25th – 27th, 2017 138:97–107 . doi: 10.3384/ecp1713897
221. Muthu Kumar M, Natarajan E (2009) CFD simulation for two-phase mixing in 2D fluidized bed. Int J Adv Manuf Technol. doi: 10.1007/s00170-008-1875-9
222. Zhao G, Shi X, Wu Y, et al (2019) 3D CFD simulation of gas-solids hydrodynamics and bubbles behaviors in empty and packed bubbling fluidized beds. Powder Technol 351:1–

15 . doi: 10.1016/j.powtec.2019.04.003

223. Gu J, Zhong W, Yu A (2019) Three-dimensional simulation of oxy-fuel combustion in a circulating fluidized bed. Powder Technol 351:16–27 . doi: 10.1016/j.powtec.2019.04.008
224. Chang J, Wu Z, Wang X, Liu W (2019) Two- and three-dimensional hydrodynamic modeling of a pseudo-2D turbulent fluidized bed with Geldart B particle. Elsevier B.V
225. Bahramian, Alireza, and Martin Olazar. 2011. "Pro Fi Ling Solid Volume Fraction in a Conical Bed of Dry Micrometric Particles : Measurements and Numerical Implementations." 212: 181–92.
226. Bandaru, K. S V S R, D. V S Murthy, and K. Krishnaiah. 2007. "Some Hydrodynamic Aspects of 3-Phase Inverse Fluidized Bed." China Particuology 5(5): 351–56.
227. Cho, Yong Jun et al. 2002. "Heat Transfer and Hydrodynamics in Two- and Three-Phase Inverse Fluidized Beds." Industrial and Engineering Chemistry Research 41(8): 2058–63.
228. Chung, S. F., and C. Y. Wen. 1968. "Longitudinal Dispersion of Liquid Flowing through Fixed and Fluidized Beds." AIChE Journal 14(6): 857–66.
229. Cornelissen, Jack T et al. 2007. "CFD Modelling of a Liquid – Solid Fluidized Bed." 62: 6334–48.
230. Das, Bimal, Uma Prasad Ganguly, and Sudip Kumar Das. 2010. "Inverse Fluidization Using Non-Newtonian Liquids." Chemical Engineering and Processing: Process Intensification 49(11): 1169–75.
231. Delgado, J. M.P.Q. 2006. "A Critical Review of Dispersion in Packed Beds." Heat and Mass Transfer/Waerme- und Stoffuebertragung 42(4): 279–310.
232. Gaikwad, R W. 2012. "Removal of Lead by Reverse Fluidization Using Granular Activated Carbon." 3(4): 314–19.
233. Geng, Shujun et al. 2017. "Prediction of Solids Residence Time Distribution in Cross- Fl Ow Bubbling Fl Uidized Bed." 320: 555–64.
234. Guo, Kai et al. 2000. "Synchronous Visual and RTD Study on Liquid Flow in Rotating Packed-Bed Contractor." Chemical Engineering Science 55(9): 1699–1706.
235. Hamdad, Imran, Shahrzad Hashemi, Dano Rossi, and Arturo Macchi. 2007. "Oxygen Transfer and Hydrodynamics in Three-Phase Inverse Fluidized Beds." Chemical Engineering Science 62(24): 7399–7405.
236. Han, Hee Dong et al. 2003. "Phase Hold-up and Critical Fluidization Velocity in a Three-Phase Inverse Fluidized Bed." Korean Journal of Chemical Engineering 20(1): 163–68.
237. Haribabu, K, and V Sivasubramanian. 2014. "Treatment of Wastewater in Fluidized Bed Bioreactor Using Low Density Biosupport." Energy Procedia 50: 214–21. http://dx.doi.org/10.1016/j.egypro.2014.06.026.

238. Iliuta, I, F C Thyrion, and O Muntean. 1998. “Axial Dispersion of Liquid in Gas-Liquid.” Institution of Chemical Engineers 76(January): 64–72.
239. Kalaga, Dinesh V., Anu Dhar, Sameer V. Dalvi, and Jyeshtharaj B. Joshi. 2014. “Particle-Liquid Mass Transfer in Solid-Liquid Fluidized Beds.” Chemical Engineering Journal 245: 323–41. http://dx.doi.org/10.1016/j.cej.2014.02.038.
240. Krishnaswamy, P. R., and L. W. Shemilt. 1973. “Frequency Response in Liquid Fluidized Systems Part I. Effect of Particle Density and Size.” The Canadian Journal of Chemical Engineering 51(6): 680–87.
241. Lakshmi, A C Vijaya et al. 2000. “Minimum Fluidization Velocity and Friction Factor in a Liquid-Solid Inverse Fluidized Bed Reactor.” Bioprocess Engineering 22: 461–66.
242. Il Lee, Kyoung et al. 2007. “Particle Dispersion in Viscous Three-Phase Inverse Fluidized Beds.” Chemical Engineering Science 62(24): 7060–67.
243. Mandal, D. 2015. “Hydrodynamics of Particles in Liquid – Solid Packed Fl Uidized Bed.” Powder Technology 276: 18–25. http://dx.doi.org/10.1016/j.powtec.2015.02.018.
244. Profile, S E E. 2014. “‘ Fluidized Bed Biofilm Reactor- A Novel Wastewater Treatment Reactor ’ ISSN 2249 – 9695 Original Article Fluidized Bed Biofilm Reactor – A Novel Wastewater Treatment Reactor.” (January).
245. Rajasimman, M, and C Karthikeyan. 2009. “Performance of Inverse Fl Uidized Bed Bioreactor in Treating Starch Wastewater.” 3(3): 235–39.
246. Rasteh, Mojtaba, Fatola Farhadi, and Alireza Bahramian. 2015. “Hydrodynamic Characteristics of Gas – Solid Tapered Fl Uidized Beds : Experimental Studies and Empirical Models.” Powder Technology 283: 355–67. http://dx.doi.org/10.1016/j.powtec.2015.06.002.
247. Renganathan, T., and K. Krishnaiah. 2004. “Liquid Phase Mixing in 2-Phase Liquid-Solid Inverse Fluidized Bed.” Chemical Engineering Journal 98(3): 213–18.
248. Sau, D. C., and K. C. Biswal. 2011. “Computational Fluid Dynamics and Experimental Study of the Hydrodynamics of a Gas-Solid Tapered Fluidized Bed.” Applied Mathematical Modelling 35(5): 2265–78.
249. Sivasubramanian, V, M Velan, K Haribabu, and B Deepanraj. 2014. “Holdup Studies in IFBR for Wastewater Treatment Holdup Studies in IFBR for Wastewater Treatment.” (August).
250. Tang, Wen-Tzung -T, and Liang-Shih -S Fan. 1989. “Hydrodynamics of a Three-phase Fluidized Bed Containing Low-density Particles.” AIChE Journal 35(3): 355–64.
251. Tang, Wen Tzung, and Liang Shih Fan. 1990. “Axial Liquid Mixing in Liquid-Solid and Gas-Liquid-Solid Fluidized Beds Containing Low Density Particles.” Chemical

Engineering Science 45(2): 543–51.

252. Ulaganathan, N., and K. Krishnaiah. 1996. “Hydrodynamic Characteristics of Two-Phase Inverse Fluidized Bed.” Bioprocess Engineering 15(3): 159–64.

253. Yu, Dianyu et al. 2018. “Numerical Simulation and Application of Nanomagnetic Enzyme in a Liquid-Solid Magnetic Fluidized Bed.” Process Biochemistry 75(July): 121–29. https://doi.org/10.1016/j.procbio.2018.09.019.

254. Ojima, S., Hayashi, K., & Tomiyama, A. (2014). Effects of hydrophilic particles on bubbly flow in slurry bubble column. International Journal of Multiphase Flow, 58, 154–167. https://doi.org/10.1016/j.ijmultiphaseflow.2013.09.005

255. Duduković, M. P., Larachi, F., & Mills, P. L. (2002). Multiphase catalytic reactors: A perspective on current knowledge and future trends. Catalysis Reviews - Science and Engineering, 44(1), 123–246. https://doi.org/10.1081/CR-120001460

256. Pourtousi, M., Sahu, J. N., & Ganesan, P. (2014). Effect of interfacial forces and turbulence models on predicting flow pattern inside the bubble column. Chemical Engineering and Processing: Process Intensification, 75, 38–47. https://doi.org/10.1016/j.cep.2013.11.001

257. Laborde-Boutet, C., Larachi, F., Dromard, N., Delsart, O., & Schweich, D. (2009). CFD simulation of bubble column flows: Investigations on turbulence models in RANS approach. Chemical Engineering Science, 64(21), 4399–4413. https://doi.org/10.1016/j.ces.2009.07.009

258. Silva, M. K., D’ávila, M. A., & Mori, M. (2012). Study of the interfacial forces and turbulence models in a bubble column. Computers and Chemical Engineering, 44, 34–44. https://doi.org/10.1016/j.compchemeng.2012.04.007

259. Tabib, M. V., Roy, S. A., & Joshi, J. B. (2008). CFD simulation of bubble column-An analysis of interphase forces and turbulence models. Chemical Engineering Journal, 139(3), 589–614. https://doi.org/10.1016/j.cej.2007.09.015

260. Cho, Y. J., Park, H. Y., Kim, S. W., Kang, Y., & Kim, S. D. (2002). Heat transfer and hydrodynamics in two- and three-phase inverse fluidized beds. Industrial and Engineering Chemistry Research, 41(8), 2058–2063. https://doi.org/10.1021/ie0108393

261. Shl, Y., Yu, Y. S., & Fan, L. T. (1984). Shi et al. (1984)-Ind. Eng. Chem. Fundam. 484–489

262. Kim, H. G., Lee, I. O., Chung, U. C., & Kim, Y. H. (2008). Fluidization Characteristics of Iron Ore Fines of Wide Size Distribution in a Cold Tapered Gas-Solid Fluidized Bed. ISIJ International, 40(1), 16–22. https://doi.org/10.2355/isijinternational.40.16

263. Schaafsma, S. H., Marx, T., & Hoffmann, A. C. (2006). Investigation of the particle flowpattern and segregation in tapered fluidized bed granulators. Chemical Engineering

Science, 61(14), 4467–4475. https://doi.org/10.1016/j.ces.2006.01.040

264. Kumar, U., & Agarwal, V. K. (2017). Simulation of 3D gas–solid fluidized bed reactor hydrodynamics. Particulate Science and Technology, 35(1), 1–13. https://doi.org/10.1080/02726351.2015.1119227

265. Vejahati, F., Mahinpey, N., Ellis, N., & Nikoo, M. B. (2009). CFD simulation of gas-solid bubbling fluidized bed: A new method for adjusting drag law. Canadian Journal of Chemical Engineering, 87(1), 19–30. https://doi.org/10.1002/cjce.20139

266. Goldschmidt, M. J. V., Kuipers, J. A. M., & Van Swaaij, W. P. M. (2001). Hydrodynamic modelling of dense gas-fluidised beds using the kinetic theory of granular flow: Effect of coefficient of restitution on bed dynamics. Chemical Engineering Science, 56(2), 571–578. https://doi.org/10.1016/S0009-2509(00)00262-1

267. Grace, J. R., & Taghipour, F. (2004). Verification and validation of CFD models and dynamic similarity for fluidized beds. Powder Technology, 139(2), 99–110. https://doi.org/10.1016/j.powtec.2003.10.006

268. Wang, S., Sun, J., Yang, Q., Zhao, Y., Gao, J., & Liu, Y. (2014). Numerical simulation of flow behavior of particles in an inverse liquid-solid fluidized bed. Powder Technology, 261, 14–21. https://doi.org/10.1016/j.powtec.2014.04.017

269. Kalaga, D. V., Reddy, R. K., Joshi, J. B., Dalvi, S. V., & Nandkumar, K. (2012). Liquid phase axial mixing in solid-liquid circulating multistage fluidized bed: CFD modeling and RTD measurements. Chemical Engineering Journal, 191, 475–490. https://doi.org/10.1016/j.cej.2012.02.091

270. Rahaman, M. S., Choudhury, M. R., Ramamurthy, A. S., Mavinic, D. S., Ellis, N., & Taghipour, F. (2018). CFD modeling of liquid-solid fluidized beds of polydisperse struvite crystals. International Journal of Multiphase Flow, 99, 48–61. https://doi.org/10.1016/j.ijmultiphaseflow.2017.09.011

271. Duan, C., Sheng, C., Wu, L., Zhao, Y., & He, J. (2015). CFD-DEM simulation of fluid-solid flow of a tapered column separation bed. International Journal of Mining Science and Technology, 25(5), 855–859. https://doi.org/10.1016/j.ijmst.2015.07.023

272. Bishop, R. F. (1975). Thermo-fluid Dynamic Theory of Two-Phase Flow. Physics Bulletin, 26(12), 544–544. https://doi.org/10.1088/0031-9112/26/12/034

273. Huilin, L., Yurong, H., Wentie, L., Ding, J., Gidaspow, D., & Bouillard, J. (2004). Computer simulations of gas-solid flow in spouted beds using kinetic-frictional stress model of granular flow. Chemical Engineering Science, 59(4), 865–878. https://doi.org/10.1016/j.ces.2003.10.018

274. Du, W., Bao, X., Xu, J., & Wei, W. (2006). Computational fluid dynamics (CFD) modeling

of spouted bed: Influence of frictional stress, maximum packing limit and coefficient of restitution of particles. Chemical Engineering Science, 61(14), 4558–4570. https://doi.org/10.1016/j.ces.2006.02.028

275. Kishore, H. U. K. A. (2020). Effect of temperature and apparent liquid viscosity on the hydrodynamics of liquid – solid tapered inverse fluidized bed : experimental studies compared with empirical models. SN Applied Sciences, 2(4), 1–13. https://doi.org/10.1007/s42452-020-2365-4

276. Upender, H., & Kishore, K. A. (2020). Effect of materials on hydrodynamics of cone-shaped inverse fluidized bed by experimental and CFD simulations. Materials Today: Proceedings, 21(xxxx), 1502–1512. https://doi.org/10.1016/j.matpr.2019.11.07

277. Wang D, Silbaugh T, Pfeffer R, Lin YS (2010) Removal of emulsified oil from water by inverse fluidization of hydrophobic aerogels. Powder Technol 203:298–309 . doi: 10.1016/j.powtec.2010.05.021

278. Alvarado-Lassman A, Rustrián E, García-Alvarado MA, et al (2008) Brewery wastewater treatment using anaerobic inverse fluidized bed reactors. Bioresour Technol 99:3009–3015 . doi: 10.1016/j.biortech.2007.06.022

279. Anantharaman A, Cocco RA, Chew JW (2018) Evaluation of correlations for minimum fluidization velocity (Umf) in gas-solid fluidization. Powder Technol 323:454–485 . doi: 10.1016/j.powtec.2017.10.016

280. Scott CD, Hancher CW, Shumate SE (2013) A Tapered Fluidized Bed as a Bioreactor. Enzym Eng XVIII:255–261 . doi: 10.1007/978-1-4757-5163-5_29

281. Lakshmi ACV, Balamurugan M, Sivakumar M, et al (2000) Minimum fluidization velocity and friction factor in a liquid-solid inverse fluidized bed reactor. Bioprocess Eng 22:461–466 . doi: 10.1007/s004490050759

282. Zhou D, Dong S, Wang H, Bi HT (2009) Minimum fluidization velocity of a three-phase conical fluidized bed in comparison to a cylindrical fluidized bed. Ind Eng Chem Res 48:27–36 . doi: 10.1021/ie8001974

283. Sur DH, Mukhopadhyay M (2017) Process aspects of three-phase inverse fluidized bed bioreactor: A review. J Environ Chem Eng 5:3518–3528 . doi: 10.1016/j.jece.2017.06.052

284. Campos-Díaz KE, Bandala-González ER, Limas-Ballesteros R (2012) Fluid bed porosity mathematical model for an inverse fluidized bed bioreactor with particles growing biofilm. J Environ Manage 104:62–66 . doi: 10.1016/j.jenvman.2012.03.019

285. Hamdad I, Hashemi S, Rossi D, Macchi A (2007) Oxygen transfer and hydrodynamics in three-phase inverse fluidized beds. Chem Eng Sci 62:7399–7405 . doi: 10.1016/j.ces.2007.08.066

286. Geng S, Qian Y, Zhan J, et al (2017) Prediction of solids residence time distribution in cross- fl ow bubbling fl uidized bed. 320:555–564 . doi: 10.1016/j.powtec.2017.07.085
287. Comte MP, Bastoul D, Hebrard G, et al (1997) Hydrodynamics of a three-phase fluidized bed - The inverse turbulent bed. Chem Eng Sci 52:3971–3977 . doi: 10.1016/S0009-2509(97)00240-6
288. Sabarunisha Begum S, Radha K V. (2014) Hydrodynamic behavior of inverse fluidized bed biofilm reactor for phenol biodegradation using Pseudomonas fluorescens. Korean J Chem Eng 31:436–445 . doi: 10.1007/s11814-013-0260-z
289. Krishnaiah K, Guru S, Sekar V (1993) Hydrodynamic studies on inverse gas-liquid-solid fluidization. Chem Eng J 51:109–112 . doi: 10.1016/0300-9467(93)80017-I
290. Rajasimman M, Karthikeyan C (2009) Performance of inverse fluidized bed bioreactor in treating starch wastewater. Front Chem Eng China 3:235–239 . doi: 10.1007/s11705-009-0020-0
291. Renganathan T, Krishnaiah K (2004) Stochastic Simulation of Hydrodynamics of a Liquid - Solid Inverse Fluidized Bed. 4405–4412 . doi: 10.1021/ie0304513
292. Lee DH, Epstein N, Grace JR (2000) Hydrodynamic Transition from Fixed to Fully Fluidized Beds for Three-Phase Inverse Fluidization. Korean J Chem Eng 17:684–690 . doi: 10.1007/BF02699118
293. Karamanev DG, Nikolov LN (1992) Bed Expansion of Liquid-Solid Inverse. 38:1916–1922
294. Fan LS, Muroyama K, Chern SH (1982) Hydrodynamic characteristics of inverse fluidization in liquid-solid and gas-liquid-solid systems. Chem Eng J 24:143–150 . doi: 10.1016/0300-9467(82)80029-4
295. Cho YJ, Park HY, Kim SW, et al (2002) Heat transfer and hydrodynamics in two- and three-phase inverse fluidized beds. Ind Eng Chem Res 41:2058–2063 . doi: 10.1021/ie0108393
296. Amare, M., Worku, A., Kassa, A., Hilluf, W., 2020. Green synthesized silver nanoparticle modified carbon paste electrode for SWAS voltammetric simultaneous determination of Cd(II) and Pb(II) in Bahir Dar Textile discharged effluent. Heliyon 6, e04401. https://doi.org/10.1016/j.heliyon.2020.e04401.
297. Bansal, M., Patnala, P.K., Dugmore, T., 2020. Adsorption of Eriochrome Black-T(EBT) using tea waste as a low cost adsorbent by batch studies: A green approach for dye effluent treatments. Curr. Res. Green Sustain. Chem. 3, 100036. https://doi.org/10.1016/j.crgsc.2020.100036.
298. Hynes, N.R.J., Kumar, J.S., Kamyab, H., Sujana, J.A.J., Al-Khashman, O.A., Kuslu, Y., Ene, A., Suresh Kumar, B., 2020. Modern enabling techniques and adsorbents based dye removal with sustainability concerns in textile industrial sector -A comprehensive review. J. Clean.

Prod. 272, 1–17. https://doi.org/10.1016/j.jclepro.2020.122636

299. Qamar, S.A., Ashiq, M., Jahangeer, M., Riasat, A., Bilal, M., 2020. Chitosan-based hybrid materials as adsorbents for textile dyes–A review. Case Stud. Chem. Environ. Eng. 2, 100021. https://doi.org/10.1016/j.cscee.2020.100021

300. Venkataraghavan, R., Thiruchelvi, R., Sharmila, D., 2020. Statistical optimization of textile dye effluent adsorption by Gracilaria edulis using Plackett-Burman design and response surface methodology. Heliyon 6. https://doi.org/10.1016/j.heliyon.2020.e05219

List of papers published in journals

1. Upender, H., Kishore, K.A. Effect of temperature and apparent liquid viscosity on the hydrodynamics of liquid–solid tapered inverse fluidized bed: experimental studies compared with empirical models. SN Appl. Sci. 2, 622 (2020). https://doi.org/10.1007/s42452-020-2365-4
2. H. Upender, K. Anand Kishore “Effect of materials on hydrodynamics of cone-shaped inverse fluidized bed by experimental and CFD simulations”, Materials today proceedings, Volume 21, Part 3, 2020, Pages 1502-1512
3. H. Upender, L. Pavan Kumar and K. Anand Kishore “Hydrodynamic studies comparison by simulation with experimental results of reverse fluidized bed”, Journal of engineering and technology, Vol 7, No 3.29 (2018)

4. H. Upender, K. Anand Kishore "Effect of restitution coefficient in CFD simulation of solid-liquid tapered inverse fluidized-bed hydrodynamics" PalArchs journal of Archology of Egpyt/Egyptology, Vol 17(9) (2020).
5. H. Upender, K. Anand Kishore "A study on removal of dye, COD, turbidity, and DO enhancement from synthetic textile wastewater by using natural adsorbent in RSM design: Isotherm analysis" chemical papers, https://doi.org/10.1007/s11696-021-01709-5.
6. H. Upender, K. Anand Kishore, "Mean residence time and mass fraction of tracer in a liquid-solid tapered inverse fluidized bed: numerical modelling with experimental validation" Accepted in Journal of the Taiwan Institute of Chemical Engineers in Elsevier publisher.
7. H. Upender, K. Anand Kishore "Hydrodynamic studies on solid-liquid tapered inverse fluidized bed: Comparison of experimental results with different drag models in 3D CFD simulations" comments received, revised and submitted in South African journal of chemical engineering in Elsevier publisher.
8. H. Upender, K. Anand Kishore," Effects of operating variables in adsorption for azo dye textile wastewater: Optimization of process parameters by Box-Behnken design of RSM: Isothermal and kinetic studies". Communicated (Under review) to Multiscale and Multidisciplinary Modeling, Experiments and Design springer publisher.

Workshops and Seminars Attended.

1. Hydrodynamic Studies of Inverse fluidized bed and CFD Simulation Analysis", proceedings of 2nd International Conference on New Frontiers in Chemical, Energy and Environmental Engineering (INCEEE-2019) organized by Department of Chemical Engineering, NIT Warangal during 15-16 February, 2019.
2. "CFD simulation on hydrodynamics of tapered fluidized bed; a comparative study", proceedings of National conference on Computational modelling of fluid dynamics problems (CMFDP-2019), organized by Department of Mathematics, NIT Warangal during 18-20 January, 2019.
3. **"**Hydrodynamic studies comparison by simulation with experimental results of reverse fluidized bed", International conference on Research Advancements in Applied

Engineering Sciences, Computer and Communication Technologies held during 12-13 July, 2018 organized jointly by BVRIT, Narsapur, Medak.

4. "CFD Simulation of Inverse Fluidization", 206th International Conference on Chemical and Biochemical Engineering (ICCBE), held at Istanbul, Turkey during 23-24 March, 2018.
5. **"**Minimum Fluidization Velocity studies by using Pressure Drop in Inverse Fluidization**",** 5th International Conference on Advancement in Engineering, Applied Science and Management (ICAEASM-2017) at Institution of Electronics and Telecommunication Engineers, Ganganagar, Bengaluru, Karnataka, India on 26th November 2017.